Der Universität Bayreuth zur Erlangung des Grades eines Doktors der Naturwissenschaften (Dr. rer. nat.) vorgelegte Abhandlung

Structure Formation in Organic and Synthetic Polymers using Atomistic and Coarse-grained Simulations

von

Sanwardhini Pantawane

Geboren in Nagpur, India

Tag der Einreichung: 17.11.2022
Tag des Kolloquiums: 25.01.2023

1. Erstgutachter: Prof. Dr. Stephan Gekle
2. Zweitgutachter: Prof. Dr. Harald Oberhofer
3. Drittprüfer: Prof. Dr. Matthias Schmidt
4. Vorsitzende : Prof. Dr. Anna Köhler

Biofluid Simulation and Modeling
Fakultät für Mathematik, Physik und Informatik
Universität Bayreuth

UNIVERSITÄT BAYREUTH

To my mother, Rekha

Abstract

Polymers, also known as macromolecules, composed of many smaller repeating units, have been among us since the beginning of time, though it is only in the 20th century that we started mastering the art of synthesizing them on industrial scale. The production of polymers for applications in various fields calls for prior detailed knowledge of their characterization via: (i) molecular structure, (ii) conformational, (iii) thermal and, (iv) bulk properties (self-arrangement, orientation, packing structure), (v) cross linking properties for gelation processes among others, before they are transformed into final products. Given the complexity of their forms and the specialized knowledge required to handle each polymer separately, generalization of their behavior is almost impossible. Therefore, this thesis aims at individually covering aspects related to the conformational properties of the polymers with applications in organic-thin-film transistors, 3D bio-fabrication, sustainable bioplastics and dental implants.

Computational modeling is a paramount aspect in the interpretation of results obtained via experiments as they provide a window to look into nanoscales to visualize the conformation attained by the polymer that explain their macroscopic properties. Theoretical and computational evaluations save up the resources involved in carrying out large-scaled experimental studies and serve as a guide for practical trails. Therefore we carried out investigation solely using computer simulations via molecular dynamics (MD) simulations employing atomistic and coarse grained models for quantifying the properties of different polymers. The computational framework presented here constitutes a systematic approach to procure morphological and structural properties of Poly(3-hexylthiophene) (P3HT), interaction of biodegradable polymers like Polylactic acid (PLA), Polyglycolic acid (PGA) and Polyhydroxyalkanoate (PHA) with DNA, gelation of Hyaluronic acid and Alginate, and bulk properties of Monofunctional Vinyl Cyclopropanes (VCP). The first chapter gives an introduction into the topic and the motivation behind each studied polymer in detail.

The working principles of organic solar cells are dependent on the morphology of the conjugated polymer P3HT and are inspected in chapter 3 and 7. Chapter 3 creates a database for proper classification of stiff, flexible and semi-flexible polymers by modeling monomers as Lennard Jones beads with different attractive potentials. This classification scheme is then applied to atomistic and coarse grained models of P3HT to solve a long going debate on the flexibility of the polymer. The collapse transition occurring due to sudden changes in conformation of polymers as a virtue of their stiffness and change in temperature and its significance in the P3HT based organic solar cells is the key highlight of this chapter.

Aliphatic polyesters such as PLA, PGA and PHA commonly used in biodegradable products largely constitute for the microplastic debris and has raised much concerns in the last 10 years. Their effect on our environmental niche raises the question if they are harmful to our bodies for causing permanent damages. With this motivation, we study the interaction of the aforementioned biodegradable polymers with DNA in chapter 4. We carry out free energy MD simulations based on atomistic force-fields between the

polymers and DNA. These simulations provide the extent of affinity each of the DNA nucleobases shows with each of the polymers.

The polymers used in 3D bio-printing are capable of forming stable hydrogel structures that facilitate cell survival, differentiation and homogeneous cellular matrix in the constructs, because of their gel formation properties. Hyaluronic acid and Alginate are two such widely used polymer. 3D printing is a macroscopic process and beyond the scope of atomistic simulations. Therefore, we need simplified polymer models for faster and longer computation of the micro channels. Chapter 5 explains the methodology to create and validate martini coarse grained force-field from atomistic force-fields using a bottom up approach. It uses the Hyaluronic acid and Alginate as examples for this process and exhibits that such models are capable of capturing the gel formation processes within minutes that would otherwise require a computation time in the range of months.

In chapter 6 we study VCPs, photopolymerizable resins, used in dental fillings due to their low shrinkage during polymerization. We compare bulk properties such as H-bonding, radial distribution functions, orientation-order parameter of VCPs with different side chains. We aim at recognizing the connection of H-bond formation to the pre-polymerization organization and compare the results with experimental polymerization rates of the monomers.

While chapter 3 studies conformational properties of individual P3HT polymers using atomistic and martini coarse grained model, chapter 7 uses the later model to create stable isolated and continuous brushes and compares them when subjected to particle/s inclusion. Conjugated polymers like P3HT are able to form π-π bonds in the brush regime (at high grafting density) that act as charge carriers in transistors. The focus of chapter 7 is to quantify the effect of a particle inclusion on spatial polymer rearrangement around an external particle and its effect on the π-π bonds of the brush for applications in biosensors.

Key words · Poly(3-hexylthiophene) · Microplastics · Hyaluronic acid · Alginates · Monofunctional vinyl cyclopropanes · molecular dynamics simulations · organic and synthetic polymers

Zusammenfassung

Polymere, auch Makromoleküle genannt, die aus vielen kleineren, sich wiederholenden Einheiten zusammengesetzt sind, gibt es seit Anbeginn der Zeit, aber erst im 20. Jahrhundert haben wir begonnen, sie in industriellem Maßstab zu synthetisieren. Die Herstellung von Polymeren für Anwendungen in verschiedenen Bereichen erfordert detaillierte Kenntnisse ihrer Charakterisierung über: (i) molekulare Struktur, (ii) Konformation, (iii) thermische und (iv) Volumeneigenschaften (Selbstanordnung, Orientierung, Packungsstruktur), (v) Vernetzungseigenschaften unter anderem für Gelierungsprozesse, bevor sie in Endprodukte umgewandelt werden. Angesichts der Komplexität ihrer Formen und des Spezialwissens, das erforderlich ist, um jedes Polymer einzeln zu handhaben, ist eine Verallgemeinerung ihres Verhaltens fast unmöglich. Daher zielt diese Arbeit darauf ab, Aspekte im Zusammenhang mit den Konformationseigenschaften von Polymeren mit Anwendungen in organischen Dünnschichttransistoren, 3D-Biofabrikation, nachhaltigen Biokunststoffen und Zahnimplantaten individuell abzudecken.

Computermodellierung ist ein wichtiger Aspekt bei der Interpretation von Ergebnissen, die durch Experimente erhalten wurden. Sie bietet ein Fenster, um in Nanoskalen zu blicken und um die vom Polymer erreichte Konformation zu visualisieren, die ihre makroskopischen Eigenschaften erklärt. Theoretische und numerische Auswertungen sparen Ressourcen bei der Durchführung groß angelegter experimenteller Studien und dienen als Leitfaden für praktische Versuche. Daher wurden in dieser Dissertation ausschließlich Computersimulationen über Molekulardynamik (MD)-Simulationen unter Verwendung atomistischer und *coarse-grained* Modelle zur Quantifizierung der Eigenschaften verschiedener Polymere durchgeführt. Die hier verwendeten Rechenmethoden stellen einen systematischen Ansatz dar, um morphologische und strukturelle Eigenschaften von Poly(3-hexylthiophen) (P3HT), Wechselwirkung von biologisch abbaubaren Polymeren wie Polymilchsäure (PLA), Polyglykolsäure (PGA) und Polyhydroxyalkanoat (PHA) mit DNA, die Gelierung von Hyaluronsäure und Alginat, sowie Volumeneigenschaften von monofunktionellem Vinylcyclopropan (VCP) zu ermitteln. Das erste Kapitel gibt eine Einführung in das Thema und die Motivation hinter jedem im Detail untersuchten Polymer.

Die Arbeitsprinzipien organischer Solarzellen hängen von der Morphologie des konjugierten Polymers P3HT ab, welches in Kapitel 3 und 7 untersucht wird. Kapitel 3 erstellt eine Datenbank für die korrekte Klassifizierung von steifen, flexiblen und halbflexiblen Polymeren, indem Monomere als Lennard-Jones-Partikel mit unterschiedlichen attraktiven Potenzialen modelliert werden. Dieses Klassifizierungsschema wird dann auf atomistische und grobkörnige Modelle von P3HT angewendet, um eine lang andauernde Debatte über die Flexibilität des Polymers zu lösen. Der Kollapsübergang, der aufgrund plötzlicher Konformationsänderungen von Polymeren als aufgrund ihrer Steifheit und Temperaturänderung auftritt, und seine Bedeutung in P3HT-basierten organischen Solarzellen ist das wichtigste Highlight dieses Kapitels.

Aliphatische Polyester wie PLA, PGA und PHA, die üblicherweise in biologisch ab-

baubaren Produkten verwendet werden, stellen große Teile des Mikroplastikabfalls dar und haben in den letzten 10 Jahren viel an Aufmerksamkeit gewonnen. Ihre Wirkung auf unsere Umweltnische wirft die Frage auf, ob sie in unserem Körper dauerhafte Schäden verursachen. Mit dieser Motivation untersuchen wir in Kapitel 4 die Wechselwirkung der oben erwähnten biologisch abbaubaren Polymere mit DNA. Wir führen Freie Energie MD Simulationen basierend auf atomistischen Kraftfeldern zwischen den Polymeren und der DNA durch. Diese Simulationen stellen das Ausmaß der Affinität jeder der DNA-Nukleobasen mit jedem der Polymere bereit.

Die beim 3D-Biodruck verwendeten Polymere sind aufgrund ihrer Gelierungseigenschaften in der Lage, stabile Hydrogelstrukturen zu bilden, die das Überleben der Zellen, die Differenzierung und eine homogene Zellmatrix in den Konstrukten erleichtern. Hyaluronsäure und Alginat sind dabei zwei weit verbreitete Polymere. 3D-Druck ist ein makroskopischer Prozess und außerhalb des Rahmens atomistischer Simulationen. Daher benötigen wir ein vereinfachtes Polymermodell für eine schnellere und längere Berechnung von Mikrokanalströmungen. Kapitel 5 erläutert die Methodik zur Erstellung und Validierung eines grobkörnigen *Martini*-Kraftfelds aus atomistischen Kraftfeldern unter Verwendung eines *bottom-up*-Ansatzes. Wir verwenden Hyaluronsäure und Alginat als Beispiele für diesen Prozess und zeigen, dass solche Modelle in der Lage sind, den Gelbildungsprozess zu reproduzieren.

Während Kapitel 3 die Konformationseigenschaften einzelner P3HT-Polymere unter Verwendung des atomistischen und grobkörnigen Martini-Modells untersucht, verwendet Kapitel 7 das letztere Modell, um stabile isolierte und kontinuierliche Bürstensturkturen zu erstellen, und vergleicht sie, wenn sie dem Einschluss von Partikeln ausgesetzt sind. Konjugierte Polymere wie P3HT können im Bürstenregime (bei hoher Pfropfungsdichte) π-π-Bindungen ausbilden, die als Ladungsträger in den Transistoren wirken. Der Schwerpunkt von Kapitel 7 liegt auf der Quantifizierung der Auswirkung eines Partikeleinschlusses auf die räumliche Polymerumlagerung um ein Fremdpartikel und deren Auswirkung auf die π-π-Bindungen der Bürste für Anwendungen in Biosensoren.

Schlüsselwörter · Poly(3-hexylthiophen) · Mikroplastik · Hyaluronsäure · Alginate · Monofunktionelle Vinylcyclopropane · Molekulardynamiksimulationen · organische und synthetische Polymere

Publications for this thesis

1. S. Pantawane and S. Gekle (2022). Temperature-Dependent Conformation Behavior of Isolated Poly (3-hexylthiopene) Chains. Polymers 14, 550. DOI: 10.3390/polym14030550

2. Effect of particle insertion on Poly(3-hexylthiopene) brush's $\pi - \pi$ stacking. Submitted to Computational Materials Science.

3. S. Schumacher, S. Pantawane, S. Gekle and S. Agarwal. Theoretical and experimental study of monofunctional vinyl cyclopropanes, bearing hydrogen bond enabling side chains. Macromolecules 54, 11-21. DOI: 10.1021/acs.macromol.0c02490

4. S. Schumacher, S. Pantawane, S. Gekle and S. Agarwal. The Effect of Hydrogen Bonding on Polymerization Behavior of Monofunctional Vinyl Cyclopropane-amides with Different Side Chains. Macromolecular Chemistry and Physics. DOI: 10.1002/macp.202200155

Contents

1 Introduction **3**
- 1.1 A short history . . . 4
- 1.2 Computer simulations . . . 5
- 1.3 Poly(3-hexylthiophene) . . . 6
- 1.4 Microplastics . . . 8
- 1.5 Hydrogels . . . 9
- 1.6 Vinyl cyclopropanes . . . 11
- 1.7 Polymer Brushes . . . 12
- References . . . 14

2 Molecular dynamics simulations **19**
- 2.1 Introduction . . . 20
- 2.2 Structure of the system . . . 21
- 2.3 Force fields . . . 23
  - 2.3.1 Bonded interactions . . . 23
  - 2.3.2 Non-bonded interactions . . . 25
- 2.4 Energy minimization . . . 26
- 2.5 Integrating Newton's second law of motion . . . 27
- 2.6 Simulation box and Periodic boundary conditions . . . 28
- 2.7 Temperature and Pressure . . . 29
  - 2.7.1 Thermostats . . . 30
  - 2.7.2 Barostats . . . 30
- 2.8 Free Energy and umbrella sampling . . . 31
- 2.9 Coarse grained Models . . . 33
  - 2.9.1 Martini Coarse graining in Carbohydrates . . . 35
- References . . . 38

3 Poly(3-hexylthiophene) chains and their temperature-dependent conformation behavior **41**
- 3.1 Introduction . . . 42
- 3.2 System setup . . . 43
  - 3.2.1 Lennard Jones Polymer . . . 43

3.2.2 Atomistic model of P3HT . . . 44
3.2.3 Martini CG model of P3HT . . . 47
3.3 Results and Discussion . . . 50
3.3.1 Lennard Jones Polymer . . . 50
3.3.2 Atomistic P3HT . . . 58
3.3.3 Martini P3HT in vacuum . . . 61
3.3.4 Martini P3HT in THF solvent . . . 64
3.4 Conclusion . . . 69
References . . . 70

4 Microplastics: Monomer effects of biodegradable polymers on building blocks of DNA 75
4.1 Introduction . . . 76
4.2 System setup . . . 77
4.3 Results and Discussion . . . 79
4.3.1 Monomer--Nucleobase Interaction . . . 79
4.3.2 Oligomer-- Nucleobase Interaction . . . 80
4.3.3 Oligomer -- DNA Interaction . . . 82
4.4 Conclusion . . . 83
4.5 Appendix of Chapter 3 . . . 84
References . . . 85

5 Martini coarse grained models of hyaluronic acid and alginate 89
5.1 Introduction . . . 90
5.2 Simulation details . . . 91
5.2.1 Atomistic simulations . . . 91
5.2.2 Coarse grained simulations . . . 91
5.3 Hyaluronic Acid . . . 92
5.3.1 CG Mapping of HA disaccharide . . . 92
5.3.2 CG mapping of HA octasaccharide . . . 97
5.3.3 Gel Formation . . . 100
5.4 Alginate . . . 103
5.4.1 CG Mapping of AG tetrasaccharide . . . 103
5.4.2 CG Mapping of AG octasaccharide . . . 108
5.4.3 Alginate Aggregation . . . 110
5.4.4 Alginate Gel . . . 111
5.5 Conclusion . . . 113
5.6 Appendix of Chapter 3 . . . 114
5.6.1 CG model bonded-parameters for HA disaccharide . . . 114
5.6.2 CG model bonded-parameters for HA octasaccharide . . . 115
5.6.3 CG model bonded-parameters for AG tetrasaccharide . . . 118
5.6.4 CG model bonded-parameters for AG octasaccharide . . . 120
References . . . 123

6 Monofunctional Vinyl Cyclopropanes: 125
6.1 Introduction . . . 126
6.2 Simulation details . . . 126
6.3 Results and Discussion . . . 128
6.3.1 Part 1 : VCPs with different side chains . . . 128
6.3.2 Part 2: VCP-amides with different side chains . . . 133
6.4 Conclusion . . . 136
6.5 Appendix of Chapter 3 . . . 137
References . . . 138

7 Poly(3-hexylthiophene) brushes: 141
7.1 Introduction . . . 142
7.2 Simulation details . . . 144
7.2.1 P3HT model . . . 144
7.2.1.1 System containing isolated brush . . . 144
7.2.1.2 System containing continuous brush . . . 145
7.2.2 Lennard Jones Particle . . . 146
7.2.3 $\pi - \pi$ stacking criteria . . . 146
7.3 Results and Discussion . . . 147
7.4 Conclusion . . . 176
References . . . 177

8 Conclusion 179
8.1 Poly(3-hexylthiophene) chains and their temperature-dependent conformation behavior . . . 180
8.2 Microplastics: Monomer effects of biodegradable polymers on building blocks of DNA . . . 181
8.3 Martini coarse grained models of hyaluronic acid and alginate . . . 182
8.4 Monofunctional Vinyl Cyclopropanes: Effect of hydrogen bonding on their polymerization behavior . . . 183
8.5 Poly(3-hexylthiophene) brushes: Effect of Particle Insertion on $\pi - \pi$ stacking . . . 184
References . . . 185

List of Figures

1.1 Connection between the experiments, the theory and the computer simulations 5
1.2 Temperature dependent absorption of P3HT predicting a conformational change in P3HT as the possible reason for the red shift– literature result from the experiments of Panzer et al. 6
1.3 Polymer structures of the radical ring-opening polymerization of VCPs. 11
1.4 Principal orientation of $\pi - \pi$ interactions in aromatic rings 12

2.1 The common algorithm that MD is formulated on. 20
2.2 Structural formula of (a) Poly(3-hexylthiophene) and (b) Polylactic acid monomers showing all the different atoms in the molecule. 22
2.3 (a) Bond stretching, (b) angle stretching, (c) proper dihedral angle torsion and (d) improper torsion dihedral between different atoms i, j, k and l. The proper dihedral angle (c) is defined as the angle between the plane formed by atom i, j and k and the plane formed by j, k and l. The improper dihedral angle (d) is the angle between planar atoms i, j, k and l. 24
2.4 Energy minimization scheme. Molecular dynamics uses thermal energy to move smoothly over surfaces. 27
2.5 *Leap-frog* algorithm. The velocities are first calculated at time $t + \frac{1}{2}\Delta t$. These are used to calculate positions, $\mathbf{r}$ at $t+\Delta t$. In this way the velocities leap over the positions, and then the positions leap over the velocities. 28
2.6 Periodic boundary conditions in two dimensions 29
2.7 Illustration of coarse graining bead structure for an atomistic model. . 34
2.8 Coarse-grained mapping for mono- and disaccharides. (a) Monosaccharides are represented by three beads B1-B3. (b) Disaccharides are represented by six beads B1-B6 and the bond between B2 and B4 represents the glycosidic bond. 36
2.9 Coarse-grained mapping for Hyaluronic disaccharide unit to understand polarity of beads. 36

3.1 (a) Model LJ polymer (b) LJ potential with different C_6 values used to tune stiffness of polymers. (c) Angle bending potential with k^θ used to change polymer stiffness. 43
3.2 (a) Schematic representation of P3HT. (b) Atomistic model of P3HT used for all atom simulations. 44
3.3 Snapshot of P3HT packing structure of 32 P3HT polymers used for validation. (a) Top view with $\pi - \pi$ stacking axis towards the viewer. (b) Side view with P3HT backbone towards the viewer 45
3.4 Torsional population at 300K for P3HT chain lengths $n = 13$ and 30. Results of α, $\beta_1$and β_2 from the literature of Bhatta et al. are shown in (a), (c) and (e) respectively. For validation of our model, α, $\beta_1$and β_2 torsional angle populations from simulations carried out in this work are plotted in (b), (d) and (f) respectively. 46
3.5 (a) 3-mer P3HT atomistic model. (b) CG mapping with mention of respective Martini bead types (c) Martini CG model with bead names used for validation. 47
3.6 Bond and angle distributions for P3HT (our simulation results in green and literature values in red.) Each label indicates the beads for whom the distribution is shown. 48
3.7 (a) Coarse grained (green bead) and atomistic (solid schematic) representation of THF. (b) Radial distribution function ($g(r)$) of THF obtained from our simulations (blue line) and its comparison to the literature data published by Patti et al (black dots) 49
3.8 $\langle S^2 \rangle$ vs Temperature for LJ polymer with 200 monomers (a) with varying non-bonded parameter C_6 and (b) varying bonded parameter k_θ. 50
3.9 $\langle D_{max} \rangle$ vs Temperature for LJ polymer with 200 monomers (a) with varying non-bonded parameter C_6 and (b) varying bonded parameter k_θ. 51
3.10 Log-log plot of $\langle S^2 \rangle$ against the number of monomers n at different temperatures. The dotted line represents the theoretical curve of 3.2. . 52
3.11 Distribution of $\langle S^2 \rangle$ for (a) stiff ($C_6 = 0.0$), (b) semiflexible ($C_6 = 0.00045$) and (c) flexible ($C_6 = 0.001$) polymers. 52
3.12 Distribution of D_{max} for (a) stiff ($C_6 = 0.0$), (b) semiflexible ($C_6 = 0.00045$) and (c) flexible ($C_6 = 0.001$) polymers. 53
3.13 From left to right illustration of *toroid*, *bundle*, *random coil*, *ring* and *hairpin*. (b) Color coded final conformations at a range of temperature for 50 simulations at different C6 values. (c) D_{max} distribution of the above five mentioned structures. 54
3.14 Structural phase diagram for polymers with varying angle bending potential at different temperatures. (a) Figure taken from Zierenberg et al. (copyright is open access) and (b) phase plot from our LJ simulations for comparison. 55

3.15 State diagram of polymers with different bending constant as a function of inverse of temperature. (a) Results taken from Ivanov et al. (b) Simulation results of our LJ polymer model using molecular dynamics. 56
3.16 The maximum distance (D_{max}) between monomers for the atomistic P3HT model in vacuum at different temperatures (T in Kelvin). (a) The averaged D_{max} as a function of T shows a sigmoidal increase at very high and a slight increase towards low temperatures (inset). (b) The D_{max} distributions at different temperatures exhibit three clear peaks corresponding to *toroids*, *globules* and *bundles* (from left to right) which are illustrated in (c). 58
3.17 (a) Color coded final conformations at a range of temperature for 50 simulations for atomistic P3HT in vacuum. (b) D_{max} distributions used for *toroid*, *globules* and *bundles*. 59
3.18 Typical toroids, globules and bundles found in the atomistic P3HT simulations at 300K 60
3.19 The maximum distance (D_{max}) between monomers for the Martini model of P3HT in vacuum at different temperatures (T in Kelvin). (a) The averaged D_{max} as a function of T shows a sigmoidal increase at very high and a slight increase towards low temperatures (inset). (b) The D_{max} distributions at different temperatures exhibit three clear peaks corresponding to *toroids*, *globules* and *bundles* (from left to right) which are illustrated in (c). 62
3.20 (a) Color coded final conformations at a range of temperature for 50 simulations for Martini CG P3HT in vacuum. (b) D_{max} distributions used for *toroid*, *globules* and *bundles*. 62
3.21 Typical *toroids*, *globules* and *bundles* found in Martini CG P3HT vacuum simulations at 300K. 63
3.22 The maximum distance (D_{max}) between monomers for the Martini model of P3HT in THF solvent at different temperatures (T in Kelvin). (a) The averaged D_{max} as a function of T shows a sigmoidal increase at very high and a slight increase towards low temperatures (inset). (b) The D_{max} distributions at different temperatures exhibit three clear peaks corresponding to *toroids*, *globules* and *bundles* (from left to right) which are illustrated in (c). Comparison between (b) and figure 1.2 shows that the transition captured in these simulations qualitatively explains the shift in the absorption spectra reported experimentally. 65
3.23 (a) Color coded final conformations at a range of temperature for 50 simulations for Martini CG P3HT in THF solvent. (b) D_{max} distributions used for *toroid*, *globules* and *bundles*. 66
3.24 D_{max} vs T between monomers for the Martini model of P3HT with $n = 68$ and $n = 112$ in THF solvent. 66
3.25 Probability of conjugation lengths in unaggregated and aggregated Martini P3HT in THF solvent. 67

3.26 Typical *toroids*, *globules* and *bundles* found in Martini CG P3HT solvent simulations at 300K. 68

4.1 Schematic illustration of (a) PLA, (b) PGA and (c) PHA polymers used in biodegradable materials used in this study. Snapshot of the monomers of the respective polymers used for the monomer-nucleobase interation are shown in (d), (e) and (f). 78
4.2 Snapshots of the nucleobases : (a) adenine, (b) cytosine, (c) guanine amd (d) thymine used for the monomer-nucleobase interation. 78
4.3 The free energy calculated by umbrella sampling as a function of the com-com distance between (a)PLA, (b) PGA and (c) PHA and the nucleobases A, G, C and T. 80
4.4 Angle distribution between the vectors consisting the nucleobase plane and C-C bond of PLA (a) at $r = 0.4nm$ and (b) at $r = 4.8nm$. 80
4.5 Snapshot of the structure of (a)PLA, (b)PGA and (c) PHA poligomer with 5 repeating units. 81
4.6 The free energy calculated by umbrella sampling as a function of the com-com distance between PLA oligomer with 5 repeating units and the nucleobases A, C, G and T. 81
4.7 Strucuture of the DNA hairloop in: (a) cartoon and (b) atomistic form used for the oligomer-DNA interation. 82
4.8 The free energy calculated by umbrella sampling as a function of the com-com distance between PLA, PGA and PHA oligomers with 5 repeating units and the spatially constrained DNA strand. 82

5.1 Martini coarse graining mapping scheme for (a) HA1-3 and (b) HA1-4 disaccharides. (c) CG representation of the model. Assignment of bead types for (d) HA1-3 and (e) HA1-4 disaccharides. 92
5.2 Bond lengths of AA and CG simulations for (A) HA1-3 and (B) HA1-4 disaccharides. 94
5.3 Angle distributions of AA and CG representations for (A) HA1-3 and (B) HA1-4 disaccharides. 95
5.4 Dihedral angle distributions of AA and CG representations for (A) HA1-3 and (B) HA1-4 disaccharides. 96
5.5 (a) Atomic representation of HA octasaccharide. (b) 4 HA CG disaccharide from previous section. (c) Connecting 4 HA CG disaccharide to create one HA octasaccharide. Bond, angle and dihedral parameters in the gray zone are used from HA disaccharide model of previous section, and in the red zone are matched additionally to the atomistic model. 97
5.6 Angle distributions of AA and CG representations for (A) HA1-3 and (B) HA1-4 octasaccharides. 98

5.8 (a) End to end distance ($R_{\text{end to end}}$), (b) radius of gyration (R_g) and (c) Root mean squared deviation ($RMSD$) for AA and CG models of HA octasaccharide. 99
5.7 Dihedral angle distributions of AA and CG representations for (A) HA1-3 and (B) HA1-4 octasaccharides. 99
5.9 The simulation configuration of HA gel at different NaCl-$CaCl_2$ concentrations. 101
5.10 Area of HA gel with 100mM NaCl vs varying $CaCl_2$concentrations. . . 102
5.11 (a) Atomistic schematic of Alginate tetrasaccharide. (b) Martini CG mapping of the tetrasaccharide and (c) its CG model. 103
5.12 Bond lengths of all-atom (AA) and martini coarse-grained (CG) model for alginate tetrasaccharide. 104
5.13 Angle distributions of all-atom (AA) and martini coarse-grained (CG) model for alginate tetrasaccharide. 106
5.14 Dihedral angle distributions of all-atom (AA) and martini coarse-grained (CG) model for alginate tetrasaccharide. 107
5.15 (a) Atomistic representation of alginate octasaccharide. (b) Alginate CG mapping. (c) Alginate octasaccharide CG model. 108
5.16 Angle distributions of all-atom (AA) and martini coarse-grained (CG) model for alginate octasaccharide. 109
5.17 Angle distributions of all-atom (AA) and martini coarse-grained (CG) model for alginate octasaccharide. 110
5.18 (a) End to end distance ($R_{\text{end to end}}$), (b) radius of gyration (R_g) and (c) Root mean squared deviation ($RMSD$) for AA and CG models of alginate octasaccharide. 110
5.19 Snapshots of bundle formation and zipper mechanism from martini coarse grained alginate simulations. 111
5.20 Simulation snapshot of the (a) the complete polymer gel with 100mM NaCl and 100mM $CaCl_2$ concentrations. The black box of (a) is emphasized in (b) and (c) that exhibit views along y-z-plane showing phase separation and x-y plane showing ion screening respectively. The polymer is shown in red, the ions in green and the water in blue. . . . 112
5.21 (a) Alginate gel snapshot for system with 100mM NaCl and 0mM CaCl ions. (b) Experimental TEM image of alginate gel produced by and taken from the work of Schuster et al. 113

6.1 (a) Snapshot of the simulation box in the NPT ensemble for determining the bulk properties of the VCPs. 127
6.2 Structures of monomer 1 (a), monomer 2 (b), monomer 3 (c), and monomer 4 (d) used for this study. Carbon is represented by green, Nitrogen by blue and oxygen by pink. The atom names will be utilized to refer to atoms for upcoming results. 128

6.3 (a) Hydrogen bonds as a function of time and (b) Time averaged hydrogen bonds with block error. 129
6.4 Herman's S factor calculated for angles between double C=C bonds averaged over all of the monomers as a function of time (a) and averaged over time (b). 129
6.5 Radial distribution function for atoms (a) C11, (b) C14, (c) C1, (d) C10, (e) C20 and (f) C21 atoms of all the four monomers for comparison. . 130
6.6 Radial distribution function for atoms (a) N16, (b) O13 and (c) O18 atoms of all the four monomers for comparison. 130
6.7 (a) Experimental results for the conversion percent over time of the monomers 1, 2, 3 and 4. (b) Expansion of the conversion percent for the first 2 hours. 131
6.8 Structures of monomer 1 (a), monomer 2 (b), monomer 3 (c), and monomer 4 (d) used for this study. Carbon is represented by green, Nitrogen by blue and oxygen by pink. The atom names will be utilized to refer to atoms for upcoming results. 133
6.9 (a) Hydrogen bonds as a function of time and (b) Time averaged hydrogen bonds with block error. 134
6.10 Herman's S factor calculated for angles between double C=C bonds averaged over all of the monomers as a function of time (a) and averaged over time (b). 134
6.11 Radial distribution function for atoms C1 (a), C2 (b), C3 (c), C4 (d), C5 (e), C6 (f), C13 (g) and O1 (h) atoms of all the four monomers for comparison. 135
6.12 Experimental results for the conversion percent over time of the monomers 1, 2, 3 and 4. 136
6.13 Root mean squared displacement of the monomers of (a) Part 6.3.1 and (b) Part 6.3.2 that show that the equilibration of the runs is achieved in all the cases with the first 5ns 137

7.1 Simulation snapshots of polymer brushes with (a) high grafting density (mushroom regime) and (b) low grafting density (brush regime). . . . 142
7.2 PART 2: Insertion of LJ particle in isolated brush 143
7.3 PART 3: Insertion of LJ particle in continuous brush 143
7.4 (a) Schematic representation of P3HT. (b) Mapping to CG model. (c) P3HT CG model used in this study. 144
7.5 Procedure used to include LJ particle into the isolated P3HT brush column. The polymer ends are pulled radially outward by applying a spring force to the end beads. The LJ particle of desired radius is place at the center of the pulled column. The pulling force is taken off and the system falls back engulfing the particle inside. 145

7.6 Procedure used to include LJ particle into the continuous P3HT brush column. The size of the LJ particle is subsequently increased from $R_p =$ 0.0 to 3.0nm at particle height H. 145

7.7 (a) stacking criteria formulated by Janiak et al. using Cambridge Structural Database for aromatic rings. (b) stacking criteria used in this work for computationally determining stack between two thiophene rings. 147

7.8 (a) Initial conformation for pull simulations and (b) snapshot for $n = 6$ the pull groups being the COM of the each chain. (c) Snapshot for $n = 9$ the pull groups being the COM of the each chain, where the polymer folds onto itself to form intra-chain $\pi - \pi$ bonds. (d) The PMF as function of the polymer distance between polymers of length $n - n$ (where n are the number of monomers). (e) The separation energy ΔE of two polymers increases linearly with the number of monomers. 148

7.9 Simulation snapshots of single particle in isolated P3HT brush (a) before insertion, (b) at $H = 13.5$nm, (c) at $H = 11.1$nm and (d) at $H = 8.4$nm. 149

7.10 Cylindrical radial monomer concentration profile for single particle insertion in isolated P3HT brush for particle radius $R_p = 0.5\text{nm}, 1\text{nm}, 2\text{nm}$, and 3nm, with height $H = 13.5$nm, 11.1nm, and 8.4nm. 151

7.11 Cylindrical radial $\pi - \pi$ bond density profile for single particle insertion in isolated P3HT brush for particle radius $R_p = 0.5\text{nm}, 1\text{nm}, 2\text{nm}$, and 3nm, with height $H = 13.5$nm, 11.1nm, and 8.4nm. 152

7.12 Histogram of the angle between monomer-monomer vector (the centroid vector) and the z-axis that do and do not form a $\pi-$ bond for (a) reference system and (b) for system with particle having $R_p = 3$nm and $x = 8.4$nm of isolated P3HT brush. Snapshot of a slice along the $y-$direction for (a) reference system and (b) system with particle. (e) Simple numerical analysis explaining the peaks at 45^0 and 135^0 of (a) and (b). 153

7.13 Percolation lines formed due to the formation of $\pi - \pi$ connection vectors for single particle insertion into an isolated brush column. View in the x-y plane (top) and x-z plane (bottom) for particle radius $R_p =$ 0.5nm, 1nm, 2nm, and 3nm, and particle height $H = 13.5\text{nm}, 11.1\text{nm}$, and 8.4nm. 156

7.14 Distribution of angle between the z-axis and the $\pi - \pi$ connection vector for single particle insertion in isolated brush with (a)$R_p = 3.0$nm; $H =$ 13.5nm and $R_p = 3.0$nm; $H = 8.4$nm (b) with $R_p = 0.5$nm; $H = 8.4$nm and $R_p = 3.0$nm; $H = 8.4$nm 157

7.15 Ratio of particles that form $\pi - \pi$ bonds with respect to the monomers that do not form $\pi - \pi$ bonds for single particle insertion in isolated brushes. 157

7.16 Simulation snapshots of two particles in isolated P3HT brush (a) before insertion, (b) at $H = 13.5$nm, (c) at $H = 11.1$nm and (d) at $H = 8.4$nm. View along $y-$direction. 158

7.17 Simulation snapshots of two particles in isolated P3HT brush (a) before insertion, (b) at $H = 13.5$nm, (c) at $H = 11.1$nm and (d) at $H = 8.4$nm. View along $z-$direction. 158

7.18 Monomer concentration profile along $x-, y-$plane for two particles insertion into an isolated brush column with particle radius $R_p = 0.5$nm, 1nm,2nm, and 3nm, and particle height $H = 13.5$ nm, 11.1 nm, and 8.4 nm. 159

7.19 Percolation lines formed due to the formation of $\pi - \pi$ connection vectors for two particles insertion into an isolated brush column. View in the x-y plane (top) and x-z plane (bottom) for particle radius $R_p = 0.5$nm, 1nm, 2nm, and 3nm, and particle height $H = 13.5$nm, 11.1nm, and 8.4nm. 160

7.20 Distribution of angle between the z-axis and the $\pi - \pi$ connection vector for two particles insertion in isolated brush with (a)$R_p = 3.0$nm; $H = 13.5$nm and $R_p = 3.0$nm; $H = 8.4$nm (b) with $R_p = 0.5$nm; $H = 8.4$nm and $R_p = 3.0$nm; $H = 8.4$nm 161

7.21 Ratio of monomers that do and do not form $\pi - \pi$ bonds for isolated brush system with two particles. 162

7.22 Simulation snapshots of single particle in continuous P3HT brush (a) before insertion, (b) at particle height $H = 13.68$nm, (c) at $H = 11.39$nm and (d) at $H = 4.39$nm. 163

7.23 Cylindrical radial monomer concentration profile for single particle insertion in continuous P3HT brush for particle radius $R_p = 0.5$nm, 1nm, 2nm, and 3nm, with height $H = 13.68$nm, 11.39nm, and 4.39nm. 165

7.24 Cylindrical radial $\pi - \pi$ bond density profile for single particle insertion in continuous P3HT brush for particle radius $R_p = 0.5$nm, 1nm, 2nm, and 3nm, with height $H = 13.68$nm, 11.39nm, and 4.39nm. 166

7.25 Histogram of the angle between monomer-monomer vector (the centroid vector) and the z-axis that do and do not form a $\pi-$ bond for (a) reference system and (b) for system with particle having $R_p = 3$nm and $H = 4.39$nm of continuous P3HT brush. Snapshot of a slice along the $y-$direction for (a) reference system and (b) system with particle. (e) Simple numerical analysis explaining the peaks at 45^0 and 135^0 of (a) and (b). 168

7.26 Percolation lines formed due to the formation of $\pi - \pi$ connection vectors for single particle insertion into continuous P3HT brush column. View in the x-y plane (top) and x-z plane (bottom) for particle radius R_p = 0.5nm, 1nm, 2nm, and 3nm, and particle height H = 13.68nm, 11.39nm, and 4.39nm. 169
7.27 Distribution of angle between the z-axis and the $\pi - \pi$ connection vector for single particles insertion in continuous brush with (a)R_p = 3.0nm; H = 13.68nm and R_p = 3.0nm; H = 4.39nm (b) with R_p = 0.5nm; H = 4.39nm and R_p = 3.0nm; H = 4.39nm. 170
7.28 Ratio of monomers that do and do not form $\pi-\pi$ bonds for single particle insertion in continuous brushes. 171
7.29 Insertion of two spherical particles into a continuous P3HT brush, view along z axis (the $\pi - \pi$ stacking axis) 172
7.30 Insertion of two spherical particles into a continuous P3HT brush, view along z axis (the $\pi - \pi$ stacking axis) 173
7.31 Monomer concentration profile along the $x - y$ plane for two particle insertion in continuous P3HT brush for particle radius R_p = 0.5nm, 1nm, 2nm, and 3nm, with height H = 13.68nm, 11.39nm, and 4.39nm. 174
7.32 Distribution of angle between the z-axis and the $\pi - \pi$ connection vector for two particles insertion in continuous brush with (a)R_p = 3.0nm; H = 13.68nm and R_p = 3.0nm; H = 4.39nm (b) with R_p = 0.5nm; H = 4.39nm and R_p = 3.0nm; H = 4.39nm 175
7.33 Ratio of particles that form $\pi - \pi$ bonds with respect to the monomers that do not form $\pi - \pi$ bonds for single particle insertion in continuous brushes. 175

List of Tables

3.1 Martini P3HT CG bonded parameters. The indices i, j, k and l refer to the consecutively bonded units. 48

4.1 ATB molids of the biodegradable monomers, oligomers, DNA and nucleobases citing the topology files 84

5.1 Equilibration bond length b_o (nm) and force constant K_b $\left(\frac{\text{kJ}}{\text{mol nm}^2}\right)$ used for HA1-3 and HA1-4 disaccharide CG force field. 114
5.2 Equilibration angle θ_0 (degrees) and force constant K_θ $\left(\frac{\text{kJ}}{\text{mol rad}^2}\right)$ used for HA1-3 and HA1-4 disaccharide CG force field. 114
5.3 Equilibration dihedral angle ϕ_0(degrees) and force constant K_ϕ $\left(\frac{\text{kJ}}{\text{mol rad}^2}\right)$ used for HA1-3 and HA1-4 disaccharide CG force field. Multiplicity was kept $m = 1$ for all the proper dihedrals. 114
5.4 Equilibration bond length b_o and force constant K_b used for HA octasaccharide CG force field. 115
5.5 Equilibration angle θ_0 and force constant K_θ used for HA octasaccharide CG force field. 116
5.6 Equilibration dihedral angle ϕ_0 and force constant K_ϕ used for HA octasaccharide CG force field. Multiplicity was kept $m = 1$ for all the proper dihedrals. 117
5.7 Comparison of equilibration bond length b_0 for AA and CG model of Alginate tetrasaccharide. 118
5.8 Equilibration angles θ_0 for AA and CG simulations and force constant K_θ for CG model of Alginate tetrasaccharide. 118
5.9 Equilibration dihedral angles ϕ_0 for AA and CG simulations and force constant K_ϕ for CG model of Alginate tetrasaccharide. 119
5.10 Equilibration bond length b_o and force constant K_b used for AG octasaccharide CG force field. 120
5.11 Equilibration angle θ_0 and force constant K_θ used for AG octasaccharide CG force field. 121
5.12 Equilibration dihedral angle ϕ_0 and force constant K_ϕ used for AG octasaccharide CG force field. Multiplicity was kept $m = 1$ for all the proper dihedrals. 122

6.1 ATB molid citing the topology files 137

Chapter 1

Introduction

This chapter aims at giving a short overview of the history of computer simulations and its impact on the development of the molecular dynamics simulation technique. The basic working principle of the atomistic simulations is explained and the its dependence on theory and experimental works is discussed. Since this thesis involves itself on detailed study of many different polymers, each having a different motivation, this chapter also gives the reader an outline of the background and application of individual polymer separately. Each of the subsections discussed in this chapter will give rise to a new chapter later on in this thesis.

1.1 A short history

Over almost 70 years have past since the first computer simulation of a liquid was published, under the title "*Equation of state calculations by fast computing machines*" at the Los Alamos National Laboratories, USA, 1953 [26]. It was carried out at Los Alamos computer, called MANIAC, the most powerful computer available at that time. Rapid development of computer hardware and computer simulation went hand in hand thereafter. The very earliest work on the foundations of modern Molecular Dynamics (MD), called "*Studies in molecular dynamics. I. General method*", was first accomplished by Alder and Wainwright in 1957 [2, 1] for a system of hard spheres describing the solution of the classical equations of motion (Newton's equations) for a set of molecules. This work made it possible, to solve the dynamic problem of particles moving at constant velocity with perfectly elastic collisions, without any approximations. It was several years thereafter until a successful attempt was achieved to solve the equations of motion for a set of Lennard-Jones particles [34] where the forces changed continuously as the particle moved. This work opened a gateway for enormous advancement in this field in the very next 5 years [44, 45, 30]. Advancements in computer simulations shot up by many folds after this initial groundwork. Modeling of a liquid comprising diatomic molecules [21, 20] in 1968 was rapidly followed by a pioneering attempt to model liquid water using MD by Rahman and Stillinger [35] in 1971 and water still remains one of the most interesting and difficult liquids to study to this date. Flexible hydrocarbons (1975) and even large molecules such as proteins (1977) have all been subjects of study in the following years [36, 25]. The techniques of computer simulations made a leap in their progress curve with the introduction of non-equilibrium methods (1979) [24, 3, 10] and development of stochastic dynamics (1977) [43]. Incorporation of quantum mechanical effect for the first time in the history of molecular dynamics was implemented by Corbin and Singer in 1982 in their article "*Semiclassical molecular dynamics of wave packets*" [13].

1.2 Computer simulations

MD simulations became the key to improve our understanding for phase transitions and nanoscopic molecular behavior because they posses the ability to provide exact results for problems in mechanics that might otherwise be out of hand. The results of MD simulations, and in fact most other computer simulations are often compared to those of real experiments and in many cases are a test for underlying model used in the simulation. Eventually, if the model is a good one, it offers the hope the provide insights to the experimentalists and assist their interpretation of new results and form a guide for their future work. This connection between experiments, theory and computer simulations (figure 1.1) act as a highway from macroscopic properties of experimentalists to microscopic details of the system such as orientational order, structural order, time and transport coefficients, long and short ranged correlations, thermodynamic averages, free energy estimations and many more. Thanks to these advantages, the entire work presented in this thesis is based on MD simulations. The basics of theory and numerical methods for step-wise evolution of trajectories in MD is discussed in detail in Chapter 2 and it deals with the general question of how to put information in a simulation box to define a model of molecule. This chapter explains the working principle of atomistic simulations and gives an insight into coarse grained (CG) models, and a guideline on building them, as a major part of this thesis will also deal with CG simulations.

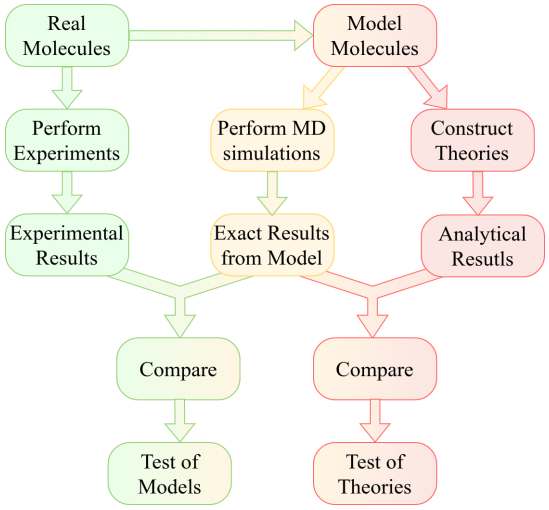

Figure 1.1: Connection between the experiments, the theory and the computer simulations

Since the focus of this thesis is not one but multiple topics, separate introduction to each topic individually is needed. Therefore, the start of each chapter will be presenting itself with a short abstract, giving the gist of the chapter, followed by a detailed introduction explaining the background and motivation of the topic discussed. The following sections describe briefly the topics covered in this thesis.

1.3 Poly(3-hexylthiophene)

Poly(3-hexylthiophene) (P3HT), a thiophene-based regioregular conjugated polymer, was first synthesized in the early 1990s and has since become the work-horse also described as "fruit fly" by Andrienko and coworkers in their article "*Morphology and Charge Transport in P3HT: A Theorist's Perspective*" [32]. P3HT used in organic solar cells and transistors because of its self-assembling and electronic properties that enriches the polymer with special conductive and optical properties [46, 6]. The charge mobility in organic solar cells and transistors is a result of $\pi - \pi$ bond formation in self-assembled P3HT polymer chains that act as carriers for electrons and holes. This property is highly dependent on the morphological properties of P3HT and a better understanding of it is needed for advancements in the efficiency of the solar cells. Panzer et al. reported a order-disorder transition in P3HT after observing a shift in the absorption spectra as a function of temperature when employing fluorescence spectroscopy. When cooling from 300K to 170K they featured a red shift by 35-50meV accompanied by increase in intensity of about 10% [31]. They suggested a change in the conformational structure of P3HT a reason for the shift, an illustration shown in figure 1.2.

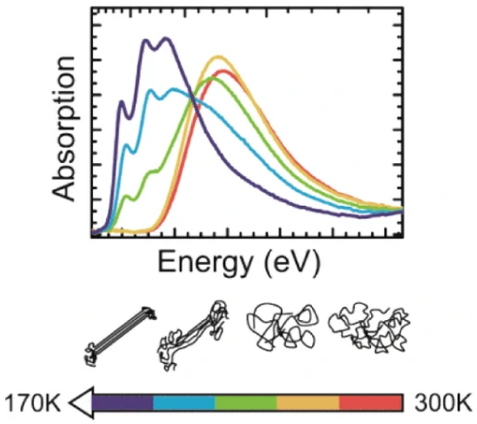

Figure 1.2: Temperature dependent absorption of P3HT predicting a conformational change in P3HT as the possible reason for the red shift. (Reprinted (adapted) with permission from the work of Panzer et al [31]. Copyright {2014} American Chemical Society.)

With this background and motivation, we carry out vacuum atomistic simulations of single P3HT polymers at different temperatures in chapter 3 and compare the conformational properties such as radius of gyration and end to end distance with a coarse grained model of P3HT to assess its validity. Then we add tetrahydrofuran, the same solvent used by Panzer et al. and determine the existence of phase transition in P3HT. We compare our simulation results of the temperature at which the phase

transition takes place in P3HT in the presence of solvent with the absorption results of Panzer et al. We also discuss in detail the aggregation properties of flexible, semi-flexible and stiff polymers using a simple Lennard Jones model as a function of temperature and create a basic data set for future reference.

1.4 Microplastics

Over the past two decades development of synthetic polymers not only brought advancements in economic development but also easied our everyday living. Their low production costs, light weight, good durability and easy processability, synthetic plastics found applications of plastics in almost everything we come in contact with today, from electronics, to shopping bags, to cosmetics. This resulted in production of plastics from 1.5 millions tons in 1950 to 400 million tons in 2018 and is estimated to reach 1800 million tons per year by 2050 [33]. This interesting statistics naturally raised globally escalating fears about the environmental fate pertaining microplastics. According to the European Chemicals Agency [12], the term "microplastic" is defined as tiny fragments of any type of plastic smaller than 5mm in length and is widely used to differentiate from larger waste like plastic bottles. Sources of primary microplastics include microfibers from synthetic clothes, microbeads, nurdles (plastic pellets). Secondary microplastics are formed from the degradation process including the breakdown of bigger plastic chunks via natural weathering processes after being a part of the environment [11, 7]. Majority of the microplastics are created from plastic products created for packaging and single used items having very small service life before they are disposed off. The growing concerns naturally drives us to find alternatives that would replace the traditional plastics with very less degradation rates. Polylactic acid (PLA) is one the champions in this race for finding alternative solutions for biodegradable polymers and has already found its place in wide range of applications. PLA can be processed with variety of techniques for commercial production, is relatively cheap and has remarkable properties to be used as short term packaging material [5]. Polyglycolic acid (PGA) is another such polymer with principle applications in the medical field of orthopedics, implants and fixation devices for bones [4]. Therefore its toxicity and biocompatibility is the foremost concern that needs to be addressed here. Polyhydroxyalkanoates (PHA) is gaining attention in the field of biodegradable polymers due to their high degradation rates and also find applications in paper coatings, packaging, fabrics, adhesives and films [8]. These biodegradable plastics can disintegrate back to its monomers and easily enter into the bodies of living organisms once let out in the environment. A rigorous understanding is mandatory to study the the strength of interaction between the biodegradable polymers and our building block, DNA. This is the motivation behind the investigation carried out in the chapter 4, where MD simulations are carried out to determine how individual PLA, PHA and PGA monomers interact with DNA nucleobases by determining the potential mean force (PMF) between them. Oligomers with 5 repeating units of the aforementioned polymers, and their interaction with a 13-mer DNA hairpin is also presented in chapter 4.

1.5 Hydrogels

Hydrogels are formed via crosslinking of hydrophilic polymers together to assemble into a network structure with the aid of polyelectrolytes. They consist of self-supporting, water swollen, 3D viscoelastic network that permit that attachment of cells. Hydrogels may be chemically stable ("permanent") if the crosslinking occurs via covalent bond or they may be reversible ("physical") if they are held together by H-bonding or hydrophobic forces. Natural hydrogels include collagen, fibrin, hyaluronic acid, chitosan, alginate and silk fibers. Due to their bio-compatibility and similarity of their physical properties to natural tissue, hydrogels have gained enormous attention for use in biomedical applications such as wound healing and cartilage/bone regeneration and printing.

Hydrogels as bioinks for 3D printing of tissue scaffolds to mimic native organs and tissues gained much attention after the recognition of their properties by using natural polymers such as gelatin, alginate, hydrogels and others [16, 29, 15, 18, 9, 40, 19]. 3D printing techniques integrate hydrogels with live cells and controlled printing apparatus for creation of complex morphological structures, capable of reproducing properties of a living tissue for grafting applications. Alginate bioinks showed better encapsulation of cells with higher survival rates, but their post-printing morphological stability is a critical point yet to be resolved. Hyaluronic acid is also widely used in the same field for over a decade now because of its biocompatibility and crucial role in regulating cellular behaviors like cell migration, angiogenesis, viability and proliferation [41, 14, 22]. However, hyaluronic acid also exhibits shape instability post processing. Fine details of their mechanical properties and their dependence on gelation conditions are poorly understood thereby making their final microstructural properties difficult to reproduce and control by the experimentalists. Therefore, using the computational tools at hand, insights into the microstructural conformations of hydrogels can improve determine the conditions required to obtain their desired properties and mechanical stability.

Since 3D printing needles are often of the scale of micrometers, carrying out atomistic simulations of such constructs would be extremely complex and almost impossible. This is because atomistic simulations are heavily restricted in terms of size of the system and the simulation time in the presence of explicit solvent. Models for the gels are needed that can be computed with much lesser wall time all the while still being able to reproduce the properties of the involved polymers. This leaves us with one option – coarse grained (CG) simulations – for investigation of the macromolecular structures of the hydrogels by eliminating much of the intra-molecular interactions, and combining many solvent molecules into one CG bead. Chapter 5 creates and validates Martini coarse grained models of hyaluronic acid and alginate, two of the most widely used polymers in 3D printing, for making large time and length scale simulations possible within realistic computation time. The CG force-field models are minimalistic and therefore very sensitive to the model parameters. Therefore, careful creation of Martini CG models is needed to capture

the gelation process of the hydrogels. Chapter 5 also explains in detail the procedure to create a Martini CG model for any polymer of desired lengths from a small atomistic unit model using bottom-up approach.

1.6 Vinyl cyclopropanes

Vinyl cyclopropanes (VCPs) were discovered in 1959 and gained considerable attention since [23]. They are potentially good candidates for dental adhesives and filling composites due to less polymerization shrinkage than other vinyl monomers [27, 28, 38]. The property of less shrinkage, that avoids micro leakage, internal stress caused due to contraction and gap formation can be understood by figure 1.3. The free radical polymerization of the VCP derivatives leads to 1,5 ring-opened units and a double bond in the polymer backbone along with a new unit, the closed cyclobutene ring in the backbone. The amount of cyclobutanes increase with increasing temperature [39]. Therefore the volume gained during the ring opening step compensates the shrinkage occurring due to the covalent bond formation between the monomers leading to very low shrinkage. After this was discovered in the early 1980s, Sadhir and Luck published a book called "*Expanding monomers*" [37] that explains the chemistry behind this mechanism in detail.

Figure 1.3: Polymer structures of the radical ring-opening polymerization of VCPs.

Despite the advantages, none of the VCPs are commercially produced due to their low polymerization rate and incomplete monomer conversions [27]. Therefore, in chapter 6, we study VCPs with varying hydrogen bonding sites at different locations to study their effect on the rate of polymerization of the monomers. We vary (i) the position and (ii) the type of hydrogen bonding (H-bonding) units in the VCPs. Firstly, we consider three different H-bonding functional units namely the amide, the urethane and the urea in the side chain of the VCPs exclusively. In the second part, we study a set of monomers that bear H-bonding sites at two different position in the VCPs: an amide group that links the side chain to the cyclopropane and different organic functional groups that are able to form H-bonding to different extents in the side chain in order to compare their behavior. We carry out MD simulations in order to have more information about the bulk properties of the VCPs like the root mean squared displacement, time averaged H-bonds in the bulk, orientation parameter, radial distribution function to give an insight to their structural and organizational differences. We then correlate the computational results with the experimental polymerization rates. The main aim of this work is to answer the following questions: Does hydrogen bonding lead to different packing of the bulk for different monomers? Does hydrogen bonding play a role in polymerization rates of the different VCP monomers? This work is of relevance for enabling a fast and better prediction on the structural designs of VCPs in the future.

1.7 Polymer Brushes

A polymer brush is an array of macro molecules grafted at one end to the surface with grafting density high enough for the molecules to be in close proximity to be able to interact with one one another . Such brushes when created from conjugated polymers, such as P3HT, are able to act as a layer of semiconductor in a organic thin film transistor (OTFT). This assembly finds its application in various kind of biosensors [42]. The working principle of OTFT-based biosensors demands stability, selectivity and sensitivity towards the target analyst followed by a specific biological event that allows adherence to the brush in a way that it changes the carrier mobility of the transistor. Therefore, when the semiconductor layer is exposed to the target, the biological event induces changes in the output parameters like current and voltage of the transistor via doping or trapping processes. For an OTFT based on conjugated polymers, detectable changes in the current mobility are caused by disruption/creation of $\pi - \pi$ bonds within the polymer brush due to the presence of the target. This event is mimicked in chapter 8 by studying a spherical particle induced perturbation to the conformation of isolated and continuous P3HT brush and its effect on the $\pi - \pi$ stacks within the brush. Conjugated polymers carry excitation energy along their entire backbone over long distances due to the $\pi-\pi$ stacks between the monomers of the brush. In chemistry, a $\pi - \pi$ stack refers to attractive, non-covalent interaction due to orbital overlap between two aromatic rings. In P3HT the thiophene rings are the entities that have the ability to form a $\pi - \pi$ stack. Experimental studies typically report that the $\pi - \pi$ stacking distance between two aromatic rings is $\sim$ 3.8Å[17]. Orientations of aromatic interactions via $\pi-$stacking is shown in figure 1.4.

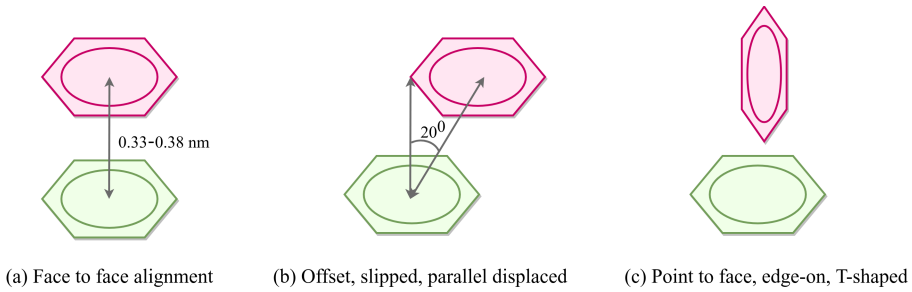

Figure 1.4: Principal orientation of $\pi - \pi$ interactions in aromatic rings

In chapter 8 we mimic the target analyst by a simple Lennard Jones (LJ) particle with varying attractive potential and radius and implant it inside a densely packed P3HT brush that already has a good $\pi - \pi$ network in the initial configuration. We study the effect of introduction of an LJ particle on the rearrangement of the polymer brush and changes in the $\pi-\pi$ network. In addition we also carry out umbrella sampling simulations of two $\pi-\pi$ stacked P3HT polymers with lengths varying between 1 and 12

for evaluating the scaling of the energy for breaking $\pi - \pi$ connections. We propose that this energy has a direct connection with the binding energy a supra-molecular assembly in OTFTs should overcome for letting the target bind and create a detectable signal.

References

[1] Berni J Alder and Thomas Everett Wainwright. Studies in molecular dynamics. i. general method. *The Journal of Chemical Physics*, 31(2):459–466, 1959.

[2] Berni Julian Alder and Thomas Everett Wainwright. Phase transition for a hard sphere system. *The Journal of chemical physics*, 27(5):1208–1209, 1957.

[3] W-T_ Ashurst and WG Hoover. Dense-fluid shear viscosity via nonequilibrium molecular dynamics. *Physical Review A*, 11(2):658, 1975.

[4] Kyriacos A Athanasiou, Gabriele G Niederauer, and C Mauli Agrawal. Sterilization, toxicity, biocompatibility and clinical applications of polylactic acid/polyglycolic acid copolymers. *Biomaterials*, 17(2):93–102, 1996.

[5] Luc Avérous. Polylactic acid: synthesis, properties and applications. In *Monomers, polymers and composites from renewable resources*, pages 433–450. Elsevier, 2008.

[6] Zhenan Bao, Ananth Dodabalapur, and Andrew J Lovinger. Soluble and processable regioregular poly (3-hexylthiophene) for thin film field-effect transistor applications with high mobility. *Applied physics letters*, 69(26):4108–4110, 1996.

[7] Julien Boucher and Damien Friot. *Primary microplastics in the oceans: a global evaluation of sources*, volume 10. Iucn Gland, Switzerland, 2017.

[8] Elodie Bugnicourt, Patrizia Cinelli, Andrea Lazzeri, and Vera Alejandra Alvarez. Polyhydroxyalkanoate (pha): Review of synthesis, characteristics, processing and potential applications in packaging. 2014.

[9] Cen Chen, Sumi Bang, Younghak Cho, Sahnghoon Lee, Inseop Lee, ShengMin Zhang, and Insup Noh. Research trends in biomimetic medical materials for tissue engineering: 3d bioprinting, surface modification, nano/micro-technology and clinical aspects in tissue engineering of cartilage and bone. *Biomaterials research*, 20(1):1–7, 2016.

[10] G Ciccotti, G Jacucci, and IR McDonald. "thought-experiments" by molecular dynamics. *Journal of Statistical Physics*, 21(1):1–22, 1979.

[11] Matthew Cole, Pennie Lindeque, Elaine Fileman, Claudia Halsband, Rhys Goodhead, Julian Moger, and Tamara S Galloway. Microplastic ingestion by zooplankton. *Environmental science & technology*, 47(12):6646–6655, 2013.

[12] European Commission. Restricting the use of intentionally added microplastic particles to consumer or professional use products of any kind. 2022.

[13] N Corbin and K Singer. Semiclassical molecular dynamics of wave packets. *Molecular Physics*, 46(3):671–677, 1982.

[14] Dipankar Das, Thi Thu Hien Pham, and Insup Noh. Characterizations of hyaluronate-based terpolymeric hydrogel synthesized via free radical polymerization mechanism for biomedical applications. *Colloids and Surfaces B: Biointerfaces*, 170:64–75, 2018.

[15] Janarthanan Gopinathan and Insup Noh. Click chemistry-based injectable hydrogels and bioprinting inks for tissue engineering applications. *Tissue engineering and regenerative medicine*, 15(5):531–546, 2018.

[16] Janarthanan Gopinathan and Insup Noh. Recent trends in bioinks for 3d printing. *Biomaterials research*, 22(1):1–15, 2018.

[17] Cristina Greco, Anton Melnyk, Kurt Kremer, Denis Andrienko, and Kostas Ch Daoulas. Generic model for lamellar self-assembly in conjugated polymers: linking mesoscopic morphology and charge transport in p3ht. *Macromolecules*, 52(3):968–981, 2019.

[18] Bon Kang Gu, Dong Jin Choi, Sang Jun Park, Min Sup Kim, Chang Mo Kang, and Chun-Ho Kim. 3-dimensional bioprinting for tissue engineering applications. *Biomaterials research*, 20(1):1–8, 2016.

[19] Murat Guvendiren, Joseph Molde, Rosane MD Soares, and Joachim Kohn. Designing biomaterials for 3d printing. *ACS biomaterials science & engineering*, 2(10):1679–1693, 2016.

[20] GD Harp and BJ Berne. Time-correlation functions, memory functions, and molecular dynamics. *Physical Review A*, 2(3):975, 1970.

[21] GD Harp and Bruce J Berne. Linear-and angular-momentum autocorrelation functions in diatomic liquids. *The Journal of chemical physics*, 49(3):1249–1254, 1968.

[22] Christopher B Highley, Glenn D Prestwich, and Jason A Burdick. Recent advances in hyaluronic acid hydrogels for biomedical applications. *Current opinion in biotechnology*, 40:35–40, 2016.

[23] T Hudlicky and JW Reed. Comprehensive organic synthesis. *by BM Trost and I. Fleming, Pergamon Press, Oxford*, 5:899, 1991.

[24] AW Lees and SF Edwards. The computer study of transport processes under extreme conditions. *Journal of Physics C: Solid State Physics*, 5(15):1921, 1972.

[25] J Andrew McCammon, Bruce R Gelin, and Martin Karplus. Dynamics of folded proteins. *nature*, 267(5612):585–590, 1977.

[26] Nicholas Metropolis, Arianna W Rosenbluth, Marshall N Rosenbluth, Augusta H Teller, and Edward Teller. Equation of state calculations by fast computing machines. *The journal of chemical physics*, 21(6):1087–1092, 1953.

[27] Norbert Moszner. New monomers for dental application. In *Macromolecular Symposia*, volume 217, pages 63–76. Wiley Online Library, 2004.

[28] Norbert Moszner, Frank Zeuner, Urs Karl Fischer, V Rheinberger, Armin de Meijere, and Viktor Bagutski. Polymerization of cyclic monomers, 10-synthesis and radical polymerization of methyl 2-(bicyclo [3.1. 0] hex-1-yl) acrylate. *Macromolecular rapid communications*, 24(3):269–273, 2003.

[29] Sean V Murphy and Anthony Atala. 3d bioprinting of tissues and organs. *Nature biotechnology*, 32(8):773–785, 2014.

[30] JJ Nicolas, KE Gubbins, WB Streett, and DJ_ Tildesley. Equation of state for the lennard-jones fluid. *Molecular Physics*, 37(5):1429–1454, 1979.

[31] Fabian Panzer, Heinz Baessler, Ruth Lohwasser, Mukundan Thelakkat, and Anna Koehler. The impact of polydispersity and molecular weight on the order–disorder transition in poly (3-hexylthiophene). *The journal of physical chemistry letters*, 5(15):2742–2747, 2014.

[32] Carl Poelking, Kostas Daoulas, Alessandro Troisi, and Denis Andrienko. Morphology and charge transport in p3ht: a theorist's perspective. *P3HT Revisited–From Molecular Scale to Solar Cell Devices*, pages 139–180, 2014.

[33] D Qualman. Global plastics production, 1917 to 2050 2017.

[34] Aneesur Rahman. Correlations in the motion of atoms in liquid argon. *Physical review*, 136(2A):A405, 1964.

[35] Aneesur Rahman and Frank H Stillinger. Molecular dynamics study of liquid water. *The Journal of Chemical Physics*, 55(7):3336–3359, 1971.

[36] J-P Ryckaert and André Bellemans. Molecular dynamics of liquid n-butane near its boiling point. *Chemical Physics Letters*, 30(1):123–125, 1975.

[37] Rajender K Sadhir and Russell M Luck. *Expanding monomers*. CRC press Boca Raton, 1992.

[38] Fumio Sanda, Toshikazu Takata, and Takeshi Endo. Radical polymerization behavior of 1, 1-disubstituted 2-vinylcyclopropanes. *Macromolecules*, 26(8):1818–1824, 1993.

[39] Fumio Sanda, Toshikazu Takata, and Takeshi Endo. Radical ring-opening polymerization of novel vinylcyclopropanes designed as low shrinkage monomers. structure of the polymer, mechanism of the polymerization, and volume change on the polymerization. *Macromolecules*, 28(5):1346–1355, 1995.

[40] Ashkan Shafiee and Anthony Atala. Printing technologies for medical applications. *Trends in molecular medicine*, 22(3):254–265, 2016.

[41] Henrike Stratesteffen, Marius Köpf, Franziska Kreimendahl, Andreas Blaeser, Stefan Jockenhoevel, and Horst Fischer. Gelma-collagen blends enable drop-on-demand 3d printablility and promote angiogenesis. *Biofabrication*, 9(4):045002, 2017.

[42] Chenfang Sun, Xue Wang, Muhammad Aminu Auwalu, Shanshan Cheng, and Wenping Hu. Organic thin film transistors-based biosensors. *EcoMat*, 3(2):e12094, 2021.

[43] Pierre Turq, Frédéric Lantelme, and Harold L Friedman. Brownian dynamics: Its application to ionic solutions. *The Journal of Chemical Physics*, 66(7):3039–3044, 1977.

[44] Loup Verlet. Computer" experiments" on classical fluids. i. thermodynamical properties of lennard-jones molecules. *Physical review*, 159(1):98, 1967.

[45] Loup Verlet. Computer" experiments" on classical fluids. ii. equilibrium correlation functions. *Physical Review*, 165(1):201, 1968.

[46] Bai Xu and Steven Holdcroft. Molecular control of luminescence from poly (3-hexylthiophenes). *Macromolecules*, 26(17):4457–4460, 1993.

Chapter 2

Molecular dynamics simulations

Molecular dynamics (MD) simulations are widespread simulation methods to model systems consisting of atoms and molecules to study their time dependent behavior. This method enables computer to carry out virtual experiments many body systems and allows to track the dynamical and statistical properties in detail. It also allows for the system to be under unrealistic or unusual conditions for ensuring the development of more accurate force-fields, i.e. interaction potentials for better accuracy and reliability. The chapter aims at outlining the theory and numerical methods behind MD that are used in the thesis.

2.1 Introduction

This method is based on classical mechanics and involves solving Newton's equation of motion to calculate the *trajectory*, which is a representation of the particle movements as a function of time. In this thesis they were carried out using the software package Gromacs and therefore this chapter has been written with the perspective of Gromacs. Further detailed information can be found in the manual [1] and related references [2, 5, 6, 16, 29, 12, 26, 25]. MD is based on an algorithm which is lined out in figure 2.1

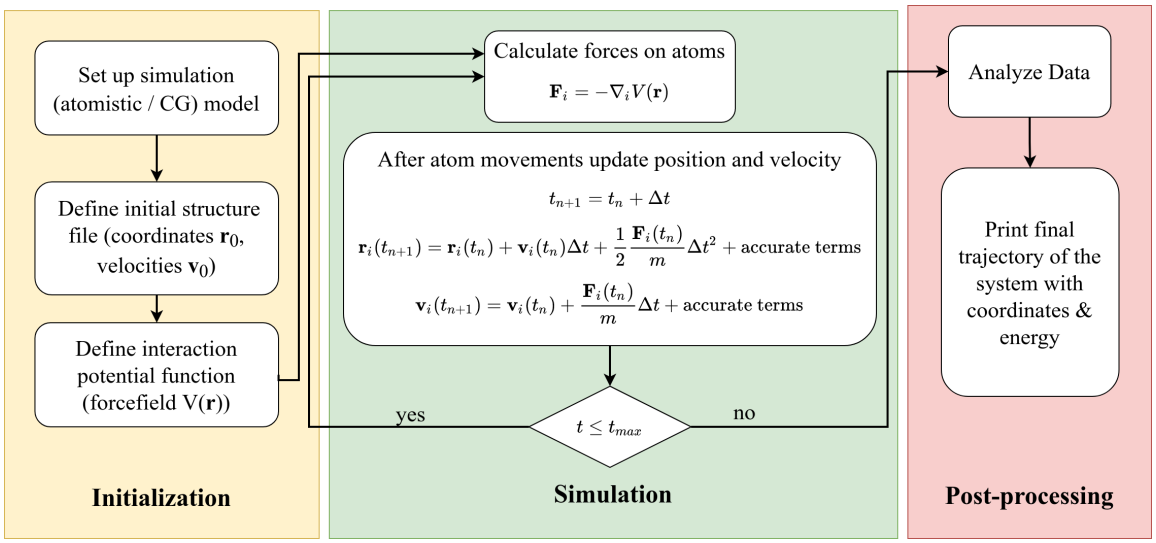

Figure 2.1: The common algorithm that MD is formulated on.

The simulations begin with the starting configuration of the system that includes all the coordinates of all the atoms $\mathbf{r}_i$, which contains necessary information about the properties of the different atoms in the system. These properties are discussed in detail in the next subsection 2.2. The next step is to calculate the total force acting on each atom in the system, for which we require a topology file. The topology file contains different potential functions that are included in the force field. Force fields are created using various methods in this thesis, including information based on *Automated Topology Builder (ATB) and Repository* [18], several papers and own calculations. The ATB repository tackles the issue of creating force-field models for molecules not known or studied previously, by allowing the user to extract Gromacs compatible topologies for virtually any molecule. Further discussions on force fields is carried out in the subsection 2.3. After computing the potential functions $V(\mathbf{r})$, the force is then calculated by differentiating $V(\mathbf{r})$, which represent how the atoms interact with one another. After this the forces are then used to calculate new positions and velocities for each atom.

This step is carried out by numerically integrating Newton's second law of motion over the time step increment Δt. This segment of the simulation process is explained in subsection 2.5. After this the trajectory of the system is updates with new coordinates and velocities for all the atoms, and the time is increased by Δt. Then the steps shown in the green block of figure 2.1 are repeated until a simulation of a desired time length is achieved. Mathematically the whole algorithm can be presented with the following framework

$$t_{n+1} = t_n + \Delta t$$

$$\mathbf{r}_i(t_{n+1}) = \mathbf{r}_i(t_n) + \mathbf{v}_i(t_n)\Delta t + \frac{1}{2}\frac{\mathbf{F}_i(t_n)}{m}\Delta t^2 + \mathscr{O}^3 \tag{2.1}$$

$$\mathbf{v}_i(t_{n+1}) = \mathbf{v}_i(t_n) + \frac{\mathbf{F}_i(t_n)}{m}\Delta t + \mathscr{O}^2 \tag{2.2}$$

$$m_i\frac{d^2\mathbf{r}_i}{dt^2} = \mathbf{F}_i = -\frac{\partial V_{tot}(\mathbf{r}_i)}{\partial \mathbf{r}_i}, i = 1, 2, \ldots N \tag{2.3}$$

where for each atom i mass is m_i, coordinate vector is $\mathbf{r}_i$ and force vector $\mathbf{F}_i$. V_{tot} describes the total of different potential functions applied on the atom and t is time. For each atom $i = 1, 2, \ldots N$ in the system, equation 2.3 is performed for many loops until time reaches the specified maximum simulation time ($t \leq t_{max}$) and the product of the simulation is a trajectory for the studied system. The trajectory contains the coordinates and velocities of all the atoms as a function of time, and various behavior can be observed and different quantities can be calculated from it.

2.2 Structure of the system

The coordinates and velocities for each atom in the system define the structure of the system when the simulation begins. The coordinates describe the location of each atom is a 3-dimensional space and can be acquired by building the molecule in a modeling software. The velocities for the atoms are also needed to define the initial system. In the absence of velocities, Gromacs generates them for a given temperature using the Maxwell-Boltzman distribution function

$$P(v_i) = \sqrt{\frac{m_i}{2\pi k_B T}} e^{\left(-\frac{m_i v_i^2}{2k_B T}\right)} \tag{2.4}$$

where P is the probability to obtain a velocity v_i for an atom with a mass m_i and k_B is the Boltzmann constant and T in Kelvin is the defined temperature.

With the positions and velocities for the atoms acquired, the individual properties of these atoms also need to be defined. Each atom has a different mass and partial charge which needs determination. The structures of a single monomer of the polymers used in this thesis, namely Poly(3-hexylthiophene) (P3HT) and polylactic acid (PLA) are shown in figure 2.2 (a) and (b) respectively containing four elements carbon, hydrogen, oxygen and sulfur.

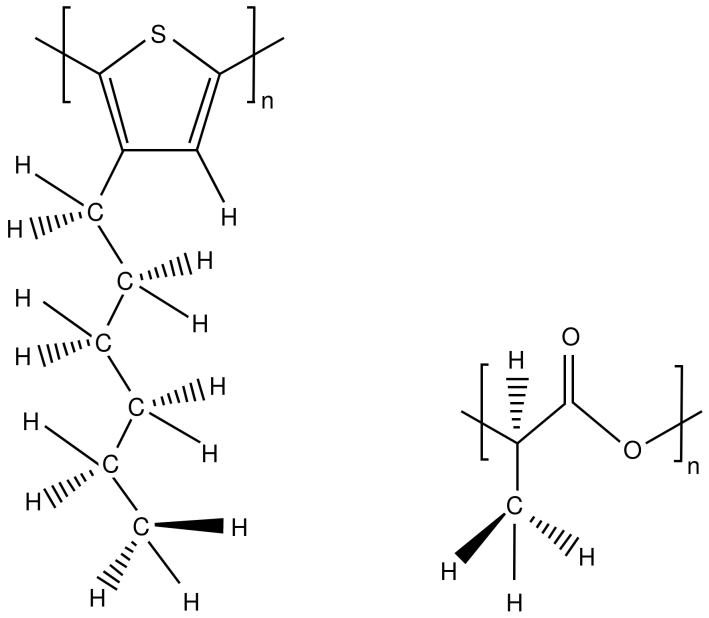

Figure 2.2: Structural formula of (a) Poly(3-hexylthiophene) and (b) Polylactic acid monomers showing all the different atoms in the molecule.

The solid lines in figure 2.2 indicate that the bonds exists in the plane of the drawing surface, the wedged lines mean that the atom are above the surface and the dotted lines mean that they are below the drawing surface. The masses of the different atoms of the same element differ even if they have different isotopes, but this aspect is often not taken into account. This is because the simulations are largely based on electromagnetic interactions and therefore the charges are of much more importance than the masses. In 2.2 (a), the central thiophene ring consisting of 4 carbon atoms and one sulfur atom forms the backbone of P3HT and the hexyl group forms the side chains. P3HT has a planar backbone, meaning that all the thiophene rings lie in one plane, also known as regioregularity [14]. This gives P3HT the special property to transfer electron cloud along the backbone. PLA polymer (figure 2.2 (b)) is a known aliphatic polyester commonly used in biodegradable products. In PLA, the monomer consists of a methyl group, a hydroxyl group, a carboxylic acid group and a hydrogen atom all attached to a central carbon atom.

Lastly the interactions between different atoms need to be defined. Gromacs uses a topology file, wherein bonded interactions such as bonds, angles, proper dihedrals, improper dihedrals and pairs are listed. These different interactions are detailed in the following section 2.3.

2.3 Force fields

The potential energy function described by the so called force fields determines the interaction energies between atoms. They are mostly calibrated to the experimental results and quantum mechanical calculations of their smaller counterparts. Each force field is suited for specific simulation conditions, i.e. for simulations in bulk, water or vacuum. Moreover, they are optimized for specific classes of molecules, such as organic molecules, inorganic molecules, biomolecules (protein, lipids, nucleic acids), etc. In this work modified OPLS-AA (Optimized Potentials for Liquid Simulations - all atom) and GROMOS54a7 (GROningen MOlecular Simulation) all-atom force field was used for the atomistic simulations. Gromacs software offers 15 default force fields to work with, however, one can in principle generate the parameters oneself and include it in the simulation. Custom force fields are used in this work when simulating polymers of different stiffness.

The total potential V_{tot} for an atom is a sum of bonded potentials V_{bonded} and the non-bonded potentials $V_{\text{non-bonded}}$.

$$V_{\text{tot}} = V_{\text{bonded}} + V_{\text{non-bonded}} \tag{2.5}$$

In addition to the above, the position or orientation of one or more atoms can be restrained, either to avoid disruptive deviations or the include the knowledge from experimental setup. They are most often used in equilibration of the system before starting the actual simulation. Further information can be found in the Gromacs user manual [1, p. 363-368]. The next two sections deal with different potentials that contribute to V_{bonded} and $V_{\text{non-bonded}}$ of equation 2.5.

2.3.1 Bonded interactions

All possible covalent bonds between the atoms are defined in the topology. Bonded potentials are defined by interactions between 2, 3 or 4 atoms. The different potentials that form V_{bonded} are bond stretching V_{bonds}, angle bending V_{angles}, proper dihedrals $V_{\text{proper dihedrals}}$ and improper dihedrals $V_{\text{improper dihedrals}}$, illustrated in figure 2.3 (a), (b), (c) and (d) respectively. The total bonded potential for an atom is therefore given by the following equation,

$$V_{\text{bonded}} = V_{\text{bonds}} + V_{\text{angles}} + V_{\text{dihedrals}} \tag{2.6}$$

Bond stretching occurs between two covalently bonded atoms i and j (figure 2.3 (a)).

The bonding potential between the atoms is associated with a harmonic potential and modeled as a spring, which can be represented as a simple quadratic function of bond length:

$$V_{\text{bonds}}(r_{ij}) = \frac{1}{2} k^b_{ij} (b_{ij} - b^0_{ij})^2 \tag{2.7}$$

where $k_{ij}^{b}$is harmonic force constant, b_{ij} the bond length between two atoms and b_{ij}^{0} is the equilibrium bond length. Equation 2.7 describes the energy change as bonds stretch and contract from their ideal length. For higher accuracy, this potential can be replaced by using an anharmonic Morse potential [1, p. 353].

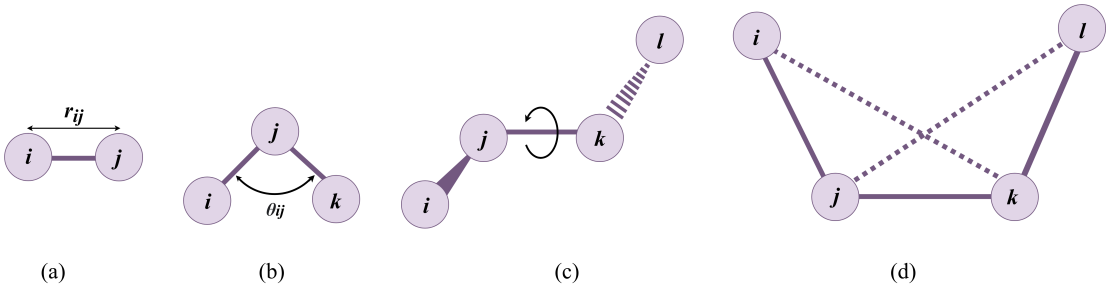

Figure 2.3: (a) Bond stretching, (b) angle stretching, (c) proper dihedral angle torsion and (d) improper torsion dihedral between different atoms i, j, k and l. The proper dihedral angle (c) is defined as the angle between the plane formed by atom i, j and k and the plane formed by j, k and l. The improper dihedral angle (d) is the angle between planar atoms i, j, k and l.

The bond angle energy is defined for three subsequently attached and covalently bound atoms i, j and k, forming an angle that deviates from an ideal value. As presented in 2.3 (b), the atoms are marked in a sequence of covalently bonded atoms with atom j being in the middle and i and k at the ends. The potential $V_{\text{angles}}$is also represented as a simple harmonic potential of the form:

$$V_{\text{angles}}(\theta_{ijk}) = \frac{1}{2}k_{ijk}^{\theta}(\theta_{ijk} - \theta_{ijk}^{0})^{2} \tag{2.8}$$

where k_{ijk}^{θ} is the angle-bending force constant, θ_{ijk} is the actual bond angle and θ_{ijk}^{0} is the equilibrium bond angle. Both in bond stretching and angle bending potentials the bond and angle values vary during the simulation, and the force constants and the equilibrium values are constants defined in the force field. The simple harmonic angle potential is used for all the simulation in this thesis however other potentials forms for angle bending can also be incorporated and Gromacs and are explained in detail in [1, p. 355].

Gromacs is also capable of implementing a cosine based angle potential to represent angle vibrations:

$$V_{\text{angles}}(\theta_{ijk}) = \frac{1}{2}k_{ijk}^{\theta}(\cos(\theta_{ijk}) - \cos(\theta_{ijk}^{0}))^{2} \tag{2.9}$$

Dihedrals define potential between four consecutively bonded atoms i, j, k and l. They are divided into proper and improper dihedrals, and the total potential is their sum. Proper dihedrals describe the angle torsion of the bond between atoms j and k,

as shown in figure 2.3 (c) and is defined by the Ryckaert–Bellemans function

$$V_{\text{proper dihedrals}}(\theta_{ijkl}) = \sum_{n=0}^{n=5} C_n(\cos(\psi))^n \tag{2.10}$$

where ψ is the dihedral angle and $C_0 - C_5$ are the six coefficients defined in the force field. This is the standard type of dihedral commonly used in Gromacs. For certain force fields, for example in Martini models, the following proper dihedral is under practice:

$$V_{\text{proper dihedrals}}(\theta_{ijkl}) = k_\phi(1 + \cos(n\phi - \phi_0)) \tag{2.11}$$

where ϕ denotes the angle between the two planes containing the beads i, j, k and j, k, l resp., with equilibration angle of ϕ_0, force constant k_ϕ and multiplicity n.

For dihedrals that lie in the same plane, we have improper dihedrals (see figure 2.3 (d)) and they are used to maintain planar groups. This is especially important in the case of P3HT where all the thiophene rings need to be planar to describe the polymer. Improper dihedral is represented by a harmonic potential according to the following equation:

$$V_{\textbf{improper dihedrals}} = \frac{1}{2} k^{\xi}_{ijkl}(\xi_{ijkl} - \xi^0_{ijkl})^2 \tag{2.12}$$

where $\frac{1}{2}k^{\xi}_{ijkl}$ is the dihedral force constant, ξ_{ijkl} is the dihedral angle between the angles and ξ^0_{ijkl} is the equilibrium value. All the angles are given in degrees in the topology file, but for calculation they are converted to radians by Gromacs.

2.3.2 Non-bonded interactions

The non-bonded interactions are calculated for two atoms that are not covalently bonded to each other but are within a certain distance range. The total non-bonded long-ranged interactions are a sum of Coulomb potential V_{Coulomb} and Van der Waals interaction which in all of our simulations are represented by the Lennard-Jones potential V_{LJ}. Coulomb potential exists between two charged atoms i and j and is of the form

$$V_{\text{Coulomb}}(r_{ij}) = \frac{q_i q_j}{4\pi\epsilon r_{ij}} \tag{2.13}$$

where r_{ij} is the distance between the two atoms i and j, q_i and q_j their charges and $\epsilon = \epsilon_0\epsilon_r$ with ϵ_0 being the vacuum permittivity and ϵ_r the relative permittivity. The Coulomb potential is inversely proportional to the distance r_{ij} and therefore the further the particles the weaker is the potential.

Lennard Jones (LJ) potential is used to model the non-electrostatic Van der Waals interaction and contains a short-range repulsion followed by a lon-ranged attraction term.

Similar to the Coulomb potential the LJ potential is also inversely proportional to the distance and is of the form:

$$V_{\mathrm{LJ}}(r_{ij}) = 4\varepsilon_{ij}\left(\left(\frac{\sigma_{ij}}{r_{ij}}\right)^{12} - \left(\frac{\sigma_{ij}}{r_{ij}}\right)^{6}\right) = \frac{C_{12_{ij}}}{r_{ij}^{12}} - \frac{C_{6_{ij}}}{r_{ij}^{6}} \tag{2.14}$$

where ε_{ij}, σ_{ij} and C_{12}, C_6 are the parameters that control the depth and position of the potential energy well for a given pair of atoms. C_{12} is the repulsive term coefficient and C_6 the attractive term coefficient. The interplay between these two values govern the attraction or repulsion between two atoms and will later be used to create stiff (repulsive), semi-flexible and flexible (attractive) polymers in chapter 3.

For two different atom types i and j with parameters $C_{12_{ii}}$, C_{6ii} and $C_{12_{jj}}$, $C_{6_{jj}}$ respectively, the following geometric averages are used to calculate their interactions:

$$C_{6_{ij}} = \sqrt{C_{6_{ii}} C_{6_{jj}}} \text{ and } C_{12_{ij}} = \sqrt{C_{12_{ii}} C_{12_{jj}}} \tag{2.15}$$

The non-bonded potentials decay over time, and from a mathematical point of view can be calculated between any two atoms over very long range. However, after a certain distance, their contribution to the total potential is negligible because with increasing distance they approach zero. This is why Gromacs uses a cut-off radius for both the Coulomb and LJ potentials. Beyond this cut-off the long ranged interactions are set to and this step saves a lot of the computational time.

2.4 Energy minimization

Before beginning the actual runs, the system needs energy minimization because the in general the crystal structures are often not in their energy minimized state and the addition of hydrogen atoms or solvents lead to much interference in the structure. In the beginning the molecules can either overlap or can be far too close to each other causing the total forces of the system to become excessively high and that often tends to a failure in the MD simulations. To avoid this, energy minimization algorithms are adopted following the algorithm depicted in figure 2.4. *Steepest decent* is the most widely used algorithm in molecular mechanics and is also implemented in Gromacs for this very purpose. The idea behind this method is to use derivative information from the potential energy and follows the direction of the negative gradient, which is the same as the direction of the driving force. By moving along the steepest local gradient of the energy function, the nearest local minimum is found and can be mathematically shown as:

$$\mathbf{r}_{n+1} = \mathbf{r}_n + \frac{\mathbf{F}_n}{\max(|\mathbf{F}_n|)} d_n \tag{2.16}$$

where $\mathbf{r}_{n+1}$ is the new positions for the atoms, $\mathbf{r}_n$ the initial position, d_n the maximum displacement, $\mathbf{F}_n$ the force or the negative gradient of the potential and $\max(|\mathbf{F}_n|)$ the largest absolute value of the force components. The minimization comes to a halt when the absolute value of the maximum force is less than the user specified value or when the simulation has been run for the maximum user specified steps. After this procedure, the simulation is ready to use for real dynamics.

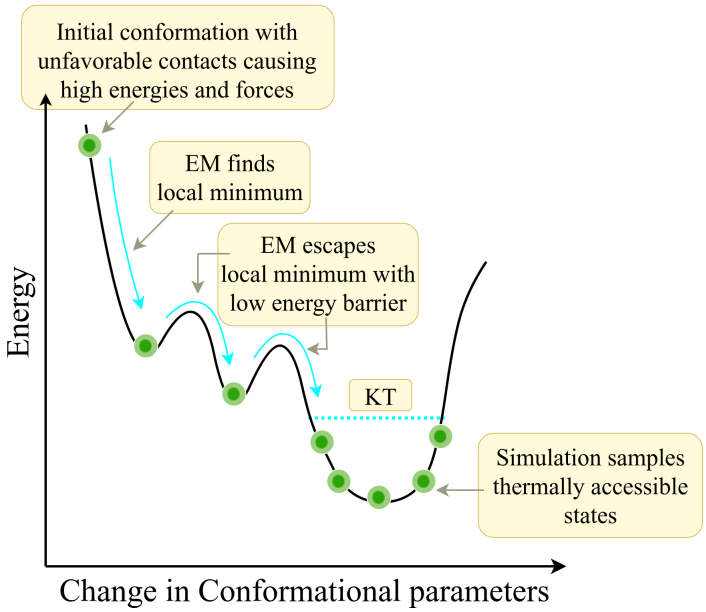

Figure 2.4: Energy minimization scheme. Molecular dynamics uses thermal energy to move smoothly over surfaces.

2.5 Integrating Newton's second law of motion

As depicted in figure 2.1, the total force acting on every atom is the calculated using equation 2.3 . From this equation the new location and velocity vectors are acquired by numerical integration. The two most commonly used are the *leap-frog* and the *Verlet* algorithms. Gromacs by default uses the *leap-frog* integrator wherein the locations $\mathbf{r}_i$ are solved at time t and velocities $\mathbf{v}_i$ at time $t-\frac{1}{2}\Delta t$ according to the following equations :

$$\mathbf{v}_i(t+\frac{1}{2}\Delta t) = \mathbf{v}_i(t-\frac{1}{2}\Delta t) + \frac{\Delta t}{m_i}\mathbf{F}_i(t) \tag{2.17}$$

$$\mathbf{r}_i(t+\Delta t) = \mathbf{r}_i(t) + \Delta t \mathbf{v}_i(t+\frac{1}{2}\Delta t) \tag{2.18}$$

where Δt is the time step, m_i is the mass of atom i, and $\mathbf{F}_i$ is the total force acting on it.

The *leap-frog* algorithm is named according to the way in which the calculations of positions and velocitiesleap over each other, as shown in figure 2.5. It evaluates the velocities at half-integer time steps and uses these velocities to compute the new positions.

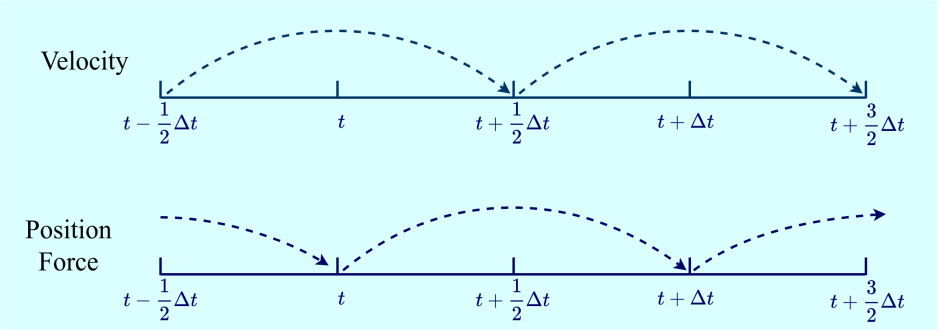

Figure 2.5: *Leap-frog* algorithm. The velocities are first calculated at time $t + \frac{1}{2}\Delta t$. These are used to calculate positions, $\mathbf{r}$ at $t + \Delta t$. In this way the velocities leap over the positions, and then the positions leap over the velocities.

After this calculation is done for every atom in the system, their locations and velocities are updated and the time goes forward by one step. This new configuration acts as the basis for the next loop and the all the calculations, starting from differentiating the total potential, are made once again (see figure 2.1 green block). When the simulation has reached maximum steps, the final coordinates, velocities and energies are saved to do further analysis.

2.6 Simulation box and Periodic boundary conditions

A simulation box is a three-dimensional space that the atoms or molecules occupy and defines the area where the calculations will be carried out. When MD simulations are carried out in explicit solvent, periodic boundary conditions (PBC) are commonly used for minimization of edge and finite size effects, otherwise a relatively large part of the particles will lie on the surface and will experience forces that are quite different from the ones in the bulk.

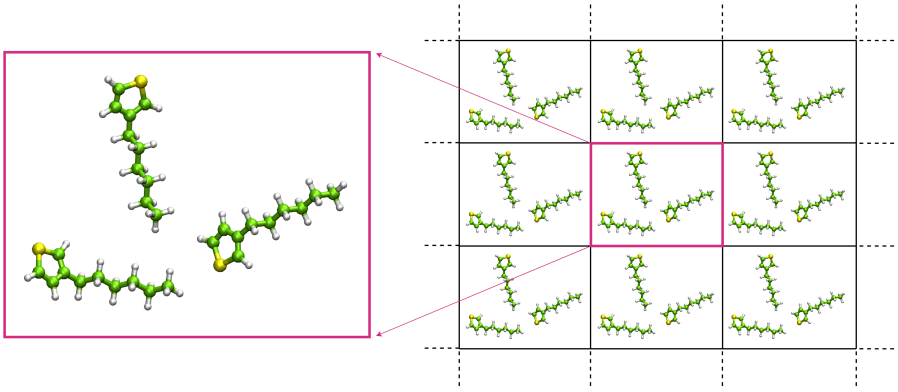

Figure 2.6: Periodic boundary conditions in two dimensions

The PBC step is fairly easy with the system in a central box and surrounded by infinite number of copies of itself and in the simulation the molecules in the original box and their periodic images move exactly in the same way, see figure 2.6. Therefore, when a molecule leaves a box, one of its images will enter from the opposite side. This way, there exits no physical boundaries and no surface molecules. Simulations that take place in vacuum do not need PBC condition though, because there is no solvent to experience edge effects. It should be noted that the size of the system should not be too small so as not to allow the one molecule to interact with itself. For example, a big polymer passing through one side of the box and entering from the opposite side should not be in the reach of its long ranged interactions discussed in section 2.3.2. This can be avoided by using significantly large boxes where half of the box length is larger than the previously mentioned cut-off radii for the non-bonded interactions.

2.7 Temperature and Pressure

If N are the total number particles in the system with volume V, temperature T, pressure P, chemical potential μ energy E, then MD simulations can be performed in various ways. The most important ensembles are microcanonical ensemble (NVE), canonical ensemble (NVT), isothermal-isobaric ensemble (NPT) and grand canonical ensemble (μVT) where the quantities in the brackets denote the quantities that are held constant in each of the ensembles.

The temperature T of a system with i particles having mass m_i, velocities v_i, and number of degrees of freedom $N_{df}$the instantaneous temperature $T(t)$ is defined as

$$T(t) = \frac{1}{N_{df} k_B} \sum_{i=1}^{N_{\text{particles}}} m_i v_i^2(t) \tag{2.19}$$

where, k_B is the Boltzmann constant. The effective temperature is a time average over a suitably long time interval, i.e. $T = \langle T \rangle$. It is often sensible to maintain the

temperature and the pressure to stay constant throughout the simulation by using either NVT or NPT ensemble. Therefore, it becomes important to set an initial temperature and control it during MD simulations.

2.7.1 Thermostats

Owing to the round-off errors in the integration step and use of non-bonded potential truncation, the temperature might have large fluctuations and drift, which is why it is important to control it during the simulation. This is achieved by including temperature coupling algorithms such as Berendsen [6], velocity-rescale [7] and Nosé–Hoover -thermostats [10]. Berendsen, which is one of the most commonly used algorithm, mimics the coupling of the system to an external heat bath that is fixed at a user defined temperature. The bath behaves as a source of thermal energy, supplying or removing heat from the system as needed. The deviation of the system temperature $T(t)$ from the bath temperature T_0 is correctly using the following notion,

$$\frac{dT(t)}{dt} = \frac{1}{\tau}(T_0 - T(t)) \tag{2.20}$$

where τ is the time constant and the coupling parameter whose value decides the strength of the coupling between the system and the bath. Therefore, by changing the value of τ the strength of the coupling can be varied. In this method we have an exponential decay of the system temperature that approaches the reference temperature. The temperature of the system is corrected by using the factor λ that acts on the atom velocities at every time step and is given as

$$\lambda = 1 + \frac{\Delta t}{\tau_T}\left(\frac{T_0}{T(t)} - 1\right)^{\frac{1}{2}} \tag{2.21}$$

A weak coupling does not generate rigorous canonical averages. The velocity scaling therefore can lead to temperature differences among different components of the system, This phenomenon is called "hot solvent, cold solute". The problem is usually avoided in Gromacs by applying temperature coupling to the solute and the solvent separately.

2.7.2 Barostats

Pressure is derived from the standard definition of force per unit area acting normal to the surface. For a simulation of N particles in cubic box with box size L, and planar surface area $A = L^2$ and volume $V = L^3$ inserted into the box, perpendicular to the x-axis, the pressure on this surface is

$$P_x = \frac{F_x}{A} = \frac{1}{A}\frac{d(mv_x)}{dt} \tag{2.22}$$

Therefore, pressure is the amount of momentum that crosses a unit area of the surface in unit time and can be defined as a momentum flux. This flux comprises of two parts

$$P = P_m + P_f \tag{2.23}$$

(i) P_m, the momentum carried by the atoms themselves as they cross the area during time dt and is derived from the kinetic theory, leading to ideal gas law

$$\langle P_m \rangle = \frac{2N}{3V} \left[\langle E_{kx} \rangle + \langle E_{ky} \rangle + \langle E_{kz} \rangle \right] = \frac{2N}{3V} \langle E_k \rangle \tag{2.24}$$

where E_k is the kinetic energy per atom and the braces $\langle\rangle$ denote time average.

(ii) P_f, the momentum transferred as a result of the forces acting between two atoms that lie on different sides of the surface and can be written as

$$P_f = \frac{1}{3V} \langle \sum_i \sum_j F_{ij} \cdot r_{ij} \rangle \tag{2.25}$$

where the index i and j run over the all the atoms on the two sides of the surface each.

The methods used for controlling the pressure are analogous to those used for temperature control. The system can be coupled to a barostat and the pressure can be maintained at a constant value by scaling the volume of the simulation box with the factor μ such that,

$$\mu = 1 - \kappa \frac{\Delta t}{\tau_p} (P - P_0) \tag{2.26}$$

where κ is the isothermal compressibility, τ_p is the relaxation constant which is the coupling constant, P_0 is the barostast pressure and P is the momentary pressure at time t. Scaling the volume μ means scaling the atomic coordinates with $\mu^{\frac{1}{3}}$. The scaling factor can be applied isotropically or anisotropically depending if you want to keep the box length constant in one direction. In Gromacs, the algorithms that are in most use are Berendsen [6], Parrinello– Rahman [21] and Martyna–Tuckerman–Tobias–Klein (MTTK) [22]. Their similarities and differences are discussed in more detail in the GROMACS manual [1, p. 321].

2.8 Free Energy and umbrella sampling

In this section we take a look at the free-energy problem. Free energy provides a connecting link between the microscopic representation of the system to its thermodynamic property, the free energy. It is to be noted that it cannot give absolute free energies but the speculation of relative free energies of two related systems is possible. According to the first law of thermodynamics the total energy E of the system is the sum of its potential V and kinetic energy$K$ which stays constant

i.e. $E = V + K =$ constant. Changes in one property are compensated by corresponding alterations in the other one. Gibbs free energy is calculated in NPT ensemble and free energy is used in NVT ensemble. This is because NPT ensemble requires an additional pressure and volume term in the partition function. Here the NVT system is discussed in detail, however, the background for NPT simulations are described in detail in [11]. For the NVT ensemble, canonical partition function Z is an integral comprising the whole phase space and is given by

$$Z = \frac{1}{h^{3N}} \int \int \exp\left(-\frac{H(\mathbf{r},\mathbf{p})}{k_B T}\right) d^N\mathbf{r} d^N\mathbf{p} \tag{2.27}$$

where the Hamiltonian $H(\mathbf{r},\mathbf{p})$ comprises of the kinetic $E_k(\mathbf{p})$ and potential $V(\mathbf{r})$ terms. For a momentum independent $V(\mathbf{r})$, the partial function is an integral over all the positions of the particles and can be written as,

$$Z = \frac{1}{h^{3N}} \int \exp\left(-\frac{V(\mathbf{r})}{k_B T}\right) d^N\mathbf{r} \int \exp\left(-\frac{E_k(\mathbf{p})}{k_B T}\right) d^N\mathbf{p} \tag{2.28}$$

$$= \frac{\mathrm{C}}{h^{3N}} \int \exp\left(-\frac{V(\mathbf{r})}{k_B T}\right) d^N\mathbf{r} \tag{2.29}$$

Free energy can is calculated as

$$A = -k_B T \ln Z \tag{2.30}$$

For carrying out umbrella sampling, one needs a characteristic property called the "reaction coordinate" ξ, that distinguishes different states. Throughout this thesis, the geometric distance between two groups is used as the reaction coordinate $\xi(\mathbf{r})$. Then the probability distribution is calculated along the reaction coordinate by the addition of delta distribution to the Boltzmann distribution, so the only contribution to the distribution would be that of the reaction coordinate and all other degrees of freedom are integrated out. The probability $P(\xi)\mathrm{d}\xi$ that the system lies in the interval $\mathrm{d}\xi$ around ξ is therefore given as,

$$P(\xi)\mathrm{d}\xi = \frac{\int \delta[\xi(\mathbf{r}) - \xi] \exp\left[\frac{V(\mathbf{r})}{k_B T}\right] d^N\mathbf{r}}{\int \exp\left[\frac{V(\mathbf{r})}{k_B T}\right] d^N\mathbf{r}} \mathrm{d}\xi \tag{2.31}$$

It is not quite feasible to numerically solve the exact canonical partition function or the probability distribution for all the possible states. It is however possible to calculate $P(\xi)\mathrm{d}\xi$ along the chosen reaction coordinate from multiple simulations. If the simulations are carried out for long enough or multiple number of times with different initial conditions then it is possible to sample the whole phase space and get an average over the statistical ensemble. This is the ergodic hypothesis and the simulation integral can be solved by noting the variation of the reaction coordinate ($\rho[\xi(t')]$) in every time interval dt'. Finally, $\rho[\xi(t')]$ is the time average of $P(\xi)\mathrm{d}\xi$.

$$P(\xi)\mathrm{d}\xi = \frac{\int \delta[\xi(\mathbf{r}) - \xi]\exp\left[\frac{V(\mathbf{r})}{k_B T}\right] d^N\mathbf{r}}{\int \exp\left[\frac{V(\mathbf{r})}{k_B T}\right] d^N\mathbf{r}}\mathrm{d}\xi = \lim_{t\to\infty}\frac{1}{t}\int_0^t \rho[\xi(t')]dt' \tag{2.32}$$

And the free energy of the system, i.e. the potential mean force $A(\xi)$ can be written as a function of the reaction coordinate as

$$A(\xi) = -k_B T \ln[P(\xi)]\mathrm{d}\xi = -k_B T\{\ln[P(\xi)] + \ln[\mathrm{d}\xi]\} \tag{2.33}$$

A proper sampling is guaranteed by applying an additional term in the energy that restrained the system to move in a region with local energy minima to reduce its energy. This method is called the umbrella sampling that allows to calculate the exact probability distribution along the reaction coordinate. This is done mainly because often certain states of the system are separated from others by extremely high energy barriers. Sometimes it might take years if not centuries of conventional MD simulations to talk through all molecular states. Umbrella sampling is one of the techniques that allows to accelerate the sampling by "flattening" those hills and ridges, which prevent MD from accessing certain states. The additional artificial potential energy term flattens the energy landscape. However, it is almost impossible to make an umbrella potential account for all degrees of freedom in the system. Therefore, the umbrella potential involves only a few (most often, one to three) degrees of freedom that form the reaction coordinate.

Gromacs creates a histogram from all the different simulation windows and produces a histogram corresponding to the probability distribution of the reaction coordinate. This algorithm is referred to as the weighted histogram analysis method (WHAM) in Gromacs. The histograms along the reaction coordinates must overlap in order to have a continuous potential mean force. In this thesis, the reaction coordinate used to calculate potential mean force of a system is always taken as the center of mass distance between two species of the system. This was majorly used in chapter 4 for determining the attractive forces between degradable polymers and DNA nucleobases.

2.9 Coarse grained Models

Coarse grained models are a reduced representation wherein several atoms are grouped into effective interaction sites represented by the so called *beads* (see fig 2.7). This decrease of chemical resolution leads to a potential loss of atom-specific interactions, however enabling the computational speed-ups of the order $> 10^3$ compared to atomistic models. This is partly due to the lower number of particles and thereby lower degrees of freedom and also partly due to the possibility of taking longer time steps. The main explanation behind CG models is that by averaging over non-essential details one reaches the time and length scales relevant for the properties of interest. Self-assembly mechanisms that require hundreds of microseconds are readily within reach, and it is

possible to simulate systems corresponding tens of millions of atoms ($< O(10^6)\text{nm}^3$ simulation box sizes) depending on the resolution of the CG model.

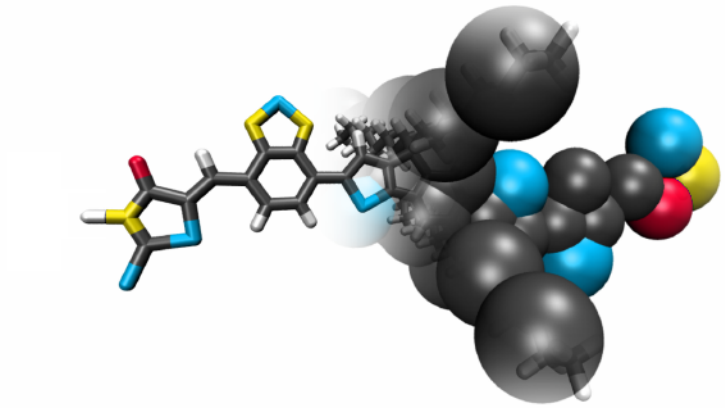

Figure 2.7: Illustration of coarse graining bead structure for an atomistic model.

By and large, two criterion can be said the exist in the field of coarse graining in molecular dynamics, each defined by either the "top down" or the "bottom up" approach. Loosely speaking, the "top down" paradigm relies on parametrising a CG model to reproduce experimentally measured structural or thermodynamic properties, whereas the "bottom up" paradigm relies on parametrising a CG model to reproduce the properties of a finer resolution model, usually atomistic and the CG forcefield developers are increasingly integrating aspects of both approaches in their models.

Various philosophies with varying resolutions have created many CG forcefields [8, 13, 24, 15, 4]. One of the most logical compromises between chemical specificity, transferability, and computational efficiency is the Martini force field [19, 20]. The Martini forcefield initially originated from the group of Siewert-Jan Marrink (University of Groningen), was originally developed for lipid bilayers [19] and made an enormous progress since 2004 and is now extended to proteins [23, 9], carbohydrates [17], nucleic acids [27, 28] and water models [3]. In the beginning it depended on four-to-one mapping meaning that the grouping of 4 non-hydrogen atoms into one Martini regular bead (R), but later one smaller beads (S) were also available for three-to-one mapping. Consequently tiny beads (T) were introduced permitting two-to-one mappings of planar atomistic residues, that lead to improvised models of conjugated ring-systems because of better descriptions of their planar structure and the consequent $\pi - \pi$ stacking effects. The Martini forcefield thus will form the basis of all the CG simulations carried out in this thesis. Detailed description on the creation and validation of a Martini forcefield from an existing atomistic force-field is explained in chapter 5 for Hyaluronic acid and Alginate polymers.

In addition to the different sized beads (R, S and T), Martini also contains six main

particle types namely: polar beads (P), non-polar beads (N), apolar beads (C), charged beads (Q), halogen beads (X) and water beads (W). These six beads (except W) can be assigned varying degree of polarity from 1 (lowest polarity) to 6 (highest polarity) and can furthermore have subtypes related to their electronic properties or hydrogen bonding capabilities (hydrogen doner (d) or accepter (a)). This in total amounts to about 800 bead types. In regards to parametrisation, martini uses a combination of both, the "top down" and "bottom up" approaches. The bonded parameters are taken from atomistic models, whereas the non-bonded parameters chosen in a way that they reproduce the free energies of transfer between polar and non-polar solvents and the densities of liquids. Bonded and non-bonded interactions are described in the similar way as to the ones used for atomistic force fields and explained in section 2.3.1 and 2.3.2 respectively. However, martini beads, in general, carry no partial charge and are not assigned bead-specific LJ parameters, so the Coulomb term can be disregarded in most cases, whereas the LJ parameters are explicitly defined in a tabulated form for each pair-interaction.

2.9.1 Martini Coarse graining in Carbohydrates

In this section we would discuss in detail Martini CG model used for basic parameterization of the carbohydrate force field because it is fully compatible with all the Martini lipid and protein models and would be used later in the chapter 5 for modeling Hyaluronic acid and Alginate. Therefore, we would look into the details of the mapping and parameterization of bonded and non-bonded interactions. Advanced details for interested readers can be found in the original articles [23, 20]. A single sugar ring can be represented by 3 Martini CG beads as shown in figure 2.8 (a) to preserve the geometrical shape of the rings and distinguish between different types of monosaccharides by the virtue of bond lengths, angles and CG particle types. Disaccharides are best represented by 6 beads as shown in figure 2.8 (b). It should be noted that to preserve the glycosidic linkage and their angle and dihedral properties, the CG beads in disaccharide are chosen to be different from the monosaccharide in a way that the beads B2 and B4 (see figure 2.8 (b)) must include the central ring carbons. The connecting oxygen (the glycosidic linkage) goes to bead B2, giving it higher polarity than B4. Oligosaccharides are constructed by connecting multiple disaccharide residues through additional bonds. Oligosaccharides are developed on the disaccharide topology by additionally using an extra angle potential (ϕ) for three successive backbone beads.

Non-bonded parameters are described by equation 2.14 and are unchanged for the work done in this thesis as the original Martini σ and ε values describe well the disaccharide beads' non-bonded properties. These σ and ε only affect the sugar-sugar interaction and do not play a role in the partition free energy. Three types of bonded interactions are considered for the carbohydrates: bonds, angles and dihedrals

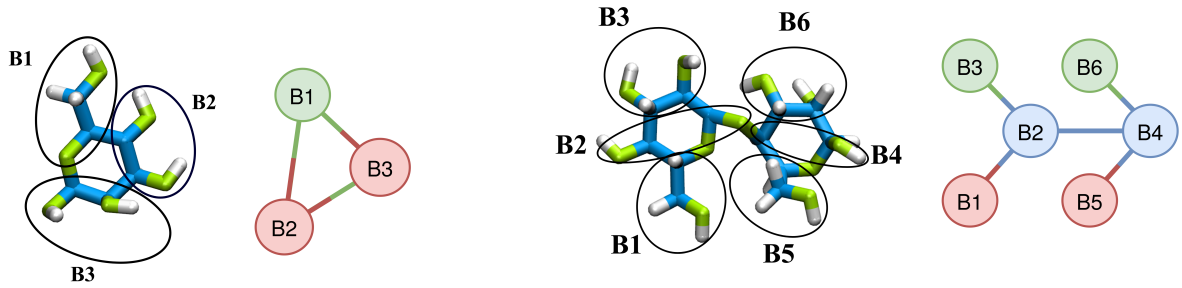

(a) (b)

Figure 2.8: Coarse-grained mapping for mono- and disaccharides. (a) Monosaccharides are represented by three beads B1-B3. (b) Disaccharides are represented by six beads B1-B6 and the bond between B2 and B4 represents the glycosidic bond.

described by the potentials in equations 2.7, 2.9 and 2.11 respectively. In iterative steps, the CG bonded values are adjusted manually to obtain as close a match as possible to the atomistic model distributions.

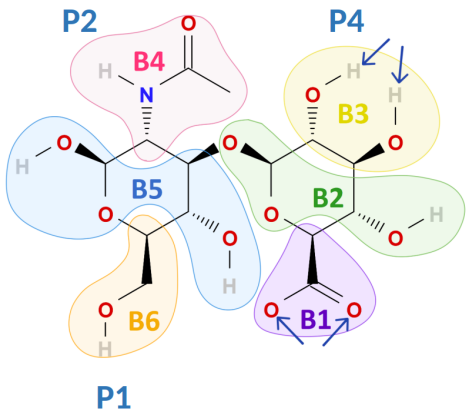

Figure 2.9: Coarse-grained mapping for Hyaluronic disaccharide unit to understand polarity of beads.

For the selection of particle types, standard Martini beads should be used to make certain the compatibility with the other force field components. In this thesis beads of the type polar (P) and charged (Q) are used to define disaccharides in Hyaluronic acid and Alginate because of the presence of high number of hydroxyl groups around the rings.

The polar beads P have further subtypes P1, P2, P3 and P4 in increasing amount of polarity. This can be understood properly from figure 2.9. Here we consider a Hyaluronic disaccharide unit and map 6 Martini CG beads B1, B2, B3, B4, B5 and B6 on the atomistic scheme. Bead B6 has only one hydroxyl group and therefore should

be assigned with lowest polarity bead P1. Bead B4 has a higher polarity due to the presence of a nitrogen and oxygen compared to a hydroxyl group and hence should be assigned with higher polarity bead P2. Bead B3 has two hydroxyl groups and therefore has highest polarity bead P4. Bead B1 contains a carboxyl group and therefore has an overall negative charge of -1.0, therefore it is no longer a polar bead but a charged bead Q. The blue arrows in figure 2.9 point out that there are two atoms that can have strong non-bonded interactions and therefore are highly recommended to be clubbed into one CG bead. If two atoms having strong non-bonded potential are placed into two different beads, the CG will not form a good match to the original atomistic model even after several iterations. Thus when assigning CG beads to an atomistic model, they should be created in a way that the backbone structure is maintained, the bead polarities are assigned properly and the two closely non-bonded atoms are clubbed into one bead for fastest convergence.

References

[1] M Abraham, D Van Der Spoel, E Lindahl, and B Hess. The gromacs development team gromacs user manual, version 2019, 2019.

[2] Mark James Abraham, Teemu Murtola, Roland Schulz, Szilárd Páll, Jeremy C Smith, Berk Hess, and Erik Lindahl. Gromacs: High performance molecular simulations through multi-level parallelism from laptops to supercomputers. *SoftwareX*, 1:19–25, 2015.

[3] Clément Arnarez, Jaakko J Uusitalo, Marcelo F Masman, Helgi I Ingólfsson, Djurre H De Jong, Manuel N Melo, Xavier Periole, Alex H De Vries, and Siewert J Marrink. Dry martini, a coarse-grained force field for lipid membrane simulations with implicit solvent. *Journal of chemical theory and computation*, 11(1):260–275, 2015.

[4] Jonathan Barnoud and Luca Monticelli. Coarse-grained force fields for molecular simulations. In *Molecular modeling of proteins*, pages 125–149. Springer, 2015.

[5] Henk Bekker, HJC Berendsen, EJ Dijkstra, S Achterop, R Vondrumen, David VANDERSPOEL, A Sijbers, H Keegstra, and MKR Renardus. Gromacs-a parallel computer for molecular-dynamics simulations. In *4th International Conference on Computational Physics (PC 92)*, pages 252–256. World Scientific Publishing, 1993.

[6] Herman JC Berendsen, David van der Spoel, and Rudi van Drunen. Gromacs: A message-passing parallel molecular dynamics implementation. *Computer physics communications*, 91(1-3):43–56, 1995.

[7] Giovanni Bussi, Davide Donadio, and Michele Parrinello. Canonical sampling through velocity rescaling. *The Journal of chemical physics*, 126(1):014101, 2007.

[8] Paola Carbone, Hossein Ali Karimi Varzaneh, Xiaoyu Chen, and Florian Müller-Plathe. Transferability of coarse-grained force fields: The polymer case. *The Journal of chemical physics*, 128(6):064904, 2008.

[9] Djurre H de Jong, Gurpreet Singh, WF Drew Bennett, Clement Arnarez, Tsjerk A Wassenaar, Lars V Schafer, Xavier Periole, D Peter Tieleman, and Siewert J Marrink. Improved parameters for the martini coarse-grained protein force field. *Journal of chemical theory and computation*, 9(1):687–697, 2013.

[10] Denis J Evans and Brad Lee Holian. The nose–hoover thermostat. *The Journal of chemical physics*, 83(8):4069–4074, 1985.

[11] A Grossfield and DM Zuckerman. Annual reports in computational chemistry. 2009.

[12] Berk Hess, Carsten Kutzner, David Van Der Spoel, and Erik Lindahl. Gromacs 4: algorithms for highly efficient, load-balanced, and scalable molecular simulation. *Journal of chemical theory and computation*, 4(3):435–447, 2008.

[13] David M Huang, Roland Faller, Khanh Do, and Adam J Moulé. Coarse-grained computer simulations of polymer/fullerene bulk heterojunctions for organic photovoltaic applications. *Journal of Chemical Theory and Computation*, 6(2):526–537, 2010.

[14] Anna Köhler and Heinz Bässler. *Electronic processes in organic semiconductors: An introduction*. John Wiley & Sons, 2015.

[15] Cheng-Kuang Lee and Chun-Wei Pao. Nanomorphology evolution of p3ht/pcbm blends during solution-processing from coarse-grained molecular simulations. *The Journal of Physical Chemistry C*, 118(21):11224–11233, 2014.

[16] Erik Lindahl, Berk Hess, and David Van Der Spoel. Gromacs 3.0: a package for molecular simulation and trajectory analysis. *Molecular modeling annual*, 7(8):306–317, 2001.

[17] Cesar A Lopez, Andrzej J Rzepiela, Alex H de Vries, Lubbert Dijkhuizen, Philippe H Huenenberger, and Siewert J Marrink. Martini coarse-grained force field: extension to carbohydrates. *Journal of Chemical Theory and Computation*, 5(12):3195–3210, 2009.

[18] Alpeshkumar K Malde, Le Zuo, Matthew Breeze, Martin Stroet, David Poger, Pramod C Nair, Chris Oostenbrink, and Alan E Mark. An automated force field topology builder (atb) and repository: version 1.0. *Journal of chemical theory and computation*, 7(12):4026–4037, 2011.

[19] Siewert J Marrink, Alex H De Vries, and Alan E Mark. Coarse grained model for semiquantitative lipid simulations. *The Journal of Physical Chemistry B*, 108(2):750–760, 2004.

[20] Siewert J Marrink, H Jelger Risselada, Serge Yefimov, D Peter Tieleman, and Alex H De Vries. The martini force field: coarse grained model for biomolecular simulations. *The journal of physical chemistry B*, 111(27):7812–7824, 2007.

[21] R Martoňák, Alessandro Laio, and Michele Parrinello. Predicting crystal structures: the parrinello-rahman method revisited. *Physical review letters*, 90(7):075503, 2003.

[22] Glenn J Martyna, Mark E Tuckerman, Douglas J Tobias, and Michael L Klein. Explicit reversible integrators for extended systems dynamics. *Molecular Physics*, 87(5):1117–1157, 1996.

[23] Luca Monticelli, Senthil K Kandasamy, Xavier Periole, Ronald G Larson, D Peter Tieleman, and Siewert-Jan Marrink. The martini coarse-grained force field: extension to proteins. *Journal of chemical theory and computation*, 4(5):819–834, 2008.

[24] William George Noid. Perspective: Coarse-grained models for biomolecular systems. *The Journal of chemical physics*, 139(9):09B201_1, 2013.

[25] Szilárd Páll, Mark James Abraham, Carsten Kutzner, Berk Hess, and Erik Lindahl. Tackling exascale software challenges in molecular dynamics simulations with gromacs. In *International conference on exascale applications and software*, pages 3–27. Springer, 2014.

[26] Sander Pronk, Szilárd Páll, Roland Schulz, Per Larsson, Pär Bjelkmar, Rossen Apostolov, Michael R Shirts, Jeremy C Smith, Peter M Kasson, David Van Der Spoel, et al. Gromacs 4.5: a high-throughput and highly parallel open source molecular simulation toolkit. *Bioinformatics*, 29(7):845–854, 2013.

[27] Jaakko J Uusitalo, Helgi I Ingolfsson, Parisa Akhshi, D Peter Tieleman, and Siewert J Marrink. Martini coarse-grained force field: extension to dna. *Journal of chemical theory and computation*, 11(8):3932–3945, 2015.

[28] Jaakko J Uusitalo, Helgi I Ingólfsson, Siewert J Marrink, and Ignacio Faustino. Martini coarse-grained force field: extension to rna. *Biophysical journal*, 113(2):246–256, 2017.

[29] David Van Der Spoel, Erik Lindahl, Berk Hess, Gerrit Groenhof, Alan E Mark, and Herman JC Berendsen. Gromacs: fast, flexible, and free. *Journal of computational chemistry*, 26(16):1701–1718, 2005.

Chapter 3

Poly(3-hexylthiophene) chains and their temperature-dependent conformation behavior

Attributing to the flexibility of the material, their cheaper production costs and promotion on usage of organic materials, polymer solar cells provide an alternative to silicon based solar cells. The working principle of these organic solar cells is dependent on the morphology of the conjugated polymers used, that are responsible for photon absorption, charge generation and current creation. One such conjugated polymer that we would have a detailed look in this study is the Poly(3-hexylthiopene) (P3HT). This chapter uses atomistic (AA) and coarse grained (CG) force-field models to study the isolated polymer conformation behavior of P3HT as a function of temperature and compare the two models. It is shown here that the polymer undergoes into two major kinds of aggregated forms, namely (a) toroids– compact form with lower conjugation length and (b) bundles– repeatedly folded elongated form with higher conjugation length. Both the force-fields show the existence of these two forms, bundles being more abundant at lower temperatures, and the models fall well in agreement with each other. This change in the aggregated forms are responsible for the phase transition observed by the spectroscopic experiments done by Panzer et al [23, 21] and it becomes more prominent in CG simulations where the polymer is solvated in tetrahydrofuran (THF) solvent compared to the vacuum CG and AA simulations. This chapter characterizes the conformations observed in P3HT by using the measure of flexibility in simple polymers modeled using Lennard-Jones potential.

3.1 Introduction

Conjugated polymers like poly-thiophenes have gathered significant research attention since the discovery of their semi-conducting properties and low production costs, light weight, environment stability and corrosion resistance compared to inorganic semiconductors [31, 14, 18, 24, 18, 25]. Especially poly(3-hexylthiophene) has become front runner in applications such as solar cells, field-effect transistors, light-emitting diodes, biosensors, and many others. Owing to its opto-electronic properties, the progress of P3HT and its significance is illustrated by a number of reviews and books explaining the synthesis of these polymers and in obtaining the control of their properties [26, 4, 33, 11, 16, 1, 9, 27, 30]. To gain a better understanding of the relationship between the morphology and the performance of an organic solar cell, a molecular level knowledge is required. Kolinski [15] showed that the polymers can be broadly be categorized into three groups, (i) *stiff*, (ii) *semi-flexible* and (iii) *flexbile* polymers on the basis of the conformation they collapse into when decreasing the temperature or changing the solvent from bad to good. There has been quite some debate in the past regarding P3HT and its stiffness and aggregated forms. Dynamic light scattering experiments on single P3HT chains were carried out by Heffner et al. [12] to show that P3HT behaved as a flexible polymer. However, neutron scattering experiments [17] and viscosity measurements [19] suggested that P3HT falls in the semiflexible category. In this work, we focused on distinguishing these categories in detail using LJ polymer and implementing the same methodology in determining the nature of P3HT. For motivation, we used the spectroscopic experimental data on highly monodisperse, regioregular P3HT published by Panzer et al. [23, 21]. In this publication they noted a shift in the absorption spectra from blue to red with increase in temperature from 170K to 300K and interpreted that P3HT is going through a phase transition from random coil at 300Kto an ordered aggregate at 170K. Their outlook towards the results was that the polymer is undergoing a swelling before collapse as noted by Kolinski [15] for semi-flexible polymers when categorizing his polymers. Therefore, the first part of our plan involved carrying out MD simulations on simple LJ polymers and reproduce the data obtained by Kolinski. Then look into the conformations in detail to relate different conformations to the three polymer categories (*stiff*, *flexible* and *semi-flexible*) and compare with Kolinski's interpretation. Lastly, carry out single P3HT simulations and visualize its conformation. Using the information from LJ polymers, determine if P3HT belong to *flexible* or *semi-flexible* group. For MD, accurate force-fields are needed to properly reproduce the behavior of the system under study with exact information about the atoms and all their interactions. This chapter will introduce two such force-fields, a fully atomistic one derived from OPLS-AA and optimized by large-scale DFT, and a corse-grained (CG) one, derived from Martini model. The atomistic force-field is more accurate, but is computationally expensive. Therefore we use these vacuum atomistic simulations to benchmark a coarse-grained (CG) model based on the Martini force field [3]. Then we solvate the CG model in THF to carry out long simulations with shorter runtime.

3.2 System setup

All the vacuum simulations were carried out at different temperatures (10K < T < 300K) in NVT ensemble along with velocity rescaling thermostat and periodic boundary condition in all the three directions. For better statistics, each system with T < 600K was run 50 times with random initial conformations for 5 ns with dt = 1fs and systems with T > 600K were run once for 200ns. The force-field used for simulating LJ polymer, atomistic P3HT and martini CG P3HT are discussed in detail in sections 3.2.1, 3.2.2 and 3.2.3 respectively. We analyze the polymers properties using two quantities, (i) D_{max} which is the maximum distance between two monomers of a polymer and (ii) $\langle S^2 \rangle$ which is the radius of gyration and is defined as,

$$\langle S^2 \rangle = \frac{1}{n} \left\langle \sum_{i=1}^{n} (r_i - r_{CM})^2 \right\rangle \tag{3.1}$$

where r_i is the position of the monomer i of a polymer with length n and r_{CM} is the polymer center of mass.

For systems with solvent, we carried out NPT simulations with isotropic Parrinello–Rahman barostat and a equilibration pressure of 1.0 bar for 2ns after energy minimisation and 100ns of NVT equilibration.

3.2.1 Lennard Jones Polymer

Each monomer is modeled using a single LJ bead of the form as shown in equation 2.14. The C_{12} values for all the polymers are fixed at $10^{-6} \frac{\text{kJ}}{\text{mol nm}^{12}}$. Monomers are connected with the harmonic potential of the form as in equation 2.7 (3.1 (a)) with $b^0 = 0.1$nm as the equilibrium distance between two monomers i and j.

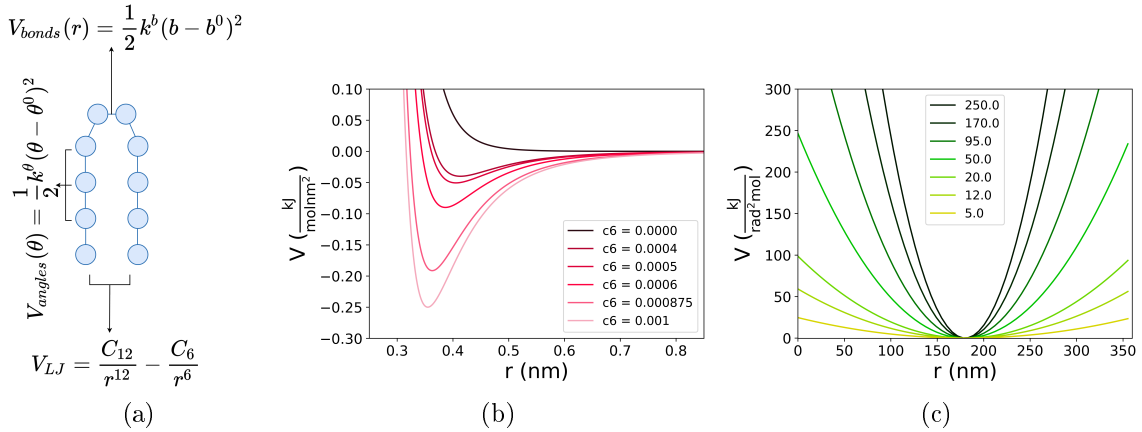

(a) (b) (c)

Figure 3.1: (a) Model LJ polymer (b) LJ potential with different C_6 values used to tune stiffness of polymers. (c) Angle bending potential with k^θ used to change polymer stiffness.

The angle potential has the form of equation 2.8 where the equilibrium angle between three atoms is $\theta^0 = 180^0$. The polymer stiffness was tuned using two different methods: (i) where bending constant k^θ is fixed and the non-bonded parameter C_6 is varied from $0.000 \frac{\text{kJ}}{\text{mol nm}^6}$ to $0.001 \frac{\text{kJ}}{\text{mol nm}^6}$ (3.1 (b)) and (i) where C_6 is fixed and bending constant k^θ is varied from $5 \frac{\text{kJ}}{\text{mol rad}^2}$ to $120 \frac{\text{kJ}}{\text{mol rad}^2}$ (3.1 (c)) .

3.2.2 Atomistic model of P3HT

The atomistic model was based on the forcefield developed by Bhatta et al. [6]. They carried out explicit treatment of all atoms to model fully relaxed equilibrium conformation of P3HT polymer with 10 repeating units. This model was able to reproduce the bulk experimental results of crystallized P3HT and matched properties like packing structure, torsional angles of backbone and the hexyl side chains. To create terminal ends of P3HT we added uncharged hydrogen at both the ends.

Figure 3.2(a) gives a schematic representation of a central two-monomer unit of P3HT and figure 3.2(b) shows its atomistic model. The torsional angle within each thiophene ring is labeled as ψ, between two consecutive thiophene rings is α and five hexyl torsions associated with skeletal carbons of the side chains are labeled as β_i. The thiophene rings in a P3HT polymer are planar in nature and therefore any deviation from $\psi = 0$ leads to increase in very rapid increase in the torsional energy. The inter-chain backbone torsional angle α is responsible for the *cis* and *trans* conformations depending on if $\alpha = 0$ or $\alpha = 180^0$. In this case the hexyl chain is kept all-*trans* conformation and the remaining polymer as planar.

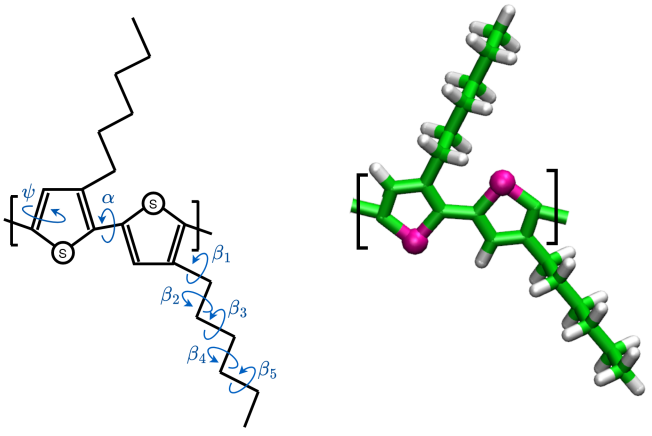

(a) (b)

Figure 3.2: (a) Schematic representation of P3HT. (b) Atomistic model of P3HT used for all atom simulations.

In order to validate the forcefied we created a P3HT packing structure containing 32 P3HT polymers similar to the description of [6]. The length of the polymers extended along the x-axis (figure 3.3 (a)) and the side chain along z-axis (figure 3.3 (b)) and y-axis was the stacking direction with stacking distance of 3.88Å. The system was then subjected to simulated annealing from 20K to 550K with 20K increment up to 300K and 10K increment thereafter. This was carried out for polymers with monomers $n = 13$,20 and 30 and the results were compared to Bhatta et al.

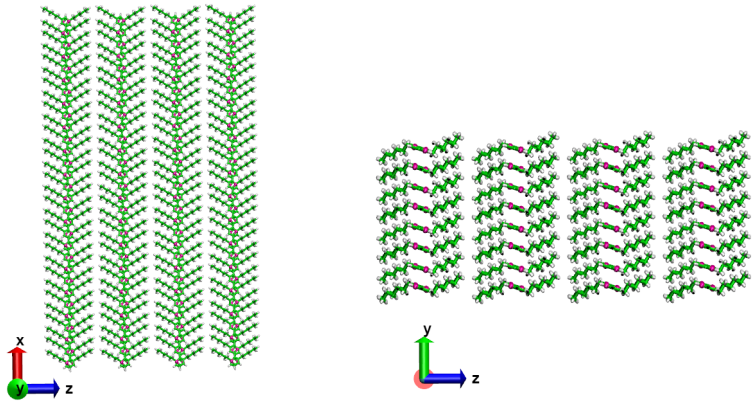

(a) (b)

Figure 3.3: Snapshot of P3HT packing structure of 32 P3HT polymers used for validation. (a) Top view with $\pi - \pi$ stacking axis towards the viewer. (b) Side view with P3HT backbone towards the viewer

Ordering of crystalline P3HT was obtained from the torsional angle population in the literature presented by Bhatta et al. Therefore we calculated torsional angles α, β_1 and β_2 of figure 3.2 (a) for all the polymers and present their distribution plots and its comparison to the results obtained by Bhatta et al. The torsional populations at 300K for the inter-ring torsional angle (α), as well as torsional angles associated with the hexyl side chains ($\beta_1$and β_2) from Bhatta et al's literature for polymers with 13 and 30 monomers are shown in figure 3.4 (a), (c) and (e) respectively. The torsional angle populations of α, $\beta_1$and β_2 from our simulated systems with $n = 13$ and $n = 30$ are shown in figure 3.4 (b), (d) and (f) respectively. The torsional angles α in figure 3.4(b) show peaks at 180^0 and confirm that the extended P3HT chains are planar and agree with Bhatta et al's α in 3.4(a).

The torsional angle population of the hexyl group that are responsible for the twisting of side chains β_1 in figure 3.4(d) shows a peak at $\sim 90^0$ and matches with the Bhatta et al's $\beta_1$angles in 3.4(c). The four C–C–C–C torsion angles that are

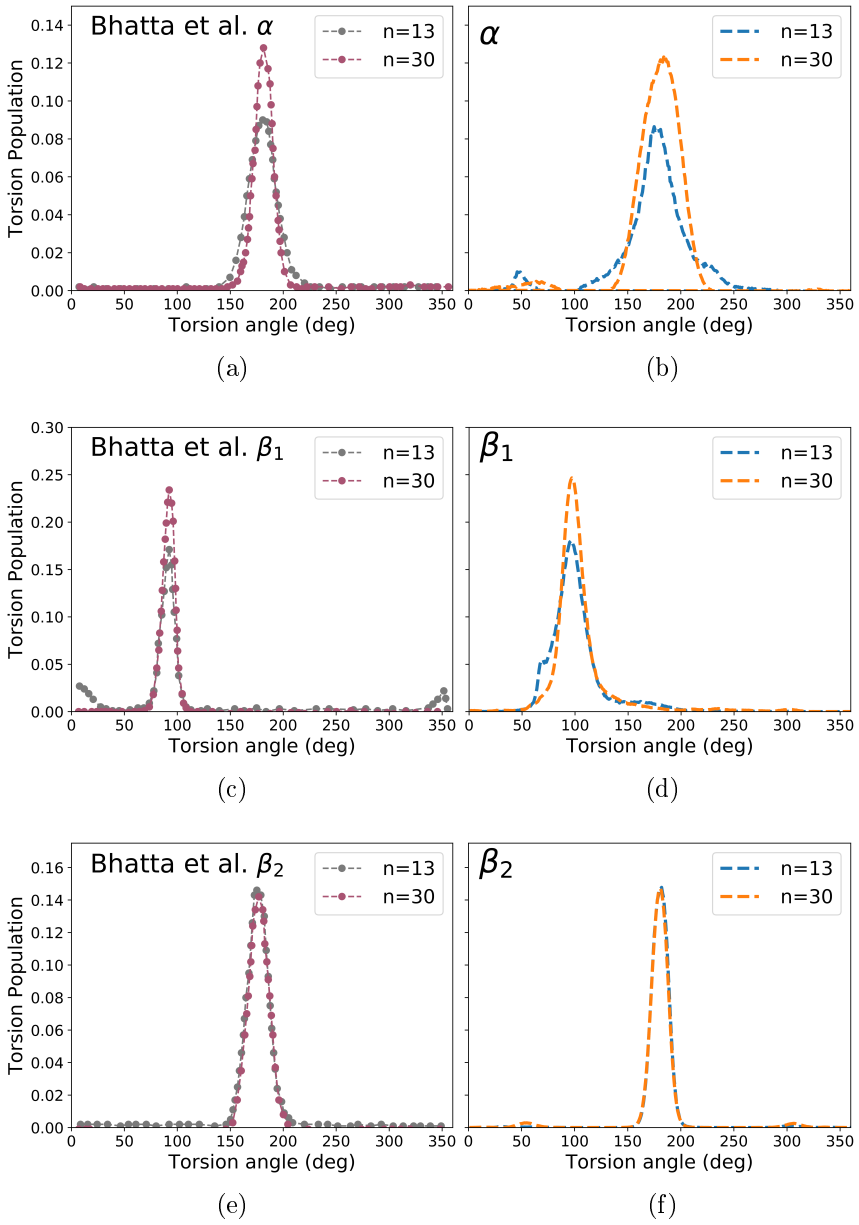

Figure 3.4: Torsional population at 300K for P3HT chain lengths $n = 13$ and 30. Results of α, $\beta_1$and β_2 from the literature of Bhatta et al. are shown in (a), (c) and (e) respectively. For validation of our model, α, $\beta_1$and β_2 torsional angle populations from simulations carried out in this work are plotted in (b), (d) and (f) respectively.

responsible for β_2 showed a preference at 180^0 in figure 3.4(f) and again shows a very good match to the β_2 obtained by Bhatta et al. as seen from 3.4(e). Thus these results clearly show that the model used for this work well reproduces the model of Bhatta et al. and the model is reliable for carrying out further studies on the

conformational properties of atomistic P3HT.

3.2.3 Martini CG model of P3HT

For modeling coarse grained model of P3HT we used the martini model directly from the work of Alessandri et al [2]. This martini coarse grained model represents the central thiophene ring of P3HT containing three heavy atoms using 3 martini beads, and the hexyl side chain with 2 beads. The beads that describe the thiophene ring are three SC5 beads that have been shown by Alessandri et al. to reproduce experimental transfer free energies for the five-member ring. A representation of the martini CG mapping is shown in figure 3.5(b) for a 2-mer atomistic model (3.5(a)) and its CG model in (3.5(c)) . The CG force-field bonded parameters are listed in table 3.1. Bonds that connect the ring structure are kept very stiff in nature and are modeled as constraints. Virtual sites (VS) with no mass and charge are defined at the center of the ring to control the polymer backbone that is of very much importance in conjugated polymers such as P3HT. Angles between the virtual sites VS and the thiophene SC5 beads are introduced to preserve the ring planarity.

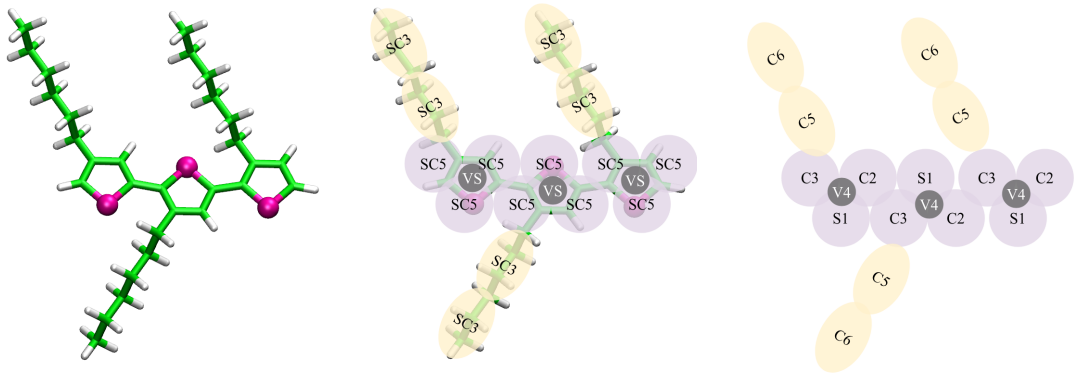

(a) (b) (c)

Figure 3.5: (a) 3-mer P3HT atomistic model. (b) CG mapping with mention of respective Martini bead types (c) Martini CG model with bead names used for validation.

For validation of the force-field, we compare the bonded length, angle and dihedral parameters in figure 3.6. The red dots show the data from the literature of Alessandri et al. and the green curves are the comparison to the simulation model reproduced for this work.

For solvation of P3HT, tetrahydrofuran (THF) is one of the most popular choice. To reproduce the experimental setup of Panzer et al. in the later sections, we used

Sr. no.	Bead types (names)	b_0(nm)	$k_b \frac{\text{kJ}}{\text{mol nm}^2}$
b_1	SC5 - SC5 (S1 - C2, S1 - C3, C2 - C3)	0.240	constraint
b_2	SC5 - SC3 (C3 - C5)	0.258	constraint
b_3	SC3 - SC3 (C5 - C6)	0.360	5000
b_4	VS_i-VS_j (VS_i-VS_j)	0.380	50000

Sr. no.	Bead types (names)	θ_0(deg)	$k_\theta \frac{\text{kJ}}{\text{mol}}$
θ_1	SC5 - SC5 - SC3 (S1 - C3 - C5)	180	250
θ_2	SC5 - SC3 - SC3 (C3 - C5 - C6)	155	25
θ_3	VS_i-$SC5_j$-$SC5_j$($V4_i$-$C3_j$-$C5_j$)	160	180
θ_4	VS_i-VS_j-VS_k($V4_i$-$V4_j$-$V4_k$)	158	180

Sr. no.	Bead types (names)	ϕ_0(deg)	$k_\phi \frac{\text{kJ}}{\text{mol}}$	n
ϕ_1	$SC5_i$ -VS_i -VS_j -$SC5_j$ ($S1_i$-$V4_i$ -$S1_j$ -$V4_j$)	0.0	1.80	1
		0.0	-9.50	2

Table 3.1: Martini P3HT CG bonded parameters. The indices i, j, k and l refer to the consecutively bonded units.

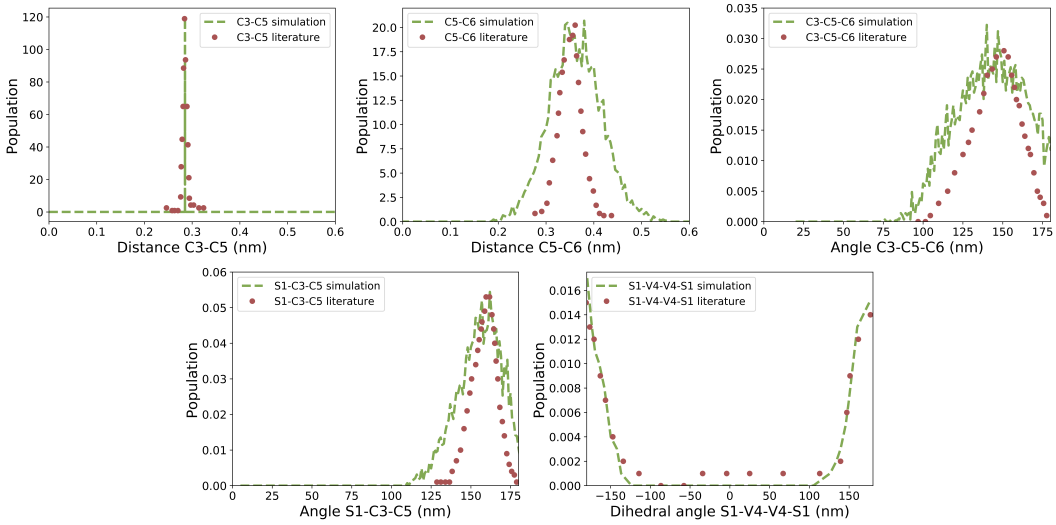

Figure 3.6: Bond and angle distributions for P3HT (our simulation results in green and literature values in red.) Each label indicates the beads for whom the distribution is shown.

a Martini CG model also for THF where we represent one molecule of THF with one Martini non-polar CG bead Na and its parameters are adopted from the work of Patti et al [8] (see figure 3.7 (a)). This model does not include any partial charges and cannot reproduce any polarization effects. However, our work does not deal with dielectric properties of the solvent or the molecular orientational correlations. It is nevertheless

quite important for us to have a model of THF that can reproduce the bulk fluid properties. Therefore we present in figure 3.7 (b) the radial distribution function of THF and compare it to the Martini CG model of Patti et al. for validation of the THF force-field we would be using in this chapter.

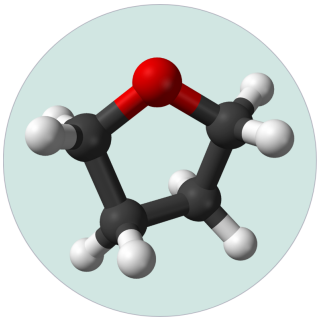

(a)

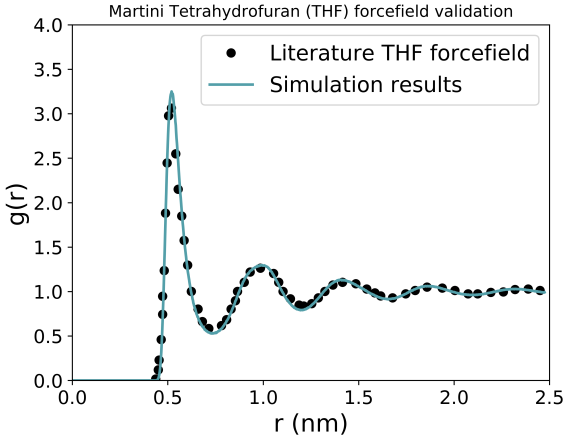

(b)

Figure 3.7: (a) Coarse grained (green bead) and atomistic (solid schematic) representation of THF. (b) Radial distribution function ($g(r)$) of THF obtained from our simulations (blue line) and its comparison to the literature data published by Patti et al (black dots) .

For Martini simulations with solvent, 5000 THF beads were added to a box containing one CG P3HT polymer for analysis and comparison to experimental results. As mentioned above, simulations with solvent were carried out using NPT ensemble for 10ns by using isotropic Parrinello–Rahman barostat with $\tau_p = 1.0$ps and a reference pressure of 1.0 bar after energy minimization and NVT equilibration of 200ps.

3.3 Results and Discussion

3.3.1 Lennard Jones Polymer

This section discusses the nature of polymers with different stiffness using the model described in sections 3.2.1. Here we present a plot of the mean squared radius $\langle S^2 \rangle$ of gyration stated in equation 3.1 in figure 3.8 (a) by varying the non-bonded parameter C_6 and in 3.8 (b) by varying the bonded parameter k_θ. Figure 3.9 plots time averaged maximum distance between any two monomers of the polymer D_{max} for LJ polymer with varying (a) C_6 and (b) k_θ.

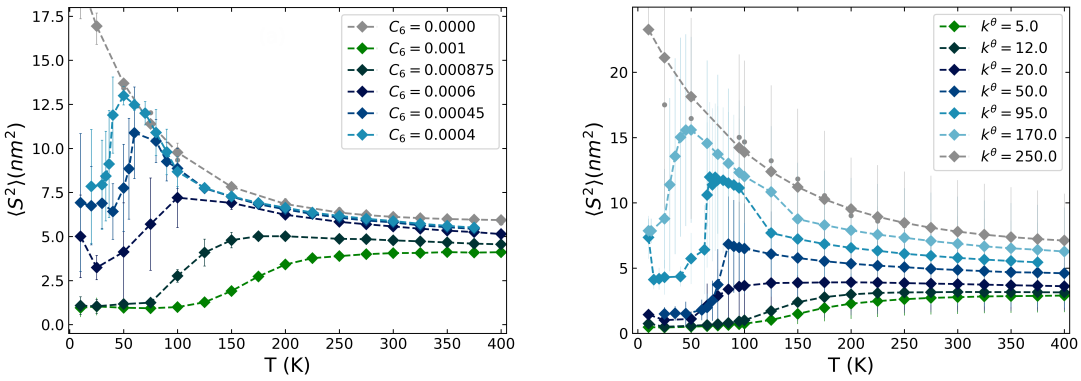

(a) (b)

Figure 3.8: $\langle S^2 \rangle$ vs Temperature for LJ polymer with 200 monomers (a) with varying non-bonded parameter C_6 and (b) varying bonded parameter k_θ.

In Figure 3.8 (a) *stiff* polymers ($C_6 = 0$) show increasing $\langle S^2 \rangle$ with decreasing temperature. *Flexible* polymers on the other hand ($C_6 \geq 0.0007$) show decreasing $\langle S^2 \rangle$ with decreasing temperature. *Semi-flexible* polymers (C6 = 0.0004, 0.00045, 0.0006) first show increasing $\langle S^2 \rangle$ with decreasing temperature followed by a sudden drop. The collapsed conformations decreases the surface energy but at the cost of high bending energy. A similar behavior is observed in figure 3.8 (b), where the stiffness of the polymer is tuned by varying the bonded parameter k_θ and proves that *stiff*, *flexible* and *semi-flexible* polymers can be created by tuning the bending potential too. Figure 3.8 confirms the intermediate swelling of polymers at critical temperatures as predicted by Kolinski et al. [15] using the simpler grid-based Monte-Carlo models. Similar to figure 3.8, *flexible* polymers show decreasing D_{max} with decreasing T in figure 3.9. *Stiff* polymers have increasing D_{max} with decreasing T and semiflexible polymers have increasing D_{max} with decreasing T followed by a drop. Thus, D_{max}

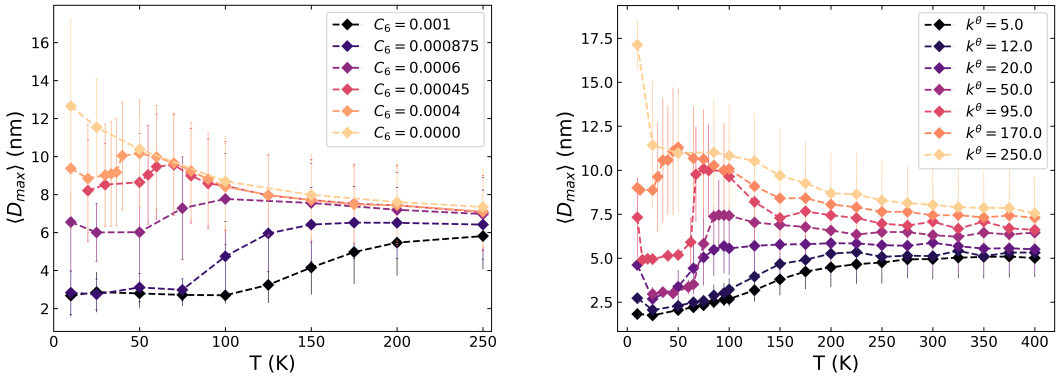

(a) (b)

Figure 3.9: $\langle D_{max} \rangle$ vs Temperature for LJ polymer with 200 monomers (a) with varying non-bonded parameter C_6 and (b) varying bonded parameter k_θ.

which is the maximum extension of the polymer, serves as an additional tool to distinguish the various conformations. It will become an important basis for further analysis of P3HT polymers.

At higher temperatures ($T > 250$K) in figures 3.8 and 3.9 all the lengths converge together, which is referred to as the "limit of random walk" which was first described by Flory [10] in 1949 . Flory suggested at the temperature at which a polymer reaches the behavior of random walk is given by the relation

$$\langle S^2 \rangle \propto n^{(\frac{6}{5})} \tag{3.2}$$

where n refers to the monomer units. For investigating Flory's theory for the LJ polymers, we simulated polymers with $n = 50$, 100, 200, 400 and 600 at temperatures 100K, 150K, 200K, 250K, 300K and 400K for *flexible* polymers ($C_6 = 0.001$) and present their $\langle S^2 \rangle$ in figure 3.10 and we find that the relation $\langle S^2 \rangle \propto n^{(\frac{6}{5})}$ is reached at $T \geq 250$K (red curves) which explains the reason behind convergence at $T \geqslant 250$K in figures 3.8 and 3.9 .

Considering one case for each kind, we'll discuss further in detail the cases $C_6 = 0.000$, $C_6 = 0.00045$ and $C_6 = 0.001$ to represent *stiff*, *semi-flexible* and *flexible* polymers respectively. Figure 3.11 gives the $\langle S^2 \rangle$ histograms at different temperatures. Figure 3.12 gives the $\langle D_{max} \rangle$ histograms.

The structures used for discussions henceforth are shown in figure 3.13 and illustrates the different forms attained by the polymer. Going from left to right, the compact circularly wound form is labeled as a *toroid* (A), the multiple folded elongated structure is a *bundle* (B), the *random coil* is (C), a single circularly wound form is termed a *ring* (D), and finally a single folded elongated structure is termed a *hairpin* (E). The corresponding colors are orange, red, yellow, dark blue, and light blue, respectively.

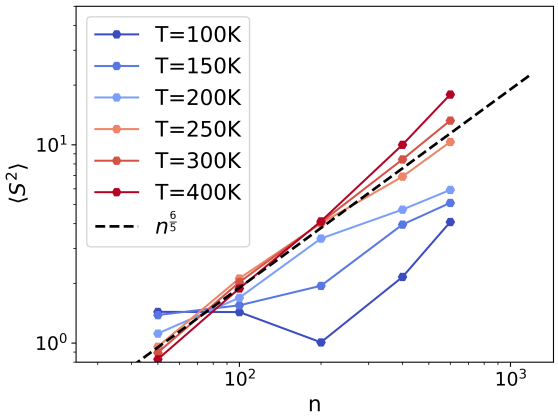

Figure 3.10: Log-log plot of $\langle S^2 \rangle$ against the number of monomers n at different temperatures. The dotted line represents the theoretical curve of 3.2.

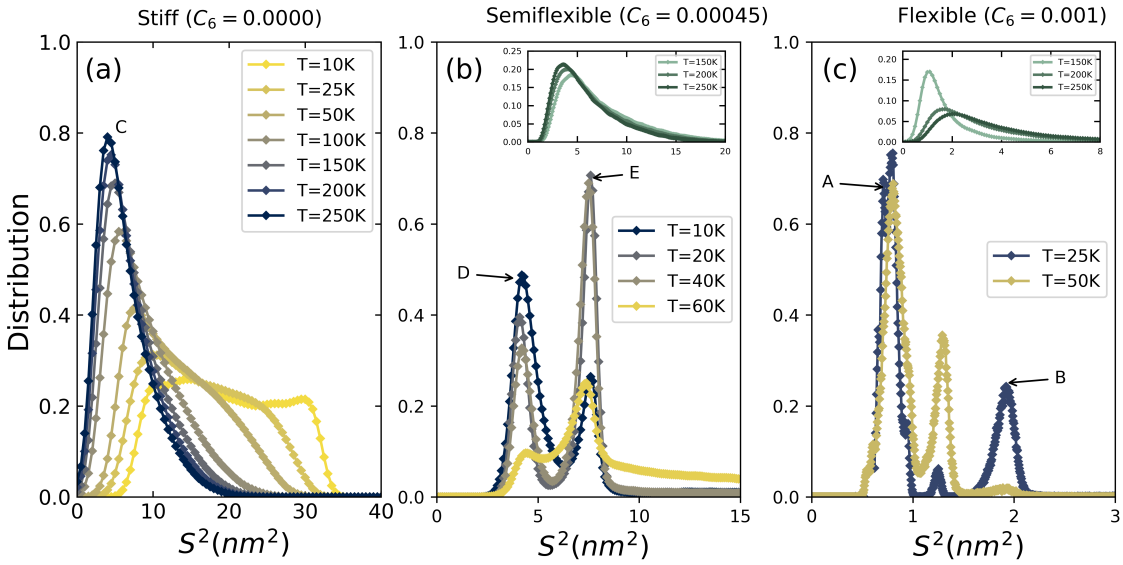

Figure 3.11: Distribution of $\langle S^2 \rangle$ for (a) stiff ($C_6 = 0.0$), (b) semiflexible ($C_6 = 0.00045$) and (c) flexible ($C_6 = 0.001$) polymers.

Looking at the distributions for the *stiff* polymer in figure 3.11 (a), we have a peak at 5nm^2 for $T = 250$K with a tail towards higher radii. This conformation relates to the random open coil in figure 3.13 that opens and closes briskly and hence is labeled as C. When T goes from 250 K to 100 K and further down to 75 K, we see a shift towards higher radii and a broadening of the distribution. At $T = 10$K, a clear second peak at about 28nm^2 appears which corresponds to a stiffened, elongated coil. This transition from rapidly opening and closing random coil to a more rigid coil gives rise to the an

exponential increase in the $\langle S^2 \rangle$ curve in figure 3.8 (a) and (b) for *stiff* polymers. D_{max} exhibits a very similar behavior as shown in figure 3.12 (a). *Semiflexible* polymers are more interesting because of their swelling-before-collapse transition. When going from higher to lower temperatures, *semiflexible* polymers at first exhibit an increase in $\langle S^2 \rangle$ due to a stiffening of the coil similar to the *stiff* polymers. However, at a certain temperature (50K $< T <$ 75K) a collapse to either *hairpins* or *rings* is observed.

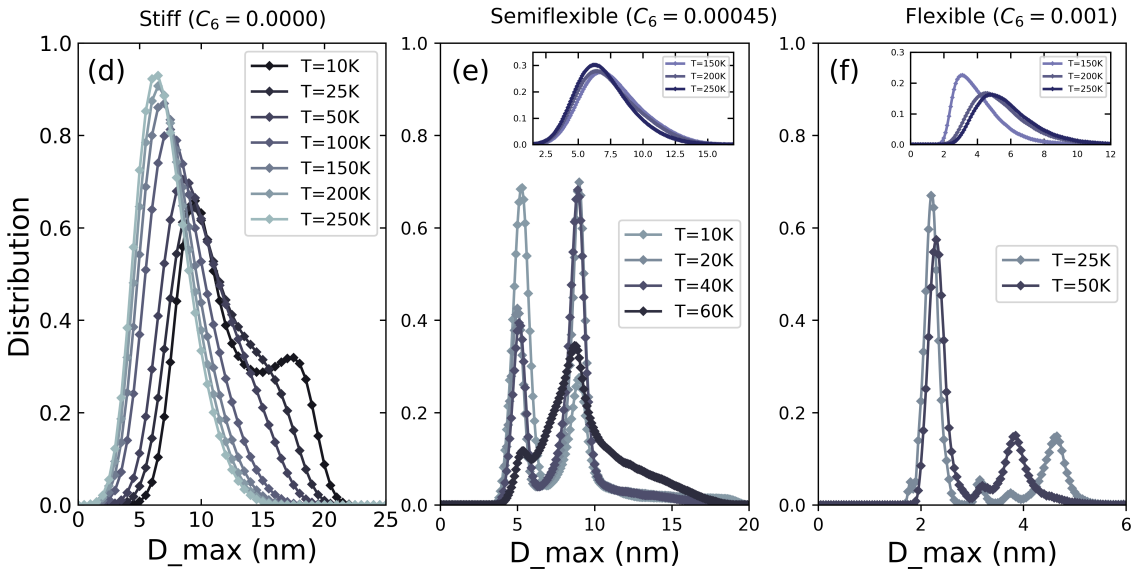

(a) (b) (c)

Figure 3.12: Distribution of D_{max} for (a) stiff ($C_6 = 0.0$), (b) semiflexible ($C_6 = 0.00045$) and (c) flexible ($C_6 = 0.001$) polymers.

Figure 3.11(b) shows the $\langle S^2 \rangle$ distribution first vs T below the collapse to detail the swelling-before-collapse phenomenon . At 10 K, we see two clear peaks at 4.1nm^2 and 7.8nm^2 marked with the labels D and E, respectively. These confirm that the probability of forming *rings* and *hairpins* exists at all temperatures. As we increase the T from 10K to 60K, the peak at 4.1nm^2 decreases and the one at 7.8nm^2 increases indicating a shift in probability of the polymer for forming rings at low temperature (10K) and hairpins at relatively higher temperatures (60K). Above 70 K, the polymer forms an open *random coil* with a wide $\langle S^2 \rangle$ distribution as shown in the inset of figure 3.11 (b). Again, the D_{max} distribution in figure 3.12 (b) exactly replicates this occurance.

Figure 3.11 (c) describes *flexible* polymers, which in principle, act similarly to semiflexible polymers, however, their interplay at lower temperatures is between a *toroid* and a *bundle* instead of a *ring* and a *hairpin*. Hence, the data for $\langle S^2 \rangle$ are smaller. For $T >$ 150K, we again observe a broad distribution that relates to the

random open coil conformation. At $T \leq 50$K the peaks appear at 0.8nm^2 (labeled as A for toroids), 1.2nm^2, and 2.0nm^2 (labeled as B for bundles) that shows the existence of both *toroids* and *bundles* as well as an unstable state between the two. In principle similar behavior is reproduced by the histograms of D_{max} in figure 3.12 (c). The random coil is a very unstable structure with Dmax ranging from 7.5 – 20nm.

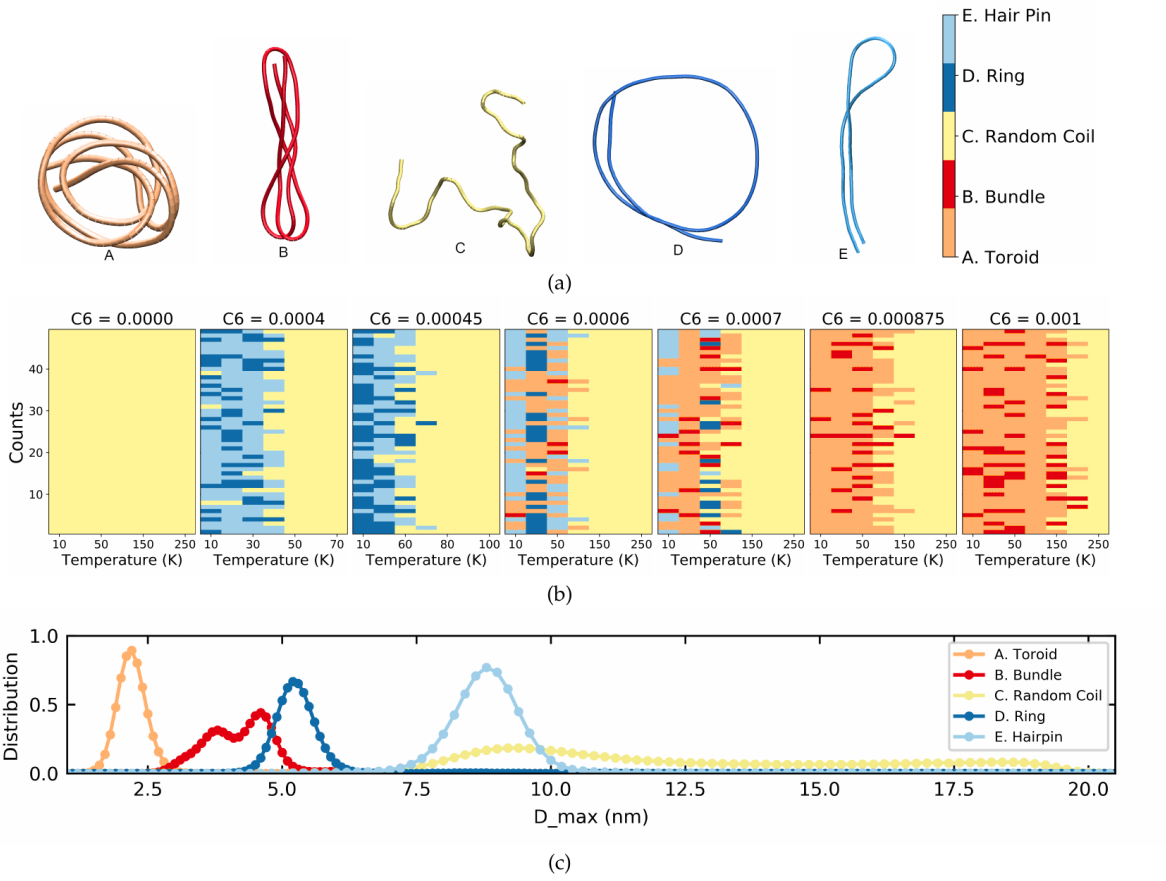

Figure 3.13: From left to right illustration of *toroid*, *bundle*, *random coil*, *ring* and *hairpin*. (b) Color coded final conformations at a range of temperature for 50 simulations at different C6 values. (c) D_{max} distribution of the above five mentioned structures.

As seen from the $\langle S^2 \rangle$ distributions, the final conformations of a polymer are sensitive to the initial conditions and are subject to change with change in initial conformation. Therefore to properly account for this behavior, 50 different simulations with different input structure files for the polymer's starting conformation were carried out for each set of parameters. By visual examination and comparison to the generic structures in figure 3.13(a), we then determined the type of conformation

for each simulation. Figure 3.13(b) shows color coded final conformations for 50 simulations at each C_6 value and T. This allows easy visualization of the transition from *flexible* to *semiflexible* to *stiff* polymers by the gradual change from orange/red to light/dark blue to yellow region, respectively. Moreover, we present the D_{max} distributions for each conformation for comparison of the sizes of these conformations. For this, we combine all conformations of a given type (A-E) independent of their C_6 and T, and plot the corresponding distributions in figure 3.13(c). It can be seen clearly that the *toroid* is the most compact form with a D_{max} peak at 2 nm, then the *bundle* at 3.75 nm, the *ring* at 5.3 nm and the *hairpin* at 8.8 nm.

Not only does the LJ model for flexible, semi-flexible and stiff reproduce the Kolinski's collapse transition and is able to form the conformations previously reported that of *toroids*, *bundles*, *rings* and *hairpins*, it also reproduces phase plots reported previously by people who worked on polymer stiffness using Lattice models, Brownian dynamics, Monte Carlo methods. We would discuss some of them in here.

Zierenberg et al [34] carried out thermodynamic behavioral studies on semi-flexible polymers that undergo temperature driven transitions. Similar to our case they considered isolated polymers that under collapse using "OFF-Lattice Polymer Models". Figure 3.14 represents the structural phase diagrams for polymers with varying bending potential k_θ as a function of temperature. Figure 3.14 (a) is the result directly adopted from the work of Zierenberg et al and figure 3.14 (b) is the phase plot derived from our LJ polymer using molecular dynamics.

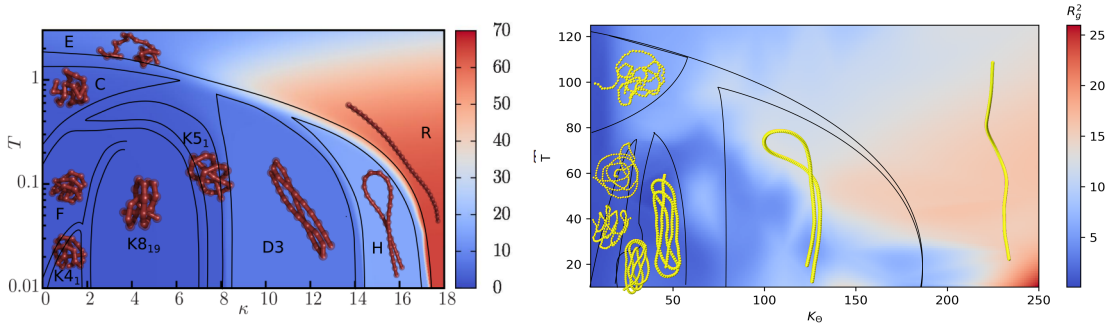

(a) (b)

Figure 3.14: Structural phase diagram for polymers with varying angle bending potential k_θ at different temperatures. (a) Figure taken from Zierenberg et al. [34] (copyright is open access) and (b) phase plot from our LJ simulations for comparison. The background encodes the mean squared radius of gyration $\langle S^2 \rangle$ and the labels represent the following: H: hairpin, D3: bundles, K&C: toroids, R: stiff random coil, E: flexible random coil

Going from left to right in 3.14(b) we see elongated rigid coil regime with highest $\langle S^2 \rangle$ at $k_\theta = 250 \frac{\text{kJ}}{\text{mol rad}^2}$ which also marks the red region. As we move left we have *hairpin* region, then *bundle* region and then *toroid* region at lowest k_θ. Similar behavior is

reported by Zierenberg et al in 3.14(a) . The k_θ and temperatures values cannot be expected to match exactly because the simulation models and parameters are different, however qualitative comparison can be made between two models for evaluating the characteristic trends.

Another study by Ivanov et al. [13] with Monte Carlo techniques was carried out using the bond fluctuation model for chain length of $N = 80$ where they presented a "State Diagram" (figure 3.15 (a)) where chain stiffness and inverse temperature are used as variables. Ivanov et al. [13] shows existence of "torus", "globule" and "coil" and show that there exists defined areas in the phase space of k_θ and $1/T$ where only one of the three structures exist. Going from one area in the phase space to the other leads to conformational transitions in the polymer.

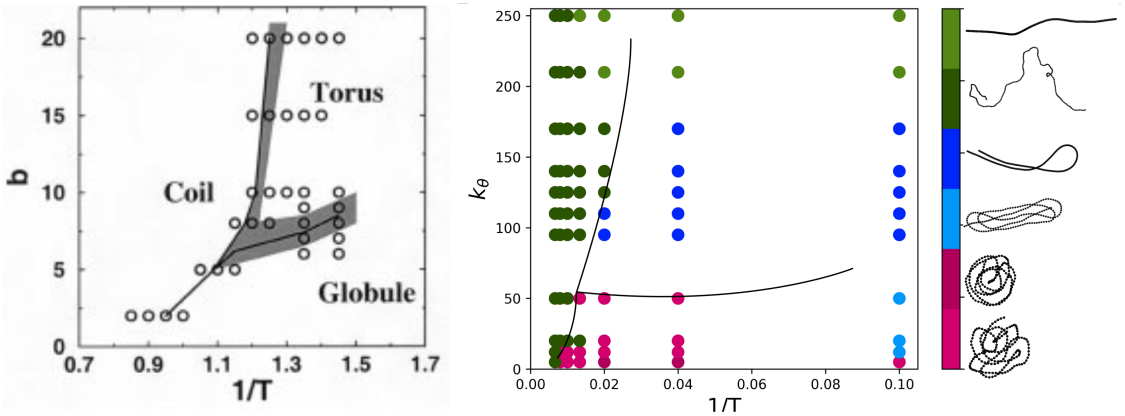

(a) (b)

Figure 3.15: "State diagram" of polymers with different bending constant k_θ as a function of inverse of temperature. (a) Results taken from Ivanov et al. [13] (copyright license is obtained) (b) Simulation results of our LJ polymer model using molecular dynamics. The circles are color coded for the conformations the polymer adopts and are illustrated in the color bar. Red corresponds to compact structures (*toroids*), blue corresponds to elongated structures (*hairpins* and *bundles*) and green corresponds to stiff and/or open *random coil*.

Ivanov et al. 3.15 (a) describes the phase diagram as being divided into three regions namely "coil", "globule" and "torus". Very similar state diagram is reproduced by the LJ polymer in figure 3.15 (b) where we have the red region, the blue region and the green region. We see phase transition when going from one region to the other similar to the description by Ivanov et al. By comparing 3.15 (a) and (b) we can see that the "globule" region described in (a) relate to the conformations in the red region in (b) for *toroids* that exist majorly at low k_θ, the "torus" region of (a) relates to the blue region

of (b) that stands for parallel folded conformations like *bundles* and *hairpins* and the "coil" region of (a) relates to the green region of (b) that represents open *random coils*.

Therefore, with the LJ model developed in this chapter for *stiff*, *flexible* and *semi-flexible* polymers not only reproduces the collapse transition observed by Kolinski et al. but also reproduces phase diagrams from the previous literature that worked with Lattice models and Monte Carlo methods.

This nature of the $\langle S^2 \rangle$ and D_{max} as well as the conformations related with the C_6/k_θ and temperature variance gives us a nice basis for distinguishing between *stiff*, *flexible* and *semi-flexible* polymers and and now be used from here onward to solve debates on the flexibility of polymers that are used different applications. In this chapter we would apply our knowledge from the results and discussion from this section to categorize the much debated question on the flexibility of P3HT and analyze if it undergoes conformational phase transition of any kind.

3.3.2 Atomistic P3HT

This section deals with atomistic model of P3HT with 200 monomers, where every atom is represented explicitly and provides most accurate description of the polymer. Here, all the simulations are in vacuum for preliminary formulation of results, as adding solvent leads to much higher the computation times. Figure 3.16 (a) shows the time averaged D_{max} at different temperatures T. We observe a sigmoidal increase of D_{max} with T which reminds of the flexible LJ polymers in figure 3.9. We note, however, that the polymer reaches the Flory's limit and shows the sigmoidal plateau at very high temperatures which are not usually accessible in experiments, as P3HT typically fully decomposes at $T \geq 850K$ [28].

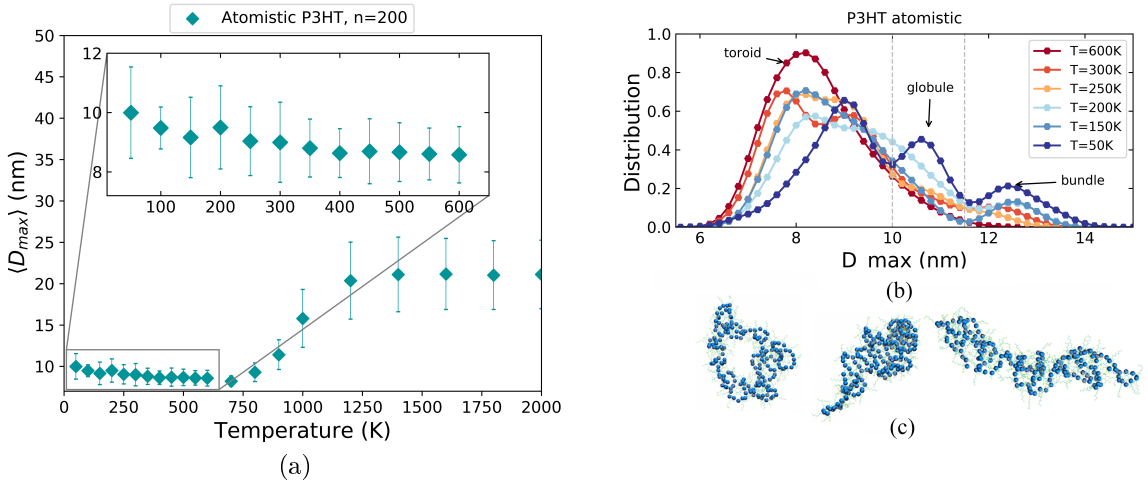

Figure 3.16: The maximum distance (D_{max}) between monomers for the atomistic P3HT model in vacuum at different temperatures (T in Kelvin). (a) The averaged D_{max} as a function of T shows a sigmoidal increase at very high and a slight increase towards low temperatures (inset). (b) The D_{max} distributions at different temperatures exhibit three clear peaks corresponding to *toroids*, *globules* and *bundles* (from left to right) which are illustrated in (c).

The experimental results are however shows for temperatures 160K $\leq T \leq$ 300K and hence we emphasize on the range $T \leq$ 600K by expanding the region in the inset. We see a slight but ordered swelling of the structure demonstrated by an increase in D_{max} towards lower temperatures. To understand this in further detail, we repeat the analysis procedure from the previous sub-section used for the LJ polymers and show in figure 3.9 (b) the D_{max} distributions for 50K $\leq T \leq$ 600K where we observe three distinct

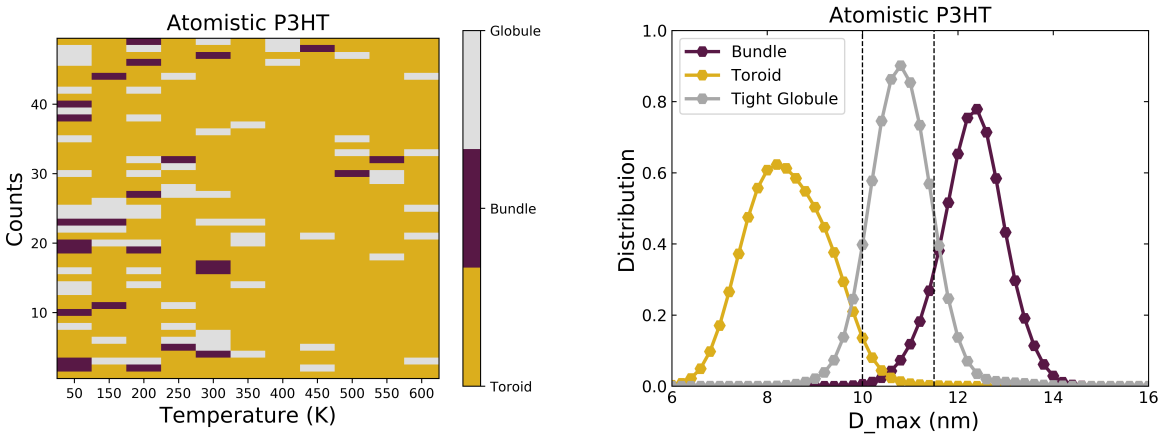

(a) (b)

Figure 3.17: (a) Color coded final conformations at a range of temperature for 50 simulations for atomistic P3HT in vacuum. (b) D_{max} distributions used for *toroid*, *globules* and *bundles*.

peaks. Having a look at the simulation movies we observe that the left peak at 8 nm is resulting from *toroid* structures and the right peak at about 12.5 nm from *bundles*. The *toroid* and *bundle* structures are illustrated in figure 3.16 (c). Unlike the LJ model polymer of figure 3.12(b), P3HT shows a noteworthy middle peak at $D_{max} \approx 11$nm . This peak corresponds to a tight globular structure whose illustration is provided in 3.16 (c). An additional extensive set of conformations for *toroids*, *bundles* and *tight globules* from the atomistic simulations is provided in figure 3.18. Similar as for the LJ polymers, for better statistics, we carried out a set of 50 simulations with different starting conditions for each T. Conditioning D_{max} from the final simulation frame as per the dashed lines in figure 3.16 (b) lets us characterize the resulting structures into *toroid*, *globule* and *bundle*. The result is shown in figure 3.17(a). *Toroids* are marked by yellow and belong to 0nm $< D_{max} <$ 10.0nm, *globules* are marked by gray and have 10.0nm $< D_{max} <$ 11.5nm while *bundles* have $D_{max} >$ 11.5nm and are marked by dark red. As the T goes from 600K to 50K, the *bundles* are seen more frequently. For $T \leq$ 300K, both *bundles* and *toroids* coexist along with *tight globule*. Eventually, selecting all the simulations in the *toroid*, *tight globule* and *bundle* regions individually we present D_{max} distribution figure 3.17(b) which accentuates how each conformation is directly correlating to a distinct peak of D_{max} .

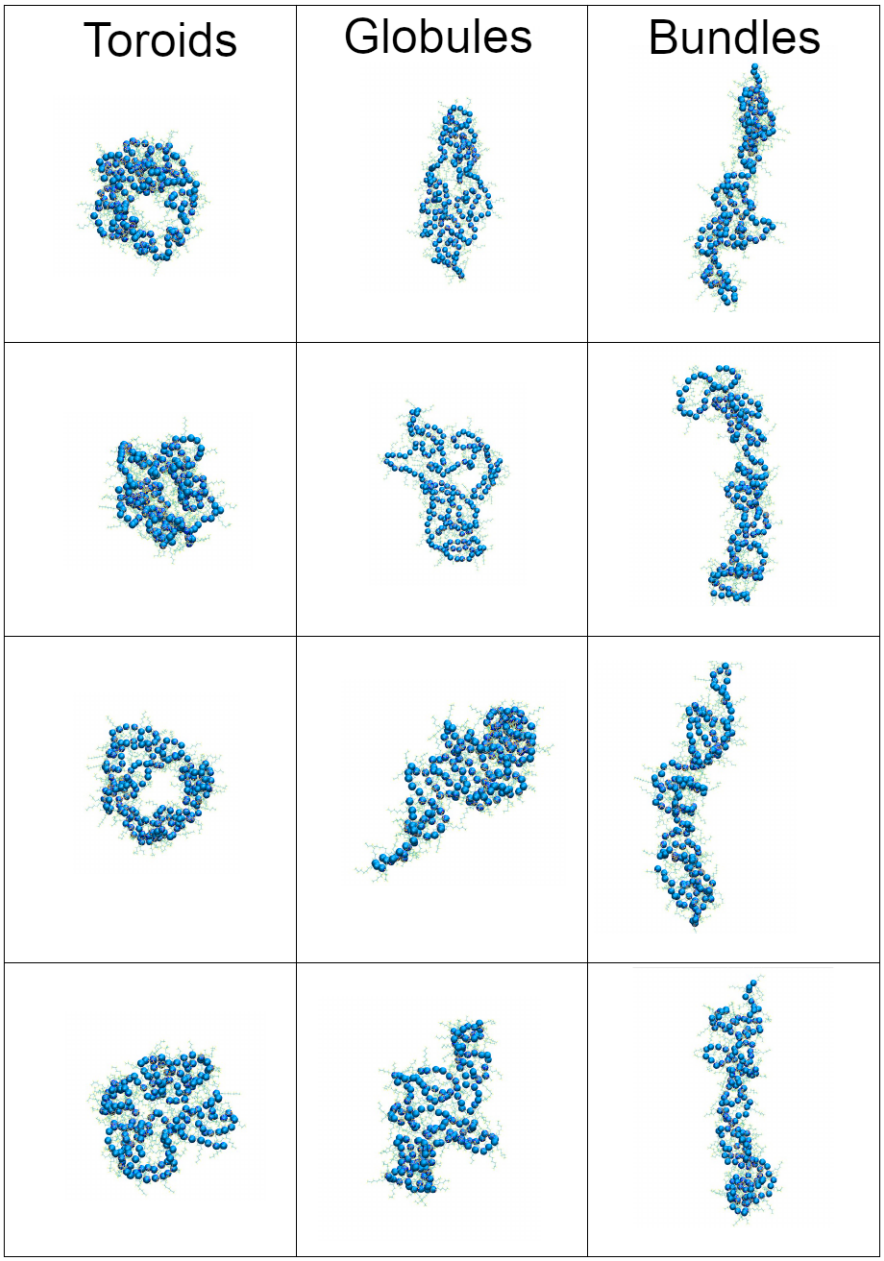

Figure 3.18: Typical toroids, globules and bundles found in the atomistic P3HT simulations at 300K

3.3.3 Martini P3HT in vacuum

In this section we repeat the procedure from the above section for coarse-grained Martini model of P3HT with 200 monomers, again starting in vacuum. As detailed in subsection 2.9, each P3HT monomer is described by six beads. Figure 3.19 (a) presents time averaged D_{max} as a fundtion of T. Here, we again see a simple sigmoidal increase in D_{max} for very high T and a less pronounced, but still ordered swelling for decreasing temperatures in the range of 600K $\leq T \leq$ 100K. Figure 3.19 (b) shows the D_{max} distributions at the different T similar to figure 3.16 in the above sub-section and the distributions are in good agreement with the atomistic model shown in figure 3.16 above. We observe three main peaks at low and a single strong peak at high T. The transition between these peaks when changing the temperature follows similar trend as in the case of atomistic with the only difference being that the Martini model overall exhibits slightly more compact structures than the atomistic model. Having a look at the simulation movie allows to identify again the sequence of *toroids*, tight *globules* and *bundles* as shown in figure 3.19 (c). The borders between these phase as marked by the gray lines in figure 3.19 (b) are 0nm $< D_{max} <$ 8.5nm for *toroids*, 8.5nm $< D_{max} <$ 10.3nm for tight *globules* and finally $D_{max} >$ 10.3nm for *bundles*. In fact, the geometric characteristics are even more pronounced than in the atomistic model. An additional extensive set of conformations for *toroids*, *bundles* and *tight globules* from the atomistic simulations is provided in figure 3.21. Figure 3.20(a) shows the color coded outcome of the last frame of the 50 simulations run for all the T with different initial conditions. Figure 3.20(b) shows the individual distribution of D_{max} for *toroids*, *globules* and *bundles*. Both figure 3.19 and 3.20 are in very good agreement with the atomistic model results in figure 3.16 and 3.20 thereby inferring that the Martini CG model well describes the P3HT's conformational characteristics even without the information on the partial charges and reduced resolution on the atoms.

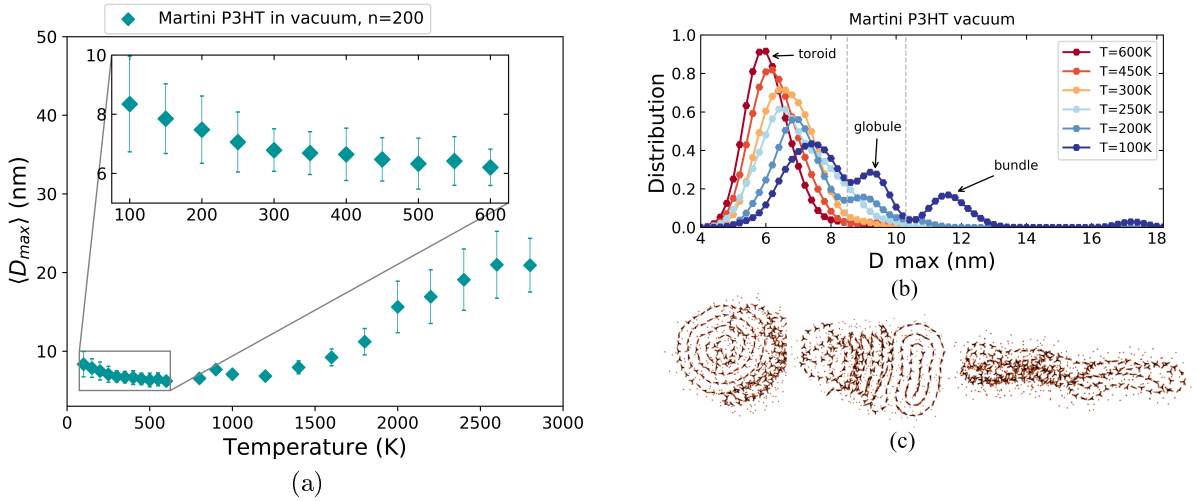

Figure 3.19: The maximum distance (D_{max}) between monomers for the Martini model of P3HT in vacuum at different temperatures (T in Kelvin). (a) The averaged D_{max} as a function of T shows a sigmoidal increase at very high and a slight increase towards low temperatures (inset). (b) The D_{max} distributions at different temperatures exhibit three clear peaks corresponding to *toroids*, *globules* and *bundles* (from left to right) which are illustrated in (c).

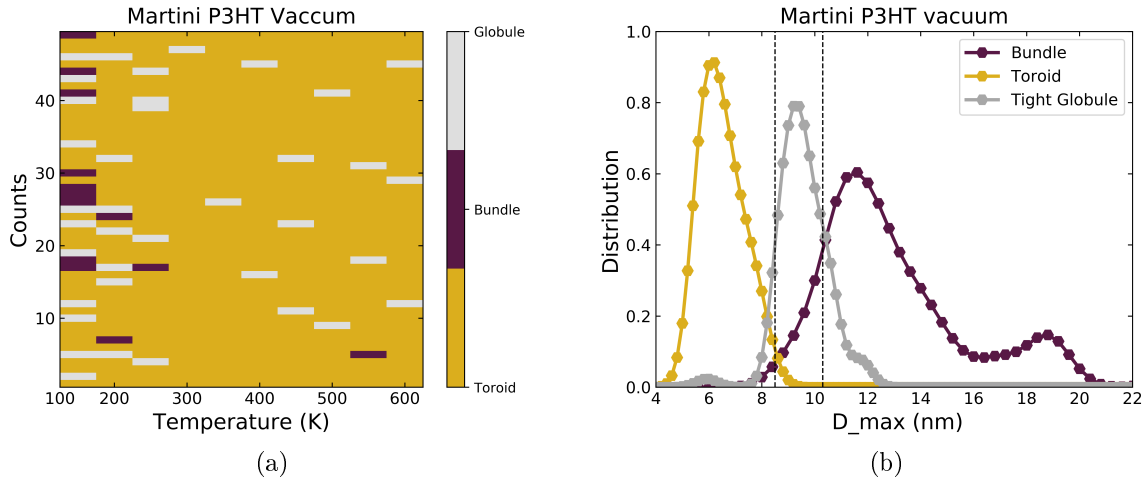

Figure 3.20: (a) Color coded final conformations at a range of temperature for 50 simulations for Martini CG P3HT in vacuum. (b) D_{max} distributions used for *toroid*, *globules* and *bundles*.

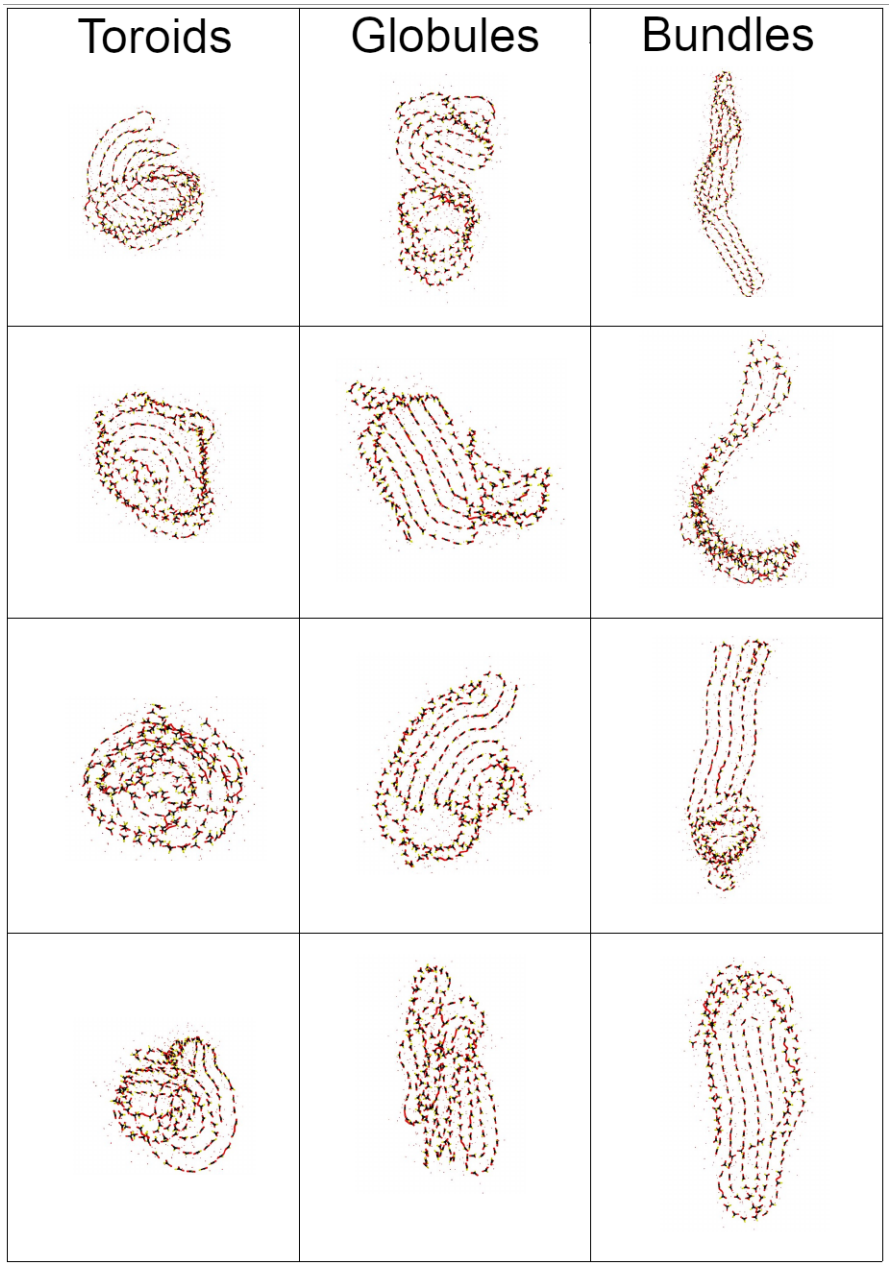

Figure 3.21: Typical *toroids*, *globules* and *bundles* found in Martini CG P3HT vacuum simulations at 300K.

3.3.4 Martini P3HT in THF solvent

This whole chapter was motivated by the experimental studies carried out by Panzer et al. in [22, 20] on P3HT and its suspicious phase transitions with changing temperature. In order to relate to the experimental findings of Panzer et al., we needed to include the solvent they used for suspending P3HT, in our system, namely tetrahydrofuran (THF). For simulating THF we used the Martini as described in section 2.9 above. D_{max} vs T obtained from simulations of the martini CG P3HT solvated in THF is shown in figure 3.22(a). It is similar to the previous cases in vacuum except for one notable exception: at about $T = 220$K we observe an immediate increase in D_{max} when going from right to left. Unlike in the vacuum simulations (figure 3.19 (b)) the middle peak in figure 3.22(b) is no longer present. The two prominent peaks at around 6nm and 10nm corresponding to *toroids* and *bundles*, respectively, are nonetheless still clearly distinct. The conformational illustrations of *toroids* and *globules* and bundles obtained from the CG solvent simulations are shown in figure 3.22(c) and they look very similar to the ones from the previous section. The *bundles*, are the conformations where the chains folds back onto itself multiple times to form $\pi - \pi$ stacked layers is clearly seen in figure 3.22(c). This point, where the *bundles* are proved as the P3HT planarized ordered aggregates was also reported previously by Schwarz et al. [29]. The *bundles* are responsible for the electronic mobility in organic transistors as a virtue of their $\pi - \pi$ stacks. Following the analysis methods of [29], we found that the distance between the $\pi - \pi$ stacked layers in our *bundle* aggregates is at 4.73 ± 0.23nm. This is mostly due to the approximation of the thiophene ring as a spherical site in the CG model, which overestimates the steric bulk of the ring in the $\pi - \pi$ direction. The planarity of the *toroids* and *bundles* are also explained in terms of conjugation length (in connection with dihedral angles) in figure 3.25. In figure 3.23 (a) we show the occurrence probabilities of *toroid*, *bundles* and *globules* for the 50 different initial conditions. Similar to the above two cases, the criteria for D_{max} that was used for the distinguishing these classes is shown by dashed gray lines in figure 3.23(b). *Toroids* are in the range of $0 < Dmax \leq 7.2$nm, *globules* in $7.2 < D_{max} \leq 9$nm and *bundles* in $D_{max} > 9$nm. Addition of the solvent increased the frequency of the *bundle* as compared to the vacuum case. As confirmed by the larger size of the bundle structure (see figure 3.22(b)), this explains the sudden rise in D_{max} at $T = 220$K.

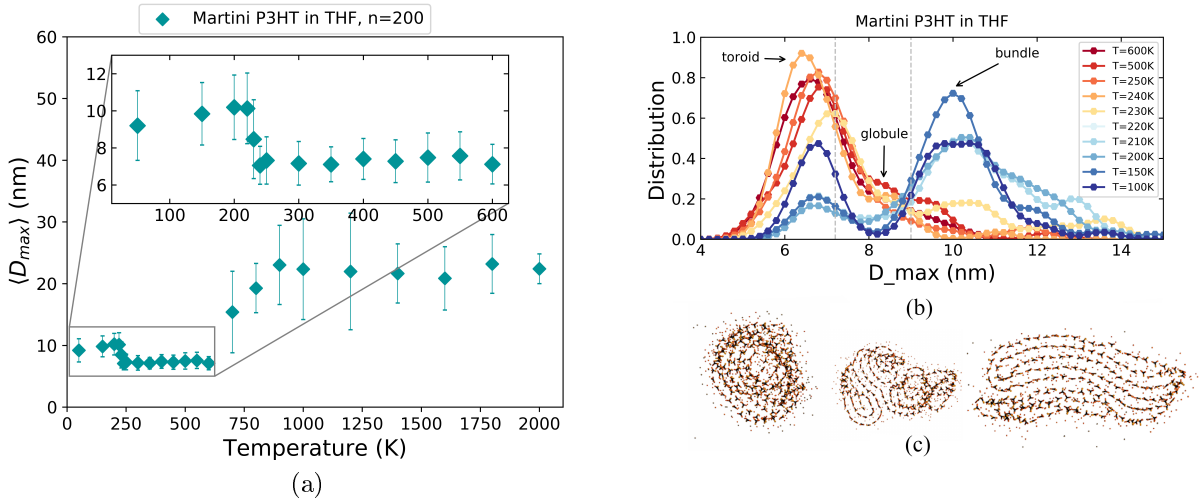

Figure 3.22: The maximum distance (D_{max}) between monomers for the Martini model of P3HT in THF solvent at different temperatures (T in Kelvin). (a) The averaged D_{max} as a function of T shows a sigmoidal increase at very high and a slight increase towards low temperatures (inset). (b) The D_{max} distributions at different temperatures exhibit three clear peaks corresponding to *toroids*, *globules* and *bundles* (from left to right) which are illustrated in (c). Comparison between (b) and figure 1.2 shows that the transition captured in these simulations qualitatively explains the shift in the absorption spectra reported experimentally.

To check the robustness of the observed conformational transitions of P3HT, we conducted simulations with chain lengths of $n = 112$ and $n = 68$. D_{max} as a function of T for these chains is shown in figure 3.24. The transition temperature at which the swelling takes place is clearly visible around $T = 185$K for $n = 112$ while it is not so clearly distinguishable for the very short $n = 68$ chain. This is in agreement with reports from the experiments of [20] that the critical temperature of P3HT chains in THF solvent decreases with decreasing chain length.

Conjugation length (LC) is an intrinsic electronic property, however, its estimates can be derived from the dihedral angle and the distance between the monomers. We calculate the dihedral angle between all the consecutive monomers, and plot the probability number of monomers that lie within a segment that bends more than 400 . Almost twice as high conjugation lengths in bundles ($\approx 4 - 5nm$) (thereby inferring twice as low dihedral angles) compared to toroids($\approx 9 - 10nm$), shows increased planarisation of the polymer chains below 220K. An easy estimate of the conjugation

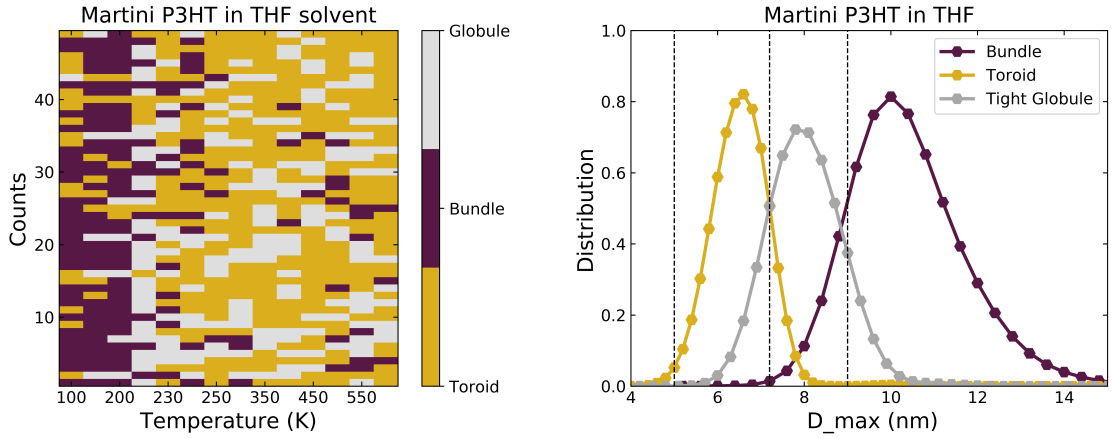

Figure 3.23: (a) Color coded final conformations at a range of temperature for 50 simulations for Martini CG P3HT in THF solvent. (b) D_{max} distributions used for *toroid*, *globules* and *bundles*.

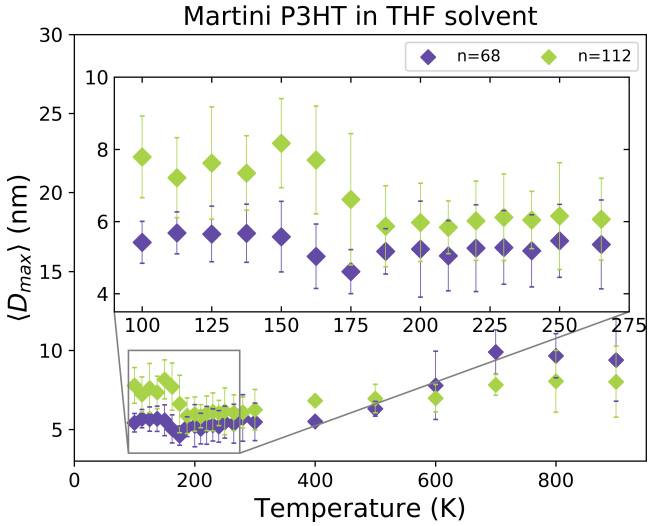

Figure 3.24: D_{max} vs T between monomers for the Martini model of P3HT with $n = 68$ and $n = 112$ in THF solvent.

length of P3HT can be acquired by assuming that P3HT is broken into electronically isolated units (chromophores) when the inter-monomer dihedral angle is above a particular threshold value. Following previous estimates of conjugation lengths in simulations of P3HT [5, 32] a threshold value of 400 was chosen, above which quantum calculations have shown that electronic properties become significantly different from the coplanar monomer case [7]. It has been estimated that this

consequences of this increased planarisation of P3HT is with aggregation on the UV-vis absorption spectrum by assuming that absorption by the chromophores in P3HT follows similar behaviour as that measured experimentally for thiophene oligomers as a function of length [29]. Fully quantitative agreement with experimental results would require a more rigorous treatment of the electronic structure of P3HT, however, this simple analysis demonstrates that the increased planarization of P3HT chains upon aggregation makes a substantial contribution to changes in the absorption spectrum of P3HT. Interestingly, our simulations predict that this swelling is closely connected to the presence of the solvent THF which might make it a worthwhile effort to study the same transition in different in the future.

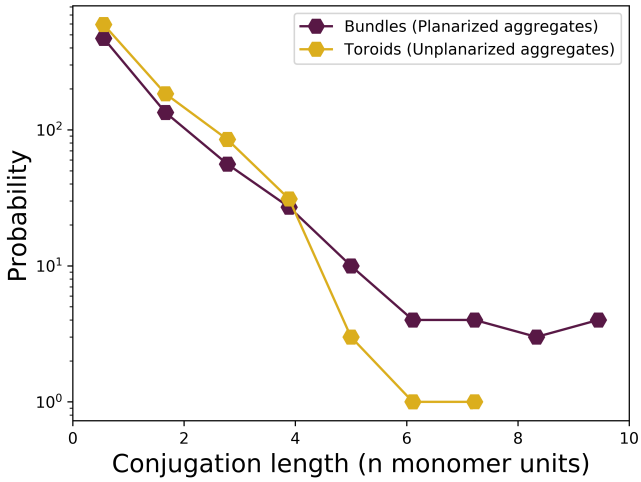

Figure 3.25: Probability of conjugation lengths in unaggregated and aggregated Martini P3HT in THF solvent.

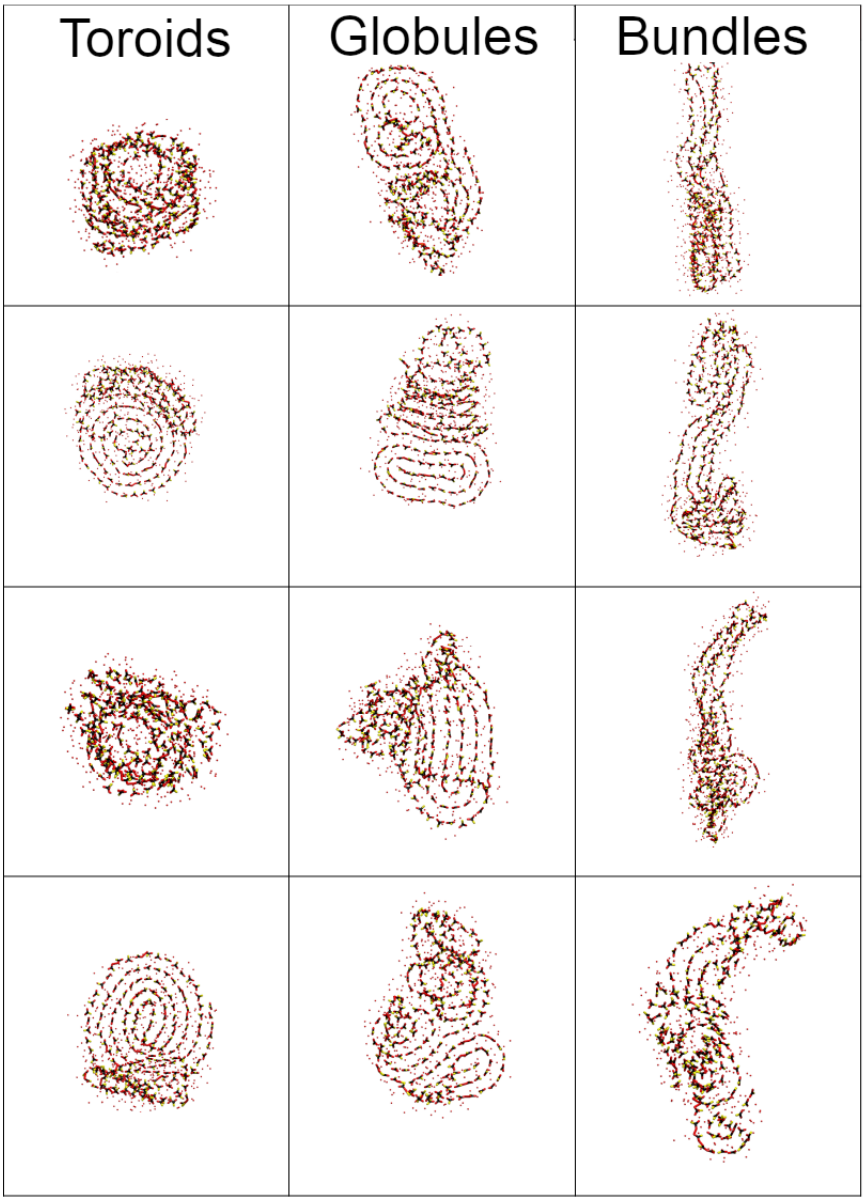

Figure 3.26: Typical *toroids*, *globules* and *bundles* found in Martini CG P3HT solvent simulations at 300K.

3.4 Conclusion

P3HT in vacuum forms bundle and toroids at low temperatures, and its $\langle S^2 \rangle$ and D_{max} behavior as a function of temperature is sigmoidal in nature, therefore it matches to the typical characteristics of flexible polymers. The Martini CG simulations of P3HT in THF solvent, unlike the vacuum simulations, show a sharp transition at around 220K. We observe a swelling close to that of the recent spectroscopic experiments by Panzer et al. [14,15,41]. Panzer et al. considered P3HT polymers with weights 5kDa to 34kDa that correspond to 30 to 200 repeats per polymer. In their experiments they found a shift from red to blue in the absorption spectra and emission spectra when they decreased the temperature from 300K to 170K. Therefore they proposed that the polymer is undergoing a conformational phase transition from random coil at high temperatures to planarized chains at low temperature (figure 1.2). They predicted that the chains must be forming ordered planarized chains, because the change in the absorption spectra was a result of bathochromic shift indicating an increase in the conjugation length. They connected this thought process to the swelling of the polymer before the collapse when reducing the temperature. With our work in this chapter we show that P3HT attains three different aggregated forms: bundles, toroids and random coils. The probability transition of P3HT morphing into one of these conformations, in the presence of solvent, changes at temperature around 220K and we report a clear swelling of D_{max} at that temperature. Our simulations help answer the hypothesis of the experiment work of Panzer et al. and reports that the swelling mentioned by Panzer et al. is a result of increasing frequency of elongated bundle structures than the comparatively smaller globule and toroid structures observed at higher temperatures.

References

[1] Takuji Adachi, Johanna Brazard, Robert J Ono, Benjamin Hanson, Matthew C Traub, Zong-Quan Wu, Zicheng Li, Joshua C Bolinger, Venkat Ganesan, Christopher W Bielawski, David A Vanden Bout, and Paul F Barbara. Regioregularity and Single Polythiophene Chain Conformation. *The Journal of Physical Chemistry Letters*, 2(12):1400 – 1404, 06 2011.

[2] Riccardo Alessandri, Jaakko J Uusitalo, Alex H De Vries, Remco WA Havenith, and Siewert J Marrink. Bulk heterojunction morphologies with atomistic resolution from coarse-grain solvent evaporation simulations. *Journal of the American Chemical Society*, 139(10):3697–3705, 2017.

[3] Riccardo Alessandri, Jaakko J. Uusitalo, Alex H. de Vries, Remco W. A. Havenith, and Siewert J. Marrink. Bulk Heterojunction Morphologies with Atomistic Resolution from Coarse-Grain Solvent Evaporation Simulations. 2017.

[4] Zhenan Bao, Ananth Dodabalapur, and Andrew J Lovinger. Soluble and processable regioregular poly(3-hexylthiophene) for thin film field-effect transistor applications with high mobility. *Applied Physics Letters*, 69(26):4108–4110, 1996.

[5] Marco Bernardi, Michele Giulianini, and Jeffrey C Grossman. Self-assembly and its impact on interfacial charge transfer in carbon nanotube/p3ht solar cells. *ACS nano*, 4(11):6599–6606, 2010.

[6] Ram S Bhatta, Yeneneh Y Yimer, David S Perry, and Mesfin Tsige. Improved force field for molecular modeling of poly (3-hexylthiophene). *The Journal of Physical Chemistry B*, 117(34):10035–10045, 2013.

[7] JL Brédas, GB Street, B Themans, and JM André. Organic polymers based on aromatic rings (polyparaphenylene, polypyrrole, polythiophene): Evolution of the electronic properties as a function of the torsion angle between adjacent rings. *The Journal of chemical physics*, 83(3):1323–1329, 1985.

[8] Gerardo Campos-Villalobos, Flor R Siperstein, and Alessandro Patti. Transferable coarse-grained martini model for methacrylate-based copolymers. *Molecular Systems Design & Engineering*, 4(1):186–198, 2019.

[9] P Y Chen, A Rassamesard, H L Chen, SA Chen Macromolecules, and 2013. Conformation and fluorescence property of poly (3-hexylthiophene) isolated chains studied by single molecule spectroscopy: Effects of solvent quality . *ACS Publications*, 46(14):5657 – 5663, 2013.

[10] Paul J Flory. The configuration of real polymer chains. *The Journal of Chemical Physics*, 17(3):303–310, 1949.

[11] Chiatzun Goh, R. Joseph Kline, Michael D. McGehee, Ekaterina N. Kadnikova, and Jean M. J. FrÃ©chet. Molecular-weight-dependent mobilities in regioregular poly(3-hexyl-thiophene) diodes. *Applied Physics Letters*, 86(12):122110, 2005.

[12] Glenn W Heffner and Dale S Pearson. Molecular characterization of poly(3-hexylthiophene). *Macromolecules*, 24(23):6295–6299, 1991.

[13] VA Ivanov, MR Stukan, VV Vasilevskaya, W Paul, and K Binder. Structures of stiff macromolecules of finite chain length near the coil-globule transition: A monte carlo simulation. *Macromolecular theory and simulations*, 9(8):488–499, 2000.

[14] M Jeffries-El and RD McCullough. Regioregular polythiophenes, vol. 1, 2007.

[15] Andrzej Kolinski, Jeffrey Skolnick, and Robert Yaris. The collapse transition of semiflexible polymers. a monte carlo simulation of a model system. *The Journal of chemical physics*, 85(6):3585–3597, 1986.

[16] Biplab K Kuila and Arun K Nandi. Structural Hierarchy in Melt-Processed Poly(3-hexyl thiophene)-Montmorillonite Clay Nanocomposites:Â Novel Physical, Mechanical, Optical, and Conductivity Properties. *The Journal of Physical Chemistry B*, 110(4):1621–1631, 2006.

[17] Bryan McCulloch, Victor Ho, Megan Hoarfrost, Chris Stanley, Changwoo Do, William T Heller, and Rachel A Segalman. Polymer Chain Shape of Poly(3-alkylthiophenes) in Solution Using Small-Angle Neutron Scattering. *Macromolecules*, 46(5):1899 – 1907, 02 2013.

[18] Richard D McCullough. The chemistry of conducting polythiophenes. *Advanced materials*, 10(2):93–116, 1998.

[19] Masaru Nagai, Jun Huang, Tiandong Zhou, and Wei Huang. Effect of molecular weight on conformational characteristics of poly(3-hexyl thiophene). *Journal of Polymer Science Part B: Polymer Physics*, 55(17):1273 – 1277, 06 2017.

[20] Fabian Panzer, Heinz Baessler, and Anna Koehler. Temperature induced order–disorder transition in solutions of conjugated polymers probed by optical spectroscopy. *The journal of physical chemistry letters*, 8(1):114–125, 2017.

[21] Fabian Panzer, Heinz Baessler, and Anna Koehler. Temperature induced order–disorder transition in solutions of conjugated polymers probed by optical spectroscopy. *The journal of physical chemistry letters*, 8(1):114–125, 2017.

[22] Fabian Panzer, Heinz Baessler, Ruth Lohwasser, Mukundan Thelakkat, and Anna Koehler. The impact of polydispersity and molecular weight on the order–disorder transition in poly (3-hexylthiophene). *The journal of physical chemistry letters*, 5(15):2742–2747, 2014.

[23] Fabian Panzer, Heinz Baessler, Ruth Lohwasser, Mukundan Thelakkat, and Anna Koehler. The impact of polydispersity and molecular weight on the order disorder transition in poly (3-hexylthiophene). *The journal of physical chemistry letters*, 5(15):2742–2747, 2014.

[24] Igor F Perepichka and Dmitrii F Perepichka. *Handbook of Thiophene-Based Materials: Applications in Organic Electronics and Photonics, 2 Volume Set*. John Wiley & Sons, 2009.

[25] Igor F Perepichka, Dmitrii F Perepichka, Hong Meng, and Fred Wudl. Light-emitting polythiophenes. *Advanced Materials*, 17(19):2281–2305, 2005.

[26] Carl Poelking and Denis Andrienko. Effect of Polymorphism, Regioregularity and Paracrystallinity on Charge Transport in Poly(3-hexylthiophene) [P3HT] Nanofibers. *Macromolecules*, 46(22):8941 – 8956, 11 2013.

[27] Dominic Raithel, Sebastian Baderschneider, Thiago B de Queiroz, Ruth Lohwasser, Juergen Koehler, Mukundan Thelakkat, Stephan Kuemmel, and Richard Hildner. Emitting Species of Poly(3-hexylthiophene): From Single, Isolated Chains to Bulk. *Macromolecules*, 49(24):9553 – 9560, 12 2016.

[28] Alexandre Rodrigues, M Cidália R Castro, Andreia SF Farinha, Manuel Oliveira, João PC Tomé, Ana V Machado, M Manuela M Raposo, Loic Hilliou, and Gabriel Bernardo. Thermal stability of p3ht and p3ht: Pcbm blends in the molten state. *Polymer testing*, 32(7):1192–1201, 2013.

[29] Kyra N Schwarz, Tak W Kee, and David M Huang. Coarse-grained simulations of the solution-phase self-assembly of poly (3-hexylthiophene) nanostructures. *Nanoscale*, 5(5):2017–2027, 2013.

[30] Kyra N Schwarz, Tak W Kee, and David M Huang. Coarse-grained simulations of the solution-phase self-assembly of poly(3-hexylthiophene) nanostructures. *Nanoscale*, 5(5):2017 – 11, 2013.

[31] G Tourillon and F Garnier. Stability of conducting polythiophene and derivatives. *Electrochemical Society, Journal*, 130:2042–2044, 1983.

[32] Nenad Vukmirovic and Lin-Wang Wang. Electronic structure of disordered conjugated polymers: Polythiophenes. *The Journal of Physical Chemistry B*, 113(2):409–415, 2009.

[33] Hoichang Yang, Scott W LeFevre, Chang Y Ryu, and Zhenan Bao. Solubility-driven thin film structures of regioregular poly(3-hexyl thiophene) using volatile solvents. *Applied Physics Letters*, 90(17):172116, 2007.

[34] Johannes Zierenberg, Martin Marenz, and Wolfhard Janke. Dilute semiflexible polymers with attraction: Collapse, folding and aggregation. *Polymers*, 8(9):333, 2016.

Chapter 4

Microplastics: Monomer effects of biodegradable polymers on building blocks of DNA

Aliphatic polyesters such as polylactic acid (PLA), polyglycolic acid (PGA) and polyhydroxyalkanoate (PHA) are commonly used in biodegradable products. These polymers when broken down into their smallest component can penetrate into our bodies and interact with our vital building blocks. Their impact and level of hazard from the interaction with our most vital entity, namely the DNA, is still unknown and with the increasing accumulation of these products it has become an important area in the field of science to study these interactions in depth. We perform free energy molecular dynamics (MD) simulations based on atomistic force-fields between monomers of the polymers mentioned above and individual nucleobases of DNA (i.e. adenine (A), guanine (G), cytosine (C) and thymine (T)). Our simulations reveal that all the polymers have shown an affinity towards the nucleobases, adenine and guanine interact a bit strongly than cytosine and thymine. This is due the additional 5-sided ring in structure of adenine and guanine which is absent in the remaining two. We also perform simulations of short length DNA helices with oligomers of 5 repeating units and present their free energy results.

4.1 Introduction

Interests about the interactions between microplastics and its effect on the living organisms is on the rise. The profound intertwining of plastic products in our everyday life has lead to their production up to about 350-400 million tons in a year [6]. Concern about micro plastics became more and more important since plastic microbeads from personal care products were first reported in the freshwater Laurentian Great Lakes [30]. Subsequently many studies were carried out on the formation of microplastics under the effects of physical wear, chemical, thermal erosion and biodegradation [28, 24]. Evaluating the organism's responses on these microplastics has become a need of the decade in order to determine their potential hazard.

Polylactic acid (PLA) is well-known as a sustainable bioplastic material and much research is currently focused on the modifications of polylactide acid to make it more suitable for a wider range of applications [25]. When studying the degradation of PLA, it was found that up to 95% of PLA can be hydrolyzed to water-soluble lactic acid (LA) within 120 minutes in the temperature range of $160 - 180^0C$ [19]. Similar data can be found on the degradation of the polymers polyglycolic acid (PGA) and polyhydroxyalkanoate (PHA) where the polymer breaks down to its individual monomers when undergoing hydrolytic degradation [4, 23]. Most of the biodegradable polymers disintegrate back to its constituting monomers get directly discarded into the enviornment and into the bodies of the living organisms. A number of reviews addressing different aspects of protein–polymer interaction have been published previously [5, 21, 21]. Deka et al. [7] reported exergonic interactions between PLA, PGA and PHA polymers with amino acids in different solvents using density funcitonal theory. Free energy studies using novel molecular dynamics techniques, O'Brien et al [17] showed strong adsorption free energy for PLA-peptide interaction as a result of hydrophobic interaction between non-polar groups of the peptide and the PLA surface.

Through the profound efficiency of nucleobases to vary its sequence, DNA not only governs most of the cell proteins that make life possible but also provides an ideal platform for diverse molecular engineering. [31] [8] [20] through their own self assembly.

By definition, biomaterials interface with our biological environment, and hence studying their properties and behavior corresponds to creating a bridge between materials science and life science at the molecular level. An in-depth understanding of the strength and nature of interaction between aforementioned biodegradable polymers and DNA is essential for evaluating its efficacy towards the polymers. However, despite having quite some literature on the interaction between protein and peptide assemblies with synthetic biodegradables polymers [12, 15, 22, 34, 14], much remains unknown about its effect on our genetic material. Keeping this in mind, we propose an important question in this paper: What is the level of interaction between the monomers of the biodegradable polymers PLA, PGA and PHA on DNA nucleobases?

We carry out molecular dynamics (MD) simulations to determine how individual monomer interacts with each of the nucleobases by determining and comparing the potential mean force (PMF) between the two. Furthermore, we also calculate the interaction of the nucleobases and oligomers of PLA, PGA and PHA with 5 repeating units.

4.2 System setup

Molecular dynamics (MD) simulations were performed using GROMACS software [1] with the GROMOS54a7 all-atom force field [26]. The structure and topology files of all the molecules used in this work were generated using the *Automated Force Field Topology Builder and Repository* (ATB) [16]. The bonded and non-bonded parameters can be accessed using the *molid* values provided in the section 4.5. For visualization of the molecular structures and trajectories, we used VMD [11]. For the free energy calculations we used umbrella sampling. The system contained two solute molecules, one monomer and one nucleobase solvated in a box full of simple point charge (SPC) water [2] to which a physiological salt concentration of 100 mM NaCl was added including neutralizing counterions (since DNA transfer efficiency happens between normal saline (150mM) and half saline (70mM) [13]). The salt ions were introduced by replacing the required amount of water molecules using the GROMACS *solvate* command. Between 10,000 to 60,000 solvent molecules were used. The distance between the center of mass of the solute molecules was used as the reaction coordinate for the umbrella sampling. The umbrella windows were first equilibrated for 100ps in NPT ensemble and then were run for 10ns with 0.002ps time step at 300K. The spacing between two umbrella windows was set at 0.2nm with 25 simulations which resulted in free energy that represented the whole space. The free energy was calculated using the Weighted Histrogram Analysis Methods, using the Gromacs command gmx wham [10]. For better comparison and in order to have a constant reference point at infinity, in all free energy data the ideal contribution -2kT ln(r), which is simply due to an increase in available volume [27, 33] and is identical for all molecules, has been subtracted.

Verlet neighbor search [29] was used to update the neighbor list while short-range electrostatic and van der Waals cutoff were set to 1.0 nm. The Parrinello-Rahman barostat [18] and velocity rescaling thermostat [3] were applied to maintain constant pressure at 1 bar and temperature at 300K, respectively. All bonds were constrained using the LINCS algorithm [9]. The particle mesh Ewald (PME) method with cubic interpolation for long-range electrostatics was employed.

The polymers that were used in the study, namely polylactic acid (PLA), polyglycolic acid (PGA) and polyhydroxybutyric acid (PHA) are illustrated schematically in figure 4.1 (a), (b) and (c) whereas the snapshots of the monomers are shown in figure 4.1(d), (e) and (f) respectively.

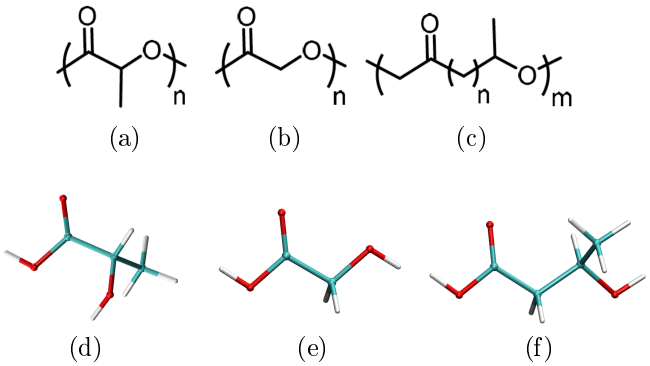

Figure 4.1: Schematic illustration of (a) PLA, (b) PGA and (c) PHA polymers used in biodegradable materials used in this study. Snapshot of the monomers of the respective polymers used for the monomer-nucleobase interation are shown in (d), (e) and (f).

The four nucleobases namely adenine, guanine, cytosine and thymine are shown in figure 4.2 (a), (b), (c) and (d) respectively.

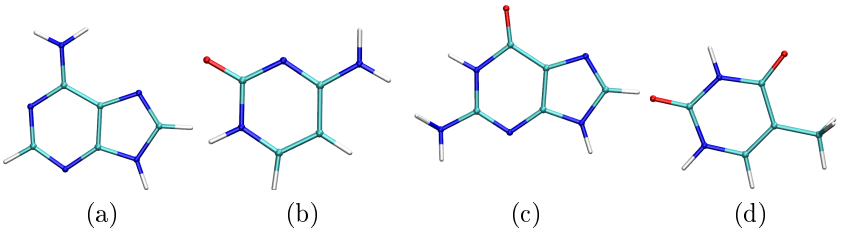

Figure 4.2: Snapshots of the nucleobases : (a) adenine, (b) cytosine, (c) guanine amd (d) thymine used for the monomer-nucleobase interation.

Systems with the same simulation conditions were also set up to study the interaction of nucleobases and polymers with 5 repeating units, the only difference being that single monomers described above were replaced with 5 repeating units of their respective polymers. PLA, PGA and PHA oligomers with 5 repeats would be henceforth reffered to as 5PLA, 5PGA and 5PHA and are illustrated in figures 4.5a, 4.5b and 4.5c respectively.

The DNA fragment used for simulations in section 4.3.3 is a hairpin loop derived from a palindrome in the Salmonella typhimurium hisD3052 gene available at RCSB website with ID *1LA8* [32]. This fragment is a hotspot for frameshift mutagenesis and is illustrated in figure 4.7.

4.3 Results and Discussion

4.3.1 Monomer--Nucleobase Interaction

We assessed free energy to study the interaction between single monomers of the polymers PLA, PGA and PHA with the nucleobases A, G, C and T at 300K, near physiological temperature, by using molecular dynamics (MD). In figure 4.3a we show the free energy as a function of center of mass between the monomer of PLA and the nucleobases: adenine (blue), cytosine (yellow), guanine (orange) and thymine (red). The insets in PMF energies shows zoomed global minimas that are shifted such that the maximum is at zero, thereby overlapping the curves with one another to see a clear difference in the nature of their interactions. The free energy plot gives an overview of binding preferences corresponding to the nucleobases and help identify the energetic barriers along the binding reaction coordinate. Overall, one can see that in water, all nucleobases exhibit a pronounced preference for the PLA monomer. We see that all of them show global minimum at same distances, i.e. at around $0.5nm$ with an energy difference of $1.2kT$. Similar analysis is shown in 4.3b and 4.3c for monomers of polymer PGA and PHA respectively. The free energy profile of the nucleobases A and G with the PGA monomer in figure 4.3b has a minima at $r = 0.46nm$ with $\Delta E = 1.2kT$. Whereas, nucleobases C and T interact weakly and have $r = 0.46nm$ with $\Delta E = 0.5kT$. The free energy profile of the nucleobases A and G with the PHA monomer in figure 4.3c has a minima at $r = 0.49nm$ with $\Delta E = 1.4kT$ and on the other hand C and T have at $r = 0.48nm$ with $\Delta E = 0.8kT$. In all the cases, but more prominently in 4.3b, the nucleobases A and G have higher ΔE values than C and T. This can be explained by the difference in the nature of structure of the purines (A, G) which have a six-ring attached to a five-ring in contrast to the pyrimidines (C, T) that have only a single six-membered ring (see figure 4.2). We observe a baisness in the affinity of the monomers towards A and C.

Although slight weaker interactions are seen with G and T than with A and C, there appears to be no significant energy barriers regardless of the base and monomer in question.

We also calculated the angle distribution between the normal vector consisting the 6-membered ring of the nucleobases and the central C-C bond of the polymers for the window of the umbrella sampling at $r = 0.4nm$ because that is around where we observed our minimas. For bench-marking, we show similar statistics at large distances ($r = 4.8nm$) where almost no interaction is present.

Figure 4.4a (i) shows the angle distribution at $r = 0.4nm$ and (ii) at $r = 4.8nm$ for PLA monomer. Figure 4.4b (i) shows the angle distribution at $r = 0.4nm$ and (ii) at $r = 4.8nm$ for PGA monomer. Figure 4.4c (i) shows the angle distribution at $r = 0.4nm$ and (ii) at $r = 4.8nm$ for PHA monomer. We observe no particular preference in the orientation of the molecules around the nucleobases at the closest and most further windows.

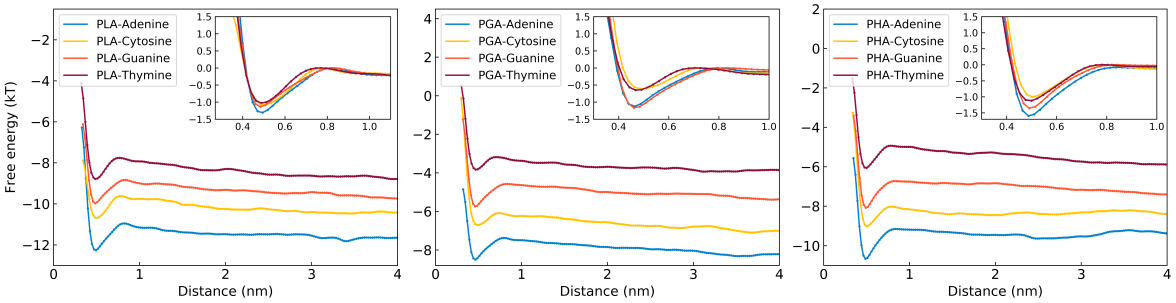

(a) (b) (c)

Figure 4.3: The free energy calculated by umbrella sampling as a function of the com-com distance between (a)PLA, (b) PGA and (c) PHA and the nucleobases A, G, C and T.

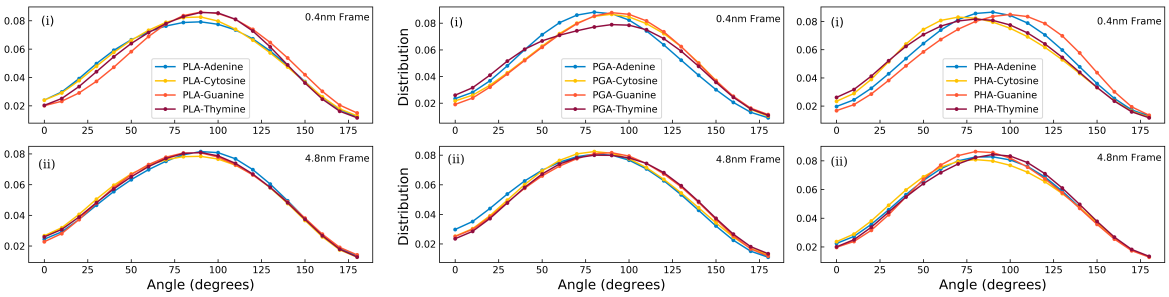

(a) (b) (c)

Figure 4.4: Angle distribution between the vectors consisting the nucleobase plane and C-C bond of PLA (a) at $r = 0.4nm$ and (b) at $r = 4.8nm$.

4.3.2 Oligomer-- Nucleobase Interaction

During the degradation process, the polymer does not always completely disintegrate into its individual monomers, but rather most of it turns into its smaller units of chains, i.e. oligomers. In this scope of study, it was possible for us to simulate oligomers with 5-repeats of PLA, PGA and PHA and look into detail, their interaction energies with DNA nucleobases. In figure 4.5a we illustrate the 5-repeat oligomer of PLA that we used for our simulations. This oligomer was solvated in a box of water and Na, Cl ions along with each of the nucleobases A, G, C and T individually at varying distances. The PMF along the reaction coordinate of the distance between the center of mass of the PLA oligomer and the nucleobase is presented in figure 4.6a. The insets in PMF energies henceforth shows zoomed global minimas that are shifted such that the maximum is at zero, thereby overlapping the curves with one another to see a clear difference in the nature of their interactions.

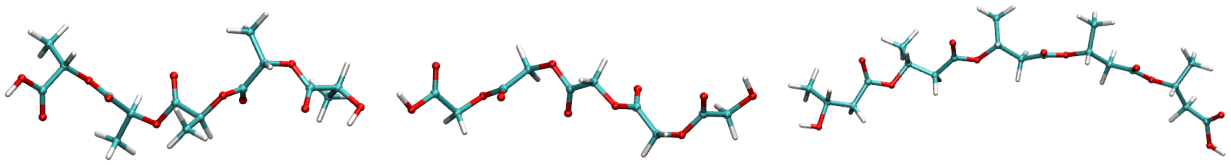

(a) (b) (c)

Figure 4.5: Snapshot of the structure of (a)PLA, (b)PGA and (c) PHA poligomer with 5 repeating units.

Overall, the free energy profiles obtained from the umbrella sampling with a total simulation time of 250ns (the sum of the time duration of all simulation windows) between PLA oligomer and all the nucleobases displays a global minima with no energy barriers. In figure 4.6a nucleobases A and G has minima at $r = 0.64nm$ and $\Delta E = 2kT$ and $\Delta E = 2.68kT$ respectively. Both C and T have minimas at $r = 0.59$ with $\Delta E = 1.2kT$.

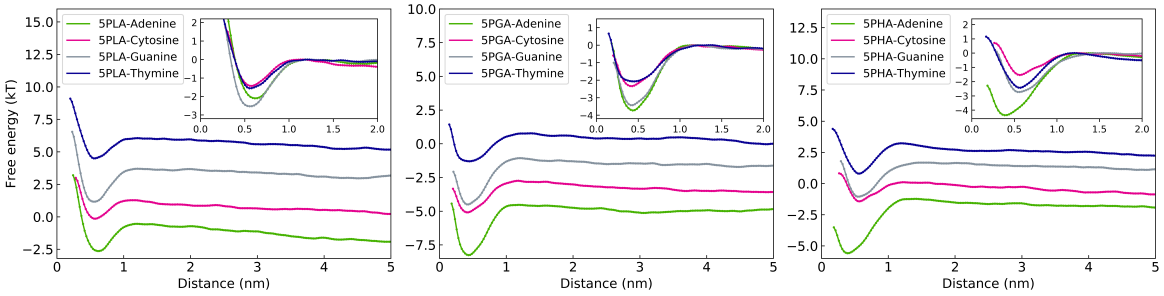

(a) (b) (c)

Figure 4.6: The free energy calculated by umbrella sampling as a function of the com-com distance between PLA oligomer with 5 repeating units and the nucleobases A, C, G and T.

We do similar analysis for oligomers with 5-repeats of PGA and PHA, illustrations of which are shown in figure 4.5b and 4.5c respectively. Figure 4.6b presents the PMF energies of the four nucleobases with PGA oligomer. All the nucleobases have a global minima at $r = 0.48nm$. The energy difference in case of C and T is $\Delta E = 2kT$ whereas A and G show more binding affinity with higher energy difference of $\Delta E = 3.8kT$.

Figure 4.6c shows the PMF energies of the nucleobases with PHA oligomer containing 5 repeats. All the nucleobases have a global minima at $r = 0.55nm$ and their energies are $\Delta E = 3.2$, 1.5,2.8 and $2.1kT$ for A, C, G and T respectively.

4.3.3 Oligomer -- DNA Interaction

Now we look into the interaction energies between the oligomers of the above section with a whole 13-mer DNA strand. The cartoon and atomistic structures of the DNA in study are shown in figure 4.7 (a) and (b) respectively.

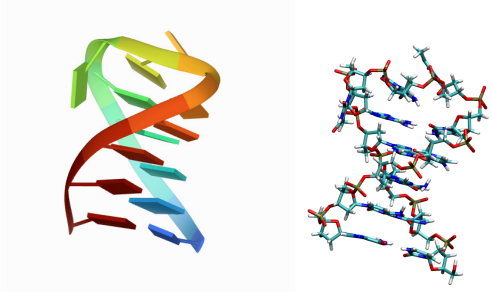

(a) (b)

Figure 4.7: Strucuture of the DNA hairloop in: (a) cartoon and (b) atomistic form used for the oligomer-DNA interation.

Figure 4.8 presents the PMF energies of PLA, PGA and PHA 5 repeat oligomers with spatially constrained DNA strand. The inset includes zoomed PMF curves with shifted y-scale for easier visualization and analysis and marks the values of ΔE for each of the cases. An interesting fact is brought into picture here, that all the oligomers show a global minima at $r = 1.25nm$. PLA oligomer has a global minima with $\Delta E = 5.03kT$, PGA has with $\Delta E = 5.39kT$ and PHA with $\Delta E = 7.46kT$. PHA oligomer shows highest affinity towards the DNA molecule, which could be a result of its higher molecular weight (as it is a bigger molecule as compared to PLA or PGA).

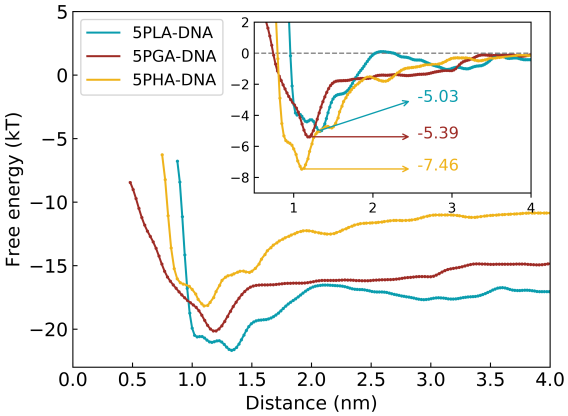

Figure 4.8: The free energy calculated by umbrella sampling as a function of the com-com distance between PLA, PGA and PHA oligomers with 5 repeating units and the spatially constrained DNA strand.

One can clearly infer from figure 4.8 that the attractive interaction for all the three oligomers towards DNA begins $= 3.0nm$ when moving closer towards DNA with maximum affinity at $1.25nm$. The ΔE magnitudes are negligible at larger distances and gradually increase (i.e., become attractive) to reach the peak values, then decrease again as the non-bonded repulsions dominates.

4.4 Conclusion

Keeping in mind the fundamental importance of the increasing traces of bio-degradable polymers in our day-to-day life, this is to the best of our knowledge the first time that binding free energy for all the combinations of the nucleobases with the smallest units of the polymers have been carried out. The calculation of the free energies strongly depends highly on the choice of the forcefields, the GROMOS forcefielld 54a8 captures highly relevant thermodynamics properties including the hydration free energies.

Overall, with water as a solvent, all nucleobases bind preferentially to the monomers PLA, PGA and PHA at a distance of around $0.5nm$. The majority of the difference in the binding preference is seen more towards the nucleobases A, G in contrast to C, T which can be reasoned with the difference in the structure of the purines and the pyrimidines. Overall the PMF energies are not greater than $\Delta E = 1.5kT$ and therefore, we see only weak interaction between the monomers and the DNA in our simulations. The interaction energies however, becomes much stronger (reaching upto $\Delta E = 7.46kT$) between 5 repeat oligomers and 13-mer DNA hairpin with most attraction eminent with PHA, followed by PGA and PLA resp.

Although preliminary deterministic in nature, the free energies have helped us demonstrate the effect such degradable polymer residues can have on the fundamental building blocks of our body. The nucleobases monomer interaction are not only relevant for the in vivo processes that govern the working of most the living beings in the nature, the presences of these biodegradable microplastics is capable of hindering the ex vivo experiments that involve DNA origami, biosensors and organic transistors.

4.5 Appendix of Chapter 3

The ATB molid to the topology files for the monomers and the nucleobases used in this study are listed below:

Moleculetype	MolID
PLA	461243
PGA	31884
PHA	38590
Adenine	363423
Cytosine	716881
Guanine	520
Thymine	363639
PLA with 5 repeats	26416
PGA with 5 repeats	736624
PHA with 5 repeats	364907
DNA hairpin	765776

Table 4.1: ATB molids of the biodegradable monomers, oligomers, DNA and nucleobases citing the topology files

References

[1] Mark James Abraham, Teemu Murtola, Roland Schulz, Szilárd Páll, Jeremy C Smith, Berk Hess, and Erik Lindahl. Gromacs: High performance molecular simulations through multi-level parallelism from laptops to supercomputers. *SoftwareX*, 1:19–25, 2015.

[2] Herman JC Berendsen, James PM Postma, Wilfred F van Gunsteren, and Jan Hermans. Interaction models for water in relation to protein hydration. In *Intermolecular forces*, pages 331–342. Springer, 1981.

[3] Giovanni Bussi, Davide Donadio, and Michele Parrinello. Canonical sampling through velocity rescaling. *The Journal of chemical physics*, 126(1):014101, 2007.

[4] CC Chu. Hydrolytic degradation of polyglycolic acid: tensile strength and crystallinity study. *Journal of applied polymer science*, 26(5):1727–1734, 1981.

[5] Dominique Costa, Pierre-Alain Garrain, and Marc Baaden. Understanding small biomolecule-biomaterial interactions: A review of fundamental theoretical and experimental approaches for biomolecule interactions with inorganic surfaces. *Journal of Biomedical Materials Research Part A*, 101(4):1210–1222, 2013.

[6] Dominik Danso, Jennifer Chow, and Wolfgang R Streit. Plastics: microbial degradation, environmental and biotechnological perspectives. *Applied and environmental microbiology*, 2019.

[7] Bhabesh Chandra Deka and Pradip Kr Bhattacharyya. A density functional study on synthetic polymer–amino acid interaction. *Journal of Chemical Sciences*, 130(9):1–11, 2018.

[8] Osman Doluca, Jamie M Withers, and Vyacheslav V Filichev. Molecular engineering of guanine-rich sequences: Z-dna, dna triplexes, and g-quadruplexes. *Chemical reviews*, 113(5):3044–3083, 2013.

[9] Berk Hess, Henk Bekker, Herman JC Berendsen, and Johannes GEM Fraaije. Lincs: a linear constraint solver for molecular simulations. *Journal of computational chemistry*, 18(12):1463–1472, 1997.

[10] Jochen S Hub, Bert L De Groot, and David Van Der Spoel. g_wham a free weighted histogram analysis implementation including robust error and autocorrelation estimates. *Journal of chemical theory and computation*, 6(12):3713–3720, 2010.

[11] William Humphrey, Andrew Dalke, and Klaus Schulten. Vmd: visual molecular dynamics. *Journal of molecular graphics*, 14(1):33–38, 1996.

[12] YL Jeyachandran, E Mielczarski, B Rai, and JA Mielczarski. Quantitative and qualitative evaluation of adsorption/desorption of bovine serum albumin on hydrophilic and hydrophobic surfaces. *Langmuir*, 25(19):11614–11620, 2009.

[13] Min-Jae Lee, Soon-Shin Cho, Hyung-Suk Jang, Young Shin Lim, Ji-Ran You, Jangwon Park, Hearan Suh, Jeong-a Kim, Jong-Sang Park, and Duk-Kyung Kim. Optimal salt concentration of vehicle for plasmid dna enhances gene transfer mediated by electroporation. *Experimental & Molecular Medicine*, 34(4):265–272, 2002.

[14] Yingzhe Liu, Ming Wu, Xizeng Feng, Xueguang Shao, and Wensheng Cai. Adsorption behavior of hydrophobin proteins on polydimethylsiloxane substrates. *The Journal of Physical Chemistry B*, 116(40):12227–12234, 2012.

[15] Donghao R Lu, Samuel J Lee, and Kinam Park. Calculation of solvation interaction energies for protein adsorption on polymer surfaces. *Journal of Biomaterials Science, Polymer Edition*, 3(2):127–147, 1992.

[16] Alpeshkumar K Malde, Le Zuo, Matthew Breeze, Martin Stroet, David Poger, Pramod C Nair, Chris Oostenbrink, and Alan E Mark. An automated force field topology builder (atb) and repository: version 1.0. *Journal of chemical theory and computation*, 7(12):4026–4037, 2011.

[17] CP O Brien, SJ Stuart, DA Bruce, and RA Latour. Modeling of peptide adsorption interactions with a poly (lactic acid) surface. *Langmuir*, 24(24):14115–14124, 2008.

[18] Michele Parrinello and Aneesur Rahman. Polymorphic transitions in single crystals: A new molecular dynamics method. *Journal of Applied physics*, 52(12):7182–7190, 1981.

[19] V Piemonte and F Gironi. Kinetics of hydrolytic degradation of pla. *Journal of Polymers and the Environment*, 21(2):313–318, 2013.

[20] Chunmei Qiu. *Novel molecular engineering approaches for genotyping and DNA sequencing*. PhD thesis, Columbia University, 2011.

[21] Michael Rabe, Dorinel Verdes, and Stefan Seeger. Understanding protein adsorption phenomena at solid surfaces. *Advances in colloid and interface science*, 162(1-2):87–106, 2011.

[22] Giuseppina Raffaini and Fabio Ganazzoli. Understanding the performance of biomaterials through molecular modeling: crossing the bridge between their intrinsic properties and the surface adsorption of proteins. *Macromolecular bioscience*, 7(5):552–566, 2007.

[23] Estelle Renard, Michael Walls, Philippe Guerin, and Valerie Langlois. Hydrolytic degradation of blends of polyhydroxyalkanoates and functionalized polyhydroxyalkanoates. *Polymer degradation and Stability*, 85(2):779–787, 2004.

[24] Chelsea M Rochman. Microplastics research from sink to source. *Science*, 360(6384):28–29, 2018.

[25] Kenji Sakai, Masayuki Taniguchi, Shigenobu Miura, Hitomi Ohara, Toru Matsumoto, and Yoshihito Shirai. Making plastics from garbage: a novel process for poly-l-lactate production from municipal food waste. *Journal of industrial ecology*, 7(3-4):63–74, 2003.

[26] Nathan Schmid, Andreas P Eichenberger, Alexandra Choutko, Sereina Riniker, Moritz Winger, Alan E Mark, and Wilfred F van Gunsteren. Definition and testing of the gromos force-field versions 54a7 and 54b7. *European biophysics journal*, 40(7):843–856, 2011.

[27] Felix Sedlmeier, Yann von Hansen, Liang Mengyu, Dominik Horinek, and Roland R Netz. Water dynamics at interfaces and solutes: disentangling free energy and diffusivity contributions. *Journal of Statistical Physics*, 145(2):240–252, 2011.

[28] Bruce Thompson. Exploratory and confirmatory factor analysis: Understanding concepts and applications. *Washington, DC*, 10694, 2004.

[29] Loup Verlet. Computer" experiments" on classical fluids. i. thermodynamical properties of lennard-jones molecules. *Physical review*, 159(1):98, 1967.

[30] C Wang, J Wang, R Liu, W Yu, and Z Shen. Mar. pollut. bull., 2013.

[31] Kemin Wang, Zhiwen Tang, Chaoyong James Yang, Youngmi Kim, Xiaohong Fang, Wei Li, Yanrong Wu, Colin D Medley, Zehui Cao, Jun Li, et al. Molecular engineering of dna: molecular beacons. *Angewandte Chemie International Edition*, 48(5):856–870, 2009.

[32] Jason P Weisenseel, G Ramachandra Reddy, Lawrence J Marnett, and Michael P Stone. Structure of the 1, n 2-propanodeoxyguanosine adduct in a three-base dna hairpin loop derived from a palindrome in the salmonella typhimurium hisd3052 gene. *Chemical research in toxicology*, 15(2):140–152, 2002.

[33] Fang Yuan. *Multi-scale Computational Studies of Waterborne Coatings.* PhD thesis, 2015.

[34] Lin Zhang, Guofeng Zhao, and Yan Sun. Molecular insight into protein conformational transition in hydrophobic charge induction chromatography: a molecular dynamics simulation. *The Journal of Physical Chemistry B*, 113(19):6873–6880, 2009.

Chapter 5

Martini coarse grained models of hyaluronic acid and alginate

3D bioprinting involves usage of bioinks containing polymers, in addition to cells, to enable proper fabrication of stable hydrogel structures due to the gelation process involved. The properties of these polymers play a major role in cell survival, cell differentiation and homogeneous distribution of the cellular matrix in the 3D printed constructs. Detailed theoretical and computational study on the bioinks can provide an initial information on the success rate of the 3D printed structure by the virtue of cell survival rate due to the mechanical and elastic response of the cell to the hydrodynamic stresses experienced during printing. To analyze such a bioink, good models for the polymers are required to correctly replicate their properties. As it would be highly computationally expensive, a 3D printer cannot be simulated on an atomistic scale due to it's enormity. Coarse grained (CG) models are therefore required in order to retain the basic polymer properties and compute the effect of the polymers in the bionks in reasonable amount of time to determine the cells' survival at the nozzle exit, where the cells experience most of the stress. Therefore this study aims at creating a martini coarse grained model on hyaluronic acid and alginate polymers, two of the most widely used polymers in bioinks for 3D printing. To achieve proper Martini CG models, following a certain set of rules results in faster convergence and better results. This chapter aims at explaining the layout behind creating Martini CG models and its proper validation to the respective atomistic forcefield.

5.1 Introduction

Hyaluronic acid (HA) and Alginates (AG) are both linear, unbranched anionic polysaccharides. Hyaluronic acid consists of repeating units of disaccharide units of D-gluronic acid (GlcA) and N-acetyl-D-glucosamine (GlcNAc) linked by alternating β(1–3) and β(1–4) glucosidic bonds [8] and is widely abundant in several locations in the body such as skin, synovial fluid, eyes and lungs. Alginates are (1→4)-linked glycuronans consisting of repeating units of β-D-mannuronate and α-L-guluronate [4] and occur as structural component in marine algae and brown seaweeds (*Phaeophyceae*) such as kelp. The wide industrial application of both the polymers is based on their properties to form gels in aqueous solutions [9]. Attributing to their hydrophilic nature, in ionic solutions these polymers swell causing the solution to thicken and increase its viscosity. This makes them perfect candidates to use in bioinks used in 3D printing of well-organized cell-laden constructs for repair and regeneration of tissues and organs. 3D printing focuses to integrate living cells in 3-dimensional biomaterials.

This ultra-modern technology permits automated, reproducible creation of 3D functional living tissues by depositing one-on-one layers of biocompatible inks with a high-precision positioning of cells. This technique permits scalable and precise geometries of 3D constructs that are not viable by other strategies such as 2D cell cultures or standard 3D cell cultures. In such bioinks the selection of a suitable bio-polymers, in terms of composition and mechanical properties, is crucial. Antich et al. [2] described the development of such a bio ink based on the main component of cartilage, HA, with suitable biological and mechanical properties, without involving toxic procedure, and its application in cartilage based tissue bioprinting. A detailed review on the usage of alginate-based bioinks in the direct fabrication of artificial living tissues is presented by Axpe et al [3]. They summarize the benefits of using alginate in 3D printing of printing vascular tissue, bone and cartilage. Jia et al. [7] present a further detailed overview by listing 30 different alginate based hydrogels with varied concentration to develop a bioink platform that can be applied to a multitude of tissue engineering platforms. The authors systematically address the viscosity and density of alginate solutions on their printabilities to recognize a suitable range of material properties of alginates to be applied to bioprinting. Combining the experiments with theoretical calculations increases our chances of betterment by many folds by reducing the trail and errors involved in setting up a bioink. Theoretical calculations, however are of quite large scales ($\sim 10^6$m) and are impossible to simulate at atomistic scale. Coarse-graining of polymers used in these bioinks is a necessity of the day to simulation larger length and time scales. Apart from the fact that CG simulations can be carried out at larger time steps compared to atomistic ones, four water molecules are combined to one CG bead thus reducing the wall time of simulating solvent itself. Thus coarse graining is not only be applied to the solute (polymer of interest) but also to the solvent thus letting us compute realistic timescales to understand the microscopic mechanism involved in structural changes

that happen during gelation and its effect on the suspended cells. In this study we develop and validate a CG model for HA and AG based on the Martini scheme for modeling coarse-grained simulations, which will make it possible to achieve greatly accelerated simulations for understanding even in gelation that lead to sturdiness and structure in the 3D printed constructs.

5.2 Simulation details

5.2.1 Atomistic simulations

All the atomistic simulations of Hyaluronic acid were carried out using CHARMM36 force field and for Alginate using GROMOS54a7 force field. Each system contains one disaccharide or octasaccharide molecule in a cubic box containing TIP3P water molecules with appropriate number of Na+ and Cl- counter-ions to neutralize the system. Each system undergoes the following four steps: (i) energy minimisation, (ii) NVT equilibration, (iii) NPT equilibration and (iv) MD runs for analysis. The energy minimization was obtained over 50,000 steps with maximum force of $1000.0 \frac{\text{kJ}}{\text{mol nm}}$ through *steepest descent* algorithm. The NVT minimization was done *md integrator* at 300K for 25000 steps with $dt = 0.002$ps along with position restrain on the polymer. The temperature was maintained using V-rescale thermostat with a time constant of 0.1ps. Periodic boundary conditions were applied in xyz directions, Particle Mesh Ewald was used for long-range electrostatics and nonbonded short-range interactions were cut off at 1.0 nm. The bonds were constrained using the LINCS algorithm. The NPT minimization was carried out for 1000000 steps with $dt = 0.002$ps and isotropic Parrinello-Rahman barostat with $\tau_p = 2.0$ ps and with position restraint on the polymer. The final MD run simulations used for analysis were NPT runs carried out for 100 nseach and last 50ns were used for analysis without any position restraints on the polymers.

5.2.2 Coarse grained simulations

The coarse grained simulations of Hyaluronic acid and Alginate went through (i) energy minimization, (ii) equilibration to produce (iii) final MD runs for analysis. The energy minimization was carried out in the same way as for atomistic simulations mentioned above. The equilibration was carried out using NPT ensemble for 100000 steps and $dt =$ 0.02ps followed by production runs of 100ns of which the last 50ns were used for analysis. The time step in CG simulations is 10 times higher than the atomistic simulations because the low amplitude high-frequency fluctuations are not present in Martini CG model. Pressure and temperature conditions were kept same as in atomistic simulations. The cut-off value of 1.1 nm was used for the short-range nonbonded interactions and LJ potential. Periodic boundary conditions were applied in xyz directions and no position restraint was put on the polymer. Martini water model was used to represent water,

where four water molecules are represented by one Martini water CG bead. This further help in reduction of the wall time for Martini CG simulations.

It should be noted that when analyzing bonded parameters (bond lengths, angles and dihedrals) of both AA and CG simulations, the periodic boundary conditions should be taken into consideration, to removed any artifacts caused by the polymer jumping over the box.

5.3 Hyaluronic Acid

5.3.1 CG Mapping of HA disaccharide

The Hyaluronic acid is mapped based on the Martini model for carbohydrates described in section 2.9. The disaccharides are modeled using 6 beads. The two central beads mimick the glycosidic linkage in carbohydrates. The two subunits of HA, GlcA and GlcNAc are connected by alternating β(1–3) and β(1–4) glucosidic bonds and hence will be parameterized separately as HA1-3 and HA1-4 respectively (see figure 5.1 (a) and (b)). In this case the CG bead types are assigned polar type (P) and charged type (Q) (see 5.1 (d) and (e)). The charged bead is used to represent the bead of GlcA containing the carboxyl group and the other two are represented by P2 and P4 bead types. In GlcNAc all the beads used are of P types P1 and P2.

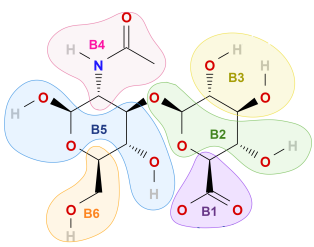

(a)

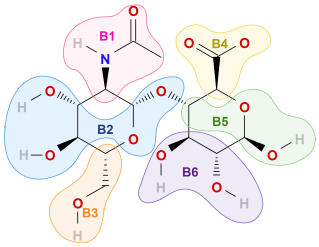

(b)

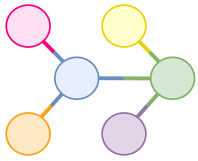

(c)

Bead Name	Bead Type	Charge
B1	Qa	-1.0
B2	P2	0.0
B3	P4	0.0
B4	P2	0.0
B5	P2	0.0
B6	P1	0.0

(d)

Bead Name	Bead Type	Charge
B1	P2	0.0
B2	P2	0.0
B3	P1	0.0
B4	Qa	-1.0
B5	P2	0.0
B6	P4	0.0

(e)

Figure 5.1: Martini coarse graining mapping scheme for (a) HA1-3 and (b) HA1-4 disaccharides. (c) CG representation of the model. Assignment of bead types for (d) HA1-3 and (e) HA1-4 disaccharides.

The non bonded interactions are represented by the 12-6 Lennard Jones potential (2.14) and the LJ parameters σ and ε are determined by the Martini bead force field and were unchanged. The electrostatic interactions are given by the Coulombic potential 2.13. The bonded interactions comprise of bond lengths, bond angles and dihedral angles and are modeled using equation 2.7, 2.9 and 2.11 respectively. The values for the equilibration bond lengths, bond angles and dihedral angles need to be adjusted in order to match with the atomistic model. The details of the bonded parameters obtained after several iterations are presented in figures 5.2, 5.3 and 5.4. The bond length comparison of martini coarse grained (CG) and atomistic simulations (AA) are given in figure 5.2.

For HA1-3 the average bond lengths between bead 1-2, 2-3, 2-5, 4-5 and 5-6 are 2.680Å, 2.240Å, 5.040Å, 3.571Å and 2.631Å respectively, where the 2-5 bond represents the glycosidic bond between the two monosaccharides. For HA1-4 the average bond lengths between beads 1-2, 2-3, 2-5, 4-5 and 5-6 are 3.620Å, 2.852Å, 6.120Å, 2.660Å and 2.240Å respectively, again 2-5 being the glycosidic bond. For both the HA1-3 and HA1-4 disaccharide units, the the CG bond lengths show an exemplary match to the AA simulations. The glycosidic bond lengths (2-5) for HA1-3 and HA1-4 differ much from one another (5.040Å and 6.120Å resp), which is why it is quite necessary to model them separately. For angle distribution comparison for CG and AA simulations are given in figure 5.3. For HA1-3 the equilibration angle for beads 1-2-5, 3-2-5, 2-5-4 and 2-5-6 converge to values 106^0, 112^0, 69.5^0 and 115^0 with force constants $300\frac{\text{kJ}}{\text{mol rad}^2}$, $600\frac{\text{kJ}}{\text{mol rad}^2}$,$75\frac{\text{kJ}}{\text{mol rad}^2}$ and $200\frac{\text{kJ}}{\text{mol rad}^2}$ respectively. The equilibration angles for HA1-4 bead 1-2-5, 3-2-5, 2-5-4 and 2-5-6 stabilize at 69, 80.7^0, 65.5^0 and 80^0 and the force constants used are $210\frac{\text{kJ}}{\text{mol rad}^2}$, $110\frac{\text{kJ}}{\text{mol rad}^2}$,$100\frac{\text{kJ}}{\text{mol rad}^2}$ and $130\frac{\text{kJ}}{\text{mol rad}^2}$ respectively. The dihedral angle distributions for HA1-3 beads 1-2-5-6, 3-2-5-4, 1-2-5-4 and 3-2-5-6 are shown in figure 5.4 (a), (b), (c) and (d) and for HA1-4 in 5.4 (e), (f), (g) and (h) respectively. The equilibration angles for HA1-3 beads 1-2-5-6, 3-2-5-4, 1-2-5-4 and 3-2-5-6 are at 25^0, 34^0, -143^0 and -163^0 with force constants $14\frac{\text{kJ}}{\text{mol}}$, $15\frac{\text{kJ}}{\text{mol}}$, $15\frac{\text{kJ}}{\text{mol}}$ and $8\frac{\text{kJ}}{\text{mol}}$ and for HA1-4 at -116^0, -134^0, 71^0 and 41^0 with force constants $20\frac{\text{kJ}}{\text{mol}}$, $10\frac{\text{kJ}}{\text{mol}}$, $8\frac{\text{kJ}}{\text{mol}}$ and $12\frac{\text{kJ}}{\text{mol}}$ respectively. During CG mapping, the dihedral distributions are relatively harder to match compared to the other two and large discrepancies are reported when creating CG models [10]. Both the angle and the dihedral distributions show a good agreement between the AA and CG models and show similar degree of differences as previously reported and accepted [10, 13]. The bonded length, dihedral and angle parameters for HA disaccharide needed to carry out Gromacs simulations are listed in appendix 5.6 table 5.1, 5.2 and 5.3 respectively.

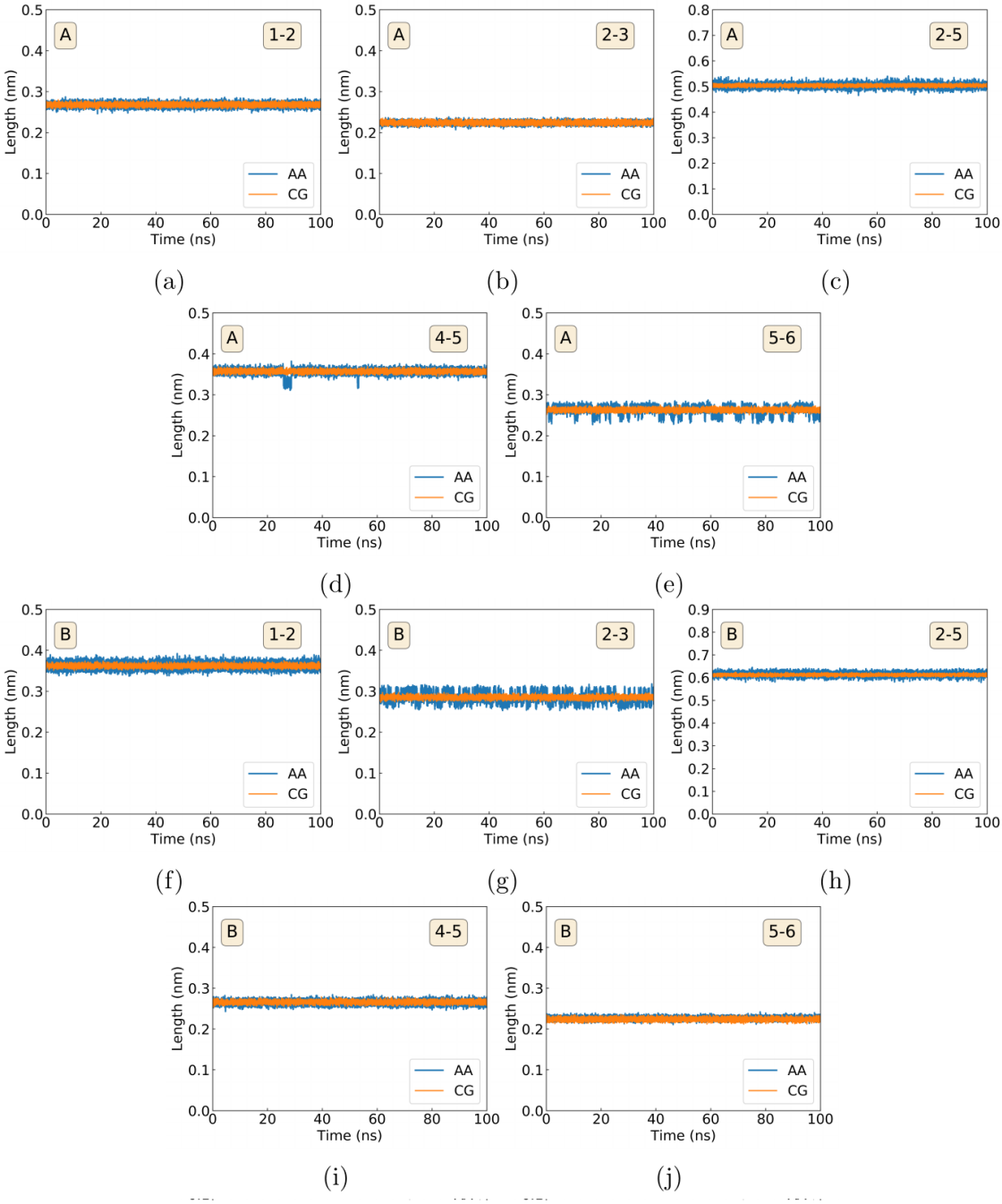

Figure 5.2: Bond lengths of AA and CG simulations for (A) HA1-3 and (B) HA1-4 disaccharides.

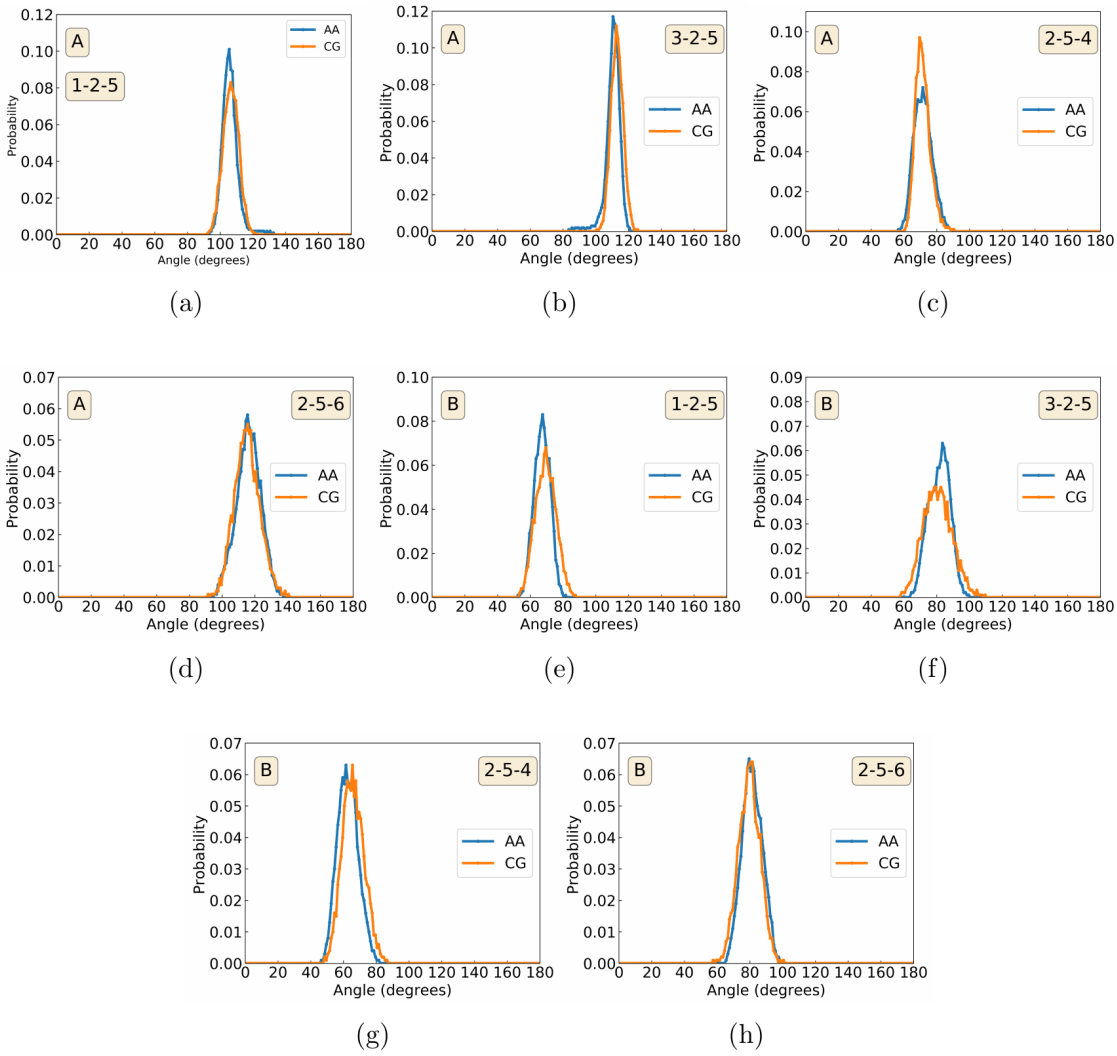

Figure 5.3: Angle distributions of AA and CG representations for (A) HA1-3 and (B) HA1-4 disaccharides.

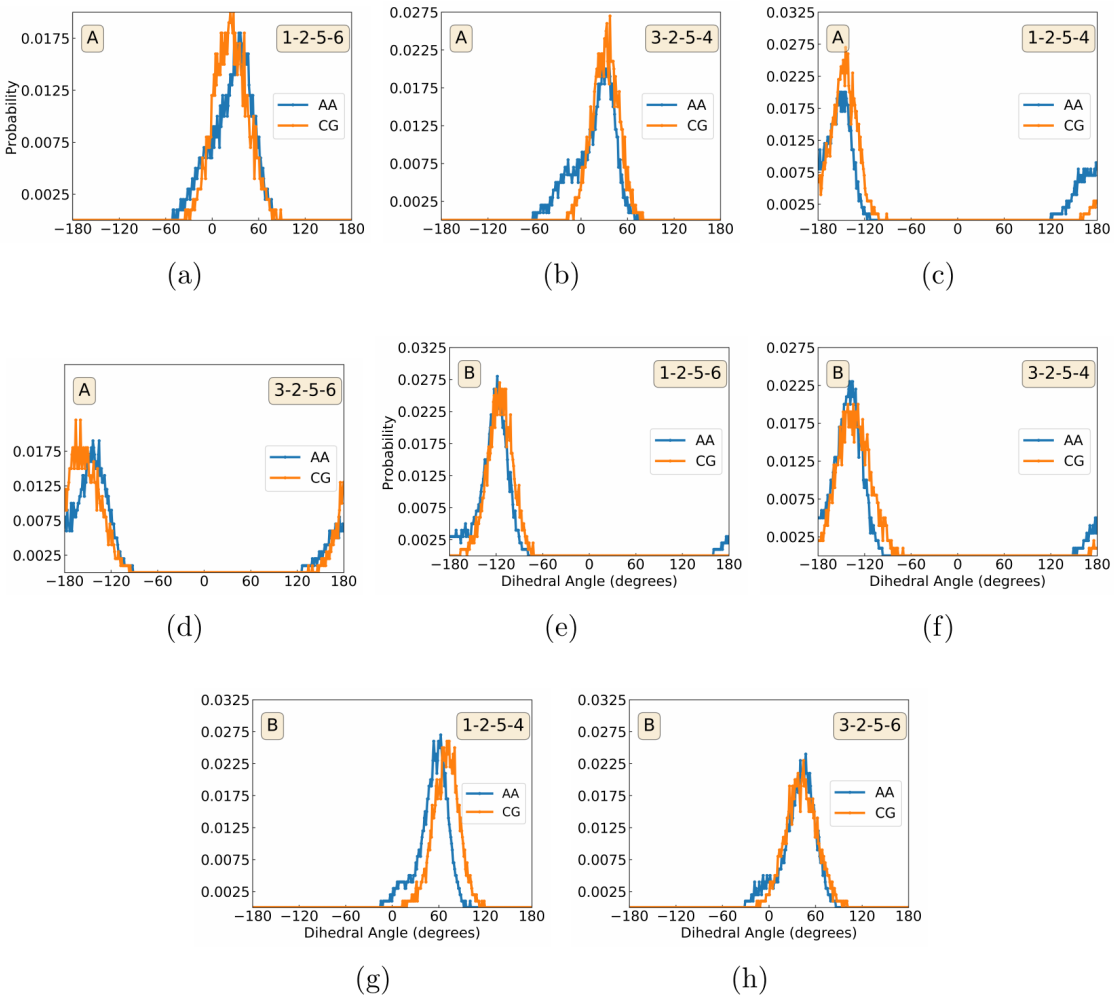

Figure 5.4: Dihedral angle distributions of AA and CG representations for (A) HA1-3 and (B) HA1-4 disaccharides.

5.3.2 CG mapping of HA octasaccharide

The atomistic structure of HA octasaccharide is taken from the RCSB database and can be accessed with the PDB ID : 2BVK [1]. The mapping from disaccharide is carried forward to the octasaccharide molecule of HA having eight monosaccharide units. This can be understood from figure 5.5. To create a CG model for an atomistic HA octasaccharide (5.5(a)), we assemble four HA CG disaccharide units (5.5(b)), keeping constant the bond, angle and dihedral parameters we matched in the previous section and denoted by the gray zone. Then add the additionally needed bond, angles and dihedrals in the red region of 5.5(c) for connecting the four units of the HA CG disaccharides to create a complete HA CG octasaccharide model. To do this, we first obtain the trajectory from the AA simulations of HA octasaccharide, and compute the bonded parameter distributions for the groups used to create CG beads. We insert these parameters into the HA CG octasaccharide model to form initial parameters for running the CG simulations. These vales are then updated in an iterative way until we get a good match to the AA simulations. Bead no. 2 and 23, which make up for the central beads of the end monomers, were treated as terminal beads in the force field and had different mass (because of additional hydrogen).

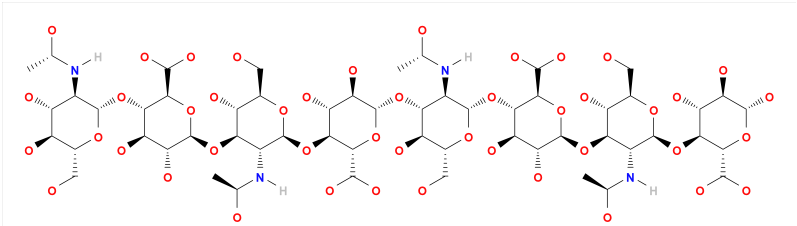

(a)

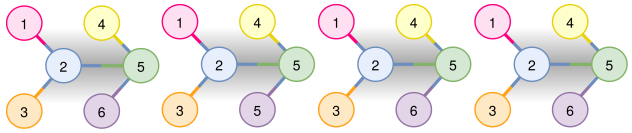

(b)

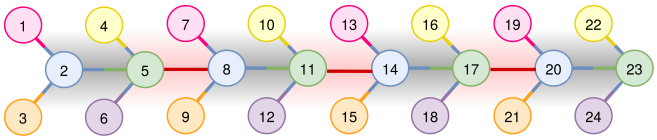

(c)

Figure 5.5: (a) Atomic representation of HA octasaccharide. (b) 4 HA CG disaccharide from previous section. (c) Connecting 4 HA CG disaccharide to create one HA octasaccharide. Bond, angle and dihedral parameters in the gray zone are used from HA disaccharide model of previous section, and in the red zone are matched additionally to the atomistic model.

Comparison of the AA and CG distributions for the additionally matched connecting angles and dihedrals between the disaccharides are presented in figure 5.6 and 5.7 respectively. The bonded length, dihedral and angle parameters for HA octasaccharide needed to carry out Gromacs simulations are listed in appendix 5.6 table 5.4, 5.5 and 5.6 respectively.

We also compare the CG and AA macroscopic properties of HA octasaccharide, namely the end to end distance ($R_{\text{end to end}}$), radius of gyration (R_g) and root mean squared displacement ($RMSD$) as a part of validation and application of the CG model. We can see a good match in the $R_{\text{end to end}}$ where the average length for CG is 2.9nm and for AA is 2.7nm in figure 5.8(a). The time averaged R_g for AA and CG are 1.1nm and 1.0nm respectively and also match closely as seen from figure 5.8(b). The $RMSD$ values for AA and CG models are 0.28nm and 0.23nm respectively (see figure 5.8(c)). Both the model's RMSD lay in very low range $0.15 < 0.45$nm thereby indicating that the HA CG and AA models are both stiff in nature and agree well with each other.

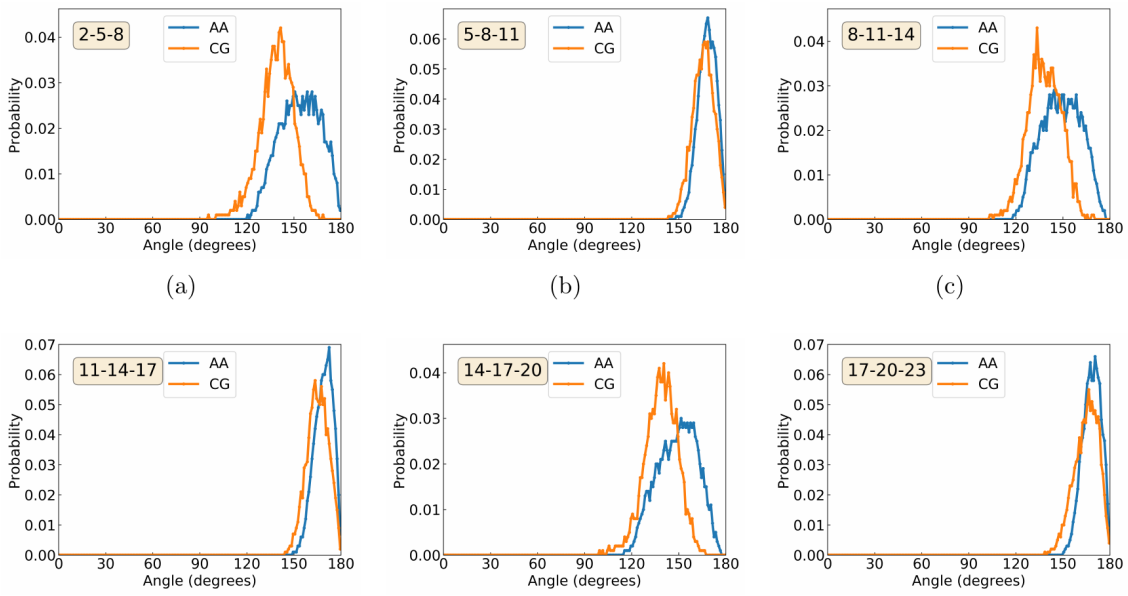

Figure 5.6: Angle distributions of AA and CG representations for (A) HA1-3 and (B) HA1-4 octasaccharides.

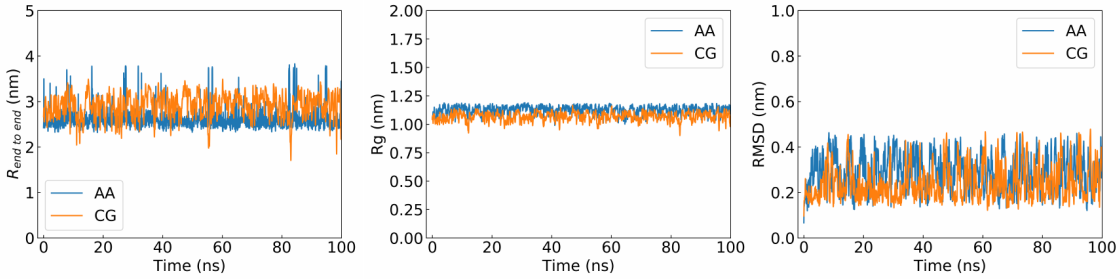

(a) (b) (c)

Figure 5.8: (a) End to end distance ($R_{\text{end to end}}$), (b) radius of gyration (R_g) and (c) Root mean squared deviation ($RMSD$) for AA and CG models of HA octasaccharide.

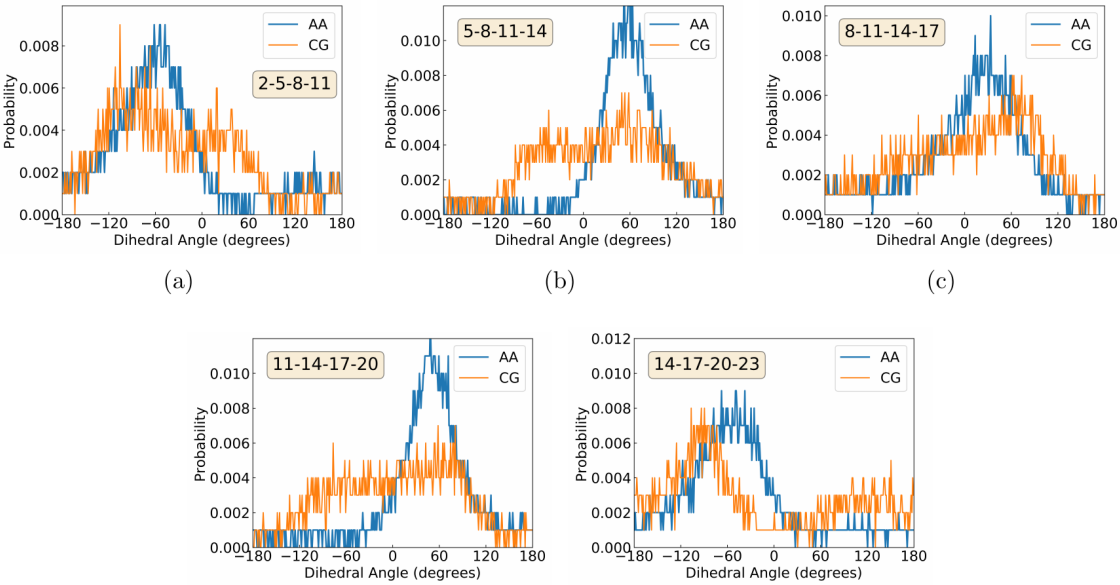

(a) (b) (c) (d) (e)

Figure 5.7: Dihedral angle distributions of AA and CG representations for (A) HA1-3 and (B) HA1-4 octasaccharides.

5.3.3 Gel Formation

Hyaluronic acid form highly entangled networks owing to its high molecular weight. To be able to utilize hyaluronic acid for several biomedical applications it is necessary to have a detailed understanding of its swelling properties. In this section, equilibrium macroscopic swelling properties of hyaluronic acid gels are investigated for varying ionic concentrations. Since it is previously established that the gel is comparatively insensitive to temperature [12], we carry out the gel formation analysis only at room temperature ($T = 300$K). We use the model developed in the previous sub-section for simulation HA polymers of length $n = 100$ to test the accuracy of the force field and its ability to reproduce the gel formation properties of HA. Since HA is a very strong anionic polymer, heavy electrostatic repulsion is required to induce the swelling. The swelling properties are also a result of hydrophobic and hydrogen bond interactions and hence it is important to represent water with explicit model. Therefore, 16 HA chains with $n = 100$ were considered in this analysis, along with Martini water model (4 water molecules combined into 1 W bead) and counter NA+ ions for neutralizing. In addition to the neutralizing ions, 100mM ionic salt concentration for Na+ was maintained and the varying $CaCl_2$ concentrations studied were 0mM, 50mM, 100mM and 200mM. This system was solvated in cubic box of size $(37.1\text{nm})^3$with volume fraction of HA set at $\frac{1}{1000}$ which resulted in ~ 419928 Martini water beads.

Equilibration of the system is an important factor when working on the formation of HA gels. After several simulations and minimization and equilibration trails, the following chronology resulted in success. The system was first subjected to energy minimization with minimization step size 0.001ps using Verlet neighbor search using simple grid. This was followed by NPT equilibration step with $dt = 0.01$ps for 100ns using Berendsen thermostat and barostat maintained at 300K and 1.0 bar respectively. After the NPT equilibration, first NVT trajectory run was carried out for 200ps with freezed HA molecules and v-rescale thermostat at 500K (high temperature short duration simulation). The second NVT trajectory run was carried out in a similar way but without freezing the HA molecules. The third and final trajectory run (NVT and used for analysis) was carried out for 1 microsecond at 300K with no constraints on the system. Simulations carried out without proper equilibration steps did not result in swelling.

HA swelling leading to get formation is shown in figure 5.9 (a), (b), (c) and (d) for $CaCl_2$concentrations of 0mM, 50mM, 100mM and 200mM respectively. Gel formation is a phase separation phenomenon and needs a continuum level for visualization. One of the simulation frames looks like the black box of figure 5.9 (a). When the periodicity of the box is enabled, the whole picture of gel formation comes into light. The periodic box having connections in x-, y-, z- directions is an indication of gel formation. This happens rather quickly in the first 100-150ns of simulation after equilibration.

With increasing ionic concentration, the number of crosslinks in HA decreases . This is clearly evident from figure 5.9.

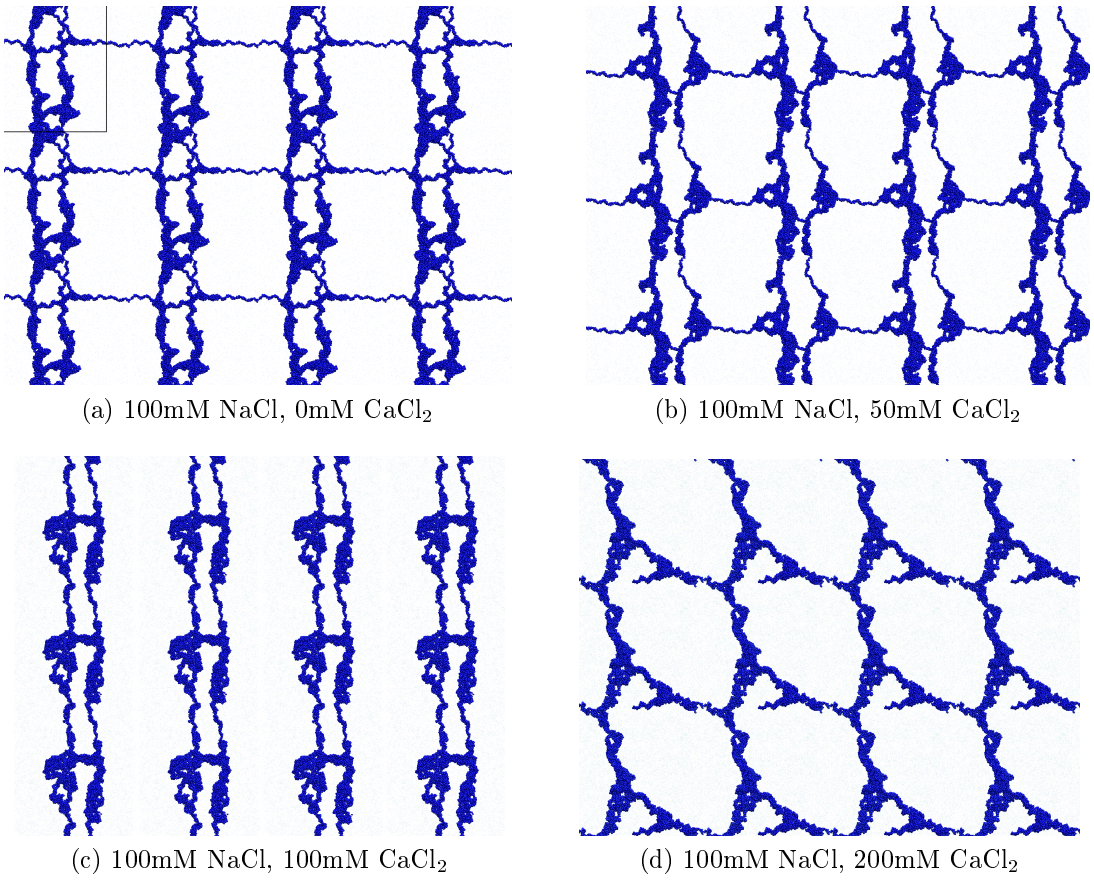

(a) 100mM NaCl, 0mM $CaCl_2$ (b) 100mM NaCl, 50mM $CaCl_2$

(c) 100mM NaCl, 100mM $CaCl_2$ (d) 100mM NaCl, 200mM $CaCl_2$

Figure 5.9: The simulation configuration of HA gel at different NaCl-$CaCl_2$ concentrations.

The osmotic pressure of a solution is the pressure that need to be administered to prevent the passage of water through semi-permeable membrane into a higher concentration solution. Osmotic pressure is the property of the solution that is dependent on the dissociation number of solute molecules. Hence, for a certain mass of solute, greater the dissociated molecule/ion size means lower is the resultant osmotic pressure. Dry hydrogels do not have osmotic pressure as they are not dissolved in a solution. On the other hand, dry hydrogel particles can be made wet and expand significantly when contacting with sufficient moisture or water.

It was explained by Horkay et al. [6] that there is a relation between the osmotic pressure of the gel and the energy stored in the volume of the gel network as follows

$$\Pi = \frac{k_B T}{l^3} \tag{5.1}$$

where l is the length of the network. Increasing ionic concentration leads to decrease in osmotic pressure resulting in increasing network length. Horkay et al. (eq. 12 of [6]) proved that the osmotic pressure relates to the concentrations of the polymer and the

solutes as

$$\Pi = \frac{1.4 \times 10^3 c^{\frac{9}{4}}}{J^{\frac{3}{4}}} \text{kPa} \tag{5.2}$$

where c is the the concentration of the polymer (which is constant in all our cases) and J is the ionic strength that scales as

$$J = \frac{1}{2}(\sum Z_i^2 \mathrm{k}_i) \tag{5.3}$$

where $\mathrm{k}_i$is the molar concentration of ions with charge Z_i. Therefore we have the following proportionality

$$\Pi \propto \frac{1}{l^3} \propto \frac{1}{J^{\frac{3}{4}}} \propto \frac{1}{\mathrm{k}^{\frac{3}{4}}} \tag{5.4}$$

The theoretical scaling of the network length l and ion concentration k is also matched well by the gels from the simulation which is is evident from figure 5.10 that presents the network area l^2 as a function of $CaCl_2$ concentration k and it scales as

$$l^2 \propto \mathrm{k}^{\frac{1}{2}} \tag{5.5}$$

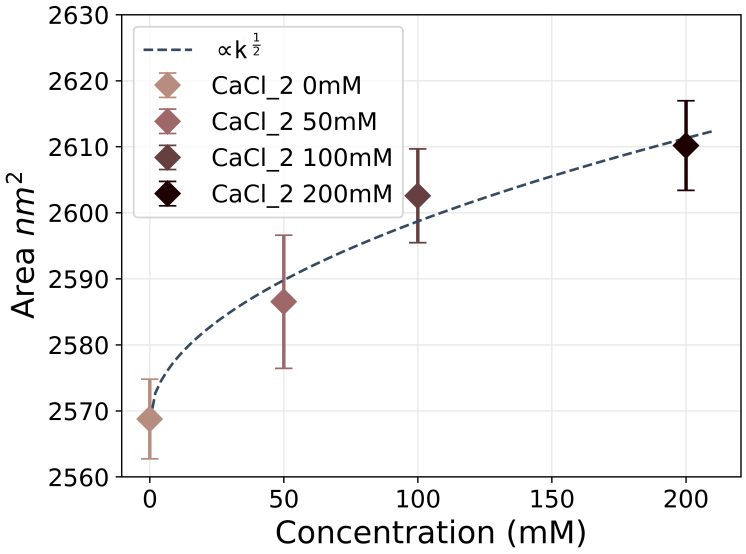

Figure 5.10: Area of HA gel with 100mM NaCl vs varying $CaCl_2$concentrations.

The area of the network is computed using Gromacs command `gmx sasa` which calculates solvent accessible surface area.

5.4 Alginate

In this section we create a Martini CG force field for alginate tetrasaccharide followed by alginate octasaccharide. Instead of starting with a disaccharide, as we did for HA, we would begin with a tetrasaccharide. This is because in AG all the beads are chemically same, we can treat the terminal units of the tetrasaccharide separately and generalize the middle two units for the rest of the polymer. This way we have the possibility of reaching faster convergence and reducing the iteration steps.

5.4.1 CG Mapping of AG tetrasaccharide

Similar to HA the AG is also mapped based on the Martini model for carbohydrates as explained in section 2.9. Each monosaccharide unit of is divided into 3 CG beads, thereby representing the tetrasaccharide in a total of 12 beads as shown in figure 5.11. Figure 5.11 (a) represents the atomistic scheme of the AG tetrasaccharide, 5.11 (b) shows the CG mapping and 5.11 (c) is the AG tetrasaccharide CG model. The bead types used for the tetrasaccharide are again polar (P) beads and charged (Qa) beads and the type of bead used for each units is listed in 5.11(d). Each monosaccharide of alginate (figure 5.11(b) beads 1, 6, 7 and 12) contains a carboxyl group and is represented by bead Qa. The beads containing 2 hydroxyl groups (beads 3, 4, 9 and 10) are represented by highest polarity beads P4 and the central beads (2, 5, 8 and 11) by polar beads of type P2.

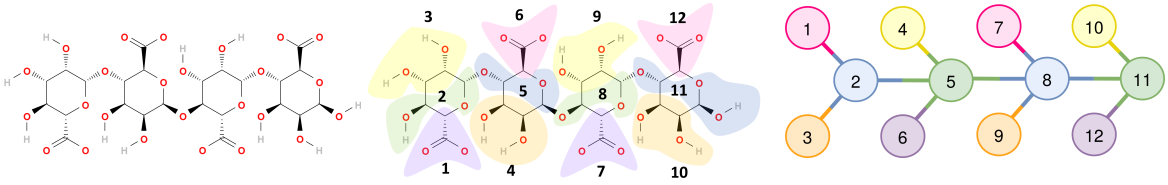

(a) (b) (c)

Bead name	Bead type	Charge
1	Qa	-1.0
2	P2	0.0
3	P4	0.0
4	P4	0.0
5	P2	0.0
6	Qa	-1.0

(d)

Figure 5.11: (a) Atomistic schematic of Alginate tetrasaccharide. (b) Martini CG mapping of the tetrasaccharide and (c) its CG model.

The non bonded parameters are same as in HA, the σ and ε values of LJ potential for the Martini beads are unchanged and the bonded parameters again include bond length, angles and dihedrals and are given by 2.7, 2.9 and 2.11 respectively. The initial values for the equilibration lengths and angles and their respective force constants are obtained from the AA trajectory. These values were iterated multiple times to reach as good of a match as possible between the AA and CG models. The bond length comparison for AA and AA models of alginate tetrasaccharide are shown in figure 5.12.

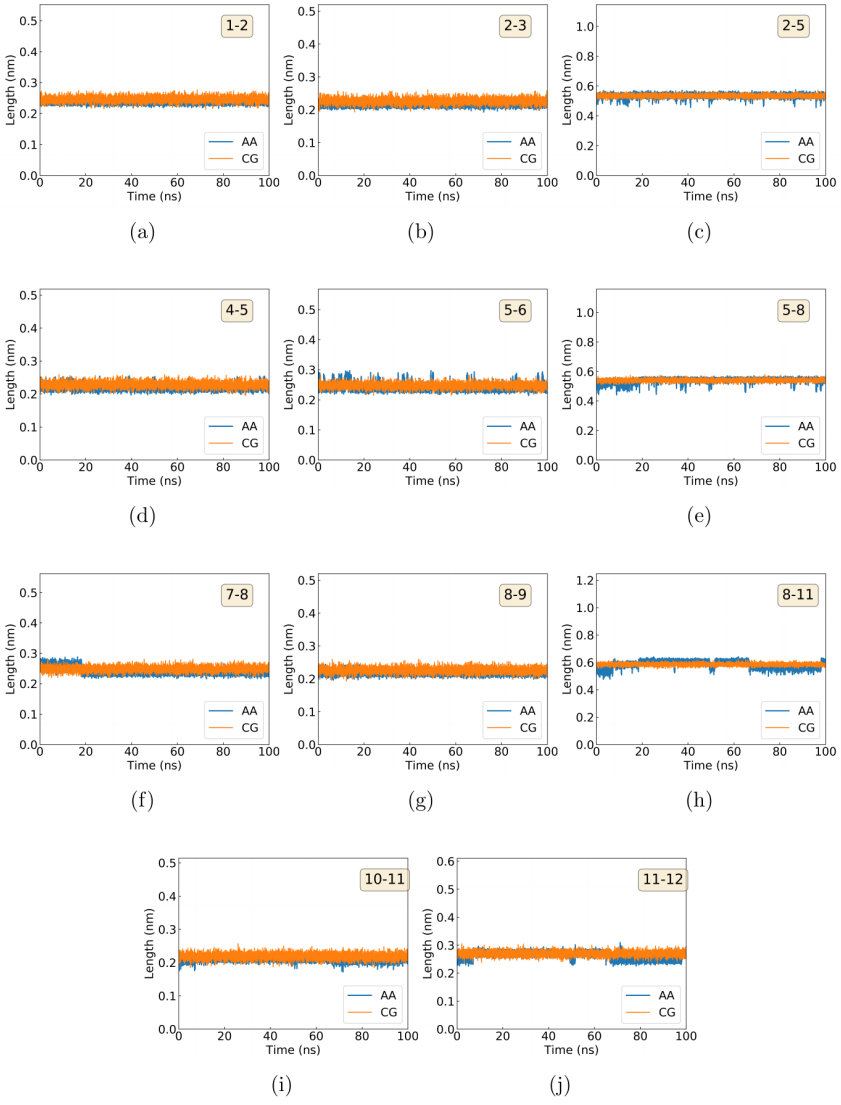

Figure 5.12: Bond lengths of all-atom (AA) and martini coarse-grained (CG) model for alginate tetrasaccharide.

The equilibration bond lengths for the CG beads and their respective force constants

for AG tetrasaccharide are listed in appendix 5.6 table 5.7. We find a good match between the CG and AA models for all the bond lengths. With this established we move forward to take a look at the angle and dihedral angle distribution in figure 5.13 and 5.14 respectively. The equilibration angle and the angle force constant used to create the CG model are listed in appendix 5.6 table 5.8 and 5.9 respectively. Compared to the bonded lengths, larger fluctuations are observed for angle and dihedral distributions but still offer a good match to the AA simulations.

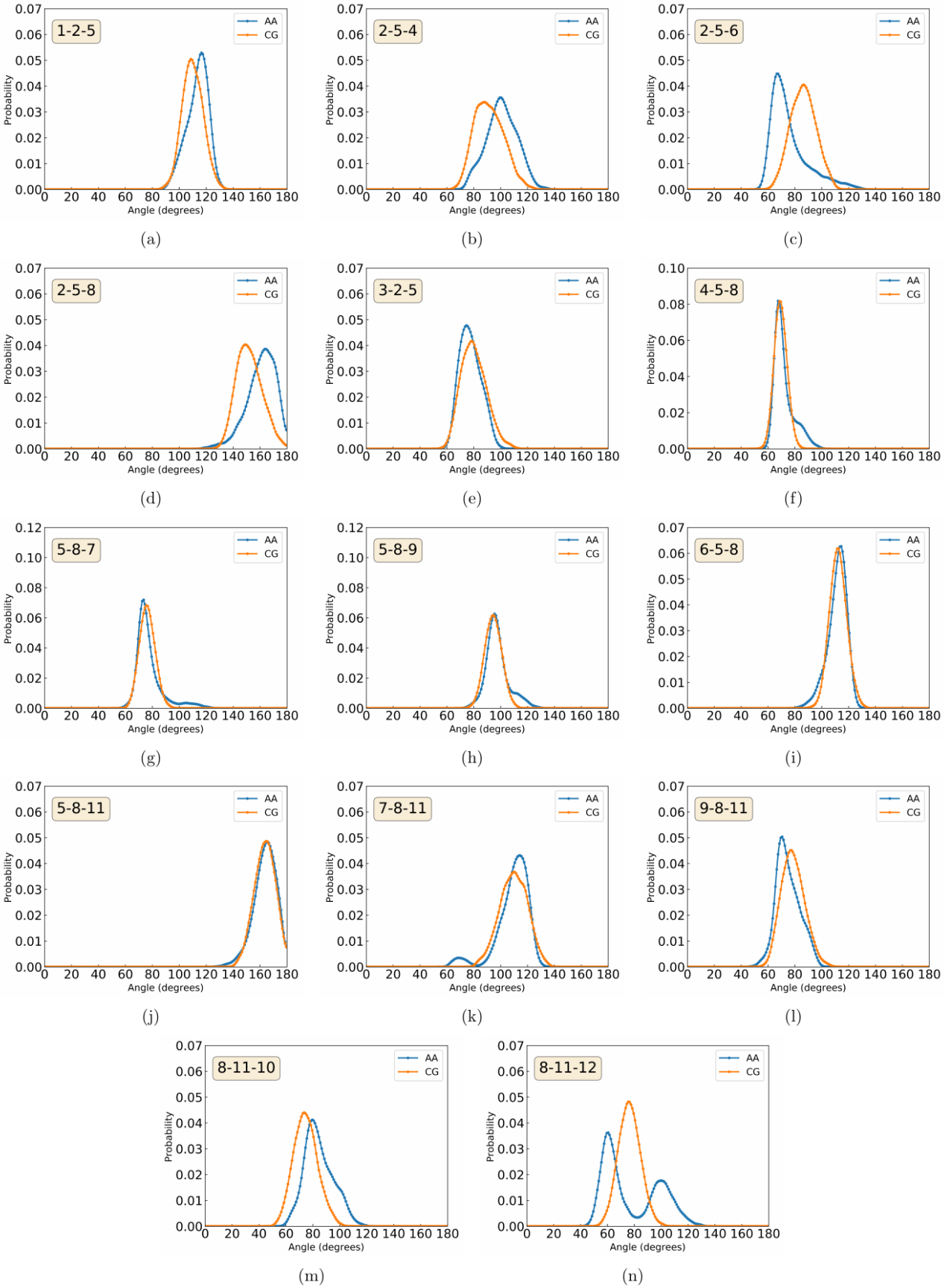

Figure 5.13: Angle distributions of all-atom (AA) and martini coarse-grained (CG) model for alginate tetrasaccharide.

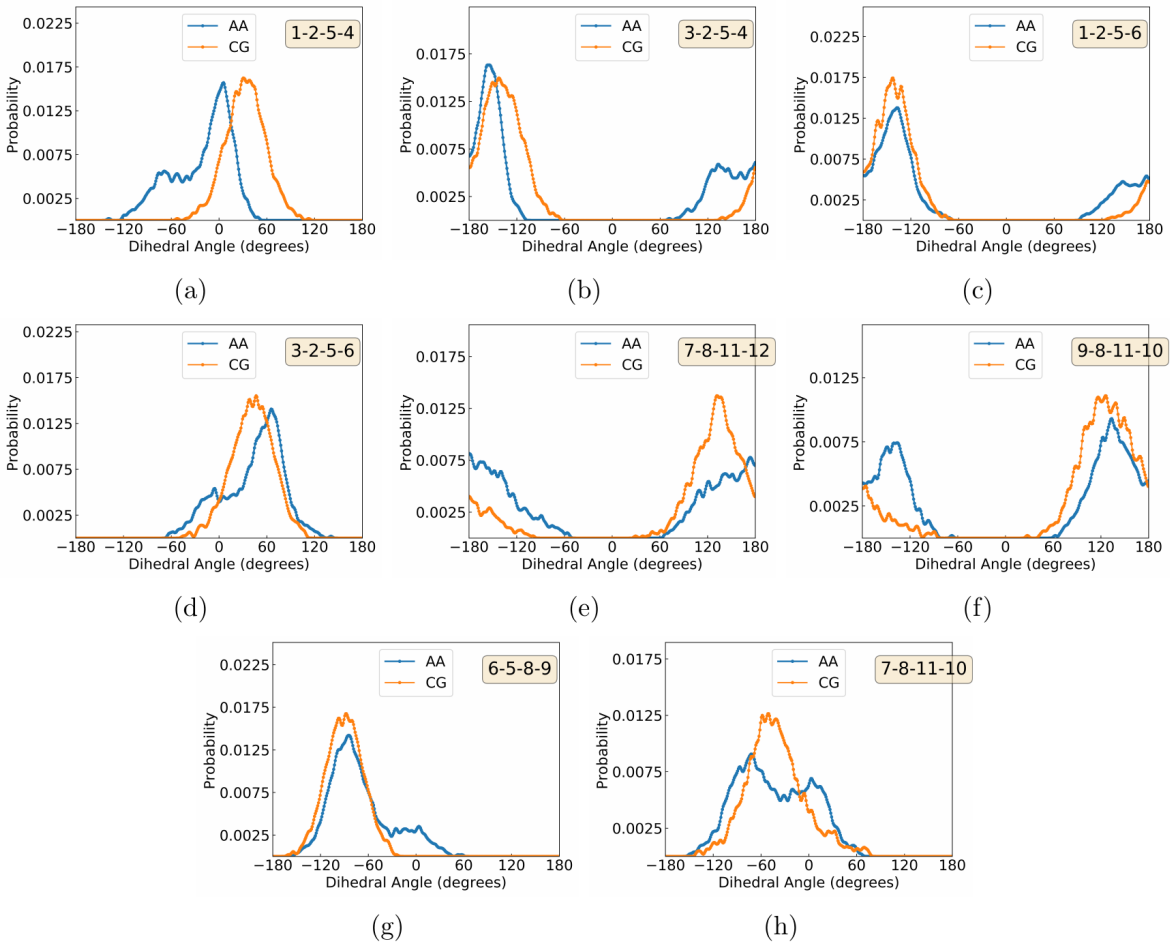

Figure 5.14: Dihedral angle distributions of all-atom (AA) and martini coarse-grained (CG) model for alginate tetrasaccharide.

5.4.2 CG Mapping of AG octasaccharide

To create an AG octasaccharide, in this section we would take two tetrasaccharide units and connect them together with bond length, angle and dihedral potentials. These additional bonded parameters are then compared to the AA model. Atomistic schematic for an alginate octasaccharide is shown in figure 5.15(a), its CG mapping is shown in figure 5.15(b) and the CG model, that's created by combining two AG tetrasaccharides is shown in 5.15(c). Unlike HA where we assembled four disaccharides together, here we treated the terminal beads separately and multiplied the central 2 beads three times to create the octasaccharide as illustrated in 5.15(c).

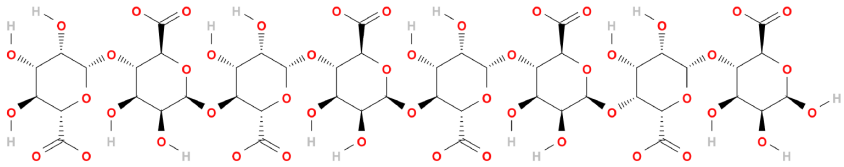

(a)

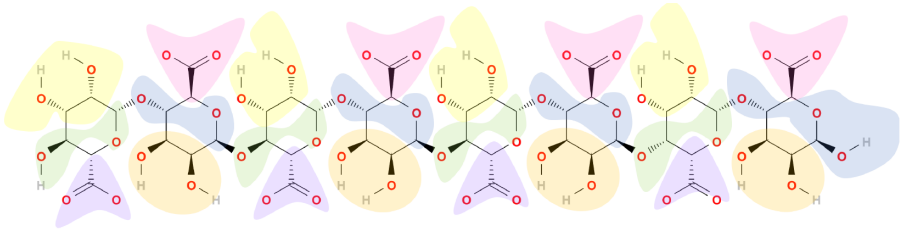

(b)

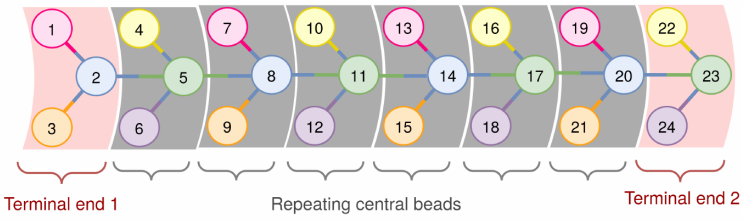

(c)

Figure 5.15: (a) Atomistic representation of alginate octasaccharide. (b) Alginate CG mapping. (c) Alginate octasaccharide CG model.

The angle and dihedral distribution comparison between the atomistic and the coarse grained models for alginate octasaccharide are shown in figure 5.16 and 5.17 respectively.

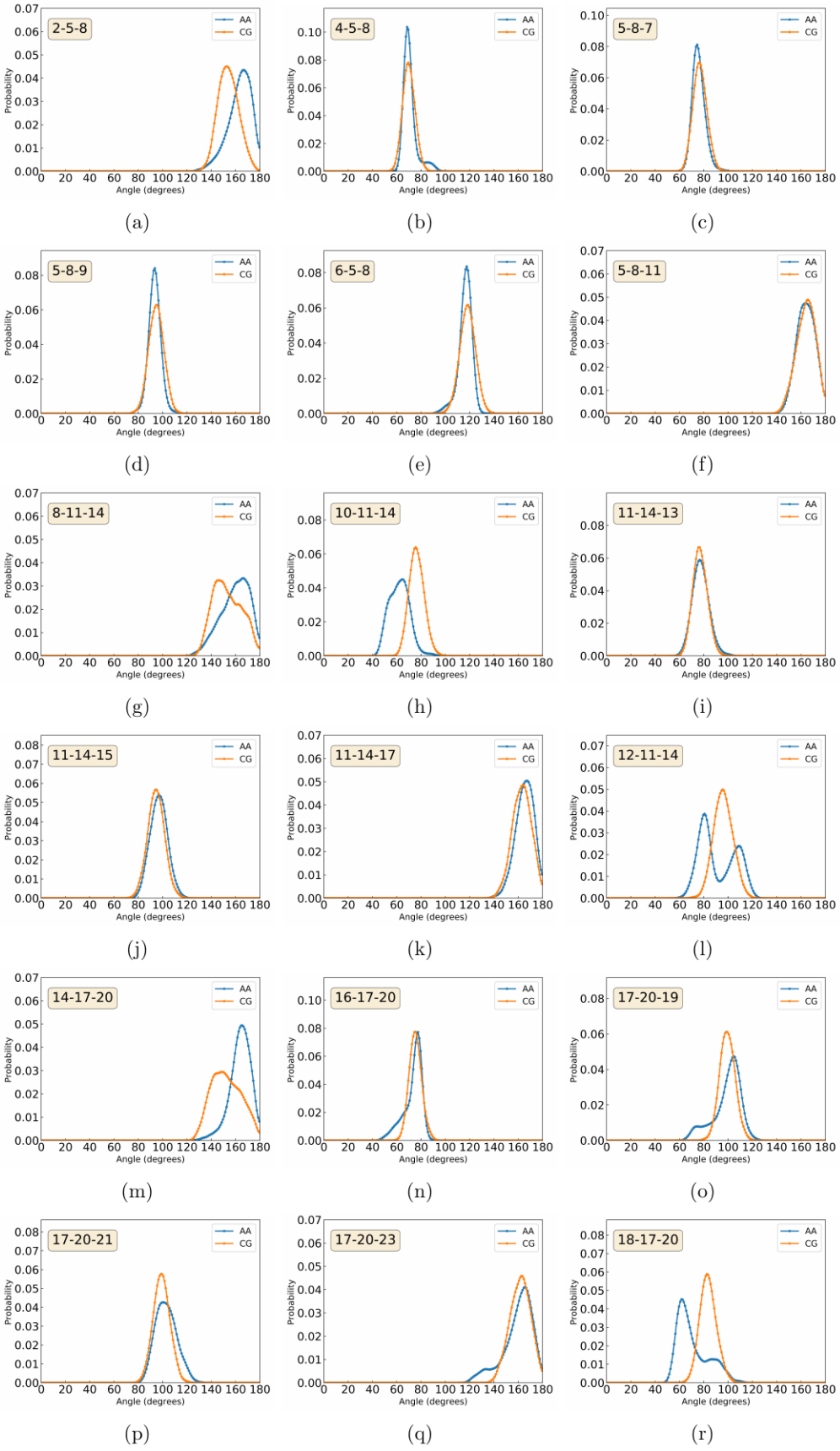

Figure 5.16: Angle distributions of all-atom (AA) and martini coarse-grained (CG) model for alginate octasaccharide.

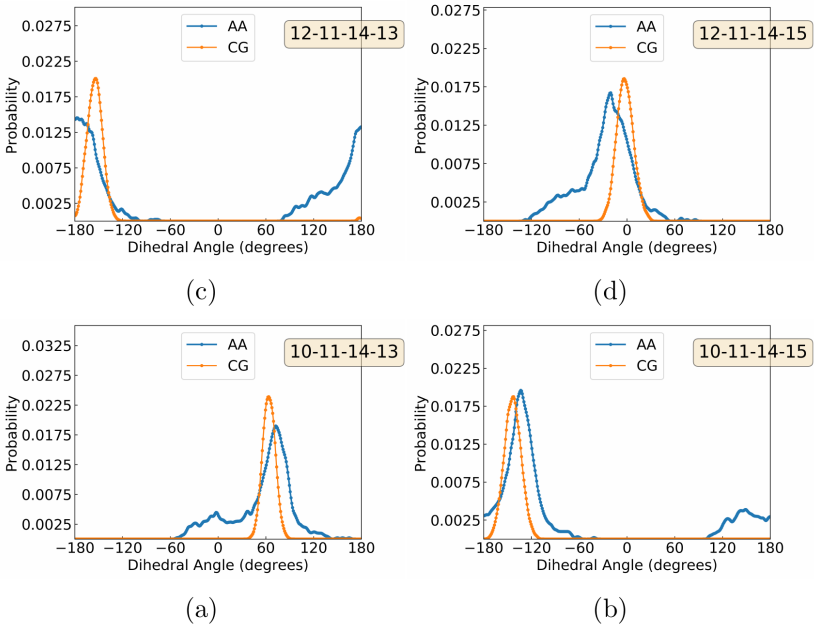

Figure 5.17: Angle distributions of all-atom (AA) and martini coarse-grained (CG) model for alginate octasaccharide.

For validation of the model, the global properties $R_{\text{end to end}}$, R_g and $RMSD$ are presented in figure 5.18. Both AA and CG models show very good agreement with each other.

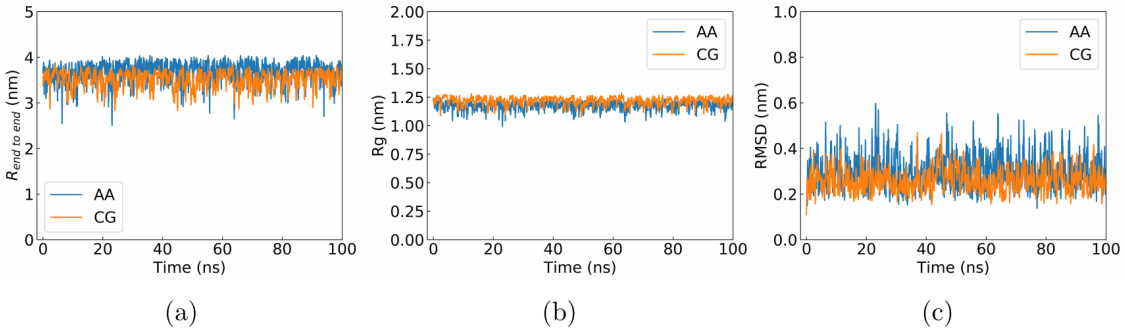

Figure 5.18: (a) End to end distance ($R_{\text{end to end}}$), (b) radius of gyration (R_g) and (c) Root mean squared deviation ($RMSD$) for AA and CG models of alginate octasaccharide.

5.4.3 Alginate Aggregation

Alginate is reported to show bundle formation and zipper mechanism in previous study [5]. To form further validation of the model, we simulate 6 alginate polymers with 30

monomers each in a water solution neutralized with Na+ and Cl- ions for 100ns. The snapshots of the simulation is shown in figure 5.19.

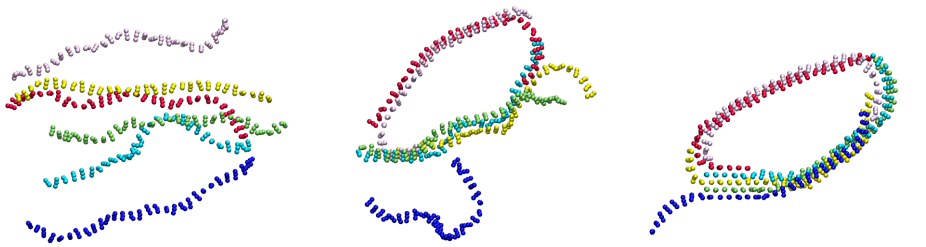

(a) $t = 0$ns (b) $t = 1.4$ns (c) $t = 8$ns

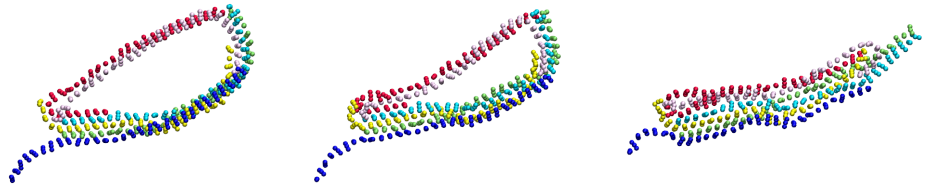

(d) $t = 24$ns (e) $t = 25$ns (f) $t = 30$ns

Figure 5.19: Snapshots of bundle formation and zipper mechanism from martini coarse grained alginate simulations.

While it is clear from figure 5.19 that our alginate model is forming planar bundle at the end of 30ns of simulation, it also shows the zipper mechanism observed by Hecht et al [5]. At $t = 24$ns the ring of polymers connects at one end, $t = 25$ns $\frac{1}{6}$th of the chains pink and red chains zip up with the cyan chain and at $t = 30$ns, this zipping up process comes to a completion leading to parallely attached planar looking structure, which depicts that our CG model not only well matches with the atomistic model but also recreates the macroscopic properties observed previously.

5.4.4 Alginate Gel

Following similar procedure as that in section 5.3.3, an attempt was made here to create gels of alginate polymer solvated in water with 100mM NaCl ions and varying $CaCl_2$ concentrations. In figure 5.20 (a) snapshot view of alginate gel with 100mM NaCl and 100mM $CaCl_2$ is presented along the x-, y-plane. As mentioned before, gel formation is a phase separation phenomenon. This is clearly seen from figure 5.20 (b) where the view (of the black box in (a)) is shown along the y-, z-plane of the polymer (in red) and the water (in blue). The screening effect of the ions can be visualized by taking a look at figure 5.20 (c), which is the view along x-, y-plane of the polymer (in red) and the ions (in green). In figure 5.21 (a) we show show alginate gel formation with 100mM NaCl and 0mM $CaCl_2$ ions. For comparison to the published experimental results, we present in figure 5.21 (b) the TEM images of alginate gel taken by Schuster et al [11].

The solution for TEM images of alginate gels in [11] was prepared by adding alginate powder to deionised water and vigorous stirring. It was thereafter heated upto 353K in a water bath and the pH was adjusted between 7- 7.3 using 0.1M HCl. Alginate gels were prepared by controlled release of calcium. $CaCO_3$ and Glucono-δ-lactone (GDL) were rapidly dispersed in water and immediately added to the alginate solution to yield a final alginate concentration of 1.8% or 2% w/w, respectively. The moulds were sealed and the samples were allowed to equilibrate and set at room temperature for 48 h prior to use. Since the conditions and ingredients for experimental alginate gel preparation differ quite a lot with the simulations, the gel properties might differ quantitatively. Further work is required for a detailed investigation in this field of area. Using the model developed in this chapter, this step would be of lot of convenience for the future work.

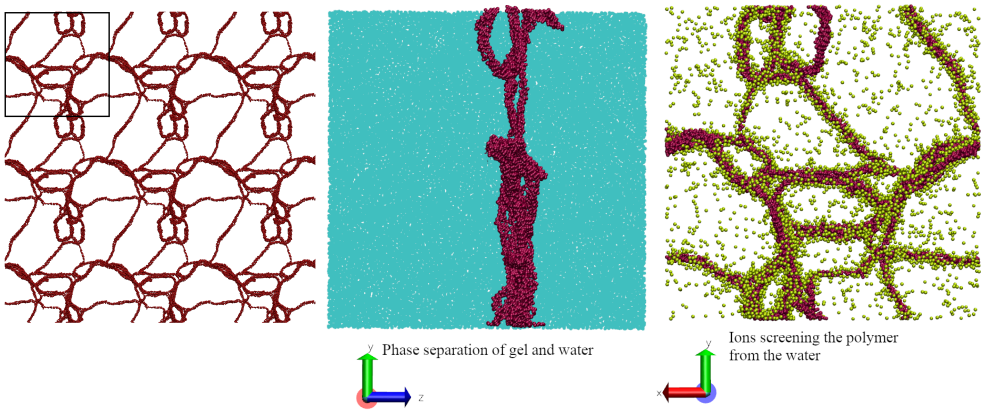

(a) (b) (c)

Figure 5.20: Simulation snapshot of the (a) the complete polymer gel with 100mM NaCl and 100mM $CaCl_2$ concentrations. The black box of (a) is emphasized in (b) and (c) that exhibit views along y-z-plane showing phase separation and x-y plane showing ion screening respectively. The polymer is shown in red, the ions in green and the water in blue.

Thus the martini CG alginate model develop in this section shows the gel formation ability of the of alginate polymer CG model. Large scale simulations of the polymeric gel can be carried out in the future for detailed analysis of its microscopic structures using the developed alginate Martini CG model.

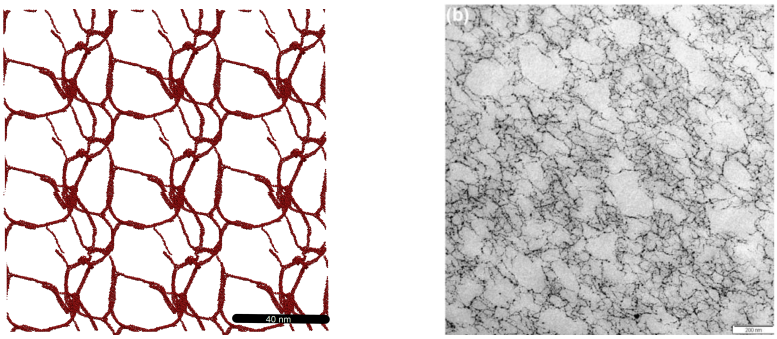

(a) (b)

Figure 5.21: (a) Alginate gel snapshot for system with 100mM NaCl and 0mM $CaCl_2$ ions. (b) Experimental TEM image of alginate gel produced by and taken from the work of Schuster et al [11].

5.5 Conclusion

Completely validated CG models for hyaluronic acid and alginate polymers are developed using the Martini scheme. The performance of the CG force field was compared to their counter atomistic parts. The hyaluronic acid and alginate martini CG model were accurately able to reproduce the bonded parameters namely, bonds, angles and dihedrals of the all-atomistic models. The obtained parameters from the top down approach of Martini coarse graining was applied to polymers of longer lengths to study their macroscopic properties. In addition to the very good agreement of the global properties like $R_{\text{end to end}}$, $RMSD$, R_g we were able to produce HA networking from the model developed in this chapter. This chapter displays very good HA gels, which are usually very demanding and troublesome in atomistic simulations due to large time and length scales. We observe an increase in the swelling of the HA gel with increasing ionic concentrations as previously reported by the experimentalists. Additionally, throughout the range of different concentrations, very stable HA gels are reported for 1 microsecond each. Similarly, the global properties of alginate were also in accordance to its atomistic counterparts. The parallel stacking of alginate polymers, as previously documented, is reproduced by this model. Thus in addition to developing the CG force fields of two important polymers used in biofabrication, this chapter establishes the technique in detail to create long CG polymers from a short atomistic strand of the relevant polymer.

5.6 Appendix of Chapter 3

5.6.1 CG model bonded-parameters for HA disaccharide

Beads	Gromacs func.	$b_0$for HA1-3	K_b for HA1-3	b_0 for HA1-4	K_b for HA1-4
1-2	1	0.268	30000.0	0.362	30000.0
2-3	1	0.224	30000.0	0.285	30000.0
2-5	1	0.504	30000.0	0.612	30000.0
4-5	1	0.357	30000.0	0.266	30000.0
5-6	1	0.263	30000.0	0.224	30000.0

Table 5.1: Equilibration bond length b_o (nm) and force constant K_b $\left(\frac{\text{kJ}}{\text{mol nm}^2}\right)$ used for HA1-3 and HA1-4 disaccharide CG force field.

Beads	Gromacs func.	$\theta_0$for HA1-3	K_θ for HA1-3	θ_0 for HA1-4	$K_\theta$for HA1-4
1-2-5	2	115.0	300.0	67.0	210.0
3-2-5	2	117.0	600.0	85.0	110.0
2-5-4	2	57.0	75.0	40.0	100.0
2-5-6	2	115.0	200.0	70.0	130.0

Table 5.2: Equilibration angle θ_0 (degrees) and force constant K_θ $\left(\frac{\text{kJ}}{\text{mol rad}^2}\right)$ used for HA1-3 and HA1-4 disaccharide CG force field.

Beads	Gromacs func.	ϕ_0 for HA1-3	K_ϕ for HA1-3	$\phi_0$for HA1-4	$K_\phi$for HA1-4
1-2-5	1	150.0	14.0	60.0	20.0
3-2-5	1	-170.0	15.0	65.0	10.0
2-5-4	1	-60.0	15.0	-180.0	8.0
2-5-6	1	150.0	8.0	-155.0	12.0

Table 5.3: Equilibration dihedral angle ϕ_0(degrees) and force constant K_ϕ $\left(\frac{\text{kJ}}{\text{mol rad}^2}\right)$ used for HA1-3 and HA1-4 disaccharide CG force field. Multiplicity was kept $m = 1$ for all the proper dihedrals.

5.6.2 CG model bonded-parameters for HA octasaccharide

Beads	Gromacs func.	b_0(nm)	$K_b \left(\frac{\text{kJ}}{\text{mol nm}^2}\right)$
1-2	1	0.264	30000.0
2-3	1	0.227	30000.0
2-5	1	0.619	30000.0
4-5	1	0.364	30000.0
5-6	1	0.29	30000.0
5-8	1	0.483	30000.0
7-8	1	0.229	30000.0
8-9	1	0.234	30000.0
8-11	1	0.549	30000.0
10-11	1	0.364	30000.0
11-12	1	0.286	30000.0
11-14	1	0.484	30000.0
13-14	1	0.229	30000.0
14-15	1	0.234	30000.0
14-17	1	0.55	30000.0
16-17	1	0.363	30000.0
17-18	1	0.286	30000.0
17-20	1	0.483	30000.0
19-20	1	0.229	30000.0
20-21	1	0.234	30000.0
20-23	1	0.551	30000.0
22-23	1	0.367	30000.0
23-24	1	0.287	30000.0

Table 5.4: Equilibration bond length b_o and force constant K_b used for HA octasaccharide CG force field.

Beads	Gromacs func.	θ_0(degrees)	$K_\theta \left(\frac{\text{kJ}}{\text{mol rad}^2}\right)$
1-2-5	2	50.0	60.0
3-2-5	2	70.0	100.0
2-5-4	2	70.0	200.0
2-5-6	2	80.0	120.0
4-5-8	2	85.0	200.0
6-5-8	2	140.0	120.0
5-8-7	2	92.0	600.0
5-8-9	2	80.0	800.0
7-8-11	2	70.0	20.0
9-8-11	2	92.0	170.0
8-11-10	2	65.0	150.0
8-11-12	2	88.0	170.0
10-11-14	2	90.0	180.0
12-11-14	2	135.0	110.0
11-14-13	2	90.0	500.0
11-14-15	2	92.0	800.0
13-14-17	2	62.0	20.0
15-14-17	2	97.0	120.0
14-17-16	2	70.0	200.0
14-17-18	2	88.0	170.0
16-17-20	2	88.0	230.0
18-17-20	2	137.0	120.0
17-20-19	2	92.0	500.0
17-20-21	2	90.0	80.0
19-20-23	2	73.0	20.0
21-20-23	2	95.0	200.0
20-23-22	2	55.0	100.0
20-23-24	2	89.0	220.0
2-5-8	2	145.0	50.0
5-8-11	2	180.0	700.0
8-11-14	2	150.0	50.0
11-14-17	2	180.0	650.0
14-17-20	2	153.0	50.0
17-20-23	2	165.0	550.0

Table 5.5: Equilibration angle θ_0 and force constant K_θ used for HA octasaccharide CG force field.

Beads	Gromacs func.	ϕ_0(degrees) for HA1-3	$K_\phi \left(\frac{\text{kJ}}{\text{mol rad}^2}\right)$ for HA1-3
1-2-5-4	1	-100.0	4.0
1-2-5-6	1	60.0	8.0
3-2-5-4	1	65.0	6.0
3-2-5-6	1	-160.0	9.0
4-5-8-7	1	120.0	12.0
4-5-8-9	1	-180.0	8.0
6-5-8-7	1	-180.0	10.0
6-5-8-9	1	65.0	10.0
7-8-11-10	1	-125.0	10.0
7-8-11-12	1	60.0	12.0
9-8-11-10	1	55.0	13.0
9-8-11-12	1	-160.0	10.0
10-11-14-13	1	150.0	14.0
10-11-14-15	1	-180.0	12.0
12-11-14-13	1	-180.0	11.0
12-11-14-15	1	60.0	10.0
13-14-17-16	1	-120.0	10.0
13-14-17-18	1	60.0	10.0
15-14-17-16	1	65.0	10.0
15-14-17-18	1	-180.0	10.0
16-17-20-19	1	110.0	14.0
16-17-20-21	1	-180.0	6.0
18-17-20-19	1	-160.0	10.0
18-17-20-21	1	50.0	9.0
19-20-23-22	1	-130.0	14.0
19-20-23-24	1	62.0	12.0
21-20-23-22	1	62.0	13.0
21-20-23-24	1	-170.0	14.0

Table 5.6: Equilibration dihedral angle ϕ_0 and force constant K_ϕ used for HA octasaccharide CG force field. Multiplicity was kept $m = 1$ for all the proper dihedrals.

5.6.3 CG model bonded-parameters for AG tetrasaccharide

Beads	Gromacs func.	b_0(nm)	$K_b \left(\frac{\text{kJ}}{\text{mol nm}^2}\right)$
1-2	1	0.237	30000.0
2-3	1	0.215	30000.0
2-5	1	0.534	30000.0
4-5	1	0.221	30000.0
5-6	1	0.242	30000.0
5-8	1	0.538	30000.0
7-8	1	0.241	30000.0
8-9	1	0.217	30000.0
8-11	1	0.587	30000.0
10-11	1	0.209	30000.0
11-12	1	0.262	30000.0

Table 5.7: Comparison of equilibration bond length b_0 for AA and CG model of Alginate tetrasaccharide.

Beads	Gromacs func.	CG: θ_0(degrees)	CG: $K_\theta \frac{\text{kJ}}{\text{mol rad}^2}$
1-2-5	2	115.0	150.0
3-2-5	2	79.0	11.0
2-5-4	2	98.0	12.0
2-5-6	2	32.0	13.0
7-8-11	2	98.0	19.0
9-8-11	2	70.0	65.0
8-11-10	2	65.0	60.0
8-11-12	2	50.0	60.0
4-5-8	2	62.0	240.0
6-5-8	2	112.0	220.0
5-8-7	2	70.0	200.0
5-8-9	2	92.0	170.0
2-5-8	2	178.0	200.0
5-8-11	2	173.0	500.0

Table 5.8: Equilibration angles θ_0 for AA and CG simulations and force constant K_θ for CG model of Alginate tetrasaccharide.

Beads	Gromacs func.	CG: ϕ_0(degrees)	CG: $K_\phi \frac{\text{kJ}}{\text{mol rad}^2}$
1-2-5-4	1	160.0	4.0
1-2-5-6	1	30.0	6.0
3-2-5-4	1	17.0	4.0
3-2-5-6	1	-110.0	5.0
7-8-11-10	1	109.0	5.0
7-8-11-12	1	0.0	3.0
9-8-11-10	1	-60.0	1.0
9-8-11-12	1	-120.0	2.0
4-5-8-7	1	150.0	10.0
6-5-8-9	1	92.0	3.0
4-5-8-9	1	-50.0	3.0
6-5-8-7	1	-55.0	3.0

Table 5.9: Equilibration dihedral angles ϕ_0 for AA and CG simulations and force constant K_ϕ for CG model of Alginate tetrasaccharide.

5.6.4 CG model bonded-parameters for AG octasaccharide

Beads	Gromacs func.	b_0(nm)	$K_b \left(\frac{\text{kJ}}{\text{mol nm}^2}\right)$
1-2	1	0.2377	30000.0
2-3	1	0.2151	30000.0
2-5	1	0.5347	30000.0
4-5	1	0.2203	30000.0
5-6	1	0.2418	30000.0
5-8	1	0.5387	30000.0
7-8	1	0.2412	30000.0
8-9	1	0.2171	30000.0
8-11	1	0.5872	30000.0
10-11	1	0.2203	30000.0
11-12	1	0.2418	30000.0
11-14	1	0.5387	30000.0
13-14	1	0.2412	30000.0
14-15	1	0.2171	30000.0
14-17	1	0.5872	30000.0
16-17	1	0.2203	30000.0
17-18	1	0.2418	30000.0
17-20	1	0.5387	30000.0
19-20	1	0.2412	30000.0
20-21	1	0.2171	30000.0
20-23	1	0.5872	30000.0
22-23	1	0.2088	30000.0
23-24	1	0.2618	30000.0

Table 5.10: Equilibration bond length b_o and force constant K_b used for AG octasaccharide CG force field.

Beads	Gromacs func.	θ_0(degrees)	$K_\theta \left(\frac{\text{kJ}}{\text{mol rad}^2}\right)$
1-2-5	2	115.0	150.0
3-2-5	2	79.0	11.0
2-5-4	2	98.0	12.0
2-5-6	2	32.0	13.0
4-5-8	2	62.0	210.0
6-5-8	2	120.0	21.0
5-8-7	2	70.0	210.0
5-8-9	2	92.0	190.0
7-8-11	2	98.0	19.0
9-8-11	2	70.0	65.0
8-11-10	2	65.0	60.0
8-11-12	2	50.0	60.0
10-11-14	2	50.0	120.0
12-11-14	2	80.0	110.0
11-14-13	2	70.0	17.0
11-14-15	2	92.0	150.0
13-14-17	2	98.0	19.0
15-14-17	2	70.0	65.0
14-17-16	2	65.0	60.0
14-17-18	2	50.0	60.0
16-17-20	2	62.0	240.0
18-17-20	2	40.0	110.0
17-20-19	2	105.0	170.0
17-20-21	2	110.0	130.0
19-20-23	2	98.0	19.0
21-20-23	2	70.0	65.0
20-23-22	2	65.0	60.0
20-23-24	2	50.0	60.0
2-5-8	2	180.0	280.0
5-8-11	2	173.0	500.0
8-11-14	2	180.0	280.0
11-14-17	2	173.0	500.0
14-17-20	2	180.0	280.0
17-20-23	2	173.0	400.0

Table 5.11: Equilibration angle θ_0 and force constant K_θ used for AG octasaccharide CG force field.

Beads	Gromacs func.	ϕ_0(degrees) for HA1-3	$K_\phi \left(\frac{\text{kJ}}{\text{mol rad}^2}\right)$ for HA1-3
1-2-5-4	1	-178.0	10.0
1-2-5-6	1	40.0	3.0
3-2-5-4	1	35.0	3.0
3-2-5-6	1	-95.0	10.0
4-5-8-7	1	150.0	3.0
4-5-8-9	1	95.0	3.0
6-5-8-7	1	-50.0	3.0
6-5-8-9	1	-55.0	3.0
7-8-11-10	1	-15.0	10.0
7-8-11-12	1	-45.0	1.0
9-8-11-10	1	-120.0	3.0
9-8-11-12	1	120.0	10.0
10-11-14-13	1	-110.0	5.0
10-11-14-15	1	70.0	5.0
12-11-14-13	1	-20.0	2.0
12-11-14-15	1	140.0	5.0
13-14-17-16	1	120.0	10.0
13-14-17-18	1	-15.0	10.0
15-14-17-16	1	-45.0	3.0
15-14-17-18	1	-120.0	10.0
16-17-20-19	1	150.0	3.0
16-17-20-21	1	92.0	3.0
18-17-20-19	1	-50.0	3.0
18-17-20-21	1	-55.0	3.0
19-20-23-22	1	109.0	3.0
19-20-23-24	1	40.0	3.0
21-20-23-22	1	-45.0	3.0
21-20-23-24	1	-120.0	10.0

Table 5.12: Equilibration dihedral angle ϕ_0 and force constant K_ϕ used for AG octasaccharide CG force field. Multiplicity was kept $m = 1$ for all the proper dihedrals.

References

[1] Andrew Almond, Paul L DeAngelis, and Charles D Blundell. Hyaluronan: the local solution conformation determined by nmr and computer modeling is close to a contracted left-handed 4-fold helix. *Journal of molecular biology*, 358(5):1256–1269, 2006.

[2] Cristina Antich, Juan de Vicente, Gema Jiménez, Carlos Chocarro, Esmeralda Carrillo, Elvira Montañez, Patricia Gálvez-Martín, and Juan Antonio Marchal. Bio-inspired hydrogel composed of hyaluronic acid and alginate as a potential bioink for 3d bioprinting of articular cartilage engineering constructs. *Acta biomaterialia*, 106:114–123, 2020.

[3] Eneko Axpe and Michelle L Oyen. Applications of alginate-based bioinks in 3d bioprinting. *International journal of molecular sciences*, 17(12):1976, 2016.

[4] Peter Gacesa. Alginates. *Carbohydrate polymers*, 8(3):161–182, 1988.

[5] Hadas Hecht and Simcha Srebnik. Structural characterization of sodium alginate and calcium alginate. *Biomacromolecules*, 17(6):2160–2167, 2016.

[6] Ferenc Horkay, Peter J Basser, David J Londono, Anne-Marie Hecht, and Erik Geissler. Ions in hyaluronic acid solutions. *The Journal of chemical physics*, 131(18):184902, 2009.

[7] Jia Jia, Dylan J Richards, Samuel Pollard, Yu Tan, Joshua Rodriguez, Richard P Visconti, Thomas C Trusk, Michael J Yost, Hai Yao, Roger R Markwald, et al. Engineering alginate as bioink for bioprinting. *Acta biomaterialia*, 10(10):4323–4331, 2014.

[8] Torvard C Laurent and J Robert E Fraser. Hyaluronan 1. *The FASEB journal*, 6(7):2397–2404, 1992.

[9] W Lindsey Zemke-White and Masao Ohno. World seaweed utilisation: an end-of-century summary. *Journal of applied Phycology*, 11(4):369–376, 1999.

[10] Cesar A Lopez, Andrzej J Rzepiela, Alex H de Vries, Lubbert Dijkhuizen, Philippe H Huenenberger, and Siewert J Marrink. Martini coarse-grained force field: extension to carbohydrates. *Journal of Chemical Theory and Computation*, 5(12):3195–3210, 2009.

[11] Erich Schuster, Johanna Eckardt, Anne-Marie Hermansson, Anette Larsson, Niklas Lorén, Annika Altskär, and Anna Ström. Microstructural, mechanical and mass transport properties of isotropic and capillary alginate gels. *Soft matter*, 10(2):357–366, 2014.

[12] Chirag B Shah and Stanley M Barnett. Swelling behavior of hyaluronic acid gels. *Journal of applied polymer science*, 45(2):293–298, 1992.

[13] Jaakko J Uusitalo, Helgi I Ingolfsson, Parisa Akhshi, D Peter Tieleman, and Siewert J Marrink. Martini coarse-grained force field: extension to dna. *Journal of chemical theory and computation*, 11(8):3932–3945, 2015.

Chapter 6

Monofunctional Vinyl Cyclopropanes:

Effect of hydrogen bonding on their polymerization behavior

Bulk properties of monofunctional vinyl cyclopropane (VCP) derivatives are studied in this chapter using molecular dynamics simulations, to understand the effect of their clustering and hydrogen bonding properties on their polymerization rates obtained via experiments. The VCPs have varying capabilities of forming hydrogen bonds depending on the number of donors and acceptors in their structure. This chapter would deal with two parts. The first part will include studying VCP with different side chains that have varying capability of forming hydrogen bonds. The second part will deal with VCP amides with hydrogen bonding near the active sites. This study mainly focuses on the question, if hydrogen bonds within the VCP unit and the side chain, govern the reorganization of the monomers and offer them higher polymerization rates. It is seen that the VCPs with side chains that capable of forming hydrogen bonds did not show much of difference in their polymerization behavior however, VCPs with hydrogen bonding near the active sites showed fast polymerization rates.

6.1 Introduction

Vinyl cyclopropanes (VCPs) are photopolymerizable resins with a low volume shrinkage during polymerization and high applicability in electrical and medical fields [16, 6, 8, 3, 4, 13]. Owing to the cyclic nature of the VCPs, the volume gained during the ring-opening step compensates the shrinkage during covalent bond formation between the monomers during the polymerization process, leading to low shrinkage, thereby avoiding internal stress caused due to contraction, gap formation or micro-leakage. VCPs are radically polymerizable entities where the cyclopropane ring is directly attached to a double bond and two polymerizable double bonds are linked through different spacer units. In VCP-amides the spacer is attached to the cyclopropane ring with an amide linkage. Despite these advantages, VCPs are less used on commercial level due to their low rates of polymerization and incomplete monomer conversion [12]. Therefore this work aims at increasing the rate of polymerization by using different hydrogen bonding sites that might leads to faster rates due to per-organization of the monomer units. This works aims at the following points: (a) the position and (b) the type of hydrogen bonding (H-bonding) units in the VCPs and its effect on the rate of polymerization. In the first part we study three different H-bonding functional units namely the amide, the urethane and the urea only in the side chain of the monofunctional VCPs, with ester as the linkage between the side chain and the VCPs for the polymerization. In the second part, we study a set of monomers that bear H-bonding sites at two different position in the VCPs: an amide group that links the side chain to the cyclopropane and different organic functional groups (amide, urethane and urea) that are able to form H-bonding to different extents in the side chain in order to compare their behavior. Theoretically, we look at the bulk properties of the VCPs like the root mean squared displacement, time averaged H-bonds in the bulk, orientation parameter, radial distribution function to give an insight to their structural and organizational differences pre-polymerization. Since polymerization involves making and breaking of bonds, it is beyond the scope of molecular dynamics. Therefore, we try to find a connection in the results obtained from the simulation that look into pre-polymerization self organizing of the monomers and the experimental results of the polymerization rates in hopes of enabling a better and speedy prediction on the structural designs of the VCPs for future use.

6.2 Simulation details

All simulations are carried out using molecular dynamics with GROMACS 2018.1 software [1]. The topology and structure parameters of all the VCPs were build using Automated Topology Builder (ATB) [9] which provides GROMACS compatible GROMOS54a7 all atom force-field for molecules that are not known or studied previously. The bonded and non-bonded parameters for the molecules can be accessed at the ATB website by inserting the molID tabulated in the table 6.1 of the appendix 6.5. The bonded length, angle and dihedral interactions are as described by equations

2.7, 2.8 and 2.12 respectively. The non-bonded forces are described by Coulomb and Lennard Jones interaction as described by equation 2.13 and 2.14 respectively with short-range electrostatic and van der Waals cutoff set to 1nm. Cubic boxes of initial dimensions $7 \times 7 \times 7\text{nm}^3$ were individually filled by monomers of each type. The simulation box was subjected to energy minimization, followed by NPT simulations of 125ns and the last 115ns were used for analysis (see figure 6.13 of appendix 6.5 for equilibration of the simulation runs). After NPT simulations the boxes shrunk to the size of approximately $5.6 \times 5.6 \times 5.6\text{nm}^3$. A snapshot of the cubic simulation box filled with monomer of one kind is shown in figure 6.1.

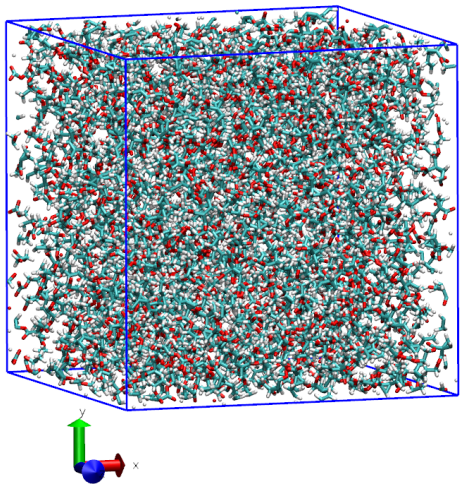

Figure 6.1: (a) Snapshot of the simulation box in the NPT ensemble for determining the bulk properties of the VCPs.

Parrinello– Rahman [10] barostat and velocity-rescale [2] thermostat was used for all the simulations with reference pressure and temperature at 1bar and 300K respectively. LINCS algorithm [7] algorithm was used for H-bond constraining and particle mesh ewald (PME) [5] was used for cubic interpolation of long ranged electrostatics. For H-bond determination, the distance cut-off between the donor (-OH, -NH) and acceptor (O, N) was set to 0.35nm and angle cut-off at 30^0 for the H-donor-acceptor trio. Another parameter used in the below discussions is the Herman's orientation order parameter (S) [11] to quantify any possible orientational correlations occurring in the system as a result of increased H-bonds or any other factors. We determine the one monomer's C=C makes with the other and compute S as

$$S = \langle P_2 \cos\theta \rangle = \frac{3\langle \cos^2\theta \rangle}{2} \tag{6.1}$$

In case of perfect alignment one would have $S = 1$, for partial alignment $0 < S < 1$, for anti-aligned system $S = -0.5$ and for a randomly oriented system $S = 0$.

6.3 Results and Discussion

6.3.1 Part 1 : VCPs with different side chains

The structure of the VCP monomers:

- Monomer 1: 1-(2-((ethoxycarbonyl)oxy)ethyl) 1-ethyl 2-vinylcyclopropane-1,1-dicarboxylate,
- Monomer 2: 1-ethyl 1-(2-propionamidoethyl) 2-vinyl- cyclopropane-1,1-dicarboxylate,
- Monomer 3: 1-ethyl 1-(2-(3- ethylureido)ethyl) 2-vinylcyclopropane-1,1-dicarboxylate,
- Monomer 4: 1-(2-((ethoxycarbonyl)amino)ethyl) 1-ethyl 2-vinyl cyclopropane-1,1-dicarboxylate

used for this part of the study are shown in figure 6.2 (a), (b), (c) and (d) respectively.

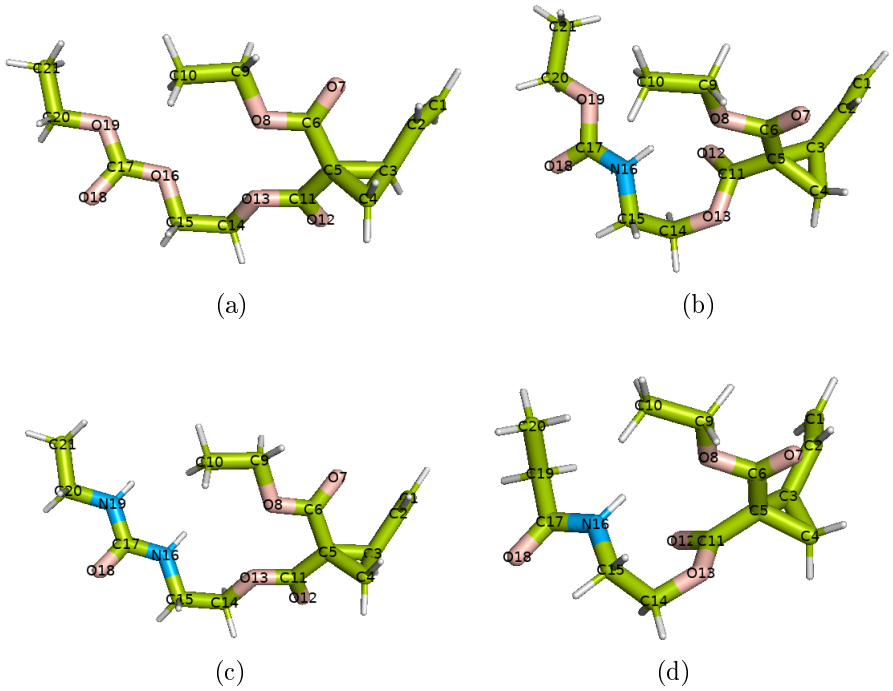

Figure 6.2: Structures of monomer 1 (a), monomer 2 (b), monomer 3 (c), and monomer 4 (d) used for this study. Carbon is represented by green, Nitrogen by blue and oxygen by pink. The atom names will be utilized to refer to atoms for upcoming results.

The time evolution of the hydrogen bonds and its time average for the four monomers is shown in figure 6.3 (a) and (b) respectively. The average number of H-bonds for monomer 2, 3 and 4 are 210 ± 4, 362 ± 7 and 185 ± 9 respectively. Monomer 1 has no H-bonds due to the absence of donor atoms. Taking into consideration the number of monomers, the H-bonds amount to an average of 0.5, 0.9, and 0.4 per monomer for types 2, 3, and 4, respectively.

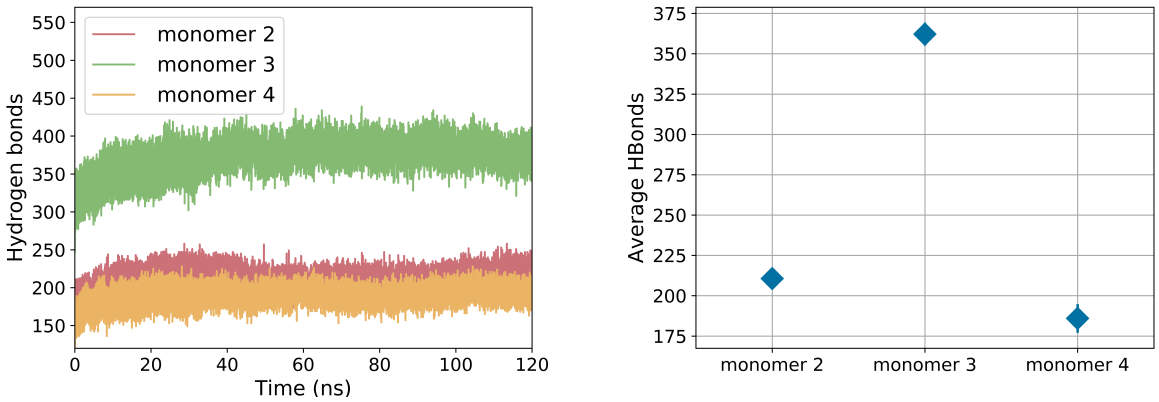

(a) (b)

Figure 6.3: (a) Hydrogen bonds as a function of time and (b) Time averaged hydrogen bonds with block error.

The Herman's orientation parameter defined in section 6.2 is plotted as a function of time in figure 6.4 (a). Figure 6.4 (b) shows its time average. For all the monomers in Figure 6.4 we see that the S factor is ~ 0.25. This tells us that there is no preference of arrangement before polymerization for all the four monomers.

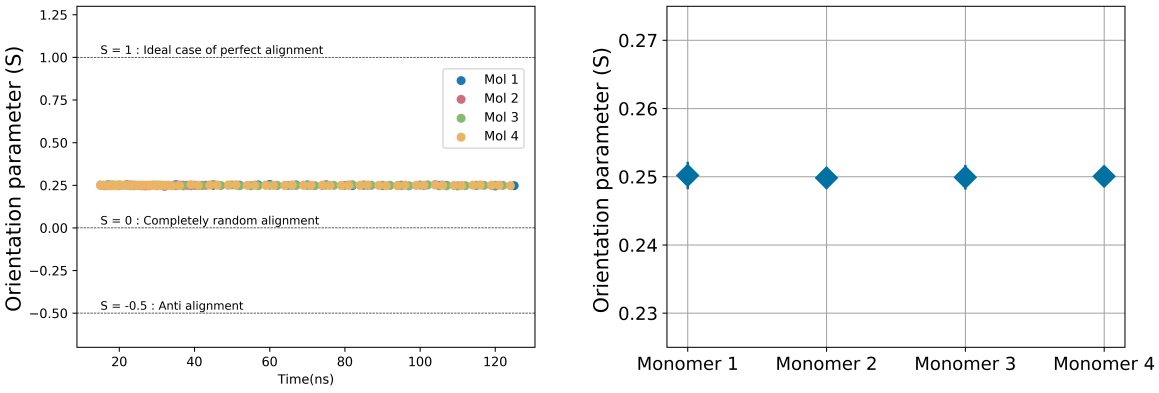

(a) (b)

Figure 6.4: Herman's S factor calculated for angles between double C=C bonds averaged over all of the monomers as a function of time (a) and averaged over time (b).

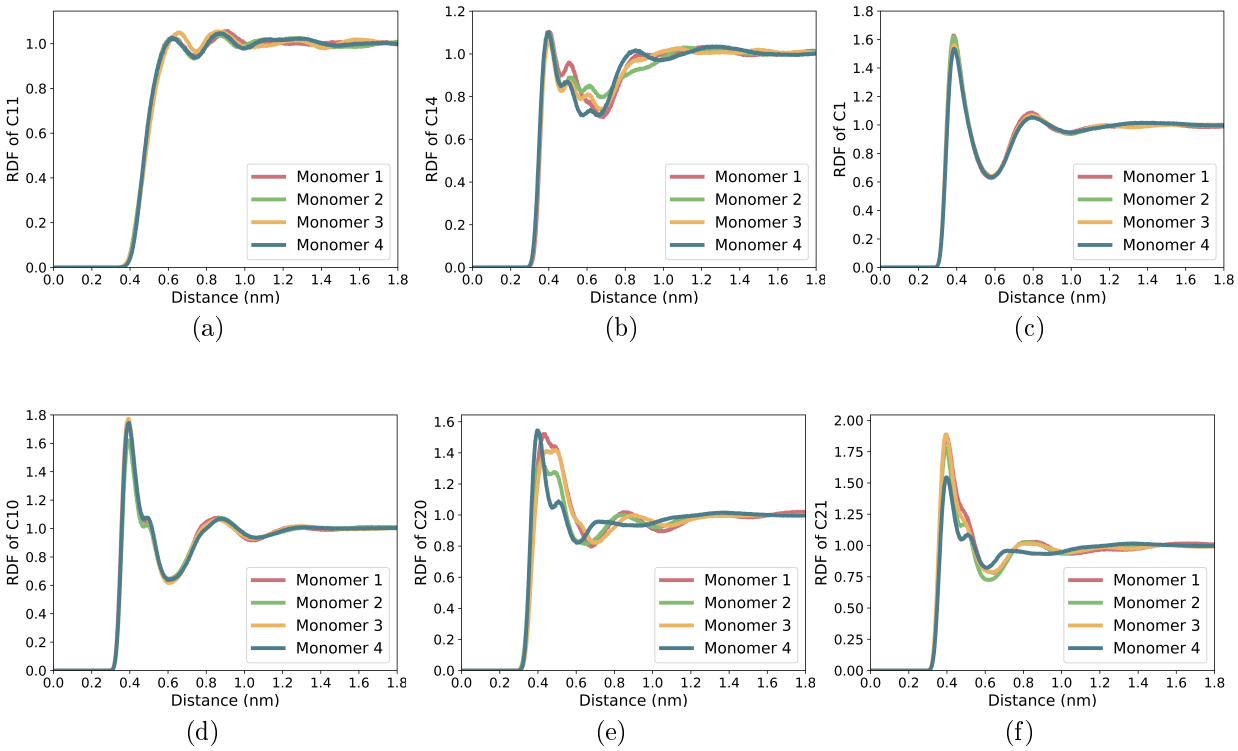

Figure 6.5: Radial distribution function for atoms (a) C11, (b) C14, (c) C1, (d) C10, (e) C20 and (f) C21 atoms of all the four monomers for comparison.

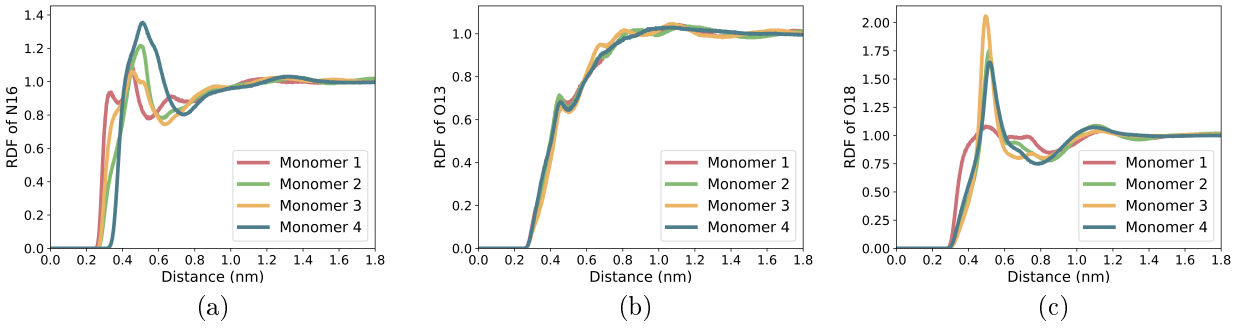

Figure 6.6: Radial distribution function for atoms (a) N16, (b) O13 and (c) O18 atoms of all the four monomers for comparison.

Furthermore figure 6.5 and 6.6 plots the radial distribution functions (RDFs) for individual atoms and shows a comparison for all the 4 monomers. We plot the RDFs for atom names C11, C14, C1, C10, C20, C21 in figure 6.5 (a), (b), (c), (d), (e), (f) respectively. Similarly for atoms N16, O13 and O18 in the RDFs are shown in figure

6.6 (a), (b) and (c) respectively. Refer to figure 6.2 for cross referencing the names with the atom position. The RDFs for the first in the C=C bond (termed C1) and the last carbon atom of the shorter side chain (termed C10) show no variation for all the monomers. The other RDFs show no substantial difference for all the heavy atoms of the monomers in the cyclic region or the side chains. Therefore, all the monomers are similarly aligning themselves pre-polymerization and no substantial self-organization is taking due to the additional H-bonding in monomer 3 compared to 1, 2, and 4.

Schaumacher et al. [14, 15] carried out polymerization experiments at different time intervals to study the polymerization rates by monitoring the monomer conversion with time. The percent monomer conversion as a function of time in minutes in shown in figure 6.7 (a) and the expanded time window of the first two hours in shown in 6.7 (b). For monomer 3, the initial rate of polymerization, i.e. the average slope of first three points is the highest with 24.7%/min. Lowest initial rate of polymerization is seen for monomer 1. However, the differences are not as significant as one would predict for pre-organized monomers. Therefore, the experimental results agree well with the theoretical studies in a way that the number of H-bonds from simulations can directly be correlated to the initial polymerization rates obtained via experiments. Monomer 3 shows higher H-bonding in the simulations and also shows highest polymerization rates in the experiments. However, the functionalisation of the side chains does only a minor impact on the reaction rates.

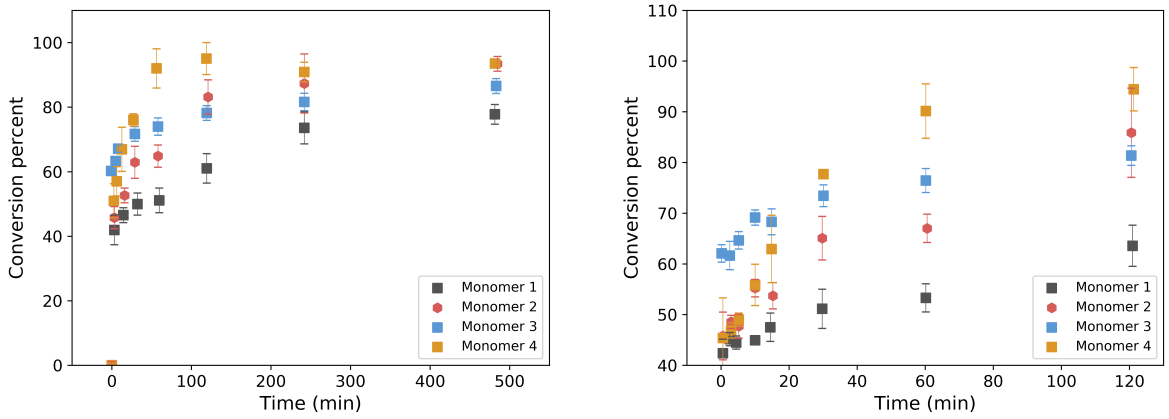

Figure 6.7: (a) Experimental results for the conversion percent over time of the monomers 1, 2, 3 and 4. (b) Expansion of the conversion percent for the first 2 hours.

Theoretically, existence of increased H-bonds does not lead to an increase in the orientation of the monomer pre-polymerization. However, monomer 1 has no H-bonds theoretically and shows lowest initial rate of polymerization. Monomer 3 has theoretically highest amounts of H-bonds compared to the rest and shows highest

initial rate of polymerization. So we observe some correlation of the theoretical H-bond forming capacity of the monomers to their experimental polymerization rates in first 20 mins. However, the difference in the initial polymerization is not notably much for all the monomers.

6.3.2 Part 2: VCP-amides with different side chains

In the previous part 6.3.1, we studied VCPs with different side chains and found out that although H-bonding had an influence on the polymerization rate, the difference among the four functional groups was little and this was probably because the H-bonding sites were present in the side chains and were far away from the active site. Therefore, in this part we study a new set of monomers that have H-bonding capability at two different position the VCPs: (a) the amide group linkage side chain at the cyclopropane ring and (b) the side chain (with amide, urethane and urea groups). We then compare the theoretical results with the experimental findings like in the previous part. The structure of the new VCP-amide monomers used for this part of the study are:

- Monomer 1: 2-((ethoxycarbonyl)oxy)ethyl) 1-ethyl 2-vinyl cyclopropane-1,1-dicarboxylat,
- Monomer 2: 1-ethyl 1-(2-propionamidoethyl) 2-vinyl cyclopropane-1,1-dicarboxylate,
- Monomer 3: 1-ethyl 1-(2-(3-ethylureido)ethyl)2-vinyl cyclopropane-1,1-dicarboxylate,
- Monomer 4: 1-ethyl 2-vinyl cyclopropane-1,1-dicarboxylate

and are shown in figure 6.8 (a), (b), (c) and (d) respectively.

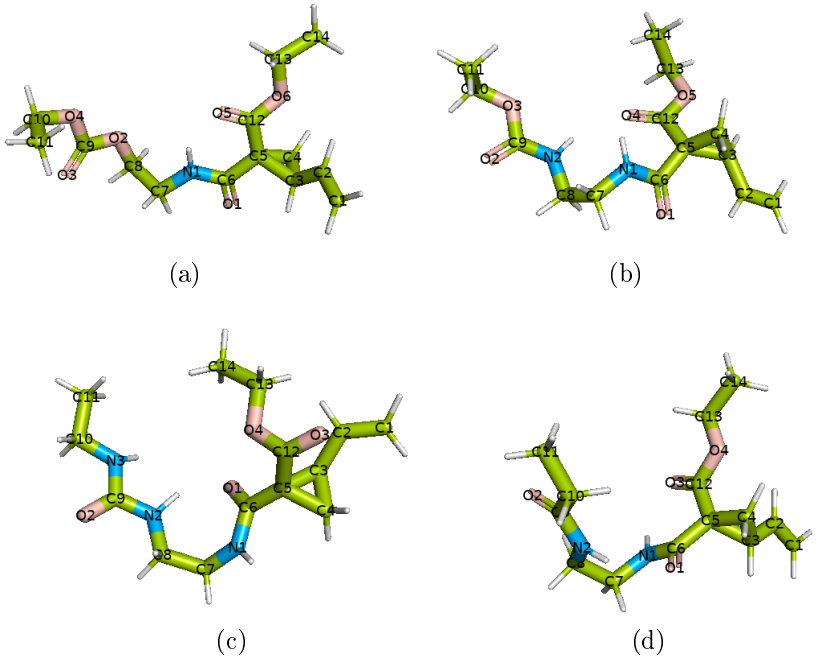

Figure 6.8: Structures of monomer 1 (a), monomer 2 (b), monomer 3 (c), and monomer 4 (d) used for this study. Carbon is represented by green, Nitrogen by blue and oxygen by pink. The atom names will be utilized to refer to atoms for upcoming results.

The time evolution of the hydrogen bonds and its time average for the four monomers is shown in figure 6.9 (a) and (b) respectively. The average number of H-bonds for monomer 1, 2, 3 and 4 are 285 ± 4, 323 ± 4, 528 ± 5 and 334 ± 7 respectively. Taking into consideration the number of monomers, the H-bonds amount to an average of 0.7, 0.8, 1.35 and 0.8 per monomer for types 1, 2, 3, and 4, respectively.

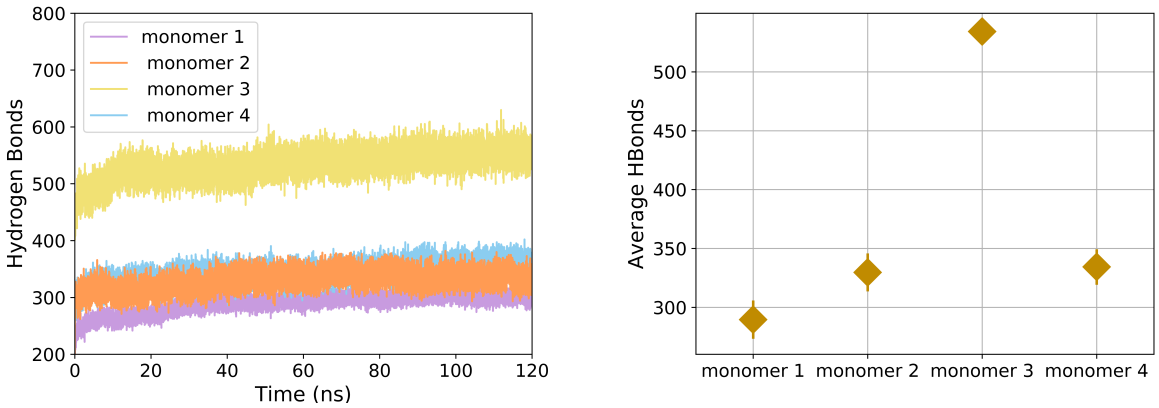

(a) (b)

Figure 6.9: (a) Hydrogen bonds as a function of time and (b) Time averaged hydrogen bonds with block error.

The Herman's orientation parameter defined in section 6.2 is plotted as a function of time in figure 6.10 (a). Figure 6.10 (b) shows its time average. For all the new monomers in figure 6.10 we again see that the S factor is ~ 0.25. The values are close to zero and indicate that all the monomers are almost randomly arranged. They have similar S-factor and show no preference of arrangement before polymerization for all the four monomers (including monomer 3 which has much higher H-bond forming capacity).

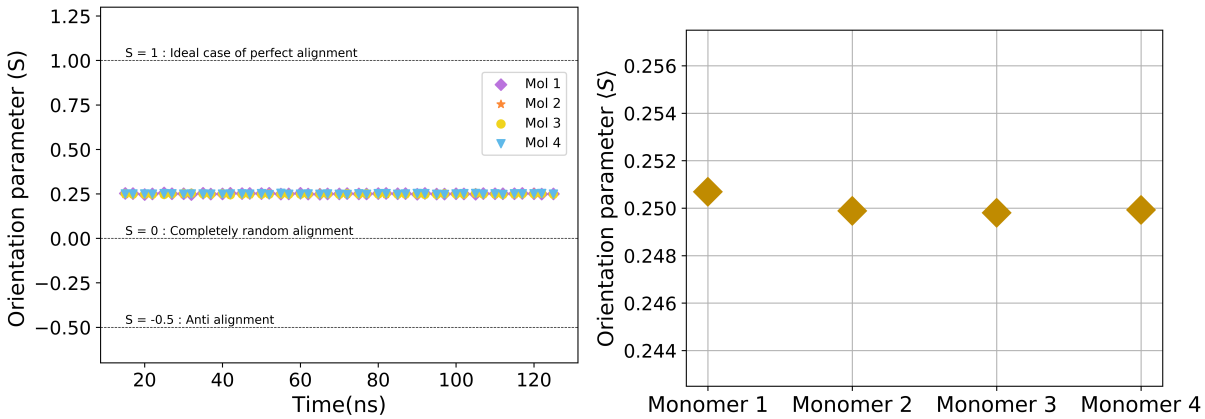

(a) (b)

Figure 6.10: Herman's S factor calculated for angles between double C=C bonds averaged over all of the monomers as a function of time (a) and averaged over time (b).

Figure 6.11 shows the radial distribution function for different atoms in the

monomers (refer to figure 6.8 for atom names and their positioning in the monomer).

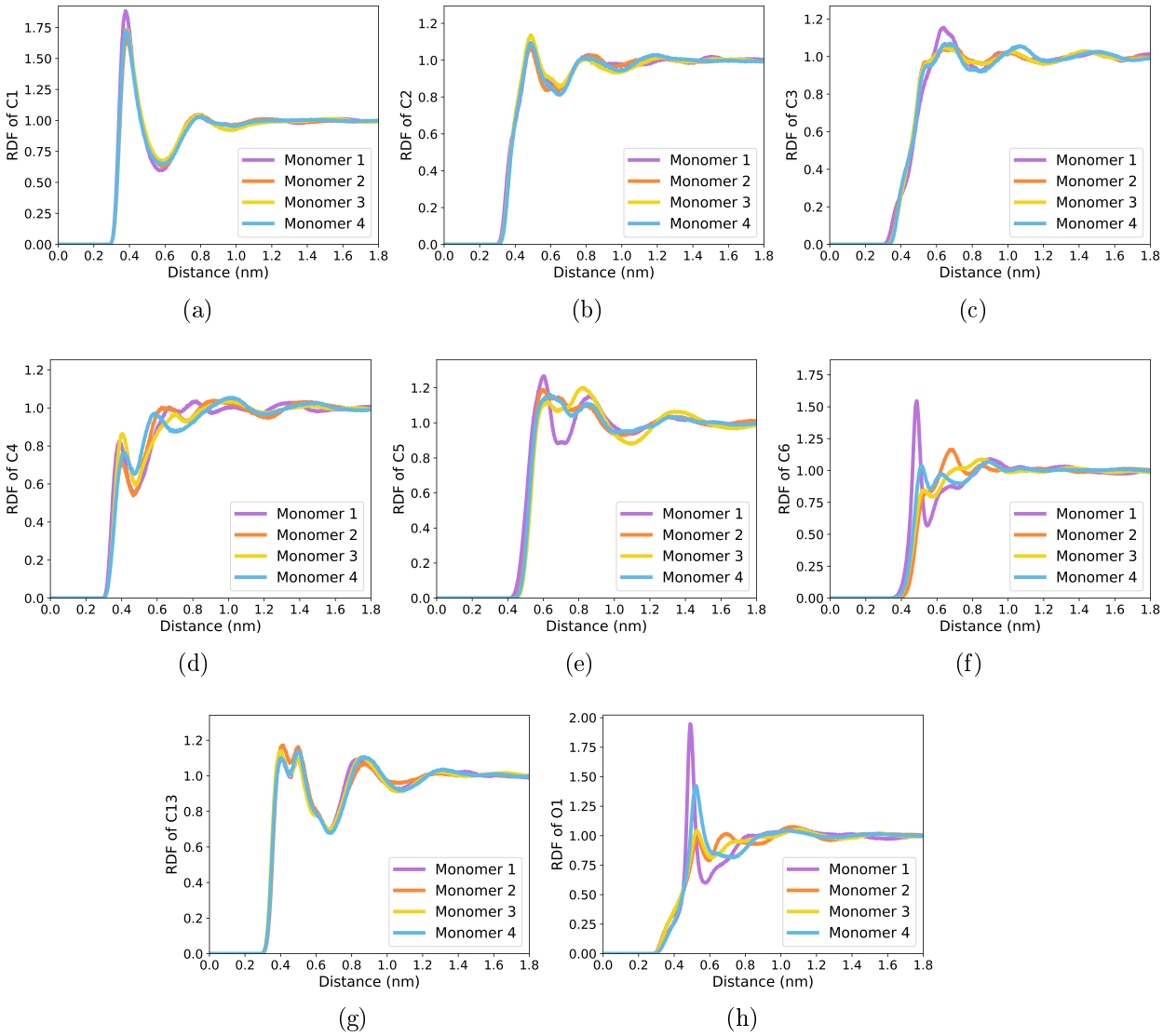

Figure 6.11: Radial distribution function for atoms C1 (a), C2 (b), C3 (c), C4 (d), C5 (e), C6 (f), C13 (g) and O1 (h) atoms of all the four monomers for comparison.

In figure 6.11, especially the RDF for the first carbon in the C=C bond (C1, 6.11(a)) and last carbon of the side chain (C13, 6.11(g)) show no difference in the distance distribution for all the four monomers. This again confirms that even though monomer 3 has much higher H-bonds than the others, it does not under any ordered pre-organization in comparison to the other three monomers.

Similar to the previous part, Schaumacher et al. carried out free radical photo-polymerization at different time intervals to study the polymerization rate by following monomer conversion with time, presented in figure 6.12. They calculated the

initial polymerization rate from the average slope of the first points at 5, 20 and 45 seconds. The highest polymerization rate was seen for monomer 3 (2.35%/s), followed by monomer 2 (1.99%/s) and 1(1.62%/s). Monomer 4 carried the amide functional group in the side chain and showed lowest polymerization rate at 1.35%/s. After 6 hours, monomer 3 showed highest conversion with 95%, followed by monomer 2 at 92%, then monomer 4 at 83% and finally by monomer 1 at 76%. Monomer 3 showed fast polymerization rate and reached a complete conversion in just about 30 mins, which the other showed slow conversion after a fast start.

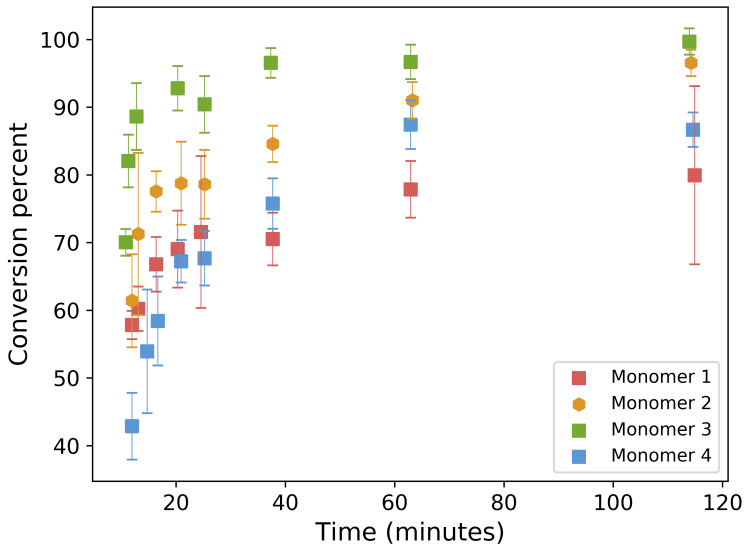

Figure 6.12: Experimental results for the conversion percent over time of the monomers 1, 2, 3 and 4.

Thus, the monomer 3 showed theoretically highest number of H-bonds and also experimentally showed higher polymerization rate with fast conversion per minutes compared to the other monomers. Therefore, H-bonding again seems to be correlated to fast polymerization rate but doesn't help pre-organization of the monomers as seem from the RDFs.

6.4 Conclusion

In the first Part 6.3.1 we studied four VCPs containing different side chains. Theoretically, the number of hydrogen bonds, the orientation parameter, and the radial distribution functions were computed and co-related to the experimental results of polymerization rates. It was found that the H-bonding does not play a role in pre-organization of the monomer bulk, but leads to a bit higher polymerization rates. In the second part (6.3.2) we considered four new VCPs, this time containing an

amide linkage to their side chains. Monomer 3 of Part 2 showed experimentally highest polymerization rates of all the monomers and theoretically highest number of hydrogen bonds. We therefore see a clear dependency between the hydrogen bonding capacity of the monomers and the polymerization speed. In general the amide linked VCPs (of Part 6.3.2) showed a much faster polymerization compared to the ester linked monomers (of Part 6.3.1). This is a new finding that helps in creating selective designs of the VCPs with fast and complete conversions.

6.5 Appendix of Chapter 3

The ATB molid to the topology files for the monomers used in this study are listed below:

Moleculetype	mol ID
Part 1: Monomer 1	344448
Part 1: Monomer 2	344437
Part 1: Monomer 3	344445
Part 1: Monomer 4	344446
Part 2: Monomer 1	363529
Part 2: Monomer 2	368208
Part 2: Monomer 3	363528
Part 2: Monomer 4	704009

Table 6.1: ATB molid citing the topology files

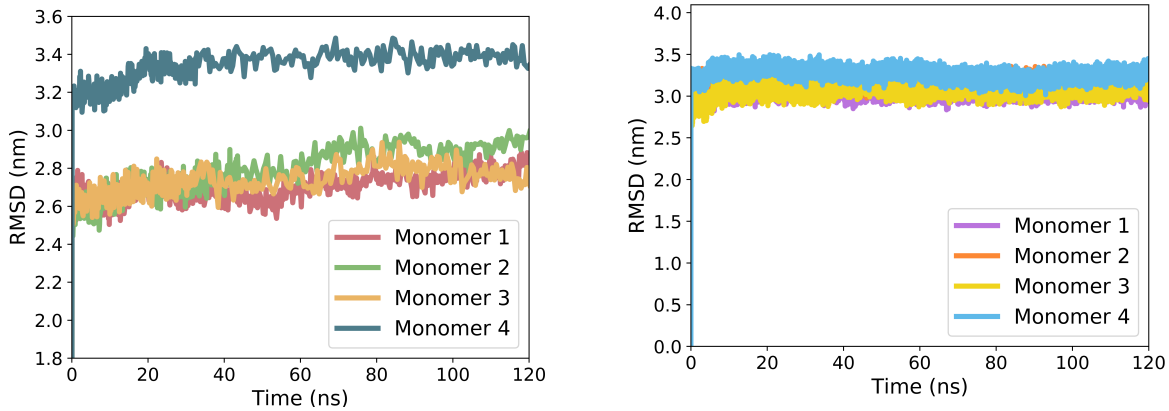

Figure 6.13: Root mean squared displacement of the monomers of (a) Part 6.3.1 and (b) Part 6.3.2 that show that the equilibration of the runs is achieved in all the cases with the first 5ns

References

[1] Mark James Abraham, Teemu Murtola, Roland Schulz, Szilárd Páll, Jeremy C Smith, Berk Hess, and Erik Lindahl. Gromacs: High performance molecular simulations through multi-level parallelism from laptops to supercomputers. *SoftwareX*, 1:19–25, 2015.

[2] Giovanni Bussi, Davide Donadio, and Michele Parrinello. Canonical sampling through velocity rescaling. *The Journal of chemical physics*, 126(1):014101, 2007.

[3] Dian-Feng Chen, Simone Bernsten, and Garret M Miyake. Organocatalyzed photoredox radical ring-opening polymerization of functionalized vinylcyclopropanes. *Macromolecules*, 53(19):8352–8359, 2020.

[4] Paul Pineda Contreras, Payal Tyagi, and Seema Agarwal. Low volume shrinkage of polymers by photopolymerization of 1, 1-bis (ethoxycarbonyl)-2-vinylcyclopropanes. *Polymer Chemistry*, 6(12):2297–2304, 2015.

[5] Tom Darden, Darrin York, and Lee Pedersen. Particle mesh ewald: An n log(n) method for ewald sums in large systems. *The Journal of chemical physics*, 98(12):10089–10092, 1993.

[6] Arnaud Delbrassinne, Maximilien Richald, Julien Janssens, and Raphaël Robiette. Divergent rearrangements of vinylcyclopropane into skipped diene and cyclopentene: Mechanism, scope, and limitations. *European Journal of Organic Chemistry*, 2021(20):2862–2868, 2021.

[7] Berk Hess, Henk Bekker, Herman JC Berendsen, and Johannes GEM Fraaije. Lincs: a linear constraint solver for molecular simulations. *Journal of computational chemistry*, 18(12):1463–1472, 1997.

[8] Tomas Hudlicky. Benefits of unconventional methods in the total synthesis of natural products. *ACS omega*, 3(12):17326–17340, 2018.

[9] Alpeshkumar K Malde, Le Zuo, Matthew Breeze, Martin Stroet, David Poger, Pramod C Nair, Chris Oostenbrink, and Alan E Mark. An automated force field topology builder (atb) and repository: version 1.0. *Journal of chemical theory and computation*, 7(12):4026–4037, 2011.

[10] R Martoňák, Alessandro Laio, and Michele Parrinello. Predicting crystal structures: the parrinello-rahman method revisited. *Physical review letters*, 90(7):075503, 2003.

[11] Geoffrey R Mitchell and Ana Tojeira. *Controlling the morphology of polymers: multiple scales of structure and processing*. Springer, 2016.

[12] Norbert Moszner. New monomers for dental application. In *Macromolecular Symposia*, volume 217, pages 63–76. Wiley Online Library, 2004.

[13] Norbert Moszner, Thomas Völkel, Frank Zeuner, and Volker Rheinberger. Synthesis and radical polymerization of 2-vinylcyclopropanes. In *Macromolecular Symposia*, volume 153, pages 151–159. Wiley Online Library, 2000.

[14] Soeren Schumacher, Sanwardhini Pantawane, Stephan Gekle, and Seema Agarwal. Theoretical and experimental study of monofunctional vinyl cyclopropanes bearing hydrogen bond enabling side chains. *Macromolecules*, 54(1):11–21, 2021.

[15] Sören Schumacher, Sanwardhini Pantawane, Stephan Gekle, and Seema Agarwal. The effect of hydrogen bonding on polymerization behavior of monofunctional vinyl cyclopropane-amides with different side chains. *Macromolecular Chemistry and Physics*, page 2200155, 2022.

[16] Jianhua Wang, Stephanie A Blaszczyk, Xiaoxun Li, and Weiping Tang. Transition metal-catalyzed selective carbon–carbon bond cleavage of vinylcyclopropanes in cycloaddition reactions. *Chemical Reviews*, 121(1):110–139, 2020.

Chapter 7

Poly(3-hexylthiophene) brushes:

Effect of Particle Insertion on $\pi - \pi$ stacking

A key mechanism in organic thin film transistor (OTFT) based biosensors is the decrease in charge carrier mobility caused by the disruption of $\pi - \pi$ bonds in the self-assembled monolayers (SAMs) of conjugated polymers due to the attachment of the target analyst. In this chapter we study the particle induced conformational changes of a $\pi - \pi$ stacked Poly(3-hexylthiopene) (P3HT) brush using Molecular Dynamics (MD) simulations to mimic this event. The polymer brush is modeled using a Martini coarse-grained (CG) forcefield and Lennard- Jones (LJ) particles of small sizes ($0.5nm < R_p < 3nm$) are inserted up to different heights in the brush. We quantify the disruption of the initially perfectly aligned $\pi-\pi$ stack network using three properties: (i) the spatial P3HT monomer density profile, (ii) the spatial distribution of $\pi - \pi$ bound monomer pairs, and (iii) the percentage ratio of $\pi - \pi$ to non-$\pi - \pi$ bonds of the disrupted network. The perturbation of the brush comprises a short-ranged depletion at the particle position and the subsequent rearrangement of the entire $\pi - \pi$ stack network. We study two different systems: (i) isolated P3HT brush and (ii) continuous P3HT brush for inserting the particle and compare the aforementioned properties. In addition, we carry out free energy calculations between individual $\pi - \pi$ stacked P3HT oligomer pairs and report a scaling behavior for the $\pi - \pi$ separation energy for polymers of length $1 < n < 14$.

7.1 Introduction

Polymer brushes refer to a self assembly of polymer chains that are tethered at one end to a surface with sufficiently enough grafting density. The grafting density is such that the polymer chains are crowded and are forced to stretch away from the grafting surface without the need for additional confining geometries or an external field. Solvent can either be present or can be absent in the polymer brushes. At low grafting densities, the polymers are effectively isolated from one another and act independently of each other. In this case, there is no additional osmotic pressure to keep the chains away from grafting surface and therefore they wound up onto themselves to form isolated chain or "mushrooms", also referred to sometimes as "pancake-like" conformations (see figure 7.1 (a)). At higher grafting densities the monomers effectively work as if they all belong to an isolated chain in a good solvent and their monomer-monomer interactions are dominated over by the excluded volume effects and they end up forming brushes (see figure 7.1 (b).

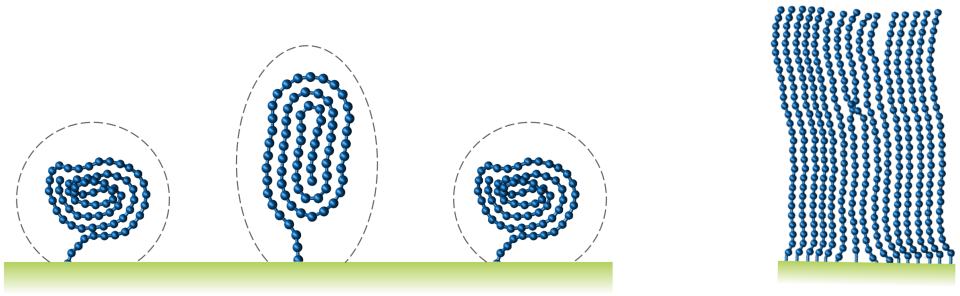

(a) (b)

Figure 7.1: Simulation snapshots of polymer brushes with (a) high grafting density (mushroom regime) and (b) low grafting density (brush regime).

The polymer brushes crafted using conjugated polymers are nowadays used extensively in organic transistors. Conjugated polymers are characterized by a backbone with a delocalized electronic structure. These materials combine semiconducting properties with light harvesting abilities making them useful components in optoelectronic devices, such as light-emitting diodes, photovoltaic cells and field effect transistors [5]. In addition to the electronic properties of their monomers, conjugated polymers are able to carry the excitation energy along the whole backbone over long distances. Sensitive detection of biomacromolecules like DNA or proteins, but also entire cells, have been successfully accomplished by making use of these amplification mechanisms [18]. Detection sensitivity is one of the key aspects in biosensor development. The charge carrier mobility of CPs strongly depends on their $\pi - \pi$ stacking; and this property can be exploited profoundly to detect the slightest of the signals created by the adherence of the target onto them.

Poly(3-hexylthiophene) (P3HT) is one of the most used semiconductive polymers for these kinds of devices due to its high carrier mobility and easy processability [11]. Recent works have extensively used P3HT in organic semiconductor biosensors for detecting lactose, glucose label-free procalcitonin, galactose from human blood, cholesterol and other biomacromolecules [14, 4, 16, 17, 15, 1]. Through spontaneous organization, P3HT forms brushes in organic electronics to act as charge transfer layers for holes or electrons due to their $\pi - \pi$ stacking ability. It therefore is of great importance to study in depth the $\pi - \pi$ stacking behavior of P3HT brushes and their perturbation in presence of a foreign body. We therefore propose a simplified model for a receptor-functional group assembly inside a biosensor in this chapter. We use Molecular Dynamics simulations to examine the rearrangement of a P3HT polymer brush caused by the adherence as well as the inclusion of Lennard-Jones (LJ) particles with radii ranging from the $\pi - \pi$ stacking distance to six times its value.

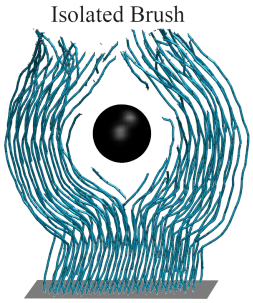

Figure 7.2: PART 2: Insertion of LJ particle in isolated brush

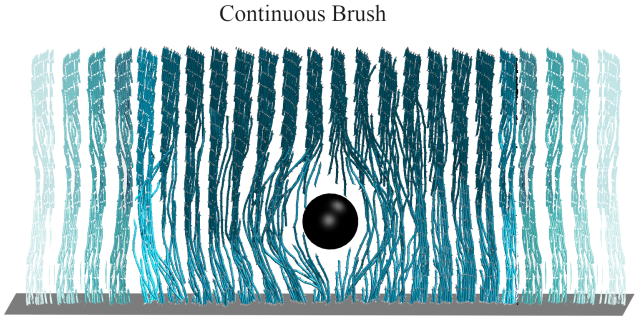

Figure 7.3: PART 3: Insertion of LJ particle in continuous brush

We would carry out the study in Three parts. Part 1 will have a look into the potential mean force (PMF) required to separate two P3HT of varying lengths ($1 < n < 14$) and establish the scaling energy of $\pi - \pi$ stacks. Part 2 will deal with inclusion of the LJ particle into an isolated brush as shown in figure 7.2. Part 3 will study the particle inclusion into a continuous brush that extends to infinity (7.3). We compute and compare particle density, $\pi - \pi$ bond density and network, and the alignment of

the $\pi - \pi$ bonds and their percent ratio for both system in Part 2 and Part 3. At the end of this chapter, the reader would have a complete overview of the nature of the $\pi-$stacking and its networking and the importance of studying the two systems individually.

7.2 Simulation details

All the simulations were performed using GROMACS software and VMD [9] was used for the visualization of the molecular structures and trajectories. For the free energy calculations we used umbrella sampling. The distance between the center of mass (COM) of the pull groups was used as the reaction coordinate for the umbrella sampling. The free energy was calculated using the Weighted Histogram Analysis Methods, using the GROMACS command `gmx wham` [7].

7.2.1 P3HT model

P3HT was modeled using coarse grained force-field used and described in section 2.9. The model consists of six CG beads per monomer, 3 CG sites for the central ring and 3 CG sites for the hexyl side chain. Schematic illustration of the structure of P3HT, CG mapping and its martini coarse-grained model is shown in figure 7.4 (a), (b) and (c) respectively.

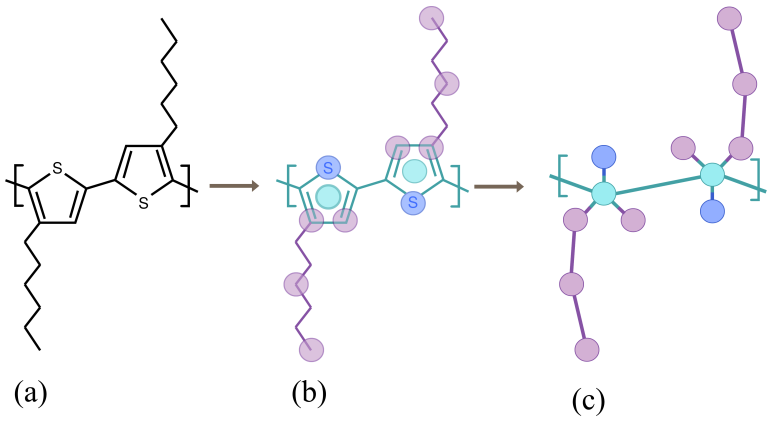

Figure 7.4: (a) Schematic representation of P3HT. (b) Mapping to CG model. (c) P3HT CG model used in this study.

7.2.1.1 System containing isolated brush

To create the isolated P3HT brush column, we created a system with 128 polymers containing 40 monomers each. The grafting surface, lies in the y-z-plane and the column height runs from $x = 0$ to $x = 14$nm. We place 16 $\pi - \pi$ stacked polymers along z-axis

and 8 polymers along the non-$\pi - \pi$ stacking direction. Then we pull the non-grafted ends of the polymer column radially, place the LJ particle in the center, and let the polymer wrap itself around the LJ particle. This process is illustrated in figure 7.5.

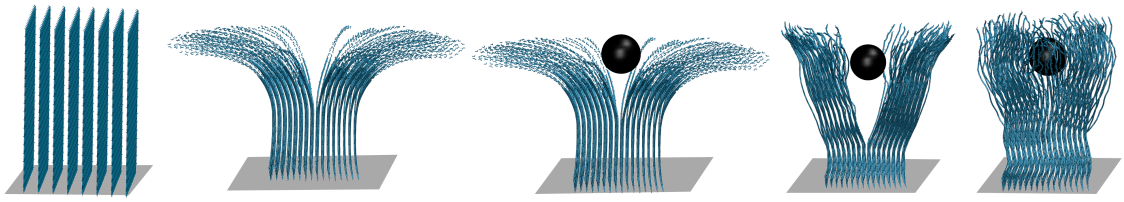

Figure 7.5: Procedure used to include LJ particle into the isolated P3HT brush column. The polymer ends are pulled radially outward by applying a spring force to the end beads. The LJ particle of desired radius is place at the center of the pulled column. The pulling force is taken off and the system falls back engulfing the particle inside.

The LJ particle is placed at a height of H =8.4nm, 11.1nm and 13.5nm from the plane of grafting. Therefore smaller the particle height H, deeper is the particle penetrated into the brush.

7.2.1.2 System containing continuous brush

To create a continuous brush column, we created a system with 512 polymers containing 40 monomers each. The grafting surface, where the first atom of each polymer is constrained, lies in the y-z-plane and the particle height runs from $x = 0$ to $x = 14$nm. We place 32 $\pi - \pi$ stacked polymers along z-axis at a spacing of 5Å and the non-$\pi - \pi$ stacking direction y has 16 polymers at a spacing of 16.5Å. We implemented periodic box conditions on the y- and z- axes, so that in principle the box is infinitely wide. Since the P3HT continuous brush is densely packed, simply inserting a large particle was thermodynamically unstable.

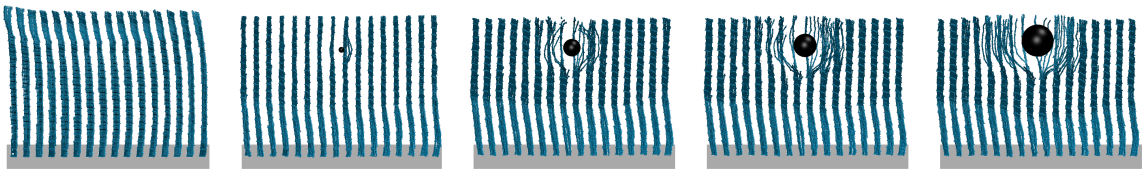

Figure 7.6: Procedure used to include LJ particle into the continuous P3HT brush column. The size of the LJ particle is subsequently increased from $R_p = 0.0$ to 3.0nm at particle height H.

The method used in figure 7.5 was also not possible since there was no additional space around the brush to pull the ends away. Therefore, for each simulation run, we

created the initial structure file with P3HT and particle in the following way. For a completely $\pi - \pi$ stacked brush, an LJ particle of size $\sigma = 0.0$nm was inserted at the desired particle height x in the P3HT brush column. Then this simulation was ran for a 10000 steps with $dt = 0.0005$ps. The final coordinate file of this simulation was used as the starting configuration for a new simulation were σ was incremented by 0.005nm. This was reran again for the same time steps with the same dt. We continued this process 600 times until the size of the LJ particle reached $R_p = 3.0$nm, all the while restraining the particle at the same place. This way we were able to create our initial structure files with the LJ particle embedded in the P3HT brush at different particle heights. Snapshots of this process is shown in figure 7.6.

7.2.2 Lennard Jones Particle

The potential of the LJ particle has the form

$$U_{\mathrm{LJ}} = 4\epsilon \left[\left(\frac{R_p}{r} \right)^{12} - \left(\frac{R_p}{r} \right)^{6} \right] \tag{7.1}$$

We choose $\epsilon = 1$kJ mol^{-1}, 2kJ mol^{-1}, 4kJ mol^{-1}, 6kJ mol^{-1} for particles of radii $R_p = 0.5$nm, 1nm, 2nm, and 3nm respectively. For comparison, one of the P3HT ring beads has $\epsilon = 2$kJ mol^{-1} and $\sigma = 0.4$nm. All simulations were carried out using NVT ensemble simulating with the time step set to $dt = 2$fs. Of the total 4ns simulations, the first 1ns was discarded and the last 3ns were used for analysis. Plain cut-off was used with neighborlist radius set to 1.1nm. In case of different LJ particle size, the cut-off radius was set to $\sigma + 0.8$nm. Bonds were constrained using LINCS algorithm [6]. To maintain constant temperature at 300K, we employ a velocity rescaling thermostat [3]. Periodic boundary conditions are applied in all three directions.

7.2.3 $\pi - \pi$ stacking criteria

We follow a procedure similar to the one proposed by Janiak [10] for determining a $\pi - \pi$ bond between two monomers. The criteria is based on the centroid-centroid distance between the rings of the monomers, their lateral displacement, and the contact angle between normal ring vectors. Previous computational studies of P3HT showed an increased $\pi - \pi$ stacking distance of approximately 5Å [13, 12] in contrast to the experimental value of 3.8Å. This deviation is attributed to the approximation of the thiophene ring as a spherical site in CG model which overestimates the steric bulk of the ring in the $\pi - \pi$ direction [13].

We therefore adapt the criteria for a $\pi - \pi$ bond to the following: (a) the centroid-centroid distance between two rings is 5Å and (b) the contact angle between the two ring normals are 20^0 and (c) the rings are laterally displaced by 1.7Å.

Figure 7.7 (a) shows the $\pi - \pi$ stacking criteria proposed by Janiak et al. [10] based on the experimental database and figure 7.7 (b) shows the modified criteria for computationally determining $\pi - \pi$ bonds between two P3HT thiophene rings.

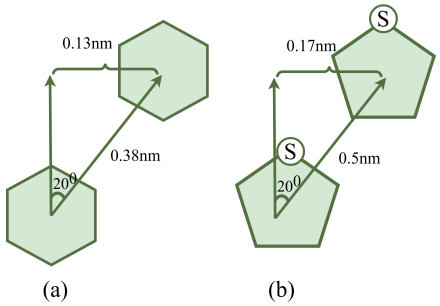

Figure 7.7: (a) $\pi - \pi$ stacking criteria formulated by Janiak et al. [10] using Cambridge Structural Database for aromatic rings. (b) $\pi - \pi$ stacking criteria used in this work for computationally determining $\pi - \pi$ stack between two thiophene rings.

7.3 Results and Discussion

Part 1 : Interaction between 2 P3HT chains of varying length

As will be shown in more detail below, the insertion of a particle into a P3HT brush leads to breaking and reformation of $\pi - \pi$ bonds between P3HT monomers of different chains. To begin with, we therefore investigate in this section the free energy required to break individual $\pi - \pi$ bonds between two neighboring P3HT chains. For this, we consider two $\pi - \pi$ stacked P3HT chains with number of monomers $2 \leq n \leq 16$. Figure 7.8 shows the starting conformation and the pull simulation snapshot, with two $\pi - \pi$ stacked P3HT chains, as an example, for the case $n = 6$ in (a) and (b) and case $n = 9$ in (c). The starting configuration has stacking distance of 4.9Å between the center of mass of the two polymers. We carry out umbrella sampling where we pull the center of masses (COM) of the whole chains as illustrated in 7.8 (b). The resulting potential of mean force (PMF) is shown as a function of the COM distance in figure 7.8(d). The step-wise increasing energy difference ΔE in the PMF (marked in figure 7.8(d)) is plotted as a function of monomer number n in figure 7.8 (e). The PMF between P3HT with $n = 1$ and $n = 1$ is 3.6 kcal mol^{-1}, for $n = 1$ and $n = 2$ is 7.28 kcal mol^{-1} and for for $n = 2$ and $n = 2$ is 14.24 kcal mol^{-1}. The influence of many-body interactions (long-distance two-body interactions, as well as nearest neighbor three-body terms) have an aggregate effect in trimers ($n = 1$ and $n = 2$) and tetramers (both $n = 2$) strengthen the $\pi - \pi$ binding interaction compared to the dimers (both $n = 1$). Therefore, the increase at low n is non-linear. For $n \geq 3$ it reaches a saturation and henceforth is

increase becomes linear. This linear scaling of ΔE, i.e PMF $\propto n$, with the number of monomers for $3 \leq n \leq 9$ is clearly evident from figure 7.8(e). For this range, we compute from figure 7.8(d) the average energy required to disrupt one $\pi - \pi$ bond as 11.392 ± 1.94 kcal mol^{-1}. For cases $n > 9$ the linear scaling of ΔE is flattened. This happens because the length of the polymer becomes sufficiently long to allow for it to fold onto itself and form intra polymer $\pi - \pi$ bonds, effectively resulting in the division of the polymer into multiple chromophores. Chromophores are P3HT chains that are broken into electronically isolated units if the dihedral angle exceeds a particular value of 40^0 [13, 2]. Therefore, once the polymer folds onto itself, two things occur: (a) the dihedral angle at the site of folding exceeds 40^0 thus creating two chromophores and (b) $\pi - \pi$ bonds are reestablished within the same polymer. This ultimately decreases the observed energy difference between the stacked and the separated polymer strand configuration, figure 7.8(a) and (c), respectively. This is the point where the linearity of the scaling is disrupted in figure 7.8(e).

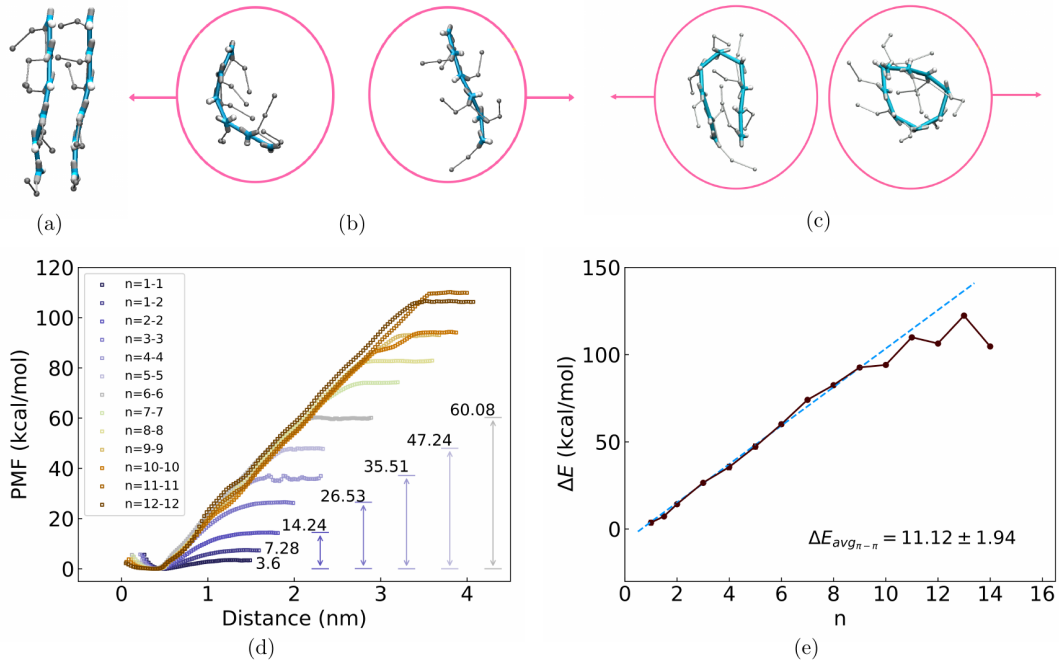

Figure 7.8: (a) Initial conformation for pull simulations and (b) snapshot for $n = 6$ the pull groups being the COM of the each chain. (c) Snapshot for $n = 9$ the pull groups being the COM of the each chain, where the polymer folds onto itself to form intra-chain $\pi - \pi$ bonds. (d) The PMF as function of the polymer distance between polymers of length $n - n$ (where n are the number of monomers). (e) The separation energy ΔE of two polymers increases linearly with the number of monomers.

In article [8] fig. 6 the energy for $\pi - \pi$ stack between two single thiophene groups is about 3.5 kcal mol^{-1}. We observe for when pulling two single monomers i.e. for

$n = 1; n = 1$ in figure 7.8 (e) the energy is 3.6 kcal mol^{-1} . The difference is likely due to the presence of the side chains in addition to the thiophene rings.

Part 2: P3HT isolated brush

One particle insertion

In this section, we quantify the structural changes of a P3HT brush caused by the insertion of a single particle, see figure 7.9 for a particle of radius $R_p = 3$nm. Starting from the undisturbed system in figure 7.9(a), we insert the LJ particle at three different heights, $H = 13.5$nm, 11.1nm, and 8.4nm measured from grafting surface as shown in figures 7.9 (b), (c), and (d), respectively.

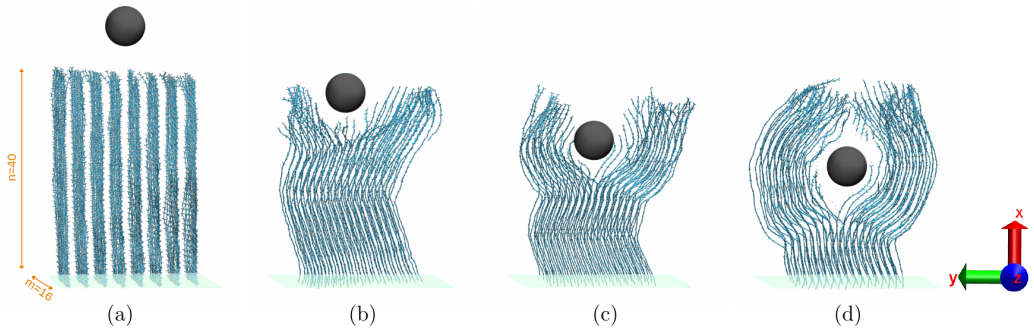

Figure 7.9: Simulation snapshots of single particle in isolated P3HT brush (a) before insertion, (b) at $H = 13.5$nm, (c) at $H = 11.1$nm and (d) at $H = 8.4$nm.

Firstly, we take a quantitative look at the rearrangement of the polymers after inserting the particle in figure 7.10 which shows the cylindrical radial monomer density for increasing R_p(left to right) with decreasing H(top to bottom). The polymers are grafted at $H = 0$ therefore the stacking structure is maintained close to $H = 0$. Inserting a particle into the brush distorts the profile of the brush. The smallest radius particle with $R_p = 0.5$nm at highest column height $H = 13.5$nm in figure 7.10 (a) creates a small depletion area for the monomers at the top of the brush. This depletion persists when the same particle is inserted deeper into the brush at $H = 11.1$nm and 8.4nm in figures 7.10 (e) and (i) respectively. In the graphs on the right, we increase the particle radius. For the largest particle of $R_p = 3$nm with decreasing column height in figures 7.10(d), (h) and (l) the polymers arrange themselves in such a way that a short-ranged monomer depletion is present at the particle position beyond which there exists a high monomer density that decreases as we approach the interface. Using the criteria explained in section 7.2.3 we present the radial $\pi - \pi$ bond density for the

one-particle system in figure 7.11. The depletion area, similar to figure 7.10 exists also for the $\pi - \pi$ bond densities. To have a detailed understanding of the orientation of particles in the brushes we plot histograms of the angle between the monomer-monomer centroid vector and the z-axis in figure 7.12 (a) for reference system and 7.12 (b) for disturbed system with particle of $R_p = 3$nm at $H = 8.4$nm.

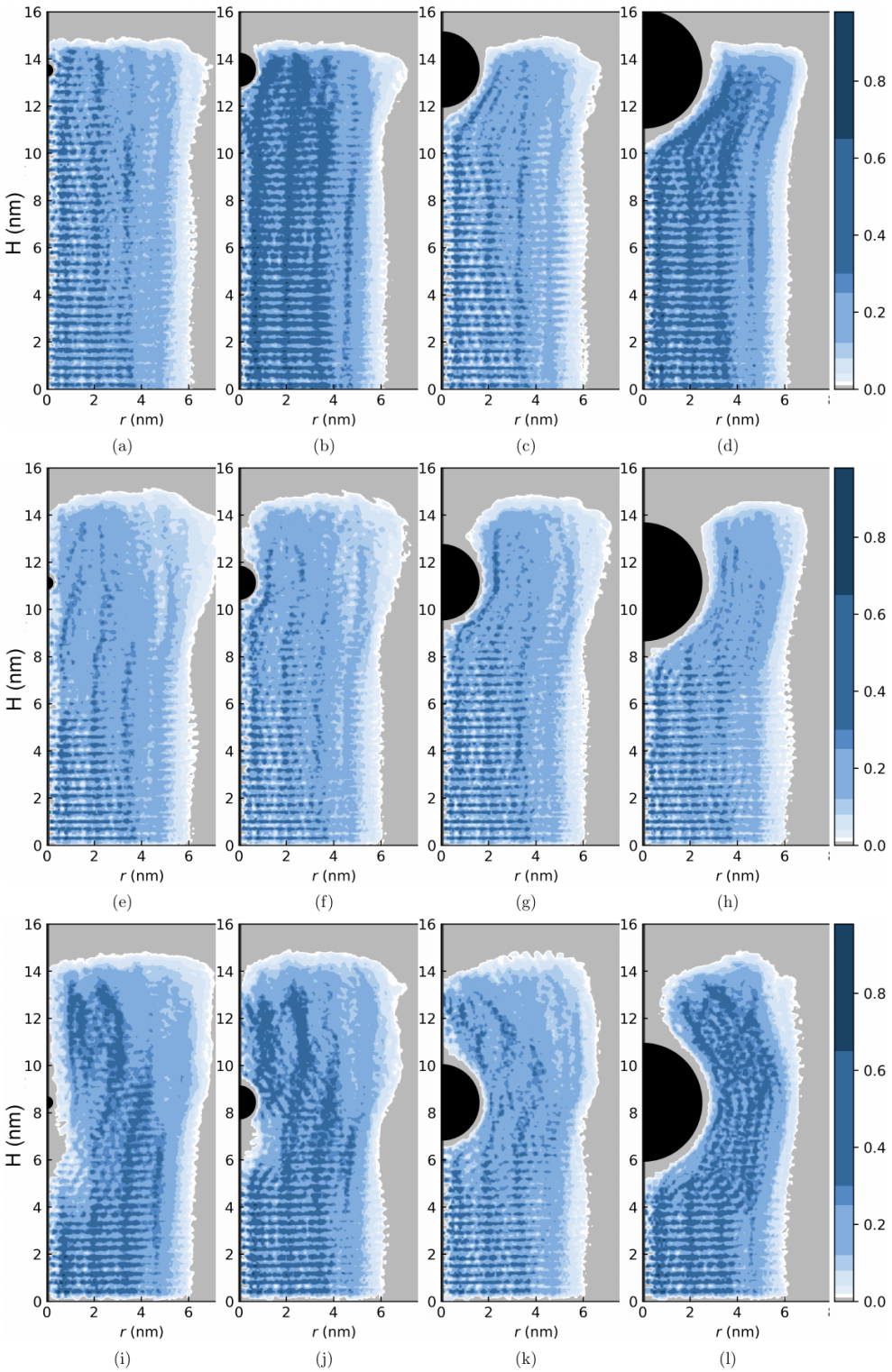

Figure 7.10: Cylindrical radial monomer concentration profile for single particle insertion in isolated P3HT brush for particle radius $R_p = 0.5\text{nm}, 1\text{nm}, 2\text{nm}$, and 3nm, with height $H = 13.5\text{nm}$, 11.1nm, and 8.4nm.

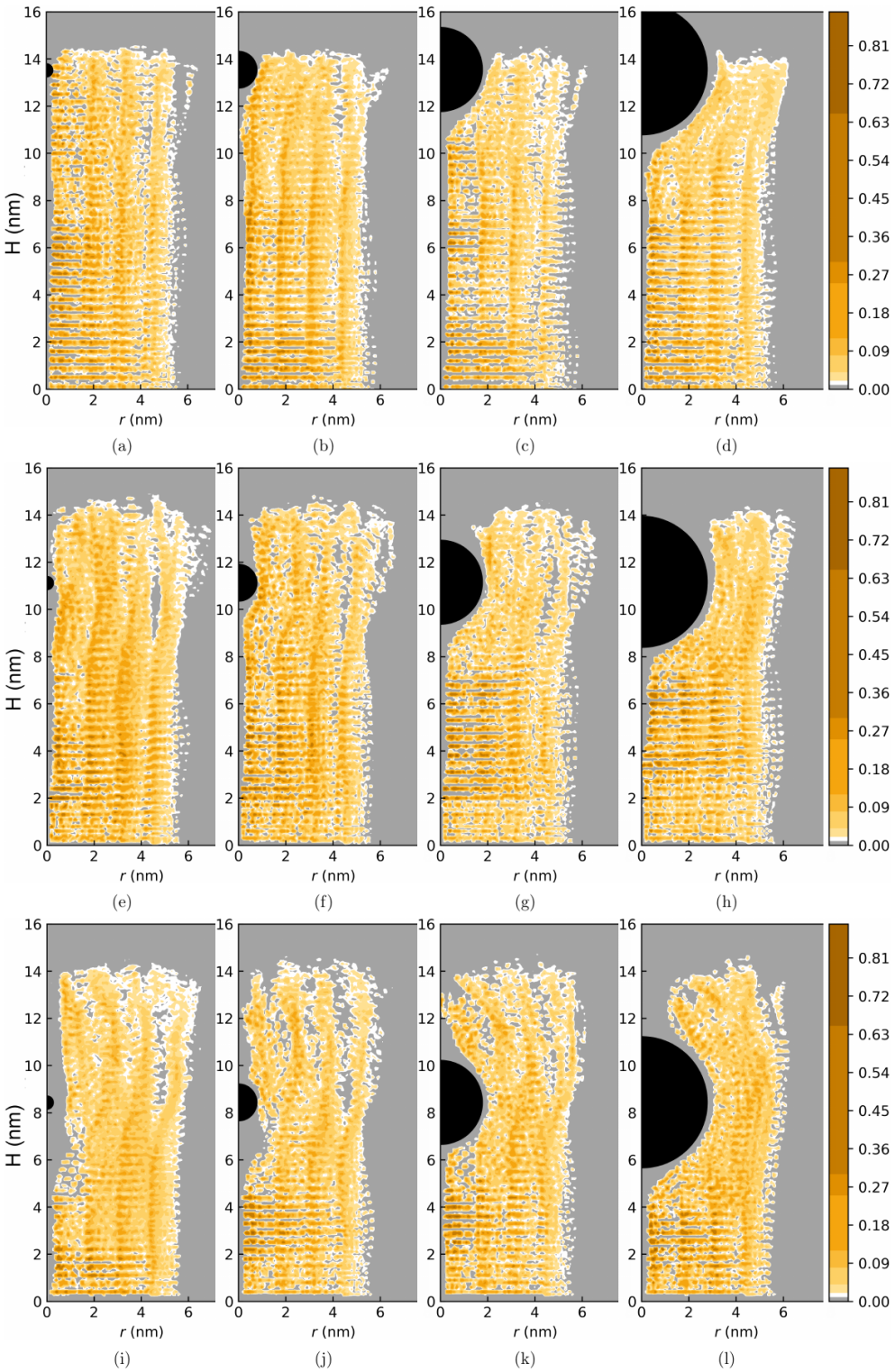

Figure 7.11: Cylindrical radial $\pi - \pi$ bond density profile for single particle insertion in isolated P3HT brush for particle radius $R_p = 0.5\text{nm}, 1\text{nm}, 2\text{nm}$, and 3nm, with height $H = 13.5\text{nm}$, 11.1nm, and 8.4nm.

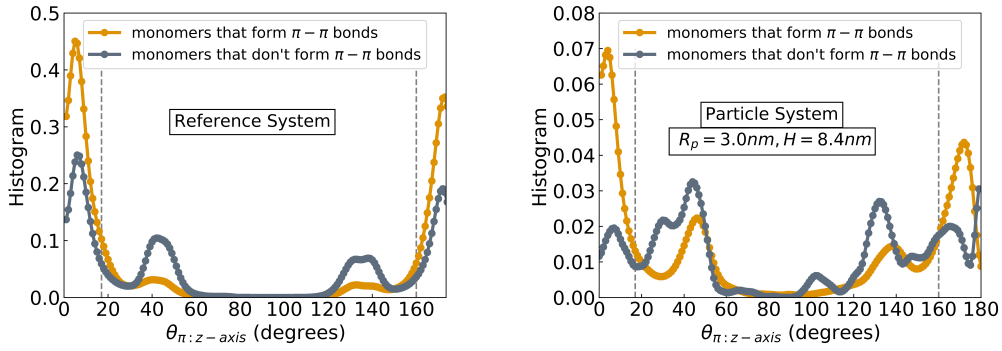

(a)

(b)

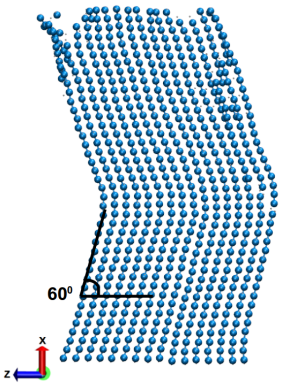

(c)

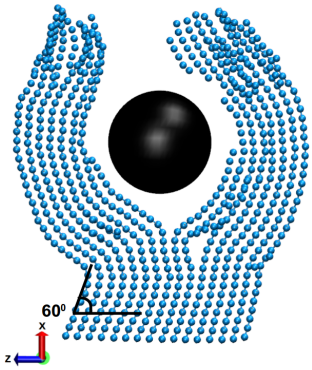

(d)

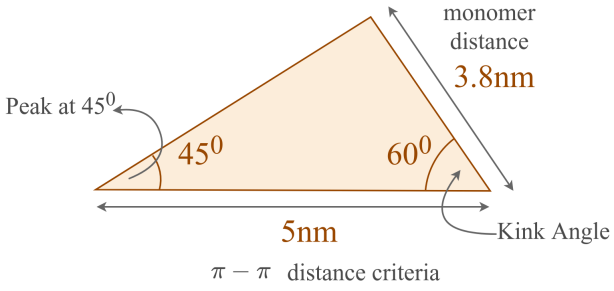

(e)

Figure 7.12: Histogram of the angle between monomer-monomer vector (the centroid vector) and the z-axis that do and do not form a $\pi-$ bond for (a) reference system and (b) for system with particle having $R_p = 3$nm and $x = 8.4$nm of isolated P3HT brush. Snapshot of a slice along the $y-$direction for (a) reference system and (b) system with particle. (e) Simple numerical analysis explaining the peaks at 45^0 and 135^0 of (a) and (b).

The $z-$axis is the $\pi - \pi$ stacking axis of the system and therefore gives us more information on the orientation of the disturbed bonds. The reference system in figure

7.12 (a) shows that the bonds that form $\pi - \pi$ bonds have prominent peaks at 0^0 and 180^0 indicating that most of the monomers that form $\pi - \pi$ bonds are aligned along the z-axis. The polymers that do no form $\pi - \pi$ bonds also have major peaks at 0^0 and 180^0, however, since their perpendicular distance is more than 1.7nm(criteria (c) of section 7.2.3) they are not considered as $\pi - \pi$ bonded. In comparison to the disturbed system in 7.12 (b), the reference system in (a) is well ordered. Introduction of the particle leads to random orientation of the monomers that do not form $\pi - \pi$ bonds (as seen from 7.12 (a)). Figure 7.12 (c) is the snapshot of the reference system and 7.12 (d) is a snapshot of the disturbed system with particle. The lesser peaks at $45^0$and 145^0 in the figure 7.12 (a) and (b) rise because of a slight kink at 60^0 as seen from figure 7.12 (c) and (d) respectively. This is responsible for the peaks at 45^0 as can be explained by the simple geometric consideration shown in figure 7.12 (e). The kink arises because of the inter-polymer grafting distance of 5nm and the system tries to minimize its energy by forming more $\pi - \pi$ bonds by bending at 60^0. Regardless of the kink, we see a ordered state of all the monomers in the reference system. This order is maintained for the monomers that form $\pi - \pi$ bond in figure 7.12 (b) but is lost for the monomers that don't form the $\pi - \pi$ bond.

A percolation line is defined as a series of connected $\pi - \pi$ bonds that leads to a path along which charge mobility occurs. Therefore, in addition to the number density of $\pi - \pi$ bonds, it is important to have a look at the connectivity of these bonds, which is the key mechanism behind the efficiency of OTFT based biosensors. These percolation lines are fairly easily visible in figure 7.13 where we plot all the vectors between two monomers that form a $\pi - \pi$ bond. Each top plot provides a view of the bonds along x-y direction while the corresponding bottom plots show the center slice in the region 26nm $< y <$ 28nm in the x-z-plane. Along the $\pi - \pi$ stacking direction z (bottom plots), we see percolation lines formed due to two or more monomers across different polymers. As the particle radius increases we see shorter percolation lines at the corresponding particle height H. When the particle is near the interface, i.e. at $H = 13.5$nm we see short percolation lines at the top but percentage of longer percolation lines are still higher below the particle (see figure 7.13 (a), (b), (c) and (d)). Shorter percolation lines are more in number at $H = 8.4$nm due to the disruption created by the particles (see figure 7.13 (i), (j), (k) and (l)).

To quantify the behavior we just observed in figure 7.13, in figure 7.14 we present the distribution of the angle between the $\pi - \pi$ bond vector and the z-axis for two cases: (a) $R_p = 3.0$nm; $H = 13.5$nm and $R_p = 3.0$nm; $H = 8.4$nm and (b) $R_p = 3.0$nm; $H =$ 8.4nm and $R_p = 0.5$nm; $H = 8.4$nm for comparison. We calculate the ratio between the areas that are close to the z-axis i.e. ($0 < \theta < 20$ and $160 < \theta < 180$) and the ones that are in the range $20 < \theta < 160$, where θ is the angle between the centroid vector and the $z-$axis. This ratio gives us information on the alignment of the π-π connection vectors along the z-axis. From figure 7.14 (a) the ratio is 3.52 for $H = 13.5$nm and 1.42 for $H = 8.4$nm indicating that less than twice as many $\pi - \pi$ bonds are aligned along the z-axis with decrease in particle height. In figure 7.14 (b) the ratio is 1.27 for $R_p = 0.5$nm; $H = 8.4$nm and 1.42 for $R_p = 3.0$nm; $H = 8.4$nm. This difference is not

much and therefore we conclude that decreasing particle height H leads to decrease in alignment with the $z-$axis however, increasing R_p from 0.5 to 3.0 leads to not much of a difference in the θ distributions.

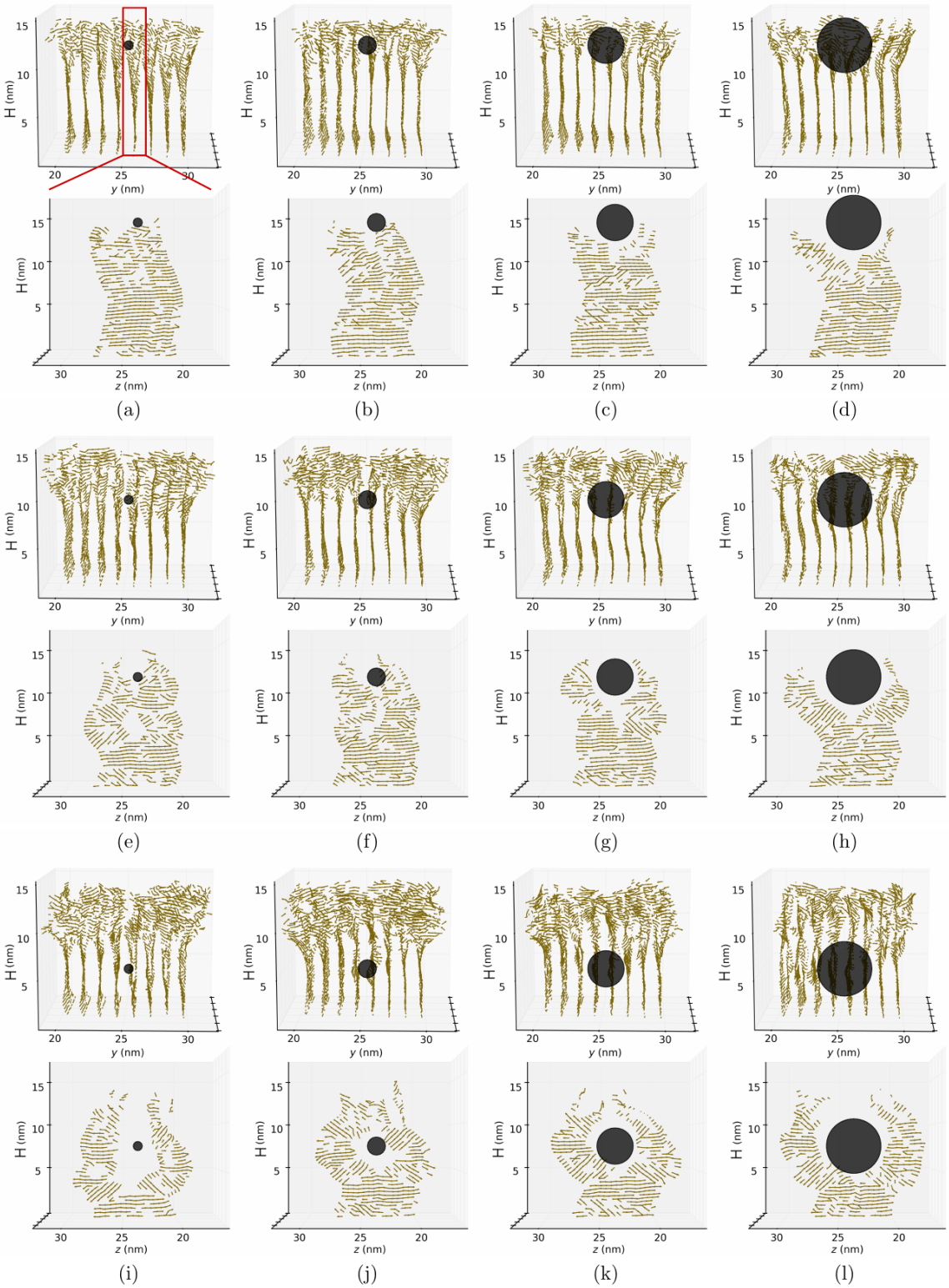

Figure 7.13: Percolation lines formed due to the formation of $\pi-\pi$ connection vectors for single particle insertion into an isolated brush column. View in the x-y plane (top) and x-z plane (bottom) for particle radius $R_p = 0.5$nm, 1nm, 2nm, and 3nm, and particle height $H = 13.5$nm, 11.1nm, and 8.4nm.

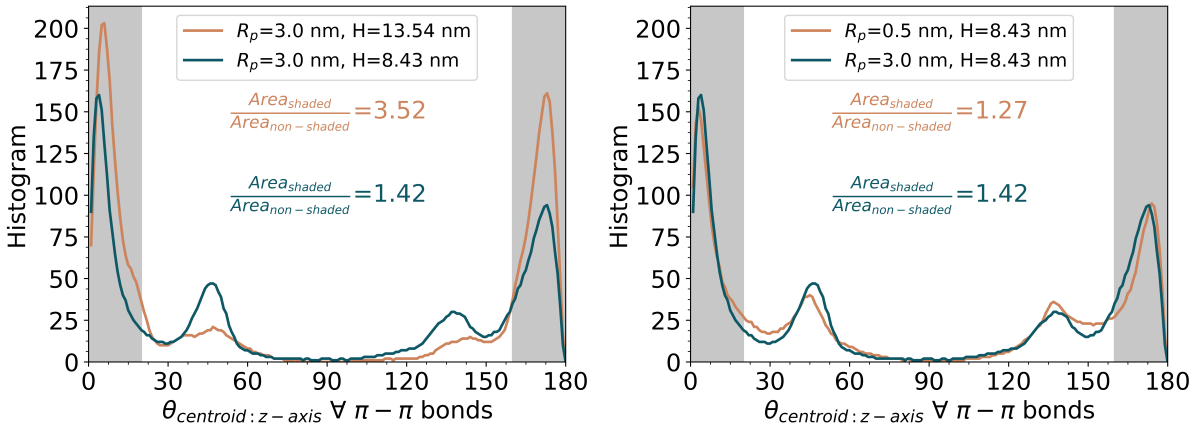

(a) (b)

Figure 7.14: Distribution of angle between the z-axis and the $\pi - \pi$ connection vector for single particle insertion in isolated brush with (a)R_p = 3.0nm; H = 13.5nm and R_p = 3.0nm; H = 8.4nm (b) with R_p = 0.5nm; H = 8.4nm and R_p = 3.0nm; H = 8.4nm

To finally have a firm stance on the effect of the particle insertion into the isolated P3HT brush, we present a color plot that shows the ratio of the number of monomers that do and do not form $\pi - \pi$ bonds in figure 7.15. Higher the ratio, more are the number of number of monomers that form $\pi - \pi$ bonds. From figure 7.15 it is clear that with decreasing H, the ratio of the monomers that form $\pi - \pi$ bonds decreases. Also, with increasing R_p the ratio decreases. Therefore, we conclude here that bigger or deeper the particle into the brush, more disturbance is observed by the brush and more $\pi - \pi$ bonds are disrupted.

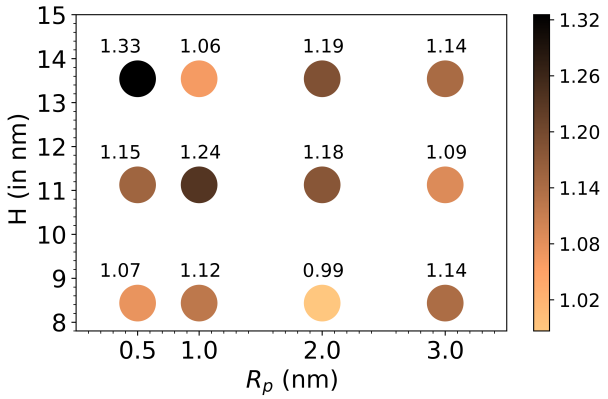

Figure 7.15: Ratio of particles that form $\pi - \pi$ bonds with respect to the monomers that do not form $\pi - \pi$ bonds for single particle insertion in isolated brushes.

Two particle insertion

In this section we insert two particles into the isolated brush. Figure 7.16 (a), (b), (c) and (d) illustrates the simulation snapshots of the particle with $R_p = 3.0$ at heights $H =$ 16.0nm (far above the brush case), 13.5nm, 11.1nm and 8.4nm respectively along the $x-, z-$plane.

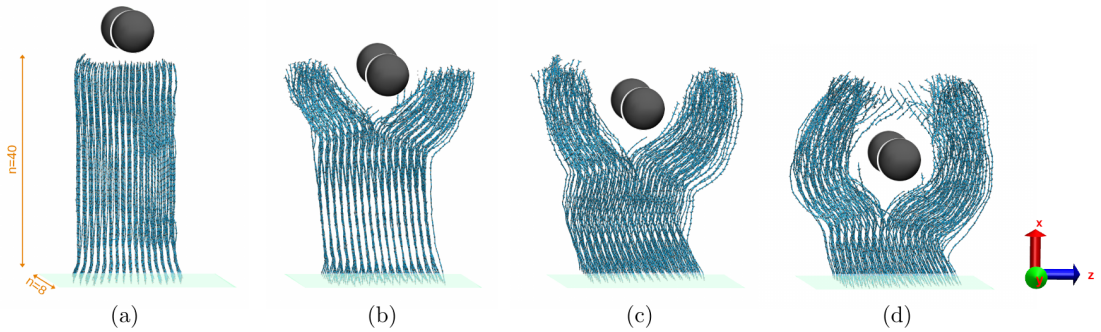

Figure 7.16: Simulation snapshots of two particles in isolated P3HT brush (a) before insertion, (b) at $H = 13.5$nm, (c) at $H = 11.1$nm and (d) at $H = 8.4$nm. View along $y-$direction.

Figure 7.17 shows the simulation snapshots along the $x-, y-$plane. Similar to the section above the π stacking direction is the z-axis.

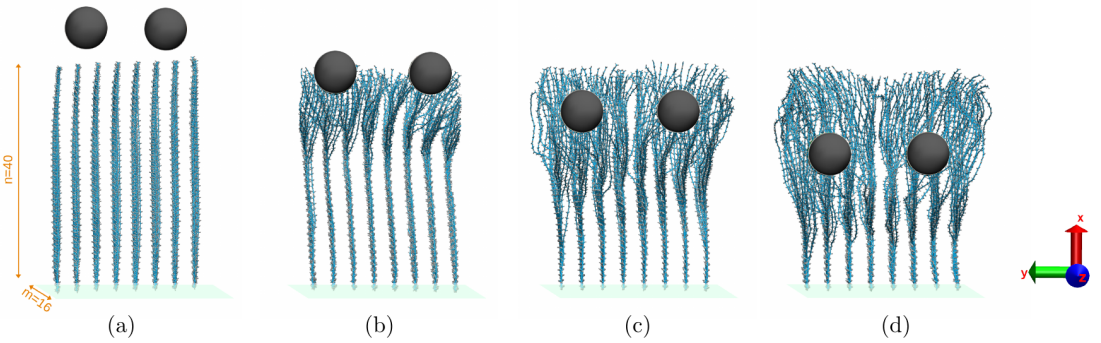

Figure 7.17: Simulation snapshots of two particles in isolated P3HT brush (a) before insertion, (b) at $H = 13.5$nm, (c) at $H = 11.1$nm and (d) at $H = 8.4$nm. View along $z-$direction.

We look at the monomer density along the $x-, y-$plane in this section because the radial symmetry is broken here as compared to the previous section. The monomer concentration profile along the $x-, y-$plane is shown in figure 7.18. A clear perturbation with increasing $R_p$and H is noticeable from the plot. This is further confirmed by figure 7.19 which plots the connections between the monomers that form $\pi - \pi$ bonds to get a

visual understanding of the percolation lines. The top plots in figure 7.19 gives a view along the $x-$,$y-$plane and the bottom plots show the view along the $x-$,$z-$plane with 26nm $< y <$ 28nm. In figure 7.19 (a), (b), (c) and (d) we see that for particle at $H = 13.5$nm the percolation lines for majority of the column remain fairly connected for all the radii. However, as the particle height is decreased down to $H = 8.4$nm in 7.19 (i), (j), (k) and (l) for $R_p = 0.5$nm, 1nm,2nm, and 3nm respectively longer percolation lines cease to exist in the column around and above which the particle is present. The disruption in the percolation lines is quite noticeable even for the smallest particle size $R_p = 0.5$nm.

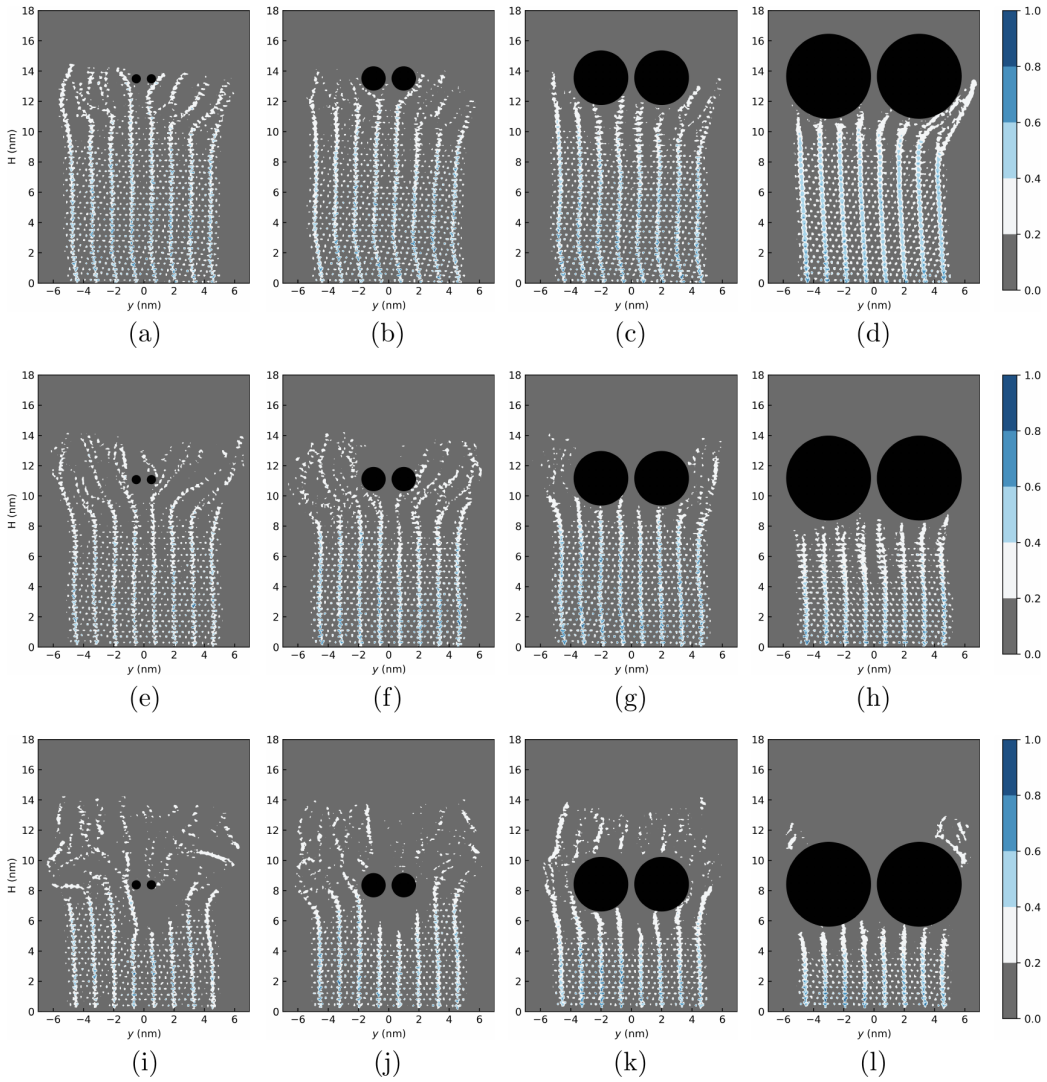

Figure 7.18: Monomer concentration profile along $x-, y-$plane for two particles insertion into an isolated brush column with particle radius $R_p = 0.5$nm, 1nm,2nm, and 3nm, and particle height $H = 13.5$ nm, 11.1 nm, and 8.4 nm.

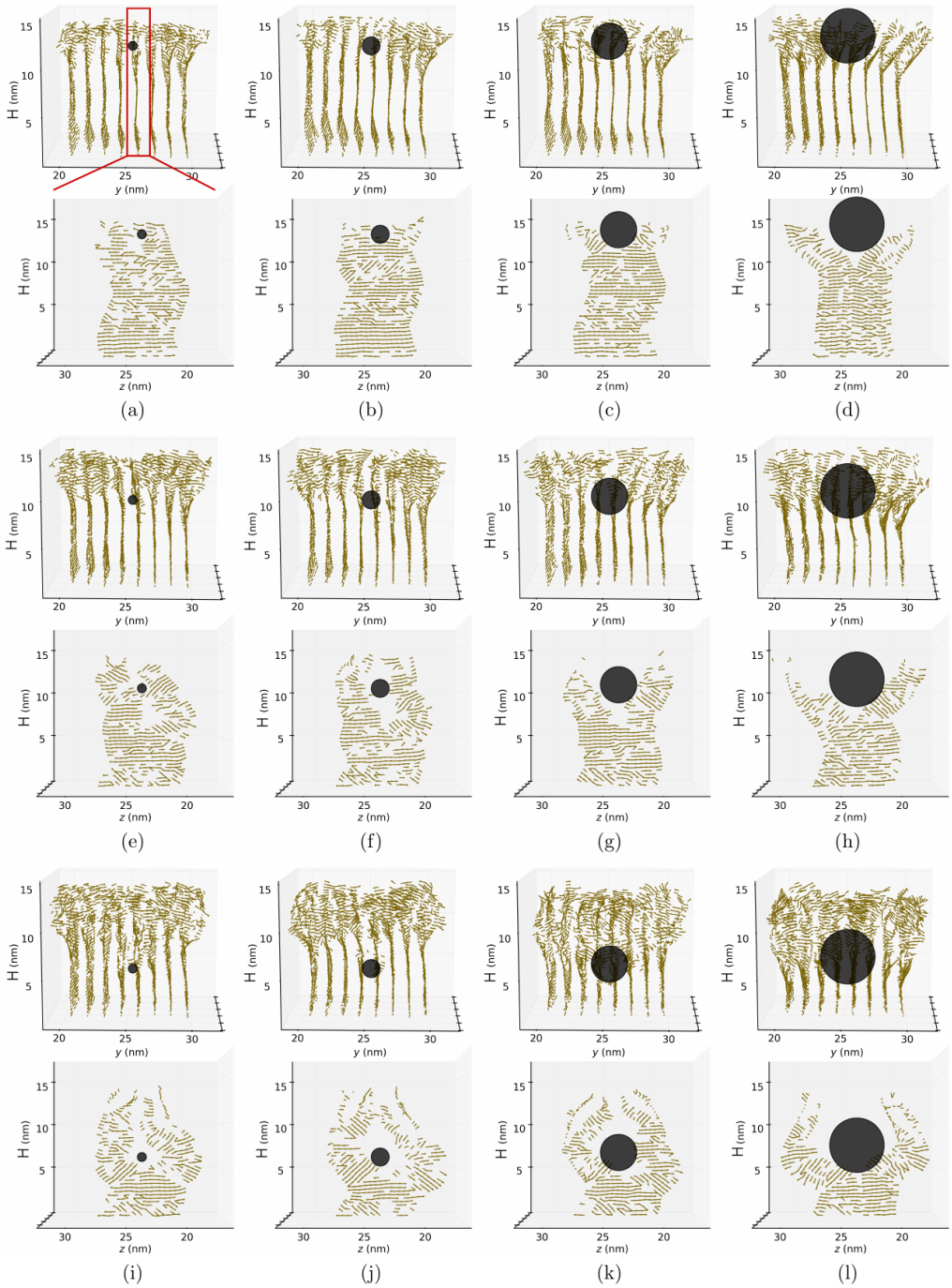

Figure 7.19: Percolation lines formed due to the formation of $\pi-\pi$ connection vectors for two particles insertion into an isolated brush column. View in the x-y plane (top) and x-z plane (bottom) for particle radius $R_p = 0.5$nm, 1nm, 2nm, and 3nm, and particle height $H = 13.5$nm, 11.1nm, and 8.4nm.

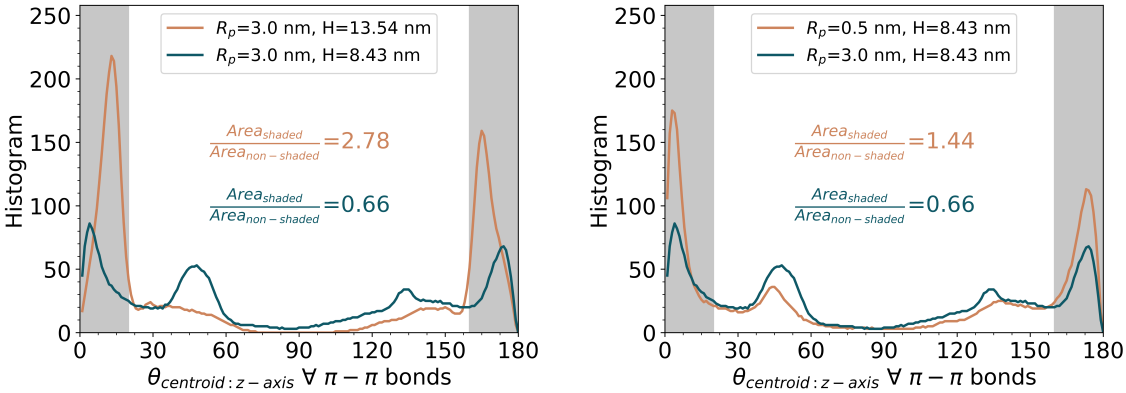

(a) (b)

Figure 7.20: Distribution of angle between the z-axis and the $\pi - \pi$ connection vector for two particles insertion in isolated brush with (a)$R_p = 3.0$nm; $H = 13.5$nm and $R_p = 3.0$nm; $H = 8.4$nm (b) with $R_p = 0.5$nm; $H = 8.4$nm and $R_p = 3.0$nm; $H = 8.4$nm

Similar to figure 7.14 we present in figure 7.20 the distribution of the angles between the $\pi-\pi$ connection vector and the z-axis for the cases (a) $R_p = 3.0$nm; $H = 13.5$nm and $R_p = 3.0$nm; $H = 8.4$nm and (b) $R_p = 3.0$nm; $H = 8.4$nm and $R_p = 0.5$nm; $H = 8.4$nm. Then we compute the area that is close to the $z-$axis (shown by shaded region) and the area that is further away from $z-$axis (the non-shaded area) and present their ratios. The higher this ratio, the more are the $\pi-$bonds aligned parallel to the $z-$axis. In figure 7.20 (a) the ratio between the areas that fall under the shaded and non-shaded region for $R_p = 3.0$nm; $H = 13.68$nm is 2.78 and for $R_p = 3.0$nm; $H = 8.4$nm is 0.66 which is 4 times less than the former. Similarly in 7.20 (b) for $R_p = 0.5$nm; $H = 8.4$nm the ratio is 1.44 and for $R_p = 3.0$nm; $H = 8.4$nm is 0.66. Therefore increasing the particle radius from 0.5nm to 3.0nm also substantially reduces the number of $\pi - \pi$ bonds that align parallel to the z-axis. Finally we calculate the number of monomers that do and no not form a $\pi - \pi$ bond to calculate their ratio. The higher the ratio, the more are the number of $\pi - \pi$ bonds in the system. The color coded percent ratios for the insertion of two particles in a isolated brush is shown in figure 7.21. Similar to figure 7.15, we see that increasing R_p and decreasing H leads to decrease in the percent ratio of the bonds that form a $\pi - \pi$ stack. Therefore, bigger or deeper the particle, less are the $\pi - \pi$ bonds.

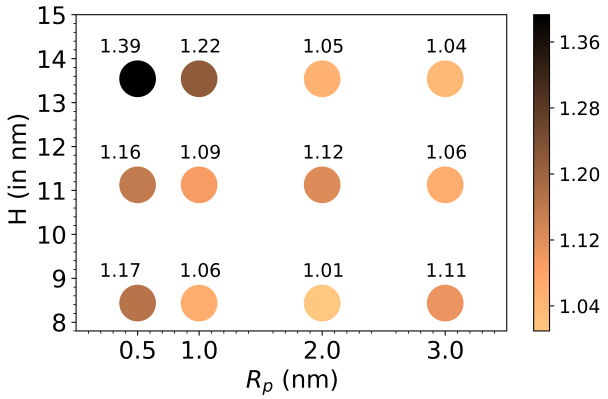

Figure 7.21: Ratio of monomers that do and do not form $\pi - \pi$ bonds for isolated brush system with two particles.

Similarly, this behavior is seen for both the study cases, where we include one LJ particle into the P3HT isolated brush and also where we include two LJ particles in the same brush. Therefore, overall, addition of particles leads to disruption of $\pi - \pi$ bonds in the brush. Bigger particles create bigger disturbances. Similarly, closer the particle/particles to the grafting surface, less are the number of $\pi - \pi$ bonds. This result is to be noted in the corner of the mind before turning to the next part.

Part 3: P3HT continuous brush

One particle insertion

In this part, we would carry the same analysis as we did in the previous part (with isolated P3HT brush) for a continuous P3HT brush that runs infinitely in the $y-z$ plane. The phenomenon of infinite P3HT brush is achieved by the virtue of periodic boundary conditions in the $y-z$ direction. Very less distance is kept between the brush and the box boundary during formation of the initial setup, so that the polymer on one end of the brush is able to interact with the polymer on the other end of the brush. Thus creating an infinitely long brush. Figure 7.22 illustrates the brush with particle of radius $R_p = 3.0$nm inserted at heights (a) very far above the brush, (b) at $H = 13.68$nm, (c) at $H = 11.39$nm and (d) at $H = 4.39$nm from the grafting surface. Therefore, smaller the H, closer is the particle to the grafting plane (the $y-z$ plane) . This part will again have one particle insertion study and two particles insertion study. The final results will in the end be compared to the isolated brush results. Although, at the moment, it seems quite rudimentary to carry out the tediously long procedure of the previous part also for the continuous brushes, it is guaranteed that the reader will not be disappointed with the end results of this chapter.

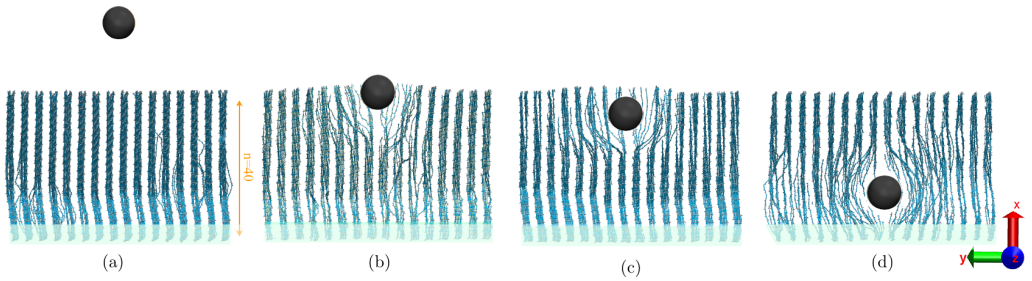

Figure 7.22: Simulation snapshots of single particle in continuous P3HT brush (a) before insertion, (b) at particle height $H = 13.68$nm, (c) at $H = 11.39$nm and (d) at $H = 4.39$nm.

Similar to figure 7.10, we look at the cylindrical radial monomer density of the polymer brush after inserting the particle in figure 7.23 for increasing R_p (left to right) and decreasing H (top to bottom). The periodicity of the thiophene rings and the packing structure is evident from the density distribution. Similar to before (figure 7.10), the area where the LJ particle is present, there exits a depletion area, followed by perturbed P3HT brushes that surround the particle. The bigger the particle, the more is the perturbation of the brush. Unlike the isolated brush, the continuous brush does not have extra space in the surrounding area to expand into. Therefore at the height where the particle is present (clearly evident for cases with $R_p = 3.0$nm, figure 7.23 (l)), we see higher monomer density after the depletion region because the polymers in the brush are pushed together due the presence of the LJ particle. Since the brush is continuously in the $y-z$ plane, there is also a push from the polymers from the box

mirror, and therefore the polymers have no other option than readjusting themselves in the confined space.

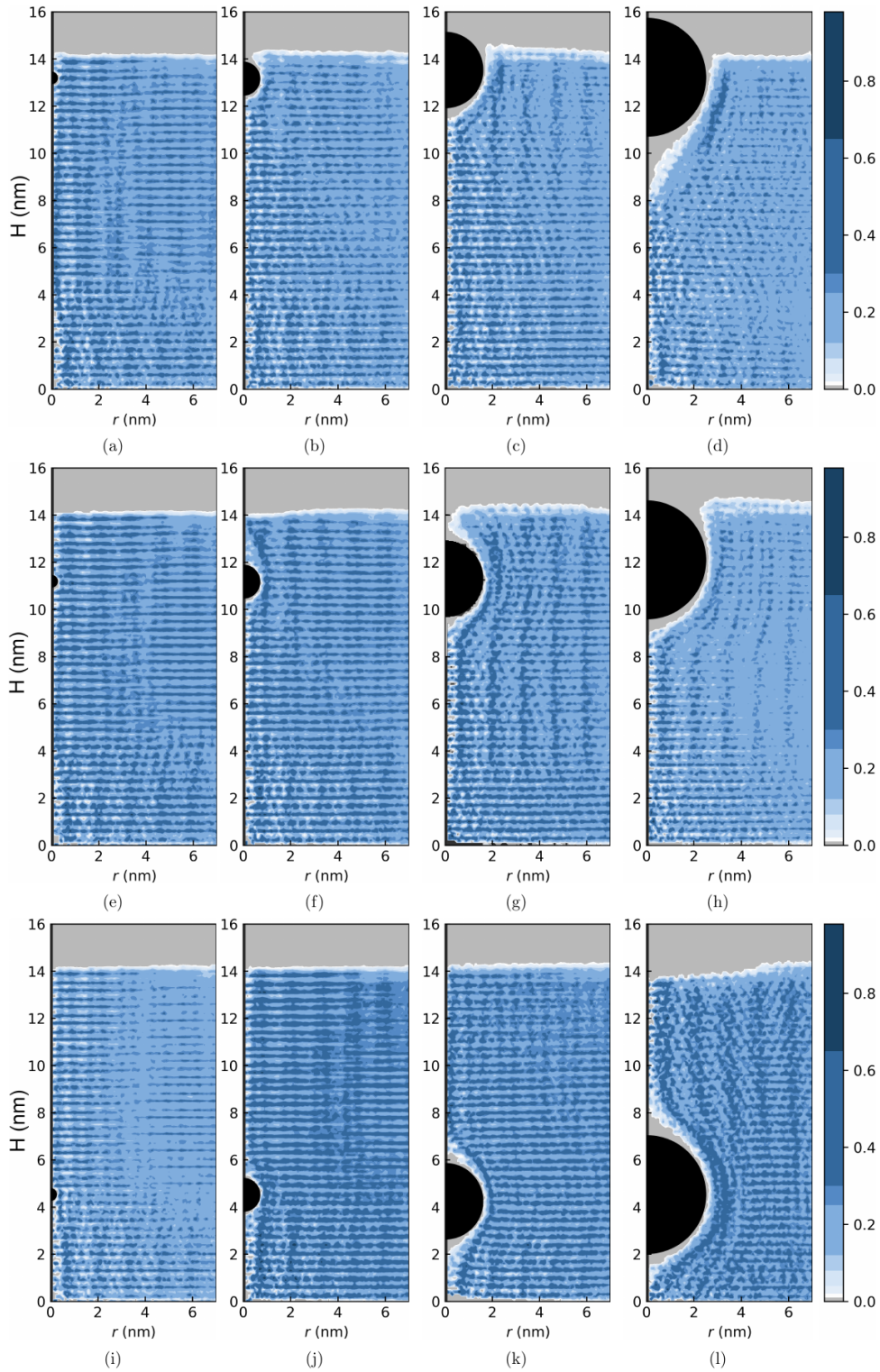

Figure 7.23: Cylindrical radial monomer concentration profile for single particle insertion in continuous P3HT brush for particle radius $R_p = 0.5\text{nm}, 1\text{nm}, 2\text{nm}$, and 3nm, with height $H = 13.68\text{nm}$, 11.39nm, and 4.39nm.

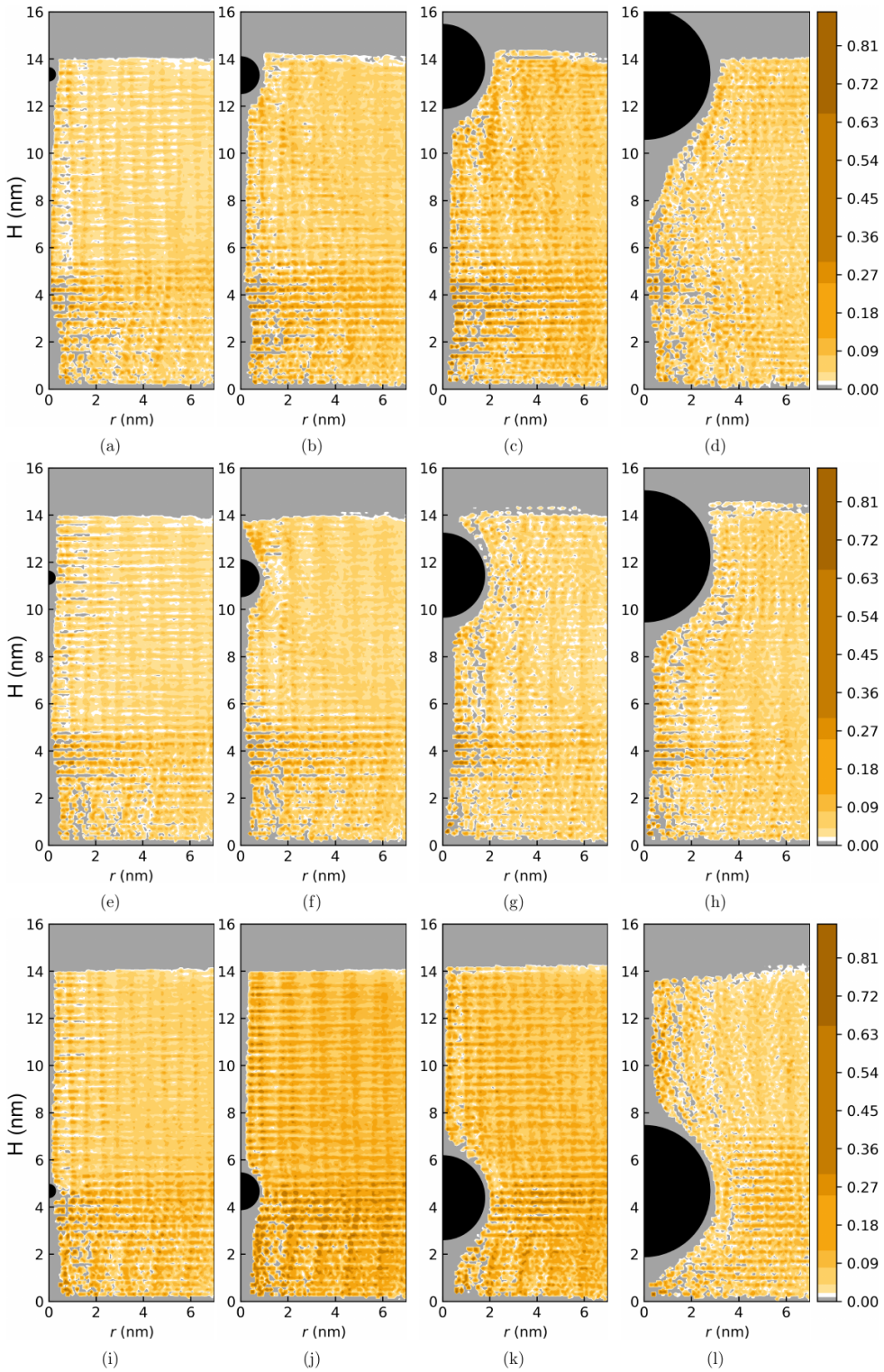

Figure 7.24: Cylindrical radial $\pi - \pi$ bond density profile for single particle insertion in continuous P3HT brush for particle radius $R_p = 0.5\text{nm}, 1\text{nm}, 2\text{nm}$, and 3nm, with height $H = 13.68\text{nm}$, 11.39nm, and 4.39nm.

Cylindrical radial π bond density for the monomers that form a $\pi - \pi$ stack with another monomer (using the rules introduced in section 7.2.3) is shown in figure 7.24 that shows the depletion area at the position of the particle, followed by rearrangement of the polymer brush around it. The $\pi-\pi$ stacking direction is along the $z-$axis. Figure 7.25 therefore plots the histogram of the angle between monomer monomer vector and the $z-$axis for undisturbed system in (a) and particle system with $R_p = 3$nm and $H = 4.39$nm in (b). In both the figures, we have 4 prominent peaks at 0^0, 45^0, 135^0 and 180^0. The peaks at 0^0 and 180^0 are an indication of the centroid vector being parallel to the $z-$axis. The peaks at $45^0$and 135^0 arise due to the kink in the brush. It is quite interesting the see that the kink we observed for isolated brush (figure 7.12) also persists for continuous brush, confirming that it not just any random artifact but is arising due to the fact that the stacking distance between the polymers in the brush govern the kink angle (7.25 (e)). Figure 7.25 (c) and (d) show a snapshot slice for the reference system and the particle perturbed system respectively. The overall result in figure 7.25 being that the reference system has ordered ($z-$axis parallelly oriented) $\pi-$bonds and non-$\pi-$bonds, however, the particle system has random oriented non-$\pi-$bonds.

As defined earlier percolation lines are the vectors connecting the center of mass of two monomers that form a $\pi - \pi$ bond. We present the percolation lines for all the cases for single particle insertion in a continuous P3HT brush in figure 7.26. For particle height $H = 13.68$nm and particle radius $R_p = 0.5$nm, 1nm, 2nm and 3nm the $\pi - \pi$ bond vectors are shown in figure 7.26 (a), (b), (c) and (d) respectively. Similarly for particle height $H = 11.39$nm it is shown in figure 7.26 (e), (f), (g) and (h) and for $H = 4.39$nm in figure 7.26 (i), (j), (k) and (l) respectively for the four radii, increasing from left to right. The top plots show view in the $x - y$ plane and the bottom plots the view along $x - z$ plane. At all the particle heights, as the particle radius increases we see increasingly longer percolation lines at the height where the particle is located. This becomes very clearly evident especially for $H = 4.39$nm in figure 7.26 (i), (j), (k) and (l). Bigger the particle, more are the $\pi - \pi$ bond connections. This figure presents a very interesting result when compared with figure 7.13 where we see the opposite effect. In the case of continuous brush, the volume taken away by the particle leads to more cramping up of the polymers thereby creating an overall reduction in monomer distance and in increase in $\pi - \pi$ bond connection. Unlike the isolated brush, the polymers in the continuous brush do not have additional surrounding space to expand into and therefore show the opposite effect compared to the isolated brush.

To quantify the aligning of the percolation lines along the $z-$axis as we see it in figure 7.26, we present the distribution of the angle the $\pi-$bond vector makes with the $z-$axis for two cases : (a) $R_p = 3.0$nm; $H = 13.68$nm and $R_p = 3.0$nm; $H = 4.39$nm and (b) $R_p = 3.0$nm; $H = 4.39$nm and $R_p = 0.5$nm; $H = 4.39$nm in figure 7.27(a) and (b) respectively. Then we compute the area that is close the $z-$axis (shown by shaded region) and the area that is further away from $z-$axis (the non-shaded area) and present their ratios, similar to the previous figures 7.14 and 7.20. For $R_p = 3.0$nm, i.e. for biggest particle radius, the ratio is 0.93 for $H = 13.68$nm and 1.94 for $H = 4.39$nm as seen from figure 7.27(a).

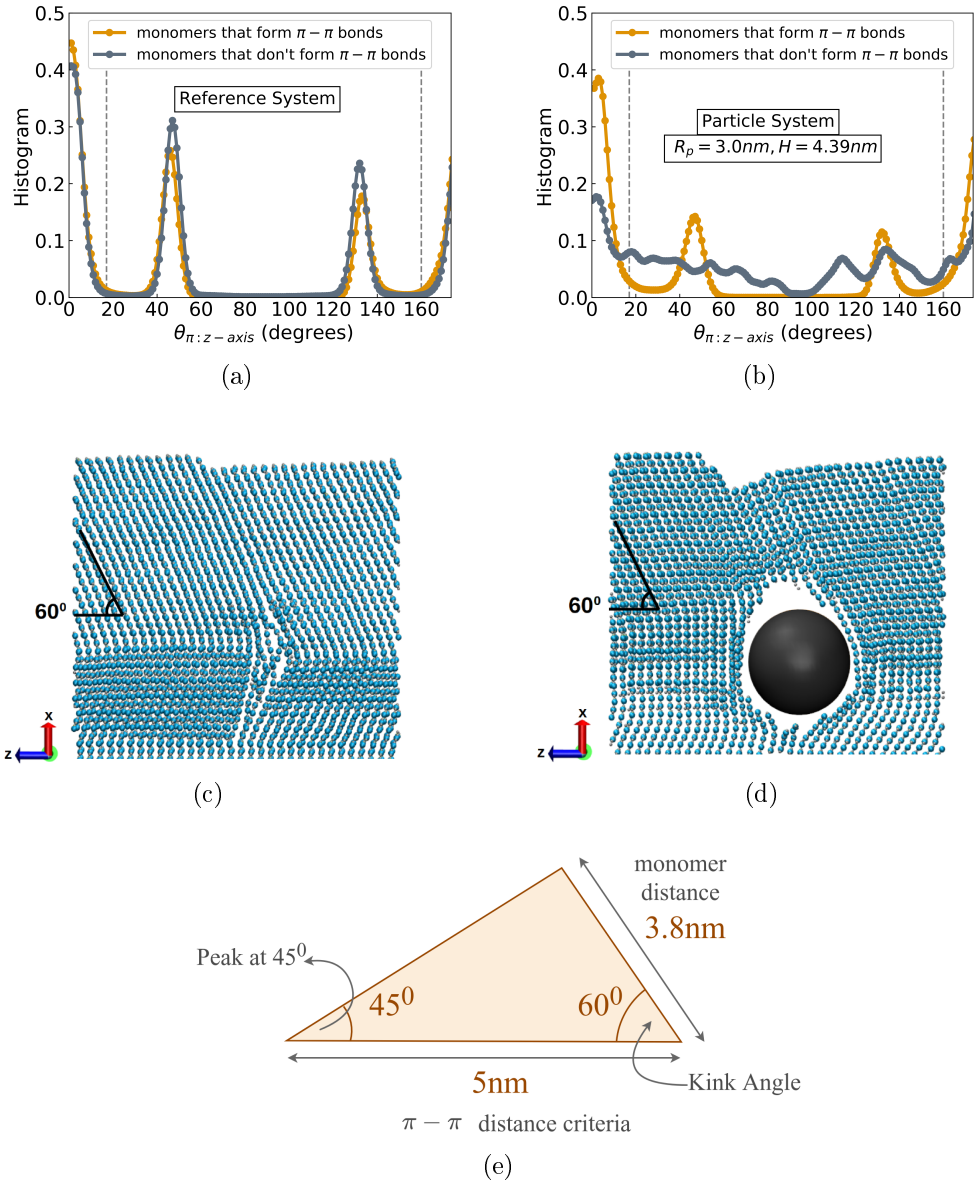

Figure 7.25: Histogram of the angle between monomer-monomer vector (the centroid vector) and the z-axis that do and do not form a $\pi-$ bond for (a) reference system and (b) for system with particle having $R_p = 3$nm and $H = 4.39$nm of continuous P3HT brush. Snapshot of a slice along the $y-$direction for (a) reference system and (b) system with particle. (e) Simple numerical analysis explaining the peaks at 45^0 and 135^0 of (a) and (b).

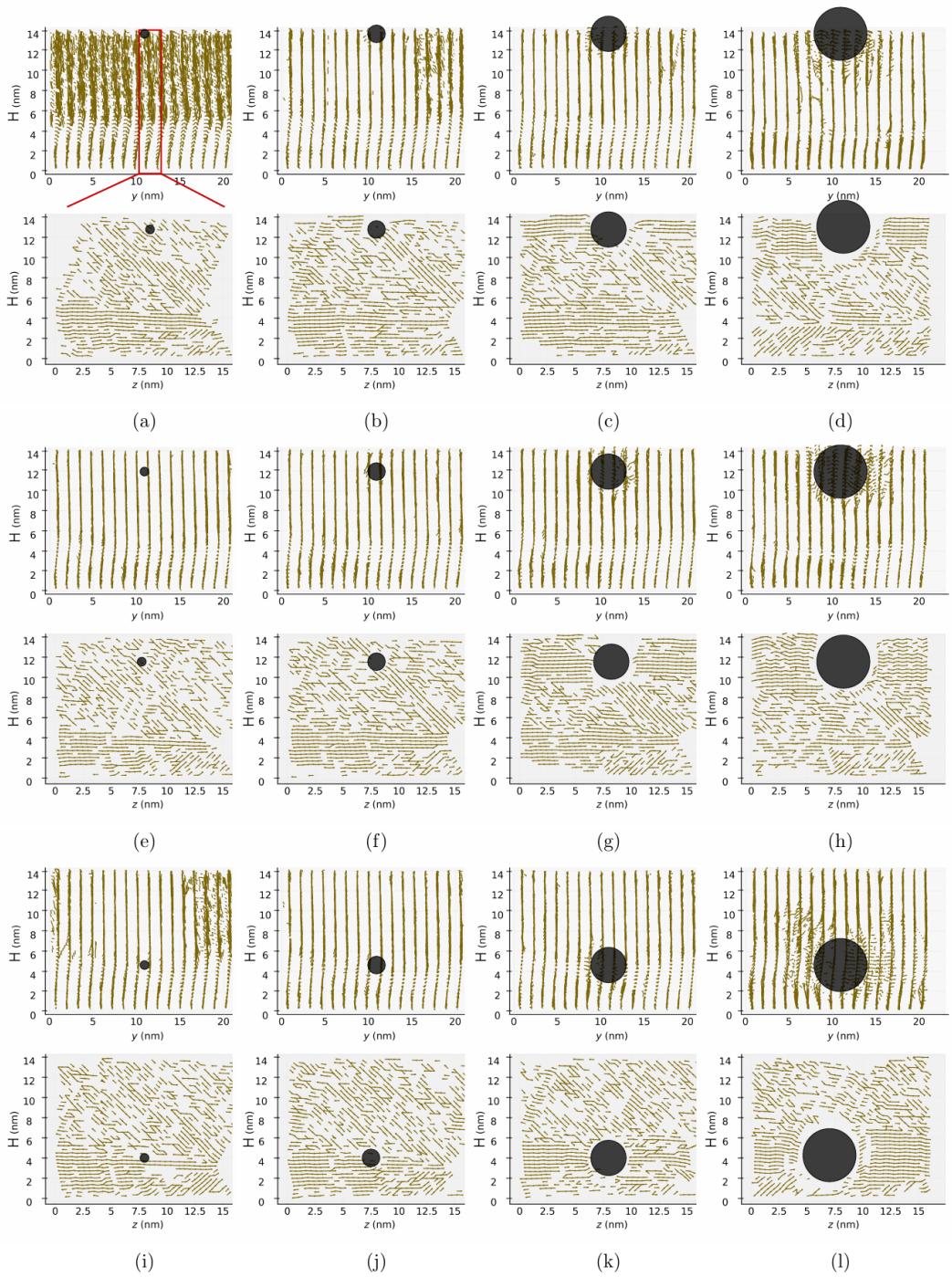

Figure 7.26: Percolation lines formed due to the formation of $\pi - \pi$ connection vectors for single particle insertion into continuous P3HT brush column. View in the x-y plane (top) and x-z plane (bottom) for particle radius $R_p = 0.5$nm, 1nm, 2nm, and 3nm, and particle height $H = 13.68$nm, 11.39nm, and 4.39nm.

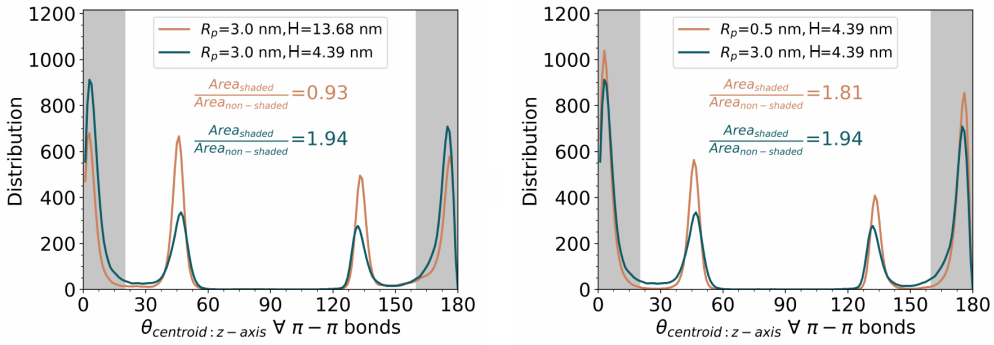

Figure 7.27: Distribution of angle between the z-axis and the $\pi-\pi$ connection vector for single particles insertion in continuous brush with (a)$R_p = 3.0$nm; $H = 13.68$nm and $R_p = 3.0$nm; $H = 4.39$nm (b) with $R_p = 0.5$nm; $H = 4.39$nm and $R_p = 3.0$nm; $H = 4.39$nm.

Therefore decreasing H increases the alignment of the percolation lines more parallel to the $z-$axis. In figure 7.27 (b) we see that for the particle height $H = 4.39$nm the ratio for $R_p = 0.5$ is 1.81 and for $R_p = 3.0$ the ratio is 1.94. The difference in the ratios in the later case is not as drastic as for the former, but is enough to conclude that increasing R_p promotes alignment of vectors along z-axis and leads to the formation of longer percolation lines. Again this result is in contradiction to what we observed for the isolated brush in figure 7.14 where decreasing particle height had resulted in decreasing alignment to the $z-$axis. The final assessment now is the calculation of total number of monomers that form $\pi - \pi$ bond and the number of monomers that do not. We present their ratios in figure 7.28. There we see that with increasing R_p and H the probability of $\pi - \pi$ over non- $\pi - \pi$ increases and attains a maximum at 0.65 for $H = 4.39$nm and $R_p = 3.0$nm.

Comparing figure 7.15 for particle insertion in isolated brush and figure 7.28 for continuous brush, we see that they show completely opposite trends. As mentioned before, this happens because the isolated brush has space around to expand into when encapsulating a particle, however for a continuous brush, there is no escape and the volume occupied by the LJ particle cramps up the P3HT polymers together decreasing their inter monomer distances and leading to formation of more $\pi - \pi$ bonds. This is a very interesting result as the nature of the P3HT (isolated or continuous) leads to two contradicting results and therefore is of particular interest when considering them as semiconductors for bio-sensing in organic transistors.

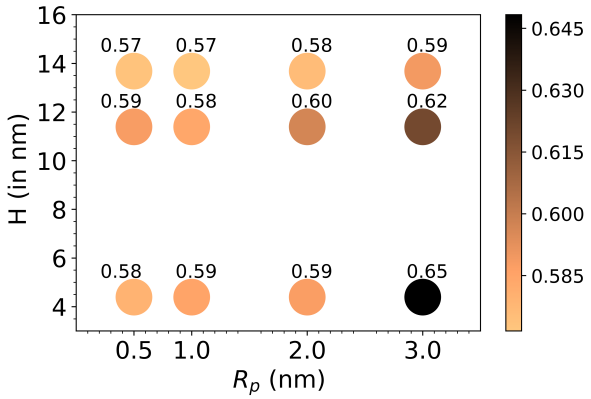

Figure 7.28: Ratio of monomers that do and do not form $\pi - \pi$ bonds for single particle insertion in continuous brushes.

Two particle insertion

This is the final part of the study where we now insert two LJ particles into the continuous brush structure. Figure 7.29 illustrates the simulation snapshots view taken from the $x-y$ plane for the particles of radii $R_p = 3$nm at heights (a) above the brush, (b) at $H = 13.68$nm, (c) at 11.39nm and (d) at 4.39nm as measured from the grafting surface which is at the bottom of the $y-z$ plane.

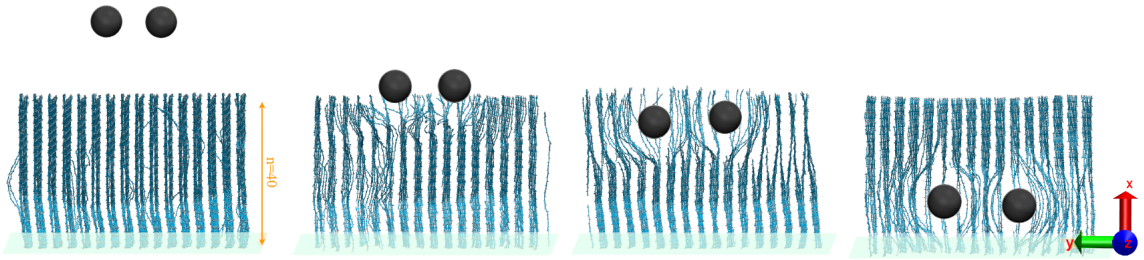

(a) (b) (c) (d)

Figure 7.29: Insertion of two spherical particles into a continuous P3HT brush, view along z axis (the $\pi-\pi$ stacking axis)

The monomer concentration profile along the $x-y$ plane is shown in figure 7.30. Again, like the in the previous parts, the particle is seen to create a clear perturbation in the brush with increasing R_p and decreasing H. For $H = 4.39$nm the polymer brush encloses the particle to be able to form $\pi-\pi$ bonds from above the particle (see figure 7.22 (i), (j), (k) and (l)). We plot the percolation lines by connecting the ring centers of the monomers that form a $\pi-\pi$ bond in figure 7.31. The top plots show the view along the $x-y$ plane and the bottom plots along the $x-z$ plane. For particle radii $R_p = 0.5$nm and 1nm we see that the presence of the particle is not creating any noteworthy change in behavior of the percolation lines at $H = 13.68$nm, 11.39nm or 4.39nm (see figure 7.31 (a), (b), (e), (f), (i) and (j)). For $R_p = 2$nm in figure 7.31 (c), (g) and (k)), the vectors are aligning parallel to the $z-$axis at the particle height H. This is seen further enhanced for $R_p = 3$nm in figure 7.31 (d), (h) and (l) below plots. The presence of the particles with larger R_p strengthens the percolation network and its alignment along the $z-$axis. Similar to the one-particle system in continuous brush, this happens because the brush is infinite in the $y-z$ plane and so particles with larger R_p push the polymers together so that they are forced to find an arrangement that tends to minimize the energy of the system leading to the formation of an enhanced $\pi-\pi$ network. Thus the overall effect of the inclusion of two particles in continuous brush leads to increasing $\pi-\pi$ connections and is therefore similar to the above section 7.3 for the one-particle system in continuous brush.

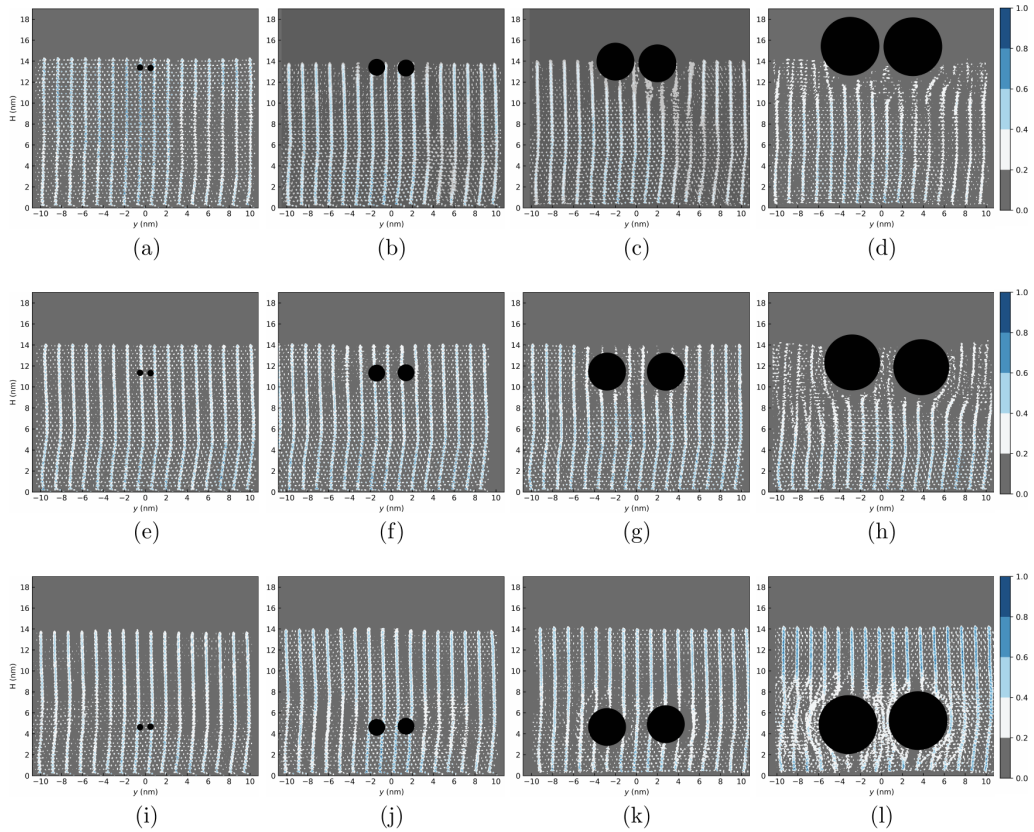

Figure 7.30: Insertion of two spherical particles into a continuous P3HT brush, view along z axis (the $\pi - \pi$ stacking axis)

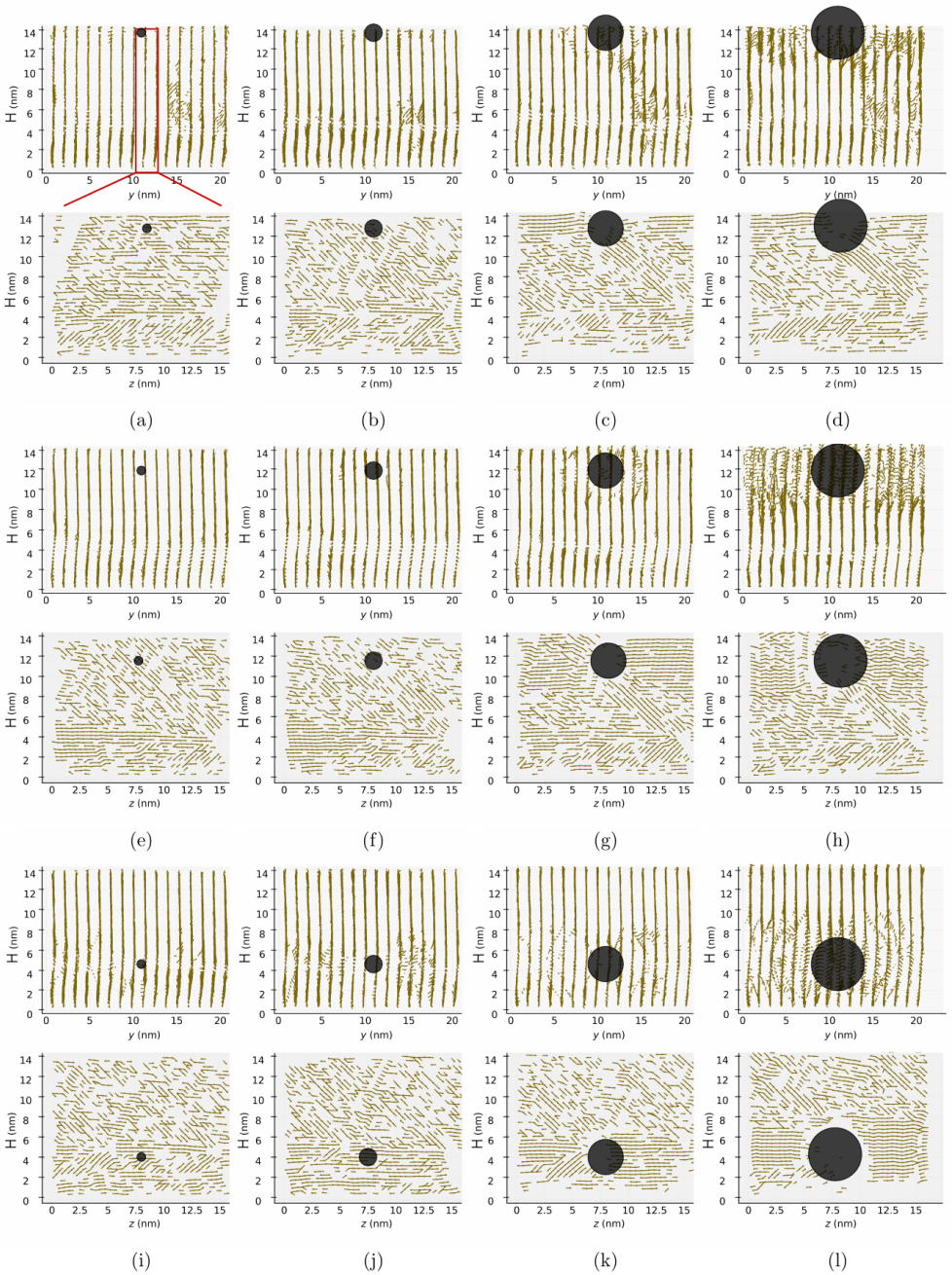

Figure 7.31: Monomer concentration profile along the $x-y$ plane for two particle insertion in continuous P3HT brush for particle radius $R_p = 0.5\text{nm}, 1\text{nm}, 2\text{nm}$, and 3nm, with height $H = 13.68\text{nm}$, 11.39nm, and 4.39nm.

Similar to figure 7.27 we present in figure 7.32 the angle histogram the $\pi-$vectors make with the $z-$axis. In figure 7.32(a) the ratio between the areas that fall under the shaded and non-shaded region for $R_p = 3\text{nm}$; $H = 13.68\text{nm}$ is 1.50 and for $R_p = 3\text{nm}$; $H = 4.39\text{nm}$ is 2.36. Therefore $x = 4.39\text{nm}$ has more $\pi - \pi$ bonds that align parallel

to the $z-$axis compared to $H = 13.68$nm. Similarly in 7.32 (b) for $R_p = 0.5$nm; $H = 4.39$nm the ratio is 1.27 and for $R_p = 3.0$nm; $H = 4.39$nm is 2.36. This denotes that increasing R_p also promotes alignment along the $z-$axis.

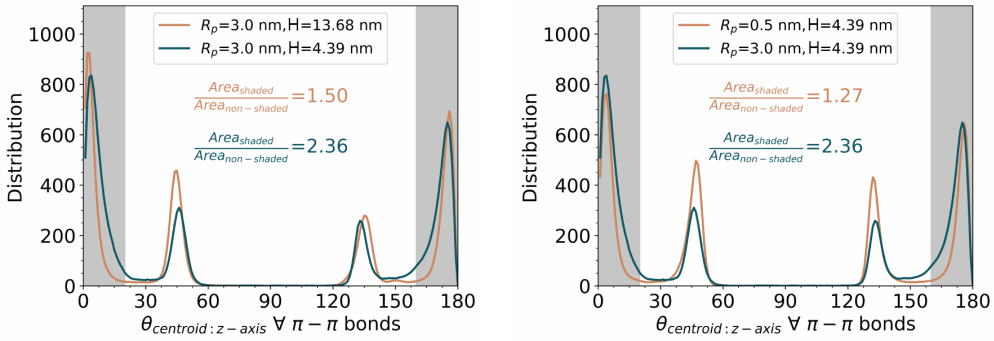

(a) (b)

Figure 7.32: Distribution of angle between the z-axis and the $\pi - \pi$ connection vector for two particles insertion in continuous brush with (a)$R_p = 3.0$nm; $H = 13.68$nm and $R_p = 3.0$nm; $H = 4.39$nm (b) with $R_p = 0.5$nm; $H = 4.39$nm and $R_p = 3.0$nm; $H = 4.39$nm

Lastly we calculate the number of monomers that do and do not form $\pi - \pi$ bonds in figure 7.33 and color code the ratio. Higher the ratio, more are the number of $\pi-$bonds. Here, we again see that with increasing R_p and decreasing H the ratio of $\pi - \pi$ to non-$\pi - \pi$ increases and is maximum at 0.76 for $H = 4.39$nm and $R_p = 3.0$nm. Therefore increasing the particle radius and decreasing the particle height again leads to formation of more $\pi - \pi$ bonds as shown by figure 7.33.

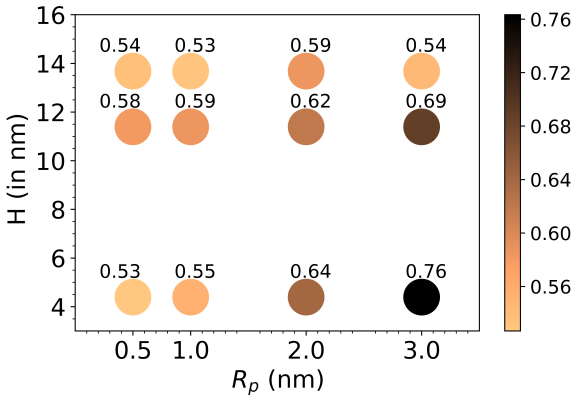

Figure 7.33: Ratio of particles that form $\pi - \pi$ bonds with respect to the monomers that do not form $\pi - \pi$ bonds for single particle insertion in continuous brushes.

7.4 Conclusion

This work used coarse grained Martini model for modeling P3HT polymer brushes using molecular dynamics. We considered two kinds of brushes: (1) isolated brush and (b) continuous brush both with a fixed grafted plane. Then we inserted an LJ particle with radius varying from 0.5nm to 3nm at varying heights from the bottom grafted plane. In both the cases, we saw that the presence of a particle disrupts the brush, changing the way it forms $\pi - \pi$ bonds.

For the first part, with isolated brushes, increasing particle radius and decreasing particle height in the brush column resulted in decrease of monomers that form $\pi - \pi$ bonds, with smaller lengths of percolation lines, and deviation from parallel alignment of the $\pi-$bond vectors with the $z-$axis. Opposite trend was seen in the second part, with continuous brush, that increasing particle radius and decreasing particle height lead to increase of $\pi - \pi$ bonds in the system. Longer percolation lines aligned along the $z-$ axis was seen for continuous brush, after the particle insertion. Therefore, the way brushes are created are critical in the performance of the OTFTs. Such an effort will be beneficial in the context of OTFTs-based biosensors that make use of conjugated polymers for current conduction.

References

[1] Sunil K Arya, Pratima R Solanki, SP Singh, K Kaneto, Manoj K Pandey, Monika Datta, and Bansi D Malhotra. Poly-(3-hexylthiophene) self-assembled monolayer based cholesterol biosensor using surface plasmon resonance technique. *Biosensors and Bioelectronics*, 22(11):2516–2524, 2007.

[2] Marco Bernardi, Michele Giulianini, and Jeffrey C Grossman. Self-assembly and its impact on interfacial charge transfer in carbon nanotube/p3ht solar cells. *ACS nano*, 4(11):6599–6606, 2010.

[3] Giovanni Bussi, Davide Donadio, and Michele Parrinello. Canonical sampling through velocity rescaling. *The Journal of chemical physics*, 126(1):014101, 2007.

[4] Stefano Casalini, Carlo Augusto Bortolotti, Francesca Leonardi, and Fabio Biscarini. Self-assembled monolayers in organic electronics. *Chemical Society Reviews*, 46(1):40–71, 2017.

[5] Xiong Gong, Matthew R Robinson, Jacek C Ostrowski, Daniel Moses, Guillermo C Bazan, and Alan J Heeger. High-efficiency polymer-based electrophosphorescent devices. *Advanced Materials*, 14(8):581–585, 2002.

[6] Berk Hess, Henk Bekker, Herman JC Berendsen, and Johannes GEM Fraaije. Lincs: a linear constraint solver for molecular simulations. *Journal of computational chemistry*, 18(12):1463–1472, 1997.

[7] Jochen S Hub, Bert L De Groot, and David Van Der Spoel. g_wham a free weighted histogram analysis implementation including robust error and autocorrelation estimates. *Journal of chemical theory and computation*, 6(12):3713–3720, 2010.

[8] Roland G Huber, Michael A Margreiter, Julian E Fuchs, Susanne von Grafenstein, Christofer S Tautermann, Klaus R Liedl, and Thomas Fox. Heteroaromatic π-stacking energy landscapes. *Journal of chemical information and modeling*, 54(5):1371–1379, 2014.

[9] William Humphrey, Andrew Dalke, and Klaus Schulten. Vmd: visual molecular dynamics. *Journal of molecular graphics*, 14(1):33–38, 1996.

[10] Christoph Janiak. A critical account on π–π stacking in metal complexes with aromatic nitrogen-containing ligands. *Journal of the Chemical Society, Dalton Transactions*, (21):3885–3896, 2000.

[11] Sabine Ludwigs. *P3HT Revisited-From Molecular Scale to Solar Cell Devices*, volume 265. Springer, 2014.

[12] Sanwardhini Pantawane and Stephan Gekle. Temperature-dependent conformation behavior of isolated poly(3-hexylthiopene) chains. *Polymers*, 14(3), 2022.

[13] Kyra N Schwarz, Tak W Kee, and David M Huang. Coarse-grained simulations of the solution-phase self-assembly of poly (3-hexylthiophene) nanostructures. *Nanoscale*, 5(5):2017–2027, 2013.

[14] Preethi Seshadri, Kyriaki Manoli, Nicole Schneiderhan-Marra, Uwe Anthes, Piotr Wierzchowiec, Klaus Bonrad, Cinzia Di Franco, and Luisa Torsi. Low-picomolar, label-free procalcitonin analytical detection with an electrolyte-gated organic field-effect transistor based electronic immunosensor. *Biosensors and Bioelectronics*, 104:113–119, 2018.

[15] Sandeep K Sharma, Rahul Singhal, BD Malhotra, Neeta Sehgal, and Ashok Kumar. Biosensor based on langmuir–blodgett films of poly (3-hexyl thiophene) for detection of galactose in human blood. *Biotechnology letters*, 26(8):645–647, 2004.

[16] Sandeep K Sharma, Rahul Singhal, BD Malhotra, Neeta Sehgal, and Ashok Kumar. Lactose biosensor based on langmuir–blodgett films of poly (3-hexyl thiophene). *Biosensors and Bioelectronics*, 20(3):651–657, 2004.

[17] Rahul Singhal, Asha Chaubey, Keiichi Kaneto, W Takashima, and BD Malhotra. Poly-3-hexyl thiophene langmuir-blodgett films for application to glucose biosensor. *Biotechnology and bioengineering*, 85(3):277–282, 2004.

[18] Samuel W Thomas, Guy D Joly, and Timothy M Swager. Chemical sensors based on amplifying fluorescent conjugated polymers. *Chemical reviews*, 107(4):1339–1386, 2007.

Chapter 8

Conclusion

In this thesis, the molecular dynamics simulations are employed to address several issues in the field of polymer characterization. We find that molecular dynamics simulations provides a very robust numerical and statistical tool to quantify the physicochemical processes that occur at the atomistic scale in this systems. Even the simplified forcefields (CG models) prove very good in replicating the conformational properties of the polymers, and can be up-scaled easily to larger time and length scales for studying microscopic systems as whole. The applications of molecular dynamics discover various polymers and their aspects. The problems addressed in this thesis are revised again in this chapter to maintain the uniformity of the whole thesis and to give the reader an overview of the conclusions.

8.1 Poly(3-hexylthiophene) chains and their temperature-dependent conformation behavior

Since 2003 up until today P3HT is one of the "fruit-fly" polymers under study for understanding the organic photovoltaic properties. Understanding the confromational behavior is the key to increasing the efficiency of these devices. However, this has not been very straightforward because of the complex way P3HT behaves with itself under different temperature and solvent conditions. Because the aggregates that are responsible for electron mobility in these devices are formed as a result of self-assembly, and changing the system conditions affect the solvation of the polymer leading to a dizzying diversity of optical, electrical and conformational features, which are not particularty quite easy to measure or interpret. This is further complicated in the literature by samples of the polymers with varying molecular weights, regioregularities and solvent types. Therefore, chapter 3 starts with a simpler approach, and as a first step, tries to show the reader a way to quantify very simple, non-branched, non-charged LJ polymers with varying attraction potential. With temperature as a variable, for polymers with 200 beads, it is shown that the $\langle S^2 \rangle$ (mean squared radius of gyration) and D_{max} (the maximum distance between any two monomers of the polymer), are two of the criteria that can be used in distinguishing *stiff*, *semi-flexible* and *flexible* polymers. *Stiff* polymers show increasing $\langle S^2 \rangle$ and D_{max} with decreasing temperature. At low temperatures *stiff* polymers are rod-like structures and at high temperatures they behave like a random coil. *Flexible* polymers show decreasing $\langle S^2 \rangle$ and D_{max} with decreasing temperature. At low temperatures, *flexible* polymers form toroid and bundle aggregates and at high temperature the polymer acts like a random coil. *Semi-flexible* polymers first show increasing $\langle S^2 \rangle$ and D_{max} with decreasing temperature followed by a sudden drop. The collapsed conformations decreases the surface energy but at the cost of high bending energy. At low temperatures, *semi-flexible* polymers form rings and hairpins and at high temperature the polymer again is a random coil. So in summary, we find a relation of the aggregation properties of the polymers to the nature of their $\langle S^2 \rangle$ vs T and D_{max}vs T curves. This simple analysis we carry forward to determine the identity of P3HT. Atomistic simulations together with solvent are very computationally expensive, therefore, for P3HT we first present atomistic simulation results of $\langle S^2 \rangle$ vs T in vacuum. Then we adopt a CG model and present the same results to validate the reliability of the CG model in comparison to the atomistic one. By proving that the CG model replicates the atomistic model quite well in vacuum, then we present the analysis of the CG model in THF solvent to reproduce the experimental setup by Panzer et al. [2, 1]. The CG model simulations in THF solvent showed very contrasting results compared to the earlier vacuum simulations. The solvent simulations of the CG polymer showed a sharp transition at around 220K, which

didn't exist for the vacuum simulations. This swelling transition was close to that of the spectroscopic experiments by Panzer et al. [2, 1] where they found a shift from red to blue absorption spectra when they decreased the temperature from 300K to 170K. This event they correlated with changes in conjugation length of the polymer (thereby a change in their aggregation forms). This phenomenon was astonishingly also captured by our CG-solvent simulations. In this chapter we showed that P3HT attains three different aggregated forms: bundles, toroids and random coils. The probability transition of P3HT aggregating into one of these three forms, in the presence of solvent, changes at temperature around 220K and we outline a clear swelling of D_{max} at that temperature. Our simulations help answer the hypothesis of the experiment work of Panzer et al. and reports that the swelling mentioned by Panzer et al. is a result of increasing frequency of elongated bundle structures than the comparatively smaller globule and toroid structures observed at higher temperatures. Using the method established for distinguishing *stiff*, *semi-flexible* and *flexible* polymers by LJ polymers in the beginning, we also report that P3HT behaves like a *flexible* polymer.

8.2 Microplastics: Monomer effects of biodegradable polymers on building blocks of DNA

Environmental issues, such as plastic pollution have pushed researchers to investigate other alternatives for the conventional plastics largely in use to this date. Biodegradable polymers such as polylactic acid (PLA), polyglycolic acid (PGA) and polyhydroxyalkanoate (PHA) are the upcoming biodegradable options already getting adopted for a large variety of applications. Since almost upto 95% of these polymers can breakdown to it's individual monomers during the process the degradation, the use of these materials will lead to saturation of phenomenally big amounts of microplastics in all kinds of ecological niches. Chapter 4 addresses to focus light on this issue by studying the free energy between the monomers of PLA, PGA and PHA with the nucleobases of our DNA namely, adenine (A), guanine (G), cytosine (C) and thymine (T). Since water is the natural solvent all living processes are carried out in, we carried out the free energy simulations between the above entities in water. All nucleobases A, G, C and T bind preferentially to the monomers PLA, PGA and PHA at a distance of around $0.5nm$. The binding preference of the monomers is seen more towards the nucleobases A, G in contrast to C, T. However, none of the PMF energies are greater than $\Delta E = 1.5kT$ thereby we notice only weak interaction between the monomers and the DNA in our simulations. This chapter also carried out free energy simulations between oligomers with 5 repeats and DNA hairpin loop. The potential mean force reported is $\Delta E = 5.03kT$ for PLA oligomer, $\Delta E = 5.39kT$ for PGA oligomer and $\Delta E = 7.46kT$ for PHA oligomer when pulled towards DNA hairpin. Thus nucleobases-monomer interactions are not very strong to hinder the working of

most the living beings in the nature.

8.3 Martini coarse grained models of hyaluronic acid and alginate

The employment of coarse grained (CG) models in a variety of simulations, as seen from chapters 3 and 7, has proven to be quite a valuable tool to extend the time and length scales beyond what is generally feasible with the conventional all atomistic models. The Martini coarse graining approach aims at providing a single model that is computationally fast and easy to use, while still being flexible enough to be suitable to a large range of biomolecular systems. However, the most common problem, for a researcher, arises due to the lack of database of such Martini forcefields. While it is quite easy to build/acquire atomistic forcefields via data banks and topology builders, no such platform exits for customizable Martini coarse grained forcefields. Chapter 5 teaches the reader a simple way to create such Martini CG forcefields by using hyaluronic acid (HA) and alginate (AG) polymers as examples. This chapter coaches a step by step approach in creating a Martini CG model for a polymer with "n" repeats from its 4 repeat atomistic model. Using this method, a code was written as a part of the PhD work, that can create all topology and structure file for a Martini CG HA as well as AG polymer with any number of repeats. Using this, we reported the gelation process of both the polymers. The HA and AG polymers where chosen in particular because of the lack of literature on their coarse grained models and large applicability in the field of 3D bioprinting as detailed in sections 1.5 and 5.1. Chapter 5 also provides a detailed validity of the Martini CG models by comparing to the atomistic model counterparts of the polymers. We report very good agreement between the atomistic and the CG models by comparing the global properties of the polymers such as end to end distance ($R_{\text{end to end}}$), root mean squared displacement ($RMSD$), radius of gyration (R_g) . This chapter also captures the whole process of gel formation for HA and CG with different solvent ionic concentrations and reports the stability of these gels upto 1 micro second, which is quite large of a timescale for MD simulations. For the gelation process of HA, we report an amazing match with the theoretical scaling network area of the gel with the ion concentration.

8.4 Monofunctional Vinyl Cyclopropanes: Effect of hydrogen bonding on their polymerization behavior

The work presented in chapter 6 was carried out hand in hand with the experiments by Schaumacher et al. [3, 4] who carried out polymerization experiments on VCPs (with different side chain groups) at different time intervals to study their polymerization rates by monitoring the monomer conversion with time. They found different polymerization of the VCPs with different side groups and attributed this phenomenon to the pre-polymerization organization of the monomers based on their H-bonding capability. This aim of this work was to computationally evaluate the pre-polymerization organization of the monomers and compute the total H-bonds for each kind. The first part of the chapter deals with three different H-bonding functional units namely the amide, the urethane and the urea only in the side chain of the monofunctional VCPs, with ester as the linkage between the side chain and the VCPs for the polymerization. We carry out bulk simulations and present the total and average number of H-bonds in each of the bulk simulations. We then present the radial distribution function (RDFs) of different atoms in each monomer to quantify if there's a difference in the bulk organisation of the monomers. We also take a look at other bulk properties of the VCPs like the root mean squared displacement, orientation parameter to give an insight to their structural and organizational differences pre-polymerization. We do not see any particular change in the RDFs and orientiation parameter for the different monomers, however, the H-bonding capacity of the monomers shows a direct relation to the polymerization rates of the monomers found experimentally. In the second part of the chapter, we study a set of monomers that bear H-bonding sites at two different position in the VCPs: an amide group that links the side chain to the cyclopropane and different organic functional groups (amide, urethane and urea) that are able to form H-bonding to different extents in the side chain in order to compare their behavior. We carry out similar bulk analysis as in the first part. The monomers that have computationally higher number of H-bonds experimentally show highest polymerization rates of all the monomers. We report a clear dependency between the hydrogen bonding capacity of the monomers and the polymerization speed. In general the amide linked VCPs the later part showed a much faster polymerization compared to the ester linked monomers earlier part. This chapter enables the future research in designing customized VCPs with better polymerization conversion rates.

8.5 Poly(3-hexylthiophene) brushes: Effect of Particle Insertion on $\pi - \pi$ stacking

Investigations in the branch of polymer brushes were traditionally started from polymers such polyethylene, polystyrene and later on more functional branches made out of ampliphilic, charged, thermo- and photo- responsive were added into the study of polymer brushes to enrich their properties and extend their application. Involvement of highly functional conjugated and conductive polymers showed a promising development in the field of brushes. Due to extraordinary increase in the magnitude of their electronic and photonic properties after formation of self-assemblies, P3HT have gained a lot of attention in the field of organic transistors for applications in solar cells and biosensors. Understanding the deformity caused in the P3HT brushes due to the intrusion of an external particle is therefore an important topic to discuss to evaluate its effect on the polymer's electronic properties as a virtue of the $\pi - \pi$ bonds in the brushes. Detailed motivation behind this work is discussed in sections 7.1 and 1.7. Chapter 7 reports various results on the inclusion of a non-charged LJ particle of varying sizes into finite and infinite P3HT brush. In this chapter we compute and compare particle density, $\pi - \pi$ bond density and network, and the alignment of the $\pi - \pi$ bonds and their percent ratio for both finite and infinite systems. It gives a complete overview of the nature of the $\pi-$stacking and its networking and the importance of studying the two systems individually.

The distribution of the polymer brush in both the cases, around the LJ praticle lead to an immediate depletion area followed by immediate increased density of the monomers. For finite brushes, with increasing LJ particle radius and decreasing particle height in the brush column resulted in decrease of monomers that form $\pi - \pi$ bonds. However, for infinite brushes, we reported and opposite trend, i.e., with increasing LJ particle radius and decreasing particle height in the brush column resulted in increase of monomers that form $\pi - \pi$ bonds.

This chapter accounts for one more study, for determining the free energy required to break individual $\pi - \pi$ bonds between two neighboring P3HT chains. $\pi - \pi$ stacked P3HT chains with monomers of length $2 \leq n \leq 16$ were considered for this case. We concluded that the energy for $\pi - \pi$ stack between two single thiophene groups is about 3.5kcal mol^{-1}. We observe for when pulling two single monomers the energy is 3.6kcal mol^{-1} . The difference is likely due to the presence of the side chains in addition to the thiophene rings.

References

[1] Fabian Panzer, Heinz Baessler, and Anna Koehler. Temperature induced order–disorder transition in solutions of conjugated polymers probed by optical spectroscopy. *The journal of physical chemistry letters*, 8(1):114–125, 2017.

[2] Fabian Panzer, Heinz Baessler, Ruth Lohwasser, Mukundan Thelakkat, and Anna Koehler. The impact of polydispersity and molecular weight on the order disorder transition in poly (3-hexylthiophene). *The journal of physical chemistry letters*, 5(15):2742–2747, 2014.

[3] Soeren Schumacher, Sanwardhini Pantawane, Stephan Gekle, and Seema Agarwal. Theoretical and experimental study of monofunctional vinyl cyclopropanes bearing hydrogen bond enabling side chains. *Macromolecules*, 54(1):11–21, 2021.

[4] Sören Schumacher, Sanwardhini Pantawane, Stephan Gekle, and Seema Agarwal. The effect of hydrogen bonding on polymerization behavior of monofunctional vinyl cyclopropane-amides with different side chains. *Macromolecular Chemistry and Physics*, page 2200155, 2022.

Erklärung

Hiermit versichere ich an Eides statt, dass ich die vorliegende Arbeit selbstständig verfasst und keine anderen als die von mir angegebenen Quellen und Hilfsmittel verwendet habe. Weiterhin erkläre ich, dass ich die Hilfe von gewerblichen Promotionsberatern bzw. -vermittlern oder ähnlichen Dienstleistern weder bisher in Anspruch genommen habe, noch künftig in Anspruch nehmen werde. Zusätzlich erkläre ich hiermit, dass ich keinerlei frühere Promotionsversuche unternommen habe. Die Arbeit wurde nicht bereits in gleicher oder vergleichbarer Form zur Erlangung eines akademischen Grades eingereicht.

Bayreuth, den	Sanwardhini Pantawane